UNIVERSITÀ DI PARMA

UNIVERSITA' DEGLI STUDI DI PARMA

DOTTORATO DI RICERCA IN
"SCIENZE CHIMICHE"

CICLO XXXIII

POLARIZABLE CHROMOPHORES FOR PHOTONIC APPLICATIONS: ENVIRONMENTAL AND INTERMOLECULAR INTERACTIONS

approved March 11th 2021

Coordinatore:
Prof. ssa Alessia Bacchi

Tutore:
Prof. ssa Francesca Terenziani

Dottorando: Brunella Bardi

Anni Accademici 2017/2018 – 2019/2020

Abstract

Polar/polarizable chromophores are highly responsive to external perturbations, such as polar solvation and intermolecular interactions. The effect of the surroundings on the optical properties of dyes, if properly understood, can be exploited to tune the material's response through the design of covalent or self-assembled supramolecular architectures.

In this Thesis we combined the computational (DFT and essential-state models, ESMs) and spectroscopic (absorption and emission spectroscopies) investigation of a selection of molecular/supramolecular systems, which allowed to disclose the impact of environmental and intermolecular interactions on the optical response of polar and polarizable dyes, paving the way to their knowledge-based exploitation in photonic devices.

The first part is devoted to the discussion of the spectroscopic properties of chromophores in solution, where only interactions with the solvent may contribute to the spectroscopic features of solvated dyes.

The first system under study consisted in a novel aza-nanographene dye obtained from the expansion of the electron rich pyrrolo[3,2-*b*]pyrrole moiety with fused aromatic rings. In spite of its nonpolar character and the lack of well defined electron donating and electron withdrawing groups, this system evidenced an underlying quadrupolar nature and undergoes excited-state symmetry breaking, which is responsible for a pronounced emission solvatochromism as for typical class I quadrupolar dyes. At the same time, thanks to the peculiar double-helical conformation and expanded architecture, this chromophore features a more complex spectroscopy arising from the interplay between CT and localized transitions, pointing to a unique excited-state scenario.

A large section is devoted to the family of squarylium dyes, also known as squaraines, for which a unified theoretical picture rationalizing their spectral features is still lacking. Although squaraines have been historically regarded as quadrupolar symmetry-preserving quadrupolar dyes, the description emerging from the theoretical approaches applied so far is neither exhaustive nor definitive. In this Work the standard essential-state approach was extended proposing new effective evidence-based models with the aim of improving the understanding of the intriguing electronic structure of a few representative squaraines.

The second part of this Thesis is occupied by the discussion of the effects promoted by aggregation, with a focus on modelling schemes and experimental strategies for self-assembly.

We introduced the topic with the detailed investigation of dimeric structures based on the naphthalimide building block, which provide a good starting point for the understanding of the nature of the interchromophoric coupling and its effect on the optical transitions. Indeed, the low-energy spectroscopy of these systems is dominated by localized excitations, and the intermolecular interactions are mainly excitonic, placing them in the class of J-aggregates.

Making a step further, we investigated the effects coming into play in aggregates of CT chromophores, with a specific attention on phosphorescence spectra. In these highly polarizable systems, other phenomena are expected in addition to standard excitonic effects, related to the redistribution of the electron density of the interacting molecules in response to the electric field generated by the neighbouring dyes, going under the name of mean-field effects. Herein, through the definition of an ESM for phosphorescent push-pull dyes and their related dimers, we were able to separate excitonic and mean-field effects, quantifying their contribution to absorption and emission energies. The general results obtained with ESMs were corroborated by the discussion of a specific case study concerning two highly phosphorescent polymorphs of a dinuclear Rhenium(I) complex, which demonstrated the relationship between emission colour of the crystals and molecular packing, setting the basis for phosphorescence tuning through aggregation.

From the experimental side, we addressed the characterization of multipolar 2,1,3-benzothiadiazole-based NIR emitters decorated with linear or

branched alkyl chains at different sites, which should assist self-organization and induce the formation of metastable states, highly sensitive to external stimuli (pressure, solvent/antisolvent ratio). The study of the different aggregation states allowed to unravel the interdependence between optical properties, aggregation, and external conditions.

The last part of this Thesis deals with the study of model bichromophoric systems (dyads) designed for energy and/or electron transfer, and based on the calix[4]arene scaffold.

The study of selected BODIPY-based dyads allowed to assess the factors affecting the dynamics and efficiency of energy transfer, such as the solvent polarity and the nature and conformation of the bridge. The investigation of the Nile Red/fullerene pair evidenced instead a possible competition between energy and electron transfer, pointing to a more complex and yet intriguing scenario. Lastly, we also proposed an innovative application of a calix[4]arene-based dyad undergoing energy transfer, containing the Coumarin 343/NBD pair. We proved that, after the appropriate chemical engineering, a bichromophoric calix[4]arene-based system can be exploited as a ratiometric temperature probe taking advantage of the conformational mobility of the scaffold as the driving force, and paving the way to an innovative strategy in nanothermometry.

Contents

List of Figures

List of Tables

List of Abbreviations

2PA	Two-Photon Absorption
A/D	Electron Acceptor/Electron Donor
$\mathcal{A}/\mathcal{D}$	Energy Acceptor/Energy Donor
BDT	2,1,3-Benzothiadiazole
CT	Charge-Transfer
EET	Excitation Energy Transfer
ESM(s)	Essential-State Model(s)
eT	Electron Transfer
FMO(s)	Frontier Molecular Orbital(s)
FRET	Förster Resonance Energy Transfer
ISC	Intersystem Crossing
LE	Localized Excitation
mf	Mean-Field
MLCT	Metal-to-Ligand Charge Transfer
NI(s)	Naphthalimide(s)
NLO	Nonlinear Optics
NTO(s)	Natural Transition Orbital(s)
OPA	One-Photon Absorption
PCM	Polarizable Continuum Model
PES	Potental Energy Surface
QY	Quantum Yield
SOCME(s)	Spin-Orbit Coupling Matrix Element(s)
TDA	Tamm-Dancoff Approximation
(TD)DFT	(Time-Dependent) Density Functional Theory
TTA	Triplet-Triplet Annihilation

Introduction

Photonics, i. e. the science of light generation, transmission, modulation and detection, is expected to play a strategic role in the industrial and academic research of the 21st century [1–6]. Indeed, many emerging technologies exploiting the interaction of light with matter find application in a large number of scientific and cutting-edge areas, including telecommunications [7], light generation (e. g. light emitting devices and displays) [8–12], production and storage of energy (e. g. photovoltaics) [13–15], optical sensing and imaging [16–18], diagnostics and therapeutics [19].

The interest in molecular materials for application in photonic devices has been growing quickly over the last decades, as they offer a promising alternative to purely inorganic and polymeric materials [20–22]. Among their advanteges, they benefit from a well-defined chemical structure, the easiness of synthesis and purification, reduced batch-to-batch variations and good processability, which allow the design of miniaturized structures with low toxicity and good biocompatibility. Last but not least, an important figure of merit of molecular materials is their tunability, granting the possibility to tailor the optoelectronic response in order to suit the specific needs [23–27].

Polar and polarizable molecules are the favourite building blocks of molecular materials, as they offer different levels of tunability. Typical structures are obtained from the conjugation of electron donating (D) and electron withdrawing (A) moieties according to different stoichiometries and geometries. The simplest systems are the so-called push-pull dyes, characterized by a DA motif, but also multibranched systems like quadrupolar (ADA or DAD) and octupolar (AD_3 or DA_3) are widely investigated for their linear and nonlinear optical (NLO) responses [28–31]. Push-pull and multipolar chromophores are characterized by intramolecular charge-

transfer (CT) transitions in the UV-Vis-NIR range, with large transition dipole moments [32–34].

The optical behaviour of multipolar dyes is firstly related to the specific chemical design of the conjugated backbone. For example, the choice of the identity and number of the donor/acceptor units allows to adjust the orbital energies, tuning the absorption and emission spectral window, while the nature and length of the spacers modulate the extent of electron transfer between the connected units [35–40].

As relevant to practical applications, however, a chromophore can never be regarded as an isolated entity, and the interactions with the surroundings may themselves contribute to the definition and amplification of its optical responses. Indeed, the low-energy spectroscopy of polarizable chromophores is highly responsive to environmental and intermolecular interactions [41–46].

In dilute solutions, interchromophoric interactions can be safely neglected, however, the residual interactions with the solvent affect the optical spectra of polar solutes. The polarization of solvent molecules induced by a polar chromophore creates a reaction field which can stabilize the electronic states of the solute itself, modifying its transition energies. The resulting displacement of the absorption or emission band of the solvated dye is related to the solvent polarity, and is known as solvatochromism [47, 48].

Although solvatochromic effects are typical of dipolar molecules, it is well-established that also chromophores lacking permanent ground-state dipole moment, like quadrupolar and octupolar dyes, can undergo solvatochromic shifts, which are usually related to symmetry breaking of either the ground or the excited state and are favoured by the interaction with polar solvents [49–52].

In concentrated solutions, solute-solute interactions become dominant, leading to the formation of aggregates. More than 80 years ago, Scheibe and Jelley observed for the first time the spectral changes of cyanine dyes dissolved in aqueous solution, a behaviour which later on was related to the formation of aggregates [53–55]. Aggregation, which is a fundamental process in the solid state (e.g. in films and crystals) as well as in nanosystems, is usually responsible for a variation of the spectroscopic properties with respect to the solvated monomer, both in terms of energy and intensity of

the optical transitions [56–58]. Moreover, it is well known that polarizable chromophores display nonadditive behaviour, so that unique collective and cooperative effects can be achieved in molecular assemblies, for example the amplification of NLO responses [46, 59–61]. Thus, the supramolecular organization of the aggregate must be carefully controlled in order to strenghten the sought properties, and supramolecular engineering represents a tool to optimize the material's optical performance [62–65]. Interestingly, the occurrence of metastable aggregated phases with different absorption/emission features which can be interconverted by soft external stimuli such as grinding and heating is a prerequisite for obtaining stimuli-responsive materials to be exploited in optical switches and sensors [66].

Multichromophoric assemblies are also naturally occurring functional systems [58]. The interactions between the (multi)chromophoric units embedded in photosynthetic organisms is responsible for a cascade of energy and electron transfer events, which enables the efficient harvesting and conversion of sunlight [67]. The same phenomena, energy and electron transfer, find a variety of applications in chemistry and biochemistry, among which diagnostics and assays [68–70], conformational studies of proteins and polymeric assemblies [71,72], and also photosynthetic mimicry [73]. Accordingly, the in-depth understanding of the mechanism of energy and charge transfer is strongly sought for the knowledge-based design of efficient experimental setups and devices [74–76].

Steady-state and time-resolved spectroscopic techniques are useful experimental means to investigate the optical properties of chromophores and their assemblies. At the same time, the development and validation of theoretical models provides a complementary and powerful tool to gain a deeper understanding of the structure-property relationships, and also to devise predictive guidelines for system engineering [77–79].

For instance, the most popular quantum chemical method for electronic structure calculations relies on the density functional theory (DFT) formalism which, thanks to its significant level of detail and accuracy, has been successfully implemented for the description of ground and excited-state properties of medium-sized molecular systems embedded in different environments [80]. At the same time, reliable theoretical frameworks are needed to describe interacting chromophores. The most popular in-

terpretative scheme is the so-called excitonic approximation, which introduced the nomenclature J- and H-aggregates to refer to specific red or blue shifts of the experimental absorption upon aggregation, and is usually taken as the reference for the description of molecular assemblies [56, 81].

A conceptually different approach is provided by the so-called essential-state models (ESMs), a family of parametric Hamiltonians developed and applied in the host laboratory during the last 20 years, and inspired by an original work by Mulliken [82] describing a CT complex *via* a limited number of basis states corresponding to the limiting resonance structures. In spite of their simplicity, ESMs provided a very accurate interpretative scheme for the major optical features of a large number of CT dyes, both in solution and in multichromophoric assemblies [41, 44, 46, 61, 83–86].

Placed in this broad context, this Thesis Work explores the effect of environmental and intermolecular interactions on the optical properties of polar and polarizable chromophores, adopting a combined experimental and computational approach. Different spectroscopic tools, including absorption and emission spectroscopies, and different theoretical frameworks, DFT and ESMs, were applied to selected chromophoric and multichromophoric systems of chemical and practical interest, which allowed us to gain significant knowledge of their structure-property relationships. An outline of this Thesis is schematically provided in Figure 1.

The first Chapter is devoted to the joint experimental and theoretical investigation of multipolar chromophores in solution, which allowed to relate their spectroscopic properties to their electronic structure and polar solvation. After a short introduction to ESMs, which will be recalled throughout the Thesis, we will focus on two different classes of molecular structures: a novel aza-nanographene dye undergoing excited-state symmetry breaking, and a few representative structures belonging to the family of squarylium dyes.

Interchromophoric interactions in molecular aggregates are the subject of Chapter 2. In this Chapter, the optical properties of different aggregated species (dimers, crystals, powders, nanoparticles) will be correlated to the supramolecular organization and to the nature of the interactions. Specifically, we will provide an extensive computational investigation of aggrega-

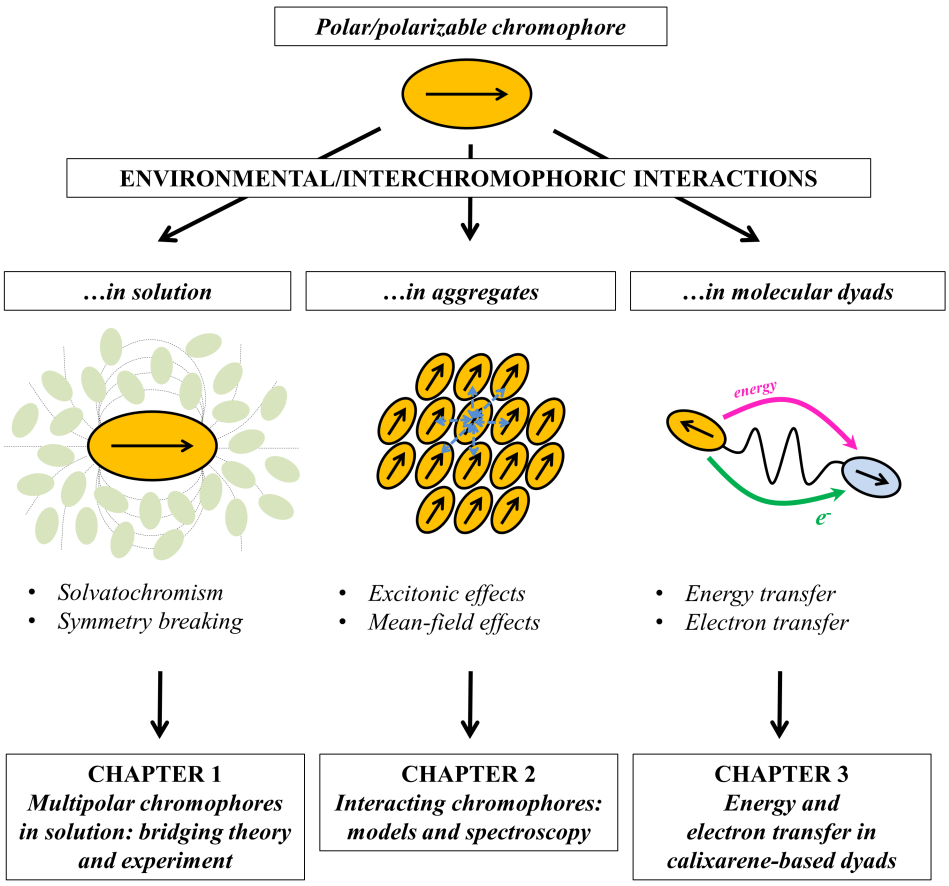

Figure 1: Outline of this Thesis work.

tion, challenging different theoretical frameworks (DFT and ESMs) with the description of selected interacting systems, but we will also provide experimental evidence of multistability in a family of multipolar NIR-emitting dyes.

Finally, Chapter 3 will be entirely devoted to energy and electron transfer in multichromophoric systems. The study of simplified structures, which are easier to handle and analyze, allows for the individuation and disentanglement of all of the key factors, setting the stage for the comprehension of more complex systems and the optimization of specific functional materials and devices. To this aim, we will report on the characterization of a few bichromophoric model systems (dyads) based on different donor/acceptor pairs bridged by a calix[4]arene scaffold, specifically designed for energy and/or electron transfer studies.

This Thesis offers new theoretical and experimental insights into the spectrosopy of polar and polarizable chromophores, emphasizing their sensitiveness to environmental and interchromophoric interactions, which can be exploited in combination with chemical design to build innovative functional materials with optimal optoelectronic responses.

Chapter 1

Multipolar dyes in solution: bridging theory and experiment

1.1 Introduction

Multipolar chromophores are networks of electron donor (D) and electron acceptor (A) groups connected by π-conjugated bridges, coming in a large variety of structures and extensively studied for opto-electronic applications [23, 31, 34, 87–91]. The simplest members of this family are dipolar chromophores, also known as 'push-pull' dyes, constituted by an electron-rich moiety joined to an electron-poor moiety through a conjugated bridge (DA structure) [32, 33, 37]. Other widely investigated structures include quadrupolar dyes, of the general formula DAD or ADA, and octupolar AD_3 or DA_3.

The photochemical behaviour of these systems is dominated by charge resonance between D and A groups, promoting low energy charge-transfer (CT) transitions, usually in the visible or near-infrared range [92, 93]. CT transitions involve massive charge redistribution over the molecule, and are highly sensitive to polar environments leading to band broadening and solvatochromic effects [94].

Solvatochromism in highly symmetric (quadrupolar and octupolar) structures is often related to symmetry-breaking phenomena affecting either the

ground or the excited state [85, 86]. According to symmetry, these dyes are expected to possess small or vanishing permanent dipole moments, limiting the interaction with polar solvents. However, the occurrence of an asymmetric charge distribution on the molecular arms driven by the interaction with polar solvents is quite common, leading to sizable solvatochromic shifts [95–101]. This phenomenon, evidenced by steady-state absorption and emission spectra, has been recently observed and confirmed by advanced time-resolved spectroscopy [50, 102–108].

The main features of multipolar CT dyes are well captured by few-state models, also called essential-state models (ESMs), constituting an alternative theoretical approach to traditional first principle methods such as (TD)DFT [83–86,109]. ESMs describe a CT dye through a minimal number of electronic basis states corresponding to its main resonating structures. These models are semi-empirical in nature, and the few parameters entering the Hamiltonian are usually extracted from experimental data or, sometimes, from independent first principle calculations. Among the advantages of ESMs is the simplicity of the approach, providing a coherent and physically sound interpretation of the electronic structure of CT dyes, usually at low computational cost, notwithstanding the complexity of the system at hand.

In this Chapter we will briefly introduce the theory of ESMs. Specifically, we will describe the two-state model for push-pull dyes [84], that will serve as an introduction to the philosophy of ESMs, and the reference three-state model for quadrupolar dyes [85], that will allow for a description of symmetry-breaking effects.

Moving on, we will present two case studies. In the first one, in collaboration with Prof. Daniel T. Gryko (Polish Academy of Sciences, Poland), we focused on excited-state symmetry breaking in a novel aza-nanographene dye possessing an underlying quadrupolar nature [110]. In this case, the ESM theoretical framework was applied in a combined approach with TDDFT and both models were validated against experimental data. The second case study, addressed in the last section of this Chapter, brings us in the intriguing world of squarylium dyes, for which first principle methods do not provide a reliable and coherent description of the electronic structure. We will examine all the challenges posed to ESMs by this family of chro-

mophores and we will consider further extension of the standard three-state model, leading us to discuss critically on its performance.

1.2 Essential-state models

The first two-state model applied to CT structures dates back to the 50's and was proposed by Mulliken to describe CT complexes [82]. With this simple model not only the stabilization of the ground state thanks to resonance was predicted, but also the presence of a low-energy state involved in the CT transition. In more recent times, the Mulliken model was adopted for the modelling of push-pull dyes, in which the D and A groups are bridged by a covalent bond [111].

Since then, the strategy was further extended with significant contributions from the host research group to include the coupling between electronic and vibrational degrees of freedom [83] and solvation effects [41,42], leading to the growth of a series of parametric Hamiltonians describing a variety of structures. ESMs were applied to systems of higher complexity such as quadrupolar [85,112] and octupolar dyes [86,113,114], metal complexes [115] and other structures [116,117]. These models were able to capture the fundamental photophysics of CT dyes with high accuracy, addressing a plethora of linear optical properties including steady-state [85, 109, 113] and time-resolved [118, 119] absorption and emission spectra, fluorescence anisotropy [120], excited-state absorption [112], electroabsorption [86, 121], vibrational (IR and Raman) spectra [122], two-dimensional electronic-vibrational spectra [123], and also NLO properties such as two-photon absorption (2PA) [124–126], two-photon excited anisotropy [99] and hyper-Rayleigh scattering (HRS) [114,127]. ESMs were able to describe symmetry breaking as well, relating it to charge instabilities of either the ground or excited state [85,86].

Moreover, starting from the modelling of the isolated (solvated) molecule, ESMs can be readily implemented for the description of clusters and aggregates, addressing their optical spectra [44, 46, 128–131] as well as more complex phenomena such as energy transfer [132–134], without redefining model parameters. ESMs description of intermolecular interactions will be addressed in detail in Chapter 2. Here, we only stick to multipolar chromophores in solution.

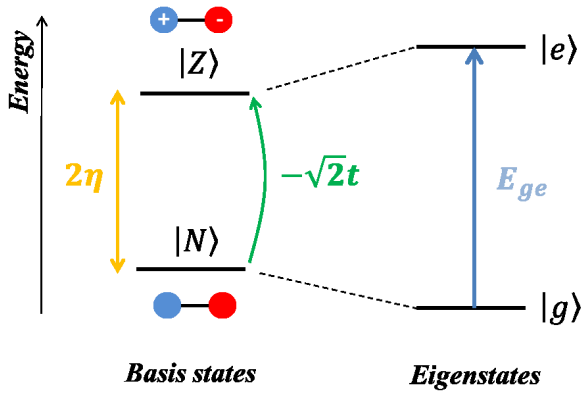

Figure 1.1: The two-state model for a dipolar (DA) dye. The basis states $|N\rangle$ and $|Z\rangle$ sketched on the left are separated by the energy 2η and are mixed by the matrix element $-\sqrt{2}t$ giving the eigenstates $|g\rangle$ and $|e\rangle$ (right). The electron donor moiety is in blue, the acceptor moiety in red.

1.2.1 Two-state Model

A push-pull system resonates between a fully neutral (DA) and a fully charge-separated structure (D^+A^-), which are chosen as the electronic basis states, called $|N\rangle$ and $|Z\rangle$ respectively [82, 83]. On this basis, the electronic Hamiltonian $\hat{H}_e$ describing the system is the following 2×2 matrix:

$$\hat{H}_e = \begin{pmatrix} 0 & -\sqrt{2}t \\ -\sqrt{2}t & 2\eta \end{pmatrix} \tag{1.1}$$

where we set 2η as the energy difference between the two basis states, corresponding to the energy required for complete charge separation, and $-\sqrt{2}t$ as the matrix element that mixes them, indicating the probability of electron transfer from the D to the A site (Figure 1.1, left).

The Hamiltonian in Eq. 1.1 can be diagonalized analytically yielding the ground state $|g\rangle$ and the excited state $|e\rangle$ (Figure 1.1, right), that can be expressed as linear combinations of the $|N\rangle$ and $|Z\rangle$ states:

$$|g\rangle = \sqrt{1-\rho}\,|N\rangle + \sqrt{\rho}\,|Z\rangle \tag{1.2}$$

$$|e\rangle = \sqrt{\rho}\,|N\rangle - \sqrt{1-\rho}\,|Z\rangle \tag{1.3}$$

In the equations above, the quantity ρ, also called ionicity, is defined as the expectation value of the ionicity operator $\hat{\rho}$ in the ground state: $\rho = \langle g| \hat{\rho} |g\rangle$, where

$$\hat{\rho} = \begin{pmatrix} 0 & 0 \\ 0 & 1 \end{pmatrix} \tag{1.4}$$

is the operator counting the charges on the A site. ρ measures the weight of the zwitterionic state in the ground state, i.e. is an indicator of the polarity of the dye. The polarity of the dye switches from ρ in the ground state to $\langle e| \hat{\rho} |e\rangle = 1 - \rho$ upon photoexcitation to the $|e\rangle$ state. Chromophores with $\rho < 0.5$ ($\eta > 0$) possess a mainly neutral ground state and are usually called neutral dyes, while $\rho > 0.5$ ($\eta < 0$) defines mostly zwitterionic chromophores. For $\rho = 0.5$ we are in the situation referred to as cyanine limit.

ρ is related to the model parameters as follows:

$$\rho = \frac{1}{2}\left(1 - \frac{\eta}{\sqrt{\eta^2 + 2t^2}}\right) \tag{1.5}$$

The energy difference between the $|g\rangle$ and $|e\rangle$ states, i.e. the energy of the $|g\rangle \rightarrow |e\rangle$ transition, E_{ge}, amounts to:

$$E_{ge} = \frac{\sqrt{2}t}{\sqrt{\rho(1-\rho)}} \tag{1.6}$$

To get the absolute intensity of the transition, a dipole moment operator $\hat{\mu}$ must be defined on the chosen basis. According to Mulliken [82], the dipole moment of the $|Z\rangle$ state, μ_0, is much larger than all other matrix elements of $\hat{\mu}$, so that in the simplest approximation, it is the only non-vanishing element:

$$\hat{\mu} = \begin{pmatrix} 0 & 0 \\ 0 & \mu_0 \end{pmatrix} = \mu_0 \hat{\rho} \tag{1.7}$$

and has only one component, aligned with the molecular axis. It follows that, the transition dipole moment for absorption, μ_{ge}, reads:

$$\mu_{ge} = \mu_0 \sqrt{\rho(1-\rho)} \tag{1.8}$$

while $\mu_0\rho$ and $\mu_0(1-\rho)$ are the permanent dipole moments of the dye in the ground and excited state, respectively.

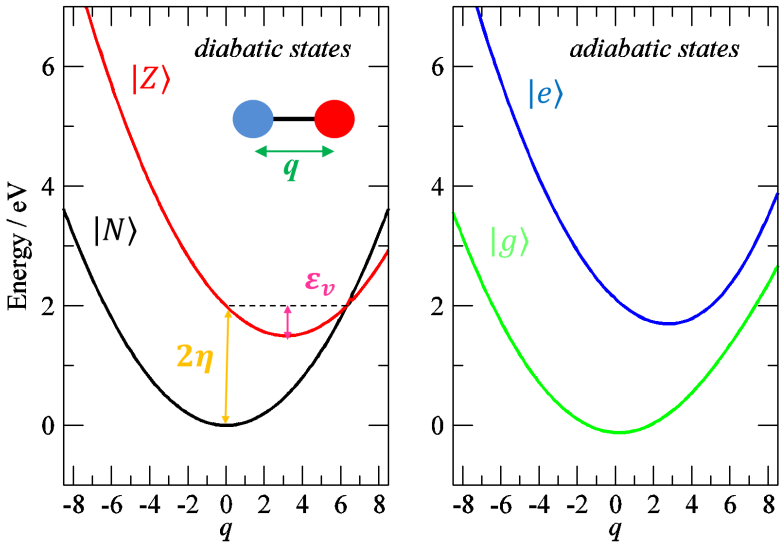

Figure 1.2: Potential energy surfaces (PES) related to the diabatic (left) and adiabatic (right) states of a dipolar (DA) dye. The vibrational relaxation energy ε_v quantifies the energy gain following nuclear relaxation of $|Z\rangle$. Model parameters: $\eta = 1.0$ eV, $\sqrt{2}t = 0.5$ eV, $\omega_v = 0.2$ eV, $\varepsilon_v = 0.5$ eV.

This simple model can be extended to include the coupling between electronic and vibrational degrees of freedom [42, 83], allowing to reproduce vibronic bandshapes. Intramolecular vibrations are described introducing a single effective vibrational coordinate q with harmonic frequency ω_v and relaxation energy ε_v. The vibrational relaxation energy quantifies the energy gained from relaxation along q after the $|N\rangle \rightarrow |Z\rangle$ transition (Figure 1.2), and, practically, measures the strength of electron-phonon coupling. On these grounds the vibrational Hamiltonian $\hat{H}_v$ reads:

$$\hat{H}_v = \omega_v \sqrt{2\varepsilon_v} q + \frac{1}{2}(\omega_v^2 q^2 + p^2) \tag{1.9}$$

where q is the vibrational coordinate and p its conjugate momentum.

The coupled electronic and vibrational problem $\hat{H} = \hat{H}_e(q) + \hat{H}_v(q)$ can be solved adiabatically, for different values of q, to get the adiabatic states $|g(q)\rangle$ and $|e(q)\rangle$ (Figure 1.2, right) [41, 42, 83, 109].

In the following, we address the non-adiabatic solution of the problem. The total Hamiltonian $\hat{H} = \hat{H}_e + \hat{H}_v$ is written on the basis given by the direct product of the two electronic basis states times the eigenstates of the harmonic oscillator associated to the vibrational coordinate. Of course the latter defines an infinite basis set and the problem is made numerically tractable truncating the basis to the first M states, reducing to a $2M$-dimensional problem. Typically, according to each specific system, the chosen value of M is large-enough to guarantee convergence. Numerical diagonalization of the Hamiltonian yields the $2M$ vibronic eigenstates of the system ψ_i.

Spectra are obtained calculating transition dipole moments between pairs of states $\mu_{jk}^2 = |\langle\psi_j|\hat{\mu}|\psi_k\rangle|^2$, assigning a Gaussian bandshape with half-width at half-maximum $\gamma = \sqrt{2\ln 2}\sigma$ to each transition and summing up on all relevant vibronic transitions as required by the property of interest. For example, absorption and emission spectra, $\varepsilon(\tilde{\nu})$ and $I(\tilde{\nu})$ respectively, can be calculated as follows [109]:

$$\varepsilon(\tilde{\nu}) = \frac{10\pi N_A \tilde{\nu}}{3\ln 10 \hbar c \epsilon_0} \frac{1}{\sqrt{2\pi}\sigma} \sum_n \mu_{gn}^2 \exp\left[-\frac{1}{2}\left(\frac{\tilde{\nu}_{gn} - \tilde{\nu}}{\sigma}\right)^2\right] \tag{1.10}$$

$$I(\tilde{\nu}) \propto \tilde{\nu}^3 \frac{1}{\sqrt{2\pi}\sigma} \sum_n \mu_{fn}^2 \exp\left[-\frac{1}{2}\left(\frac{\tilde{\nu}_{fn} - \tilde{\nu}}{\sigma}\right)^2\right] \tag{1.11}$$

where N_A is the Avogadro number, c the speed of light in vacuum, ϵ_0 the vacuum electric permittivity, g and f label the ground and fluorescent states respectively and n runs over the vibronic states ($n = 2, \ldots, 2M$ for absorption and $n = 1, \ldots, f-1$ for emission). Individuation of the fluorescent state is a nontrivial task, since all states are vibronic in nature and the ground and excited-state manifold are ill-defined in this picture. Usually, the choice of the fluorescent state is based on the evaluation of transition dipole moment from the ground state, getting the state possessing a dipole moment larger than a fixed threshold, having the character of electronic excited state.

So far we have described an isolated molecule in gas-phase. Usually spectroscopic data are collected in dilute solution, where the solute interacts with the surrounding solvent molecules. This interaction may lead to important spectroscopic effects, namely solvatochromism [41, 42, 94] and inhomogeneous broadening [122]. Hence, the description of solvation is a required step further.

Solvation is introduced in the ESMs in a reaction-field approach [42, 84, 109]. The solute is placed in a cavity inside the solvent, treated as a continuous dielectric medium. The (polar) solute polarizes the surrounding solvent molecules, which generate a reaction field F_R proportional to the dipole moment of the solute itself. Two contributions to the reaction field can be distinguished: an electronic and an orientational component [94,135].

The electronic component is originated by the distortion of the electronic clouds of solvent molecules in response to the electronic excitation of the solute, and occurs on a very short timescale compared to the electronic and vibrational degrees of freedom of the solute, with typical frequencies in the UV. This fast component can be treated in the anti-adiabatic approximation, and results in a renormalization of model parameters mainly dependent on the solvent refractive index [41, 42, 84]. Since common organic solvents are characterized by very similar refractive indexes, we consider the parameters to be solvent-independent.

The orientational component, relevant to polar solvents only, originates from the reorientation of solvent molecules around the solute [136] and is characterized by slow motion (typical frequencies are in the microwave range), therefore it enters the Hamiltonian as an overdamped coordinate. Assuming that the solvent response to an external electric field is linear, the orientational component of the reaction field at equilibrium F_{or}^{eq} is proportional to the dipole moment of the solute $\langle\mu\rangle$: $F_{or}^{eq} = r_{or}\langle\mu\rangle$, where r_{or} is related to solute cavity and the dielectric properties of the solvent, namely refractive index and dielectric constant. Treating the solvent as an elastic medium, the Hamiltonian describing polar solvation $\hat{H}_s$ reads:

$$\hat{H}_s = -F_{or}\hat{\mu} + \frac{\mu_0^2 F_{or}^2}{4\varepsilon_{or}} \tag{1.12}$$

where the solvation relaxation energy $\varepsilon_{or} = \frac{r_{or}\mu_0^2}{2}$ is the solvation counterpart of ε_v for vibrations and increases with solvent polarity.

This approach naturally describes solvatochromic shifts of push-pull dyes: for chromophores which are mainly neutral in the ground state, an increase of solvent polarity reduces the energy gap between $|g\rangle$ and $|e\rangle$, leading to a positive solvatochromism. On the opposite, molecules which are mainly ionic in the ground state withstand an increase of the transition energy

with solvent polarity, showing a negative solvatochromism. Spectra of chromophores in the cyanine limit are instead insensitive to solvent polarity.

Another solvent effect concerns band broadening in polar solvents. This phenomenon is related to thermal disorder, that causes fluctuations of F_{or} around its equilibrium value. Specifically, each molecule in the sample experiences a slightly different orientational field, due to the disordered arrangement of the surrounding molecules, so that a distribution of F_{or} values must be considered, according to Boltzmann probability at the given temperature [84, 109, 122].

To tackle this issue, a grid of F_{or} values is defined, and the total Hamiltonian $\hat{H} = \hat{H}_e + \hat{H}_v + \hat{H}_s$ is diagonalized for each point of the grid, calculating the corresponding spectrum. The thermally-averaged spectrum is obtained summing up the spectra calculated for all the F_{or} values, each one weighted by the corresponding Boltzmann probability, remembering that the F_{or} distribution relevant to absorption is the one induced by the ground state dipole moment, while the distribution relevant to emission is the one generated by the excited state.

The few parameters entering the Hamiltonian (η, t, ω_v, ε_v, μ_0, γ and ε_{or}) are semi-empirical in nature and are usually extracted from the comparison with experiment, selecting the set that best fits available experimental data (usually steady-state absorption and emission spectra at room temperature). In more detail, η and t are related to the transition energy and intensity, ω_v, ε_v and γ are tuned to reproduce the vibronic progression in non-polar solvents and μ_0 is fixed after the molar extinction coefficient. ε_{or} is the only solvent-dependent parameter and accounts, alone, for the effects of polar solvation. All the other parameters are solvent-independent and are only related to the specific system at hand: once they have been fixed they allow for the calculation of all spectroscopic properties of interest without the need for re-optimization.

1.2.2 Three-state Model

A quadrupolar ADA (or, equivalently, DAD) chromophore can be described *via* three basis states: a neutral $|N\rangle$ state, corresponding to the ADA structure, and two degenerate zwitterionic states, $|Z_1\rangle$ and $|Z_2\rangle$, corresponding to the A^-D^+A and AD^+A^- resonance structures, respectively [85]. To ac-

quire more generality, we assume that the chromophore possess a V-shaped structure, with the molecular arms forming an angle α [127, 130, 137]. Exploiting C_{2v} symmetry, the zwitterionic states can be conveniently combined into symmetry-adapted $|Z_+\rangle$ and $|Z_-\rangle$ wavefunctions:

$$|Z_+\rangle = \frac{1}{\sqrt{2}}(|Z_1\rangle + |Z_2\rangle) \tag{1.13}$$

$$|Z_-\rangle = \frac{1}{\sqrt{2}}(|Z_1\rangle - |Z_2\rangle) \tag{1.14}$$

On this basis we define the following operators:

$$\hat{\rho} = \begin{pmatrix} 0 & 0 & 0 \\ 0 & 1 & 0 \\ 0 & 0 & 1 \end{pmatrix} \tag{1.15}$$

$$\hat{\sigma} = \begin{pmatrix} 0 & 1 & 0 \\ 1 & 0 & 0 \\ 0 & 0 & 0 \end{pmatrix} \tag{1.16}$$

$$\hat{\delta} = \begin{pmatrix} 0 & 0 & 0 \\ 0 & 0 & 1 \\ 0 & 1 & 0 \end{pmatrix} \tag{1.17}$$

where $\hat{\rho} = \hat{\rho}_1 + \hat{\rho}_2$ measures the average charge on the D site, $\hat{\sigma}$ mixes the symmetric states and $\hat{\delta} = \hat{\rho}_1 - \hat{\rho}_2$ measures the charge unbalance between the acceptors. The electronic Hamiltonian $\hat{H}_e$ reads:

$$\hat{H}_e = 2\eta\hat{\rho} - \sqrt{2}t\hat{\sigma} = \begin{pmatrix} 0 & -\sqrt{2}t & 0 \\ -\sqrt{2}t & 2\eta & 0 \\ 0 & 0 & 2\eta \end{pmatrix} \tag{1.18}$$

where 2η is the energy gap between the neutral and the zwitterionic states, and the CT integral $-\sqrt{2}t$ quantifies the probability of electron hopping from the central donor to either of the A groups. Analytical diagonalization of Eq. 1.18 yields the following eigenstates:

$$|g\rangle = \sqrt{1-\rho}\,|N\rangle + \sqrt{\rho}\,|Z_+\rangle \tag{1.19}$$

$$|c\rangle = |Z_-\rangle \tag{1.20}$$

$$|e\rangle = \sqrt{\rho}\,|N\rangle - \sqrt{1-\rho}\,|Z_+\rangle \tag{1.21}$$

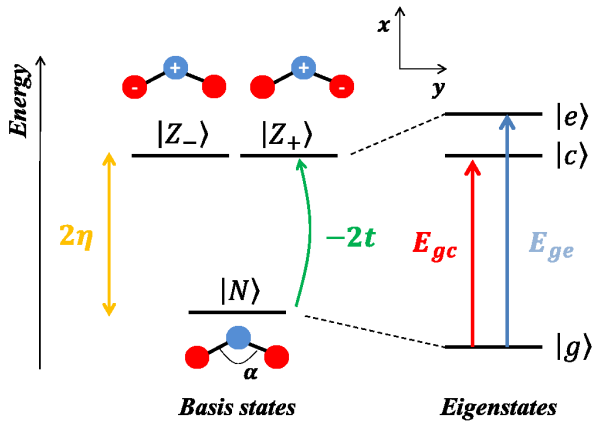

Figure 1.3: The three-state model for a quadrupolar (ADA) dye. Left: sketch of the basis states $|N\rangle$, $|Z_1\rangle$ and $|Z_2\rangle$. The electron donor moiety is in blue, the acceptor moiety in red. The dye has a bent structure, with the molecular arms forming an angle α. Cartesian axes are introduced for the definition of the dipole moment operator (see text). Right: sketch of the eigenstates. Two CT transitions from the ground state $|g\rangle$ to the excited states $|c\rangle$ and $|e\rangle$ are allowed in absorption, with energies E_{gc} and E_{ge} respectively.

The $|c\rangle$ state coincides with $|Z_-\rangle$ which, being the only antisymmetric state, stays unmixed. The mixing of the symmetric states $|N\rangle$ and $|Z_+\rangle$ yields the ground state $|g\rangle$ and the excited state $|e\rangle$ (Figure 1.3). The ionicity ρ, defined as the expectation value of $\hat{\rho}$ (Eq. 1.15) in the ground state, gives the weight of the $|Z_+\rangle$ state in the $|g\rangle$ state, and is a measure of the quadrupolar character of the dye. The following relation exists between ρ and the model parameters η and t:

$$\rho = \frac{1}{2}\left(1 - \frac{\eta}{\sqrt{\eta^2 + 4t^2}}\right) \tag{1.22}$$

From the ground-state, two CT transitions can occur, $|g\rangle \rightarrow |c\rangle$ and $|g\rangle \rightarrow |e\rangle$, with energies E_{gc} and E_{ge} respectively (see Figure 1.3, right):

$$E_{gc} = 2t\sqrt{\frac{1-\rho}{\rho}} \tag{1.23}$$

$$E_{ge} = 2t\sqrt{\frac{1}{\rho(1-\rho)}} \tag{1.24}$$

The dipole moment operator $\hat{\mu}$ has two components, $\hat{\mu}_x$ and $\hat{\mu}_y$ aligned with the short and long molecular axes respectively. We neglect all the

matrix elements of the dipole moment operator except from μ_0, the dipole moment of the zwitterionic states, obtaining:

$$\hat{\mu}_x = \mu_0 \sin\frac{\alpha}{2}(\hat{\rho}_1 - \hat{\rho}_2) \tag{1.25}$$

$$\hat{\mu}_y = \mu_0 \cos\frac{\alpha}{2}(\hat{\rho}_1 + \hat{\rho}_2) \tag{1.26}$$

It follows that the transition dipole moments for the CT transitions are:

$$\mu^x_{gc} = \sqrt{\rho}\mu_0 \sin\frac{\alpha}{2} \quad \mu^y_{gc} = 0 \tag{1.27}$$

$$\mu^x_{ge} = 0 \quad \mu^y_{ge} = \sqrt{\rho(1-\rho)}\mu_0 \cos\frac{\alpha}{2} \tag{1.28}$$

In a V-shaped dye, both $|g\rangle \rightarrow |c\rangle$ and $|g\rangle \rightarrow |e\rangle$ transitions are symmetry-allowed and are polarized along the x and y axes respectively [127,130,137]. In the limit $\alpha = 180°$, i.e. for linear centrosymmetric molecules, only the transition towards the $|c\rangle$ state is bright in linear absorption, while the $|e\rangle$ state can be reached upon two-photon absorption only [85].

Nuclear motion in a quadrupolar dye can be described introducing two equivalent mutually independent vibrational coordinates, q_1 and q_2, with frequency ω_v, one for each molecular arm. The vibrational relaxation energy ε_v measures the energy gained upon relaxation towards the equilibrium geometry following the $|N\rangle \rightarrow |Z_1\rangle$ and $|N\rangle \rightarrow |Z_2\rangle$ processes. q_1 and q_2 can be combined into the symmetrized coordinates $q_+ = 1/\sqrt{2}(q_1 + q_2)$ and $q_- = 1/\sqrt{2}(q_1 - q_2)$, and the vibrational Hamiltonian $\hat{H}_v$ can be written as follows [85]:

$$\hat{H}_v = -\sqrt{\varepsilon_v}\omega_v q_+ \hat{\rho} - \sqrt{\varepsilon_v}\omega_v q_- \hat{\delta} + \frac{1}{2}(\omega_v^2 q_+^2 + p_+^2) + \frac{1}{2}(\omega_v^2 q_-^2 + p_-^2) \tag{1.29}$$

where we indicated with p_+ and p_- conjugated momenta. The first two terms express the electron-phonon coupling, while the last two terms are the Hamiltonians of the harmonic oscillators associated to the vibrational coordinates. The q_- coordinate is coupled to the antisymmetric $\hat{\delta}$ operator, therefore oscillations along q_- modulate the mixing between states with different symmetry, inducing a charge unbalance between the external A groups, and is the coordinate responsible for symmetry-breaking.

Adiabatic solution of $\hat{H} = \hat{H}_e + \hat{H}_v$ gives three (q_+, q_-)-dependent eigenstates, whose energies define the potential energy surfaces (PES) of the system. Stable states relative to symmetry breaking are characterized by a

single minimum located at $q_- = 0$ and $q_+ = \sqrt{\varepsilon_v}\langle\rho\rangle/\omega_v$, being $\langle\rho\rangle$ the expectation value of $\hat{\rho}$ in the relevant state. Unstable states are characterized by a saddle point at $q_- = 0$ and two equivalent minima at $q_- = \pm\sqrt{\varepsilon_v}\langle\delta\rangle/\omega_v$.

Looking at the PES, we can recognize three different behaviours, depending on the quadrupolar character (ρ) and the strength of electron-phonon coupling (ε_v), allowing us to define the phase diagram in Figure 1.4 [85].

Chromophores with small degree of charge-transfer in the ground state, i.e. low quadrupolar character ($\rho \lesssim 0.2$), belong to class I. In this region the first excited state is bistable and the system can relax in one of the two equivalent minima, breaking its symmetry. The symmetry-broken $|c\rangle$ state possess a dipolar character, and is stabilized by polar solvents, originating positive emission solvatochromism. Systems with intermediate ionicity ($\rho \approx 0.3-0.6$) belong to class II. In this region all the PES are characterized by a single minimum, thus for these systems we do not expect solvatochromic shifts neither in absorption nor in emission. Molecules with high quadrupolar moment ($\rho \to 1$) are located in the rightmost region of the diagram (class III). Their excited states are all stable, but charge instability occurs in the ground-state. For such systems, a negative solvatochromic shift is predicted in absorption together with important inhomogeneous broadening effects.

Examples of quadrupolar chromophores are known for all the three classes presented above. Class I comprises a wide series of molecules with weak or moderate D and A groups. Dyes modelled so far include substituted distyrylbenzenes [85], fluorene-based [85, 99] and benzothiadiazole-based [130] chromophores. Many other dyes have not been parametrized yet but show the characteristic spectroscopic features of excited-state symmetry breaking [50, 95–98, 100–108, 138]. The modelling of a pyrrolo[3,2-*b*]pyrrole quadrupolar-like dye belonging to class I will be presented in the next section [110]. Squaraines were originally presented as typical class II dyes [85]. However, the modelling of squaraines has always been controversial, at least when looking in detail at their spectroscopic properties in the whole UV/vis range [139]. We will devote the last section of this Chapter to the critical review and discussion of ESMs for this family of dyes. Long chain cyanine dyes are instead an example of class III chromophores [112, 140].

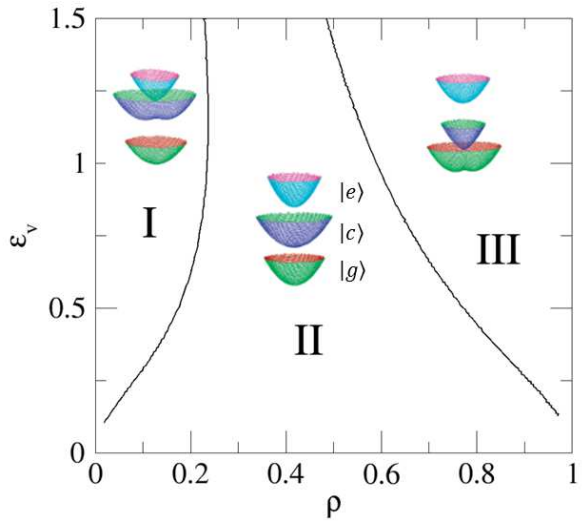

Figure 1.4: Phase diagram for quadrupolar dyes indicating the stability of the potential energy surfaces for the states $|g\rangle$, $|c\rangle$ and $|e\rangle$ (sketched in each region) as a function of the ionicity ρ and the vibrational relaxation energy ε_v (units of $\sqrt{2}t$). Region I: the $|c\rangle$ state is bistable; region II: all states have a single minimum; region III: the $|g\rangle$ state is bistable.

As for dipolar chromophores, polar solvation is introduced in a reaction-field approach [85]. The relevant Hamiltonian, $\hat{H}_s$, reads:

$$\hat{H}_s = -\hat{\mu}_x F_x - \hat{\mu}_y F_y + \frac{\mu_0^2}{4\varepsilon_{or}}(F_x^2 + F_y^2) \tag{1.30}$$

where F_x and F_y are the x and y components of the orientational field. F_x couples to the $\hat{\delta}$ operator as the q_- coordinate, and therefore cooperates with vibrational coupling in driving symmetry breaking. Also in this case, the orientational field enters the Hamiltonian as a classical variable and the total Hamiltonian $\hat{H} = \hat{H}_e + \hat{H}_v + \hat{H}_s$ is diagonalized non-adiabatically for different (F_x, F_y) points obtaining a set of $3M^2$ vibronic eigenstates, being M the dimension of the basis for each oscillator, and thermally-averaged spectrum is obtained.

1.3 Excited-state symmetry breaking in an aza-nanographene dye

Compound **1** (Figure 1.5) belongs to a family of butterfly-shaped π-expanded pyrrolo[3,2-*b*]pyrroles recently reported by Gryko and coworkers [141]. Pyrrolo[3,2-*b*]pyrrole (PP) is a heterocyclic electron-rich building block exploited in organic chemistry for the construction of materials for organic electronics, photonics and photovoltaics [142–144]. In **1**, the PP core is expanded with 12 fused aromatic rings forming two large wings at the periphery. The resulting structure is an aza-nanographene analogue, in which two Nitrogen atoms are embedded in a graphene-like architecture [145–147]. Steric hindrance between hydrogen atoms pointing inside the wings force this aza-nanographene in a non-planar conformation [141]. Because of its non-planar structure, **1** possesses three confomational isomers: two enantiomeric double-helical twisted forms, and a folded *meso* form (Figure 1.5, bottom). Conformational study in gas phase indicated that the twisted forms are more stable by 8.9 kJ mol^{-1} with respect to the folded form, the interconversion barrier between the two forms amounting to 56.0 kJ mol^{-1}. Thanks to this low energy barrier it was not possible to separate the isomers, that were found to coexist in the crystalline phase [141].

The absorption spectrum of **1** (Figure 1.6 (a)) [141] spans a large portion of the UV range, with a tail in the blue. It shows a complex structure, with

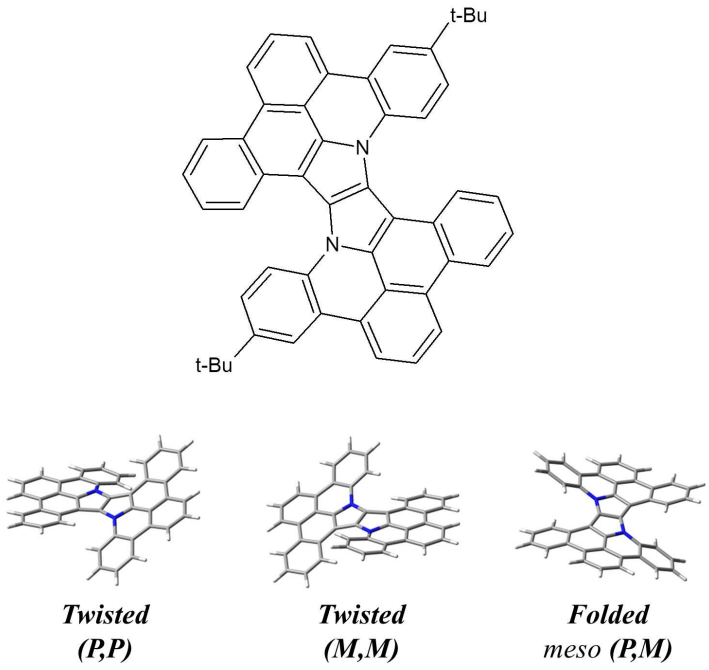

Figure 1.5: The butterfly-shaped aza-nanographene dye **1**. Top: molecular structure of **1**. Bottom: the conformational isomers of **1**, two twisted enantiomeric forms and one *meso* folded form. For clarity *tert*-butyl groups are substituted with hydrogen atoms.

two groups of closely spaced bands, one in the 300-350 region, with a maximum at $\lambda \approx 350$ nm, and another below 400 nm, peaking at $\lambda \approx 430$ nm. Absorption bands are almost insensitive to solvent polarity.

A solvatochromic behaviour was instead found in emission (Figure 1.6 (b)) [141]. Fluorescence occurs in the blue in cyclohexane ($\lambda \approx 450$ nm) and is red-shifted to $\lambda > 500$ nm in dimethyl sulfoxide. The shift is accompanied by a change of bandshape as well: the vibronic progression is recognizable in non-polar solvents and is smeared out as the solvent polarity increases. Fluorescence quantum yields are in the range 17 to 32% and do not follow a trend with polarity, with emission lifetimes in between 16.8 and 18.9 ns.

Solvatofluorochromism of **1** is hardly explained by its nonpolar structure, which should grant for small dipole moment both in the ground and excited states. Spectroscopic evidence suggests the occurrence of excited-state symmetry-breaking, as it occurs for class I quadrupolar dyes. Indeed, PP is known to act as electron donor in quadrupolar dyes undergoing symmetry breaking, when conjugated to strong electron-withdrawing groups such as cyano [104, 105], nitro [138, 148, 149] and carbonyl groups [150].

The structure of **1** is however qualitatively different, since the molecular structure originates by the expansion of the PP itself and lacks well-defined acceptor groups. Observation of symmetry-breaking in a non quadrupolar-like structure inspired further detailed experimental and theoretical study of **1** [110]. Firstly, we undertook a more in-depth characterization of the electronic transitions, performing fluorescence anisotropy measurements. Even more interestingly, anisotropy was found to behave very differently with respect to standard quadrupolar dyes. Quantum mechanical study through time-dependent density functional theory (TDDFT) was crucial in rationalizing experimental data, confirming an underlying quadrupolar nature of **1**. On TDDFT results we finally validated the three-state model, safely locating **1** in class I.

1.3.1 Fluorescence anisotropy measurements

Fluorescence anisotropy is a phenomenon widely exploited for the investigation of the relative polarization of the transitions of organic fluorophores [151]. Specifically, the fundamental anisotropy r_0 of a chromophore is related

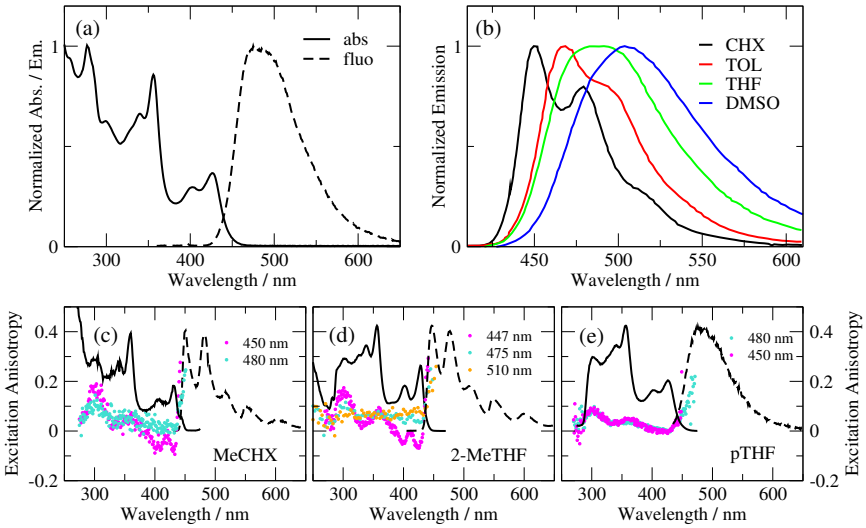

Figure 1.6: Experimental data of **1**. (a) Absorption (continuous line) and emission (dashed line) spectra in 2-methyltetrahydrofuran at room temperature. (b) Emission spectra in solvents of different polarity (CHX: cyclohexane, TOL: toluene, THF: tetrahydrofuran, DMSO: dimethyl sulfoxide). (c-e) Fluorescence excitation anisotropy (dots) in different solvents (MeCHX: glassy methyl cyclohexane at 77K, 2-MeTHF: glassy 2-methyltetrahydrofuran at 77K, pTHF: polytetrahydrofuran at room temperature). Emission wavelengths are reported in the legends. Excitation and emission spectra (continuous and dashed lines respectively) collected under the same experimental conditions are reported as a guide to the eye.

to the angle α between its absorption and emission dipole moments [151,152]:

$$r_0 = \frac{2}{5}\left(\frac{3\cos^2\alpha - 1}{2}\right) \tag{1.31}$$

A detailed introduction to the theory as well as the experimental setup for anisotropy measurements can be found in Appendix A.

Fluorescence anisotropy measurements on **1** were performed in frozen solvents of different polarity, namely a nonpolar solvent, methylcyclohexane, and a mildly polar solvents, 2-methyltetrahydrofuran (Figure 1.6 (c-d)) and also in a viscous solvent, polytetrahydrofuran, at room temperature (Figure 1.6 (e)). These conditions prevent the solute molecules to rotate during the excited-state lifetime, avoiding depolarization effects and allowing the direct measurement of r_0. In addition, while in liquid solvents the solvent molecules can reorient around the solute stabilizing polar excited states, in frozen solvents the rotational motion is hindered and the solvent is blocked in the configuration equilibrated with the ground-state of the solute.

Excitation anisotropy of **1** is independent of the experimental conditions (solvent, temperature and emission wavelength). Starting from $r_0 \approx 0.1$ at $\lambda \approx 300$ nm, anisotropy smoothly decreases to about $r_0 = 0$ at $\lambda \approx 430$ nm, corresponding to the first absorption maximum. In frozen solvents, for detection at the 0-0 vibronic line of the emission spectrum ($\lambda = 450$ nm), r_0 covers a wider range of values, between -0.1 and 0.2. For excitation at wavelenghts longer than 430 nm, r_0 increases steeply, reaching $r_0 \approx 0.25$ on the red-edge of the absorption band which overlaps with emission.

On more general grounds, when a chromophore is excited to one of its optically allowed states S_n, it then relaxes on a fast timescale through internal conversion to the lowest-energy excited state S_1, which is responsible for fluorescence emission (Kasha rule). It follows that the emission dipole moment addressed in an anisotropy experiment is always the same (the one of $S_0 \leftarrow S_1$), while the excitation dipole moment depends on the transition promoted in absorption. For excitation inside the $S_0 \rightarrow S_1$ band, the very same states are involved in absorption and emission, so that relevant dipole moments are parallel and $r_0 = 0.4$. This strategy is useful to locate the $S_0 \rightarrow S_1$ transition in the absorption spectrum. Indeed, for prototypical quadrupolar chromophores $r_0 \approx 0.4$ over a wide spectral range in the low-energy region [127, 130].

Excitation anisotropy of **1** suggests that the absorption peak at $\lambda \approx 430$ nm is not involving the S_1 state, as in this region $r_0 \approx 0$, rather indicating a $S_0 \rightarrow S_n$ transition forming with emission an angle close to the magic angle ($\alpha = 54.7°$). Indeed, anisotropy increases for $\lambda > 430$ only, suggesting the presence of another state with different polarization ($\alpha \approx 30°$, or an angle with the same squared cosine) and low oscillator strength.

Another hint of the non-coincidence of the state absorbing at $\lambda \approx 430$ nm with the emitting state comes from the inspection of excitation and emission spectra in glassy solvents, where stabilization of the excited state by polar solvation cannot occur, leading to vanishing Stokes shift. Emission spectra overlap with excitation spectra only in the weak tail in which $r_0 \rightarrow 0.25$, suggesting an underlying band of the $S_0 \rightarrow S_1$ transition.

Moreover, the oscillator strength of the band at $\lambda \approx 430$ nm amounts to ~ 0.3, corresponding to a transition dipole moment of ~ 6 D, while the emission transition dipole estimated from the Weisskopf-Wigner equation [153, 154] amounts only to ~ 3 D independently of the solvent, claiming at the non-correspondence between absorbing and emitting states.

All these observations will be fully supported by the theoretical investigation reported below.

1.3.2 TDDFT study

Both conformational isomers of **1** were considered in theoretical modelling (for the twisted form, the (*P*,*P*) enantiomer was selected). Optimization of the ground-state geometry of **1** was performed at DFT level [155–157] with Becke, 3-parameters, Lee-Yang-Parr (B3LYP) [158] hybrid functional and Pople 6-31+G(d,p) basis set, as implemented in the Gaussian16 package [159]. For the theoretical background of (TD)DFT the reader is referred to Appendix B. We are interested in the symmetry-breaking phenomenon, which is favoured by polar solvation [85], therefore all calculations were made in a highly polar solvent, dimethyl sulfoxide ($\epsilon_{DMSO} = 46.7$), implemented in the framework of the polarizable continuum model (PCM) approach [160,161]. In order to save computational resources, *tert*-butyl groups were substituted with hydrogen atoms, assuming that this has marginal spectroscopic effects.

The twisted isomer was found to be more stable by 9.9 kJ mol^{-1} than the folded form. Thus, at equilibrium, the chromophore is expected to exist mainly in one of its twisted forms which are responsible for the spectroscopic features of **1**. In the following, however, for the sake of completeness, we will report results obtained for both isomers, even if we will focus mainly on the twisted form.

The lowest-energy electronic transitions were investigated *via* time dependent DFT (TDDFT) [162–165], obtaining the data in Table 1.1. In gas-phase, two main transitions were found at $\lambda = 413.4$ and $\lambda = 357.9$ nm, corresponding to $S_0 \rightarrow S_3$ and $S_0 \rightarrow S_5$, polarized along the ideal plane of the molecule. The lowest-energy excitations ($S_0 \rightarrow S_1$ and $S_0 \rightarrow S_2$) are two quasi-degenerate transitions at $\lambda \approx 436$ nm. $S_0 \rightarrow S_1$ is dark, directed along the C_2 axis, and is almost exclusively a HOMO $\rightarrow$ LUMO+1 transition. $S_0 \rightarrow S_2$ is instead weakly allowed, and involves mainly a HOMO $\rightarrow$ LUMO excitation.

In dimethyl sulfoxide the highest oscillator strength is associated again with the $S_0 \rightarrow S_3$ and $S_0 \rightarrow S_5$ transitions, found at $\lambda = 416.8$ and $\lambda = 358.6$ nm respectively, while $S_0 \rightarrow S_1$ and $S_0 \rightarrow S_2$ ($\lambda \approx 432$ nm) are one order of magnitude weaker. Frontier molecular orbitals (FMOs) involved in the aforementioned transitions are reported in Figure 1.7. Doubly-occupied orbitals (HOMO and HOMO-1) are delocalized over the whole molecule, especially on the PP core. LUMO extends over the peripheral wings, involving only in part the atoms of the PP, while LUMO+1 is localized at the periphery of the chromophore and has nodes on the core. Accordingly, both $S_0 \rightarrow S_1$ and $S_0 \rightarrow S_2$ transitions possess a partial CT character, implying a migration of electronic density from the PP to the wings. On the opposite, the intense $S_0 \rightarrow S_3$ transition coincides with HOMO$\rightarrow$ LUMO+2 excitation, and involves a redistribution of electron density over the whole molecule.

State-specific solvation [166] was considered for the three lowest-energy transitions. As expected, the largest corrections were found for CT transitions, which were red-shifted by $\sim$ 32 nm (0.2 eV) compared to linear-response, while the $S_0 \rightarrow S_3$, as for typical localized (LE) transitions, was only slightly affected, being shifted to higher energy by $\sim$ 0.04 eV only.

Very similar results were obtained for the folded isomer, as expected from the structural similarity. While the twisted isomer belongs to C_2 point group, so that all transitions are allowed by symmetry, the folded form is centrosymmetric (C_i point group), and transitions which are *gerade* with respect to the inversion centre (A_g symmetry) are symmetry-forbidden. $S_0 \rightarrow S_1$ was found at the same energy of the twisted isomer, and close to the $S_0 \rightarrow S_2$ transition that, in this case, is dark. $S_0 \rightarrow S_1$ is mainly a HOMO→LUMO excitation, thus possessing a partial CT character (FMOs of the folded isomer, not shown, are identical to those of the twisted). The most intense transitions coincide with $S_0 \rightarrow S_3$ and $S_0 \rightarrow S_4$ and do not have CT nature.

Since the folded form has a minority contribution to experimental spectra, we will compare to experiment only TDDFT results for the twisted form. Accordingly, the experimental bands at $\lambda = 427$ and $\lambda = 360$ nm can be safely assigned to the $S_0 \rightarrow S_3$ and $S_0 \rightarrow S_5$ transitions respectively, with an error within 0.02 eV. Two bright CT states having significantly lower oscillator strength (S_1 and S_2) are found at lower energy, and one of them is responsible for fluorescence, in agreement with the picture emerging from excitation anisotropy data.

When dealing with CT transitions with TDDFT, we should be aware of artifacts that could arise from the choice of the functional. B3LYP is known for pathologically underestimating the energy of CT states, and sometimes is responsible for the appearance of low-lying dark CT transitions [167–169]. In order to check the reliability of B3LYP for **1**, calculations on the twisted isomer were performed also with the exchange-correlation CAM-B3LYP functional [170].

The performance of CAM-B3LYP is quantitatively poorer: the main transitions are predicted at $\lambda = 363$ and $\lambda = 309$ nm, i.e. shifted to the blue by 0.5-0.6 eV compared to experiment. In more qualitative terms, the first three transitions are predicted in a narrow spectral range (less than 0.15 eV-wide, accounting for state-specific solvation), confirming that, irrespective of the choice of the functional, low-energy spectroscopy of **1** is governed by the interplay of the S_{1-3} states, as it emerged from B3LYP results, validating the results discussed above. For this reason in the rest of the discussion we will focus on B3LYP results only.

Table 1.1: TDDFT results for **1**: transition energies/wavelengths, oscillator strenghts (f) and main excitations involved in the lowest $S_0 \rightarrow S_n$ transitions. Calculations were done in gas phase and dimethyl sulfoxide (DMSO) for the twisted isomer, with B3LYP and CAM-B3LYP functionals. Calculations on the folded isomer were performed in DMSO only (B3LYP functional). The basis set is always 6-31+G(d,p). Data in italic were computed with state-specific solvation.

	S_n	Energy/eV	Wavelength/nm	f	Type (>20%)
	S_1	2.841	436.4	0.006	H→ L+1 (98%)
Twisted	S_2	2.843	436.1	0.055	H→ L (87%)
gasphase	S_3	3.000	413.4	0.251	H→ L+2 (79%)
B3LYP	S_4	3.393	365.4	0.002	H-1→ L+1 (82%)
	S_5	3.465	357.9	0.374	H-1→ L (79%)
	S_1	2.871 (*2.673*)	431.9 (*463.8*)	0.009	H → L+1 (98%)
Twisted	S_2	2.872 (*2.673*)	431.6 (*463.8*)	0.092	H → L (84%)
DMSO	S_3	2.974 (*3.010*)	416.8 (*411.9*)	0.410	H → L+2 (78%)
B3LYP	S_4	3.412	363.4	0.003	H-1 → L+1 (79%)
	S_5	3.457	358.6	0.547	H-1 → L (84%)
	S_1	3.410 (*3.538*)	362.8 (*350.4*)	0.967	H → L (50%)
					H → L+2 (39%)
Twisted	S_2	3.535 (*3.591*)	350.7 (*345.3*)	0.355	H → L (34%)
DMSO					H → L+2 (46%)
CAM-B3LYP	S_3	3.561 (*3.631*)	348.2 (*341.5*)	0.032	H → L+1 (84%)
	S_4	3.993	310.5	0.028	H-2 → L+2 (23%)
					H-1 → L+1 (29%)
					H → L+3 (29%)
	S_5	4.017	308.6	1.540	H-1 → L (74%)
	S_1	2.871 (*2.719*)	431.9 (*456.0*)	0.334	H → L (95%)
Folded	S_2	2.891 (*2.719*)	428.8 (*456.0*)	-	H → L+1 (98%)
DMSO	S_3	2.947 (*3.023*)	420.7 (*410.1*)	0.620	H → L+2 (92%)
B3LYP	S_4	3.340	371.2	0.957	H-1 → L (90%)
	S_5	3.375	367.3	-	H-1 → L+1 (90%)

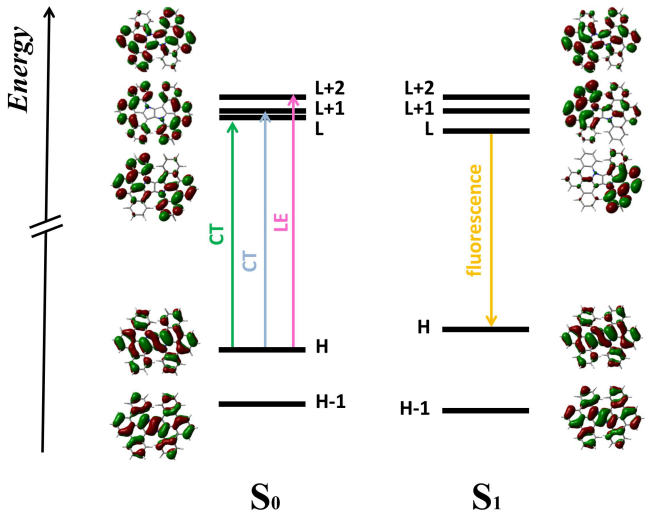

Figure 1.7: Frontier molecular orbitals (FMOs) of **1** (isovalue 0.02) for the optimized ground-state (S_0, left) and first excited-state (S_1, right) of the twisted isomer. Calculations were performed in dimethyl sulfoxide at B3LYP/6-31+G(d,p) level of theory. $S_0 \rightarrow S_1$ (green arrow) and $S_0 \rightarrow S_2$ (blue arrow) are mainly CT excitations, $S_0 \rightarrow S_3$ (in magenta) is delocalized over the whole molecule. Fluorescence ($S_0 \leftarrow S_1$) is given in orange.

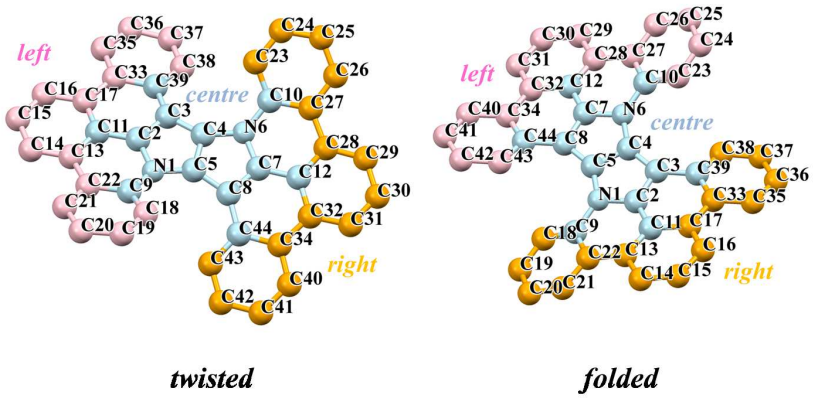

twisted ***folded***

Figure 1.8: Optimized S_1 geometries of twisted and folded isomers of **1** in dimethyl sulfoxide (B3LYP/6-31+G(d,p)). The molecules are partitioned in three regions: left (pink), centre (light blue) and right (orange) to define charge distribution (*vide infra*).

The geometry of the S_1 state was optimized at TDDFT level in dimethyl sulfoxide (Figure 1.8). At first sight S_1 optimized geometries are indistinguishable from the ground state geometry. Indeed, bond lengths and angles are basically unaffected by nuclear relaxation. Larger variations are those involving dihedral angles, especially in the region connecting the PP with the wings, and amount up to 6.5° for the twisted isomer (Table 1.2). Although these variations may seem small, they are actually quite significant given the fused, and intrinsically rigid, nature of **1**. Most interestingly, the equivalence between pairs of symmetry-related angles in the ground state is lost in S_1, giving a hint of symmetry-breaking.

Another proof of excited-state symmetry breaking comes from the inspection of FMOs related to the S_1 geometry (Figure 1.7). While occupied orbitals are unaffected compared to those in the ground-state, virtual orbitals are strongly distorted with respect to their ground-state counterpart, especially the lowest-energy ones, LUMO and LUMO+1. The two halves of the molecule are no more equivalent by symmetry, and orbitals become mainly localized on one wing. The same distortions occur also for the folded isomer (not shown).

Table 1.2: Selected dihedral angles of the twisted and folded isomers of **1** in the S_0 and S_1 optimized geometries calculated in dimethyl sulfoxide at B3LYP/6-31+G(d,p) level.

	Twisted		Folded	
Dihedral angle/deg	S_0	S_1	S_0	S_1
N1-C5-C8-C44	7.09	1.59	7.32	6.99
N6-C4-C3-C39	7.09	0.92	-7.31	-8.77
C9-N1-C5-C8	35.65	40.91	17.06	15.63
C10-N6-C4-C3	35.65	39.74	-17.05	-13.97
C2-N1-C5-C8	-162.64	-156.80	-176.93	-175.23
C7-N6-C4-C3	-162.64	-156.21	176.93	176.37
C18-C9-N1-C5	2.36	1.88	12.17	15.57
C23-C10-N6-C4	2.36	1.71	-12.16	-14.38
C5-C8-C44-C43	2.89	5.64	14.43	14.99
C4-C3-C39-C38	2.89	6.79	-14.43	-14.62
N1-C5-C4-N6	177.56	178.85	180.00	-179.53
C3-C4-C5-C8	163.77	158.51	180.00	179.81

Localization of excitation on one molecular wing has important consequences on dipole moments. The twisted isomer of **1** possess a residual dipole moment of 0.79 D in the ground state, directed along the C_2 axis. After vertical excitation to the S_1 state, it reduces to 0.61 D. Relaxation of the S_1 geometry induces a large variation of the dipole moment, that was found to reach 13.5 D and lying in the perpendicular plane. Similarly, the dipole moment of the folded isomer is vanishing in the ground and in the vertical excited states because of symmetry, while amounts to 12.2 D in the relaxed S_1 state. Thus, S_1 (symmetry-broken) relaxed state is highly polar and can be stabilized by polar solvents originating emission solvatochromism.

To better visualize the molecular substructures involved in charge redistribution following excitation, we computed Hirshfeld atomic charges [171] in the ground and first excited state for the optimized S_0 and S_1 geometries (Table 1.3). Data can easily be interpreted splitting the molecule in three parts: the centre, including the PP and neighbouring C atoms, and the left and right parts comprising the remaining atoms of the wings (see colour code in Figure 1.8). In the ground state the center bears a small positive charge, and the balancing negative charge is equally shared by the wings. This

Table 1.3: Charge distribution of twisted and folded isomers of **1** obtained from Hirshfeld charge analysis in dimethyl sulfoxide at B3LYP/6-31+G(d,p) level. The molecule has been partitioned in three regions, as depicted in Figure 1.8

Twisted				
	S_0 geometry		S_1 geometry	
	S_0	S_1	S_0	S_1
center	0.0361	0.1883	0.0327	0.1930
left	-0.0180	-0.0941	-0.0120	-0.3962
right	-0.0180	-0.0941	-0.0206	0.2032
Folded				
	S_0 geometry		S_1 geometry	
	S_0	S_1	S_0	S_1
center	0.0342	0.1596	0.0325	0.1777
left	-0.0171	-0.0799	-0.0126	-0.3525
right	-0.0171	-0.0798	-0.0199	0.1748

charge distribution is typical of a quadrupolar ADA arrangement, where the PP acts as weak electron donor towards the peripheral wings, behaving like weak electron acceptors. Vertical $S_0 \rightarrow S_1$ excitation induces further charge separation, with electron density flowing in a symmetrical way from the centre to the periphery of the dye. Relaxation of S_1 to its equilibrium position drives a sizeable charge unbalance between the external regions, leading to an highly asymmetric charge distribution. When the system relaxes back to the ground state through vertical $S_1 \leftarrow S_0$ de-excitation, a charge distribution similar to the pristine situation is recovered, even if a slight residual asymmetry of the wings is maintained.

Fluorescence of **1** consists mainly (98%) in a HOMO←LUMO de-excitation. Our calculations locate the transition at $\lambda = 512$ nm, with a transition dipole moment of 4 D, in good agreement with experimental data ($\lambda = 505$ nm and an estimated dipole moment of 3 D). The high emission dipole moment guarantees a good fluorescence quantum yield, irrespective of the solvent.

In Figure 1.9 we plotted the emission dipole moment together with the absorption dipole moment for the three lowest-energy transitions (we focused

on the twisted isomer only). This allowed us to extract the angle between the relevant transition moments, amounting to 77°, 28° and 126°, for excitation to S_1, S_2 and S_3 respectively. From these values, through Eq. 1.31, we obtained an estimate of the predicted values for the fundamental anisotropy: -0.17, 0.27 and 0.006 respectively.

Anisotropy is an additive quantity, so that at a given wavelength λ it can be calculated as

$$r(\lambda) = \sum_n r_n f_n(\lambda) \tag{1.32}$$

where the sum runs over all electronic transitions of the molecule, while r_n and f_n are the anisotropy of the n-th transition and its fractional contribution to total absorption at λ [151].

In order to simulate excitation anisotropy through Eq. 1.32, f_n must be known for each λ. The vibrational structure is an essential constituent of bandshapes, so that a Franck-Condon analysis would be necessary to extract a reliable estimate for f_n, which is beyond the purpose of the present work. We preferred to stick to more general, but very meaningful, considerations. The S_{1-3} states of **1** lie within a very narrow spectral range ($\sim$ 0.2 eV-wide) so that, as a first approximation, in the 400-450 nm window all transitions overlap because of band broadening (inhomogeneous and homogeneous). The most intense transition, $S_0 \rightarrow S_3$, gives the largest contribution to anisotropy, and at its maximum ($\lambda \approx$ 430 nm) $r_0 \approx r_{S_1 \rightarrow S_3}$. Indeed, in this region we calculated $r_0 \approx 0$, in very good agreement with experimental data. In the red-edge of the absorption spectrum, the $S_0 \rightarrow S_2$ transition is found, and its contribution is expected to increase as the $S_0 \rightarrow S_3$ band decreases. Indeed, we expect $r_0 \approx r_{S_1 \rightarrow S_2} \approx 0.27$, in very good agreement with the experimental value of $r_0 \approx 0.25$. Finally, $S_0 \rightarrow S_1$ is degenerate with $S_0 \rightarrow S_2$ and, according to our calculations, is associated to a large and negative anisotropy. However, its oscillator strength is one order of magnitude lower, so that its contribution to anisotropy is negligible, in line with experiment.

1.3.3 Essential-state modelling

TDDFT results discussed in the previous section suggest that, despite its peculiar 3D structure, **1** possess an underlying quadrupolar nature of the

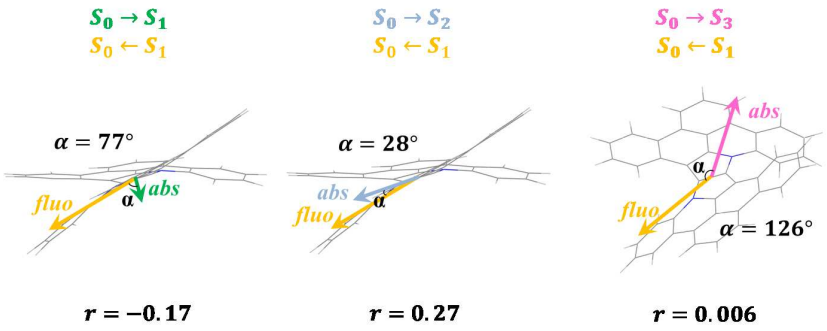

Figure 1.9: Transition dipole moments of the first three absorption transitions (depicted as green, blue and magenta arrows) and emission (orange arrow) obtained from TDDFT calculations in dimethyl sulfoxide (twisted isomer). The angle α is the angle accessed by anisotropy measurements, and r the corresponding calculated value of fundamental anisotropy.

type *ADA*, where the PP acts as a weak electron donor towards the two fused wings. Moreover, this system undergoes symmetry breaking in the first excited state, responsible for fluorescence solvatochromism, as typical of class I dyes. However, the electronic structure of **1** is more complex, and absorption is dominated by LE transitions, which have a significantly higher intensity respect to CT transitions and are responsible for the unusual behaviour of fluorescence anisotropy.

Given its quadrupolar nature, the three-state model [85] should be suitable for the description of absorption and fluorescence of **1**. However, before attempting the essential-state modelling of **1**, we must separate CT features, which can be addressed by ESMs, from the LE contributions, that will be disregarded. The two CT transitions $S_0 \rightarrow S_1$ and $S_0 \rightarrow S_2$ obtained by TDDFT can be easily mapped on the $|g\rangle \rightarrow |c\rangle$ and $|g\rangle \rightarrow |e\rangle$ transitions of the three-state ESM respectively. Their energy cannot be extracted reliably from absorption spectra, since they are hidden below the $S_0 \rightarrow S_3$ transition, therefore we relied on TDDFT data. The two transitions are almost degenerate, suggesting a small mixing between $|N\rangle$ and $|Z_+\rangle$ (i.e. small t). Indeed, inserting the TDDFT transition energies (gas phase values) in Eq. 1.23 and 1.24 we obtained $t = 0.03$ eV and $\rho \approx 6 \times 10^{-4}$, locating the dye in class I. For simplicity we assumed that the chromophore is linear: only the $|g\rangle \rightarrow |c\rangle$ transition is bright in absorption, with a very small transition

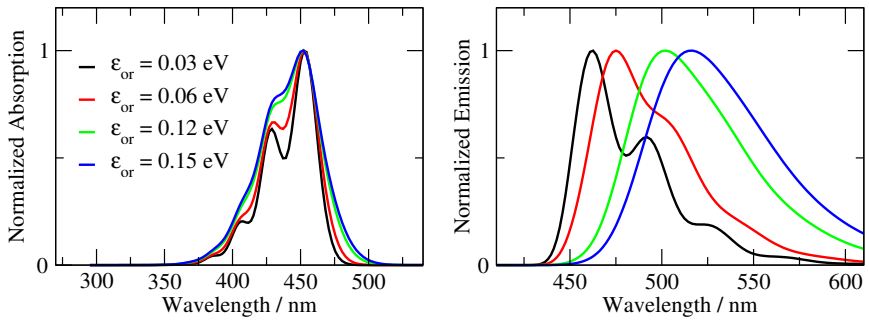

Figure 1.10: Spectra of **1** calculated with the three-state model. Absorption (only relevant to CT transitions, left panel) and emission (right panel) in solvents of different polarity. Model parameters: $\eta = 1.42$ eV, $\sqrt{2}t = 0.04$ eV, $\omega_v = 0.16$ eV, $\varepsilon_v = 0.10$ eV, $\gamma = 0.05$ eV. All parameters were kept fixed except for ε_{or}, which was tuned to mimic solvent polarity (cyclohexane: 0.03 eV, toluene: 0.06 eV, tetrahydrofuran: 0.12 eV, dimethyl sulfoxide: 0.15 eV).

dipole moment, being proportional to $\sqrt{\rho}$ (Eq. 1.27). The remaining model parameters were extracted from experiment: ω_v was obtained from the vibrational spacing, ε_v and γ were tuned to reproduce the vibronic progression and the vibrational bandwidth in cyclohexane, while ε_{or} was tuned to get the solvatochromic shift in the various solvents.

Absorption and emission spectra of **1** calculated with the three-state model are reported in Figure 1.10. The absorption spectrum looks very different from the experimental spectrum, since it contains only the $|g\rangle \rightarrow |c\rangle$ band. The increase of solvent polarity leaves the transition energy unaffected, but promotes significant inhomogeneous broadening effects. A more sound comparison can be done for emission spectra, where the essential-state approach captures well all experimental spectral features. Not only the emission band moves to the red as the polarity of the solvent (ε_{or}) is increased, in quantitative agreement with experimental data, but also the evolution of bandshape is well accounted for.

The accuracy provided by the three-state picture confirms the quadrupolar nature of **1**, despite the novelty and complexity of its structure. It was also an assessment of the robustness of the ESM, which is able to work in complex scenarios, in which LE and CT transitions are strongly correlated.

To the best of our knowledge, chromophore **1** represents the first example of quadrupolar-like dye originating from the π-expansion of an electron-rich

moiety and this work opens new perspectives in the design and application of aza-nanographenes.

1.4 The intriguing case of squaraines

Squarylium dyes, also known as squaraines, are a family of polymethine dyes obtained for the first time in the 60's as the condensation product of squaric acid with aromatic or heterocyclic compounds [172,173]. A typical squaraine is constituted by an electron-deficient oxocyclobutenolate group symmetrically conjugated to two electron-rich moieties. Squaraines are characterized by high chemical and photochemical stability, and can be subject to versatile functionalization [174]. Their typical spectroscopic features include narrow absorption bands in the near-IR, with molar extinction coefficients on the order of 10^5 mol^{-1} L cm^{-1}, mirror-image emission bands with small Stokes shift and good emission quantum yields. Squaraines are also characterized by an intense 2PA band at approximately twice the energy of the linear absorption band, amplified by quasi-resonance effects. [175] Thanks to these properties, squaraines found many applications in electronics and photonics, for example they were used as reporter units in optical sensors, as photosensitizers in photodynamic therapy and photovoltaic devices, as building blocks in low-band gap semiconducting polymers, and were exploited in a variety of NLO applications [176–184].

The growing interest of synthetic chemists in achieving more and more complex structures with optimized optical responses requires reliable theoretical tools for their investigation. However, theoretical modelling of squaraines is far from trivial. Unfortunately, squaraines possess a fairly large biradicaloid character in the ground state, that makes them unsuitable for DFT analysis [185, 186]. More accurate results could be obtained with post Hartree-Fock methods, which are computationally demanding and, to date, are applicable only to the smallest structures [187].

In this context, ESMs provide an ideal alternative to costly first principle methods. The first attempt of essential-state modelling of squaraines was based on the standard three-state model, treating them as DAD quadrupolar chromophores, with the central C_4O_2 unit playing the role of the acceptor group [85]. This model was effective in the description of the main spectro-

scopic features of squaraines: it was able to reproduce the intense absorption band with mirror-image emission and small Stokes shift, and also the large, almost resonant, 2PA band in the UV. According to the three-state model, squaraines were classified as class II dyes, explaining the lack of absorption and emission solvatochromism as related to the stability of their ground and excited states. Moreover, the model was successfully extended to describe the anomalous solvatochromism of unsymmetrical squaraines [188].

Nevertheless, a more detailed inspection of experimental data suggests other features that cannot be captured by this simple three-state model, mostly concerning the fine structure of the 2PA spectrum and excitation anisotropy. Although these data are available only for a limited set of molecular structures, they share common characters, whose assignment is sometimes controversial. 2PA spectra of squaraines show at least a shoulder on the red-edge of the main band [189–193], while excitation anisotropy is characterized by a dip between the OPA and 2PA bands, in a region where the absorbance is null [190, 191, 194–198].

For cyanine dyes, a closely related family of polymethine dyes, the description of 2PA spectrum was improved adding a fourth state to the three-state model [126]. A dip in excitation anisotropy in proximity of the 2PA band is common to cyanine dyes too [190, 199]. In that case, this observation was ascribed to the slightly bent, and hence noncentrosymmetric, structure of cyanines, that makes the transition responsible for 2PA partially allowed also in absorption [139]. However, this argument is hard to apply for squaraines, especially for those possessing a rigid and centrosymmetric backbone, so that a different origin should be invoked.

More recently, the ESM for squaraines was revisited in order to get a finer description of experimental data. In the paper by Liu *et al.* [139], the original three-state model was extended accounting for the inner degrees of freedom of the squaric ring, treating the Oxygen atoms as separate A groups. In this way, five states were considered for the definition of the electronic Hamiltonian. This model, hereafter referred to as five-state model, was tested for a series of rigid aniline-based squaraine dyes, providing a substantial improvement over the three-state results. According to this model, the anisotropy dip originates from a transition to a one-photon allowed state located in-between the main OPA and 2PA bands, polarized perpendicularly

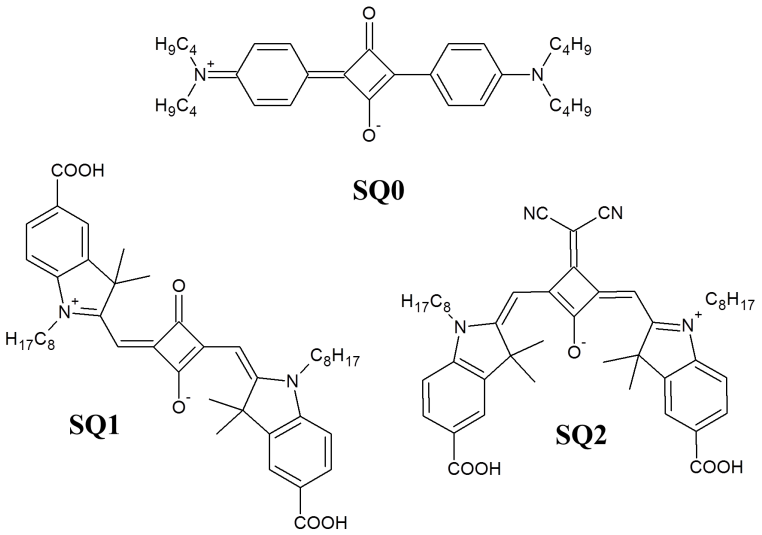

Figure 1.11: Molecular structure of the investigated squaraines.

to the main molecular axis. However, the computed dip was fairly too pronounced and too red-shifted compared to experiment. Also the modelling of 2PA spectra, in spite of qualitative improvements, was judged as not exhaustive.

In the next section we will further extend the ESM for squaraine dyes, with the aim of achieving an accurate and comprehensive description of their spectroscopy. The first step consists in the addition of a doubly charge-separated state to the five-state model (six-state model), in the attempt to refine 2PA spectra as previously done for cyanines. Then, we will work on the possibility of adding more states describing charge delocalization over the squaric ring (eight-state model). Both models will be tested against experimental data of a model squaraine, **SQ0** (Figure 1.11).

While a virtually unlimited number of different structures can be obtained from chemical modification of the electron-rich moieties [200], another source of structural modification of squaraines is the functionalization of the squaric core [201, 202]. A novel class of squaraines was obtained recently from substitution of one oxygen atom on the oxocyclobutenolate with a bulkier and electron-withdrawing group [203–209]. This functionalization

blocks the molecule in a *cis* conformation [204, 210, 211], preventing photoisomerization [212, 213]. Moreover, core-substitution affects the position of the main absorption band, shifting it to longer wavelengths, and results in the appearance of new bands in the UV [201, 203–210]. Despite the interest of many experimentalists in these structures, especially for application as solar cells sensitizers for their ability to harvest high-energy photons with low photodamage, in-depth spectroscopic and theoretical investigation is limited [203, 205–209, 214, 215].

In the last section of this Chapter we will undertake a deeper investigation of the spectroscopic effect promoted by core-substitution of squaraines. We will present the spectroscopic characterization of a pair of symmetric indolenine-based squaraine dyes, **SQ1** and **SQ2** (Figure 1.11), one of them substituted on the squaric ring with a dicyanovinyl group. Finally, we will attempt the rationalization of experimental data through ESMs.

1.4.1 Beyond the three-state model: SQ0

Aniline-based squaraine **SQ0** was selected as test for the ESMs proposed in this Section. For this molecule, a complete set of experimental data was available, including linear absorption and emission spectra, 2PA spectra and excitation anisotropy [193]. The choice was motivated by the rigidity of the molecule and its high symmetry (D_{2h} point group) that can be conveniently exploited in the modelling, allowing to reduce the number of parameters, granting a more sound physical interpretation. Moreover, an analogue of **SQ0** (with butyl groups replaced with methyls) was recently studied with a variety of highly-accurate post Hartree-Fock methods, which provide a complementary insight [187]. The main spectroscopic features of this dye are common to most members of the squaraine family, so that discussing the properties of **SQ0** we do not loose in generality.

An overview of experimental data

Optical spectra of **SQ0** are collected in Figure 1.12. In toluene **SQ0** features a narrow absorption band peaking at $\lambda = 636$ nm with a maximum molar extinction coefficient $\varepsilon = 3.65 \times 10^5$ mol^{-1} L cm^{-1}. This band, as for all squaraines, can be safely assigned to a one photon allowed $S_0 \rightarrow S_1$

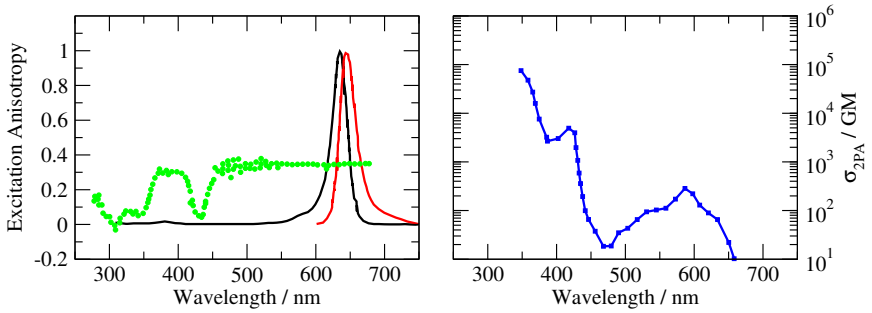

Figure 1.12: Experimental data on **SQ0**. Left panel: normalized absorption (black) and emission (red) spectra in toluene, excitation anisotropy (green dots) in polytetrahydrofuran. Right panel: 2PA spectrum in toluene (1 GM = 10^{-50} cm^4 s photons^{-1}). Adapted with permission from *J. Phys. Chem. Lett.* 2010, 1, 15, 2354–2360. Copyright 2010 American Chemical Society.

transition, which possess a partial CT character and is polarized along the main molecular axis [189, 191, 192, 194, 196, 198]. Looking into more detail at the absorption spectrum, another weak peak is found in the UV, at $\lambda \approx 380$ nm. The same feature was noticed for many other squaraines and was assigned to generic $S_0 \rightarrow S_n$ transitions [191, 192, 194, 198]. **SQ0** shows intense emission (QY = 95%) that is the mirror image of absorption and peaks at $\lambda = 646$ nm, with a Stokes shift amounting to less than 250 cm^{-1}. As for most squaraines, solvent polarity has a marginal impact on band position, and in the following we will not attempt to reproduce the small experimental shifts.

The 2PA spectrum of **SQ0** consists of a weak band around 580 nm, the same region of the vibronic shoulder of the main OPA band, with a cross-section $\sigma < 300$ GM. Apart from one study suggesting the presence of an additional electronic contribution to 2PA in this region [195], it was experimentally and theoretically proven that this low energy 2PA band of squaraines has a vibronic origin [189, 197, 215, 216]. Specifically, the $S_0 \rightarrow S_1$ transition, one-photon forbidden by symmetry, becomes partially allowed because of the coupling to a 2PA-active A_g state mediated by a B_u vibrational mode. In the high-energy region of the 2PA spectrum, at least two distinct features can be recognized: the tail of an intense band, characteristic of squaraines, peaking outside the experimental window ($\lambda < 350$ nm) and a shoulder ($\sigma \approx 4500$ GM) around 420 nm.

Excitation anisotropy of **SQ0** is almost flat and close to the limiting 0.4 value ($r \approx 0.35$) within the main OPA band. Starting from $\lambda \approx 470$ nm and moving to shorter wavelengths, anisotropy decreases steeply, reaching $r \approx 0$ at $\lambda \approx 430$ nm, and then increases again to $r \approx 0.3$ before declining at higher energy. The anisotropy dip at $\lambda \approx 430$ nm does not correspond to a distinct absorption band, and indicates a transition polarized according to an angle $\alpha \approx 52°$ with respect to emission. For the secondary absorption peak we get instead $\alpha = 24°$. The origin of the anisotropy dip is still subject to discussion. Many papers discussing anisotropy of squaraines suggest that anisotropy dips give information on the position of 2PA states, which are not accessible upon linear absorption [190, 191, 193, 195–198]. However, this interpretation is questionable, since anisotropy relies on absorption and emission, which are both linear processes and are subject to the same selection rules. We thus have to seek for a different origin. One could be electronic, i.e. due to the presence of a OPA-allowed state with suitable polarization and small transition dipole moment. Another hypothesis could be a vibronic origin. Accordingly, the transition responsible for the dip is a 2PA transition that becomes partially allowed in OPA thanks to the vibronic coupling to a high-energy OPA-active state polarized along the short molecular axis. To date, there is not enough experimental data to definitely support either of the hypotheses and the available data from first principle calculations on **SQ0** are not resolutive in this direction [187].

The six-state model

The first step towards the improvement of the ESM for squaraines is to take the five-state model of Ref. [139], which was able to give a better description of anisotropy, and add one more state, a doubly-excited state, as was done for cyanines to improve 2PA [126]. Indeed, first principle calculations on **SQ0** revealed a doubly-excited character of the high-energy 2PA transitions [187].

As in the five-state model, **SQ0** was described as a DA_2D dye, with the donor groups extending over the aniline moieties, and the acceptors corresponding to the two Oxygen atoms on the squaric core. This structure belongs to the point group D_{2h} and was placed on the xy plane, with the A groups aligned with the x axis (Figure 1.13 (a)).

In the spirit of ESMs, the main resonance structures of the dye, sketched in Figure 1.13 (a), were chosen as the electronic basis states. As in Ref. [139], the basis set includes a neutral $|N\rangle$ state and four degenerate zwitterionic states, obtained after electron hopping from one D site to either of the A groups, $|Z_{1u}\rangle$, $|Z_{1d}\rangle$, $|Z_{2u}\rangle$ and $|Z_{2d}\rangle$. The subscripts 1 and 2 indicate a positive charge on the left and right D group respectively, while the subscripts 'u' and 'd' indicate the position of the negative charge, on the upper (up) or lower ($d$own) A site. Here, we add the doubly zwitterionic state $|ZZ\rangle$, describing the situation in which all four groups bear a unitary charge. The dipole moment of the zwitterionic states lies on the xy plane, with components μ_0^x and μ_0^y, while the dipole moment of $|ZZ\rangle$ vanishes because of symmetry (see Figure 1.13 (a)). Typically a squaraine is elongated along the y axis, so that $\mu_0^x \ll \mu_0^y$. Given 2η the energy difference between the neutral and the four charge-separated states, the energy of $|ZZ\rangle$ amounts to 4η. On this basis the electronic Hamiltonian $\hat{H}_e$ reads

$$\hat{H}_e = \begin{pmatrix} 0 & -\tau & -\tau & -\tau & -\tau & 0 \\ -\tau & 2\eta & -\beta & 0 & 0 & -\tau' \\ -\tau & -\beta & 2\eta & 0 & 0 & -\tau' \\ -\tau & 0 & 0 & 2\eta & -\beta & -\tau' \\ -\tau & 0 & 0 & -\beta & 2\eta & -\tau' \\ 0 & -\tau' & -\tau' & -\tau' & -\tau' & 4\eta \end{pmatrix} \tag{1.33}$$

The CT integral τ mixes the neutral state with each of the zwitterionic states. A different mixing between the zwitterionic states and the double zwitterion was accounted for, described by τ'. $|N\rangle$ and $|ZZ\rangle$ mix only through the zwitterionic states. We expect that charge separation on a zwitterionic state is more costly that on a neutral state, so that typically $\tau' < \tau$. An additional parameter β was required to describe charge resonance between the A moieties.

The electronic problem can be better understood resorting to symmetry. The four degenerate zwitterionic states can be conveniently combined into the following symmetry-adapted wavefunctions (symmetry species are reported in brackets):

$$|Z_{++}\rangle = \frac{1}{2}(|Z_{1u}\rangle + |Z_{1d}\rangle + |Z_{2u}\rangle + |Z_{2d}\rangle) \quad (A_g) \tag{1.34}$$

$$|Z_{-+}\rangle = \frac{1}{2}(|Z_{1u}\rangle - |Z_{1d}\rangle + |Z_{2u}\rangle - |Z_{2d}\rangle) \quad (B_{3u}) \tag{1.35}$$

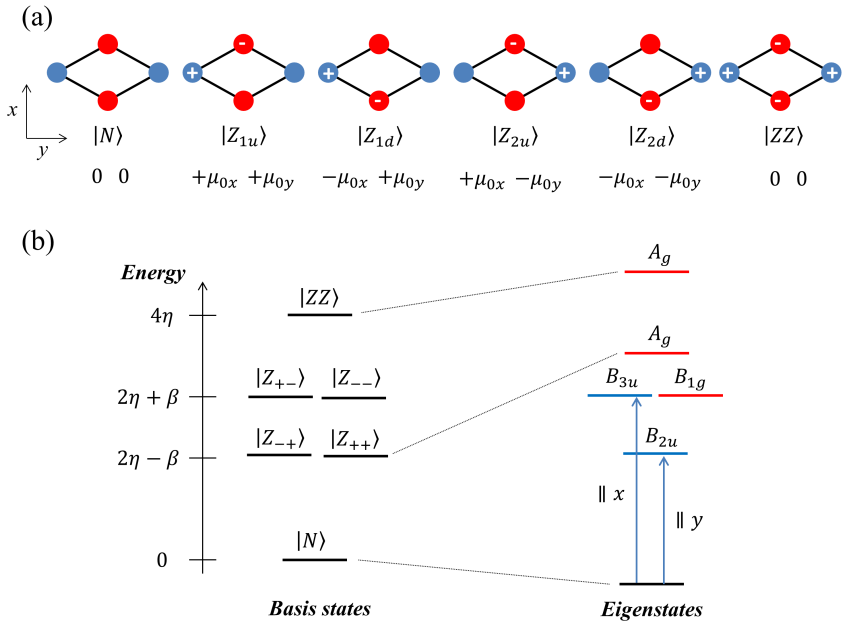

Figure 1.13: The six-state model for a DA_2D squaraine (D_{2h} symmetry). (a) Schematic representation of the six basis states. Red and blue circles represent electron acceptor and electron donor groups respectively. Components of the dipole moment of the states (direction from the positive to the negative charge) are shown according to the Cartesian axes sketched on the left. (b) Left: energy of the symmetrized basis states. Right: the eigenstates and their symmetry. States in blue (red) are accessible via one photon (two photon) absorption. The ordering of the eigenstates may vary according to the specific parametrization.

$$|Z_{+-}\rangle = \frac{1}{2}(|Z_{1u}\rangle + |Z_{1d}\rangle - |Z_{2u}\rangle - |Z_{2d}\rangle) \quad (B_{2u}) \tag{1.36}$$

$$|Z_{--}\rangle = \frac{1}{2}(|Z_{1u}\rangle - |Z_{1d}\rangle - |Z_{2u}\rangle + |Z_{2d}\rangle) \quad (B_{1g}) \tag{1.37}$$

Of course the states $|N\rangle$ and $|ZZ\rangle$ belong to the totally-symmetric A_g.

On the symmetrized basis Eq. 1.33 can be rewritten as

$$\hat{H}_e = \begin{pmatrix} 0 & -2\tau & 0 & 0 & 0 & 0 \\ -2\tau & 2\eta-\beta & 0 & 0 & 0 & -2\tau' \\ 0 & 0 & 2\eta+\beta & 0 & 0 & 0 \\ 0 & 0 & 0 & 2\eta-\beta & 0 & 0 \\ 0 & 0 & 0 & 0 & 2\eta+\beta & 0 \\ 0 & -2\tau' & 0 & 0 & 0 & 4\eta \end{pmatrix} \tag{1.38}$$

Only A_g states, $|N\rangle$, $|Z_{++}\rangle$ and $|ZZ\rangle$, are mixed, giving the ground state and two excited states, as depicted in Figure 1.13 (b). The $|Z_{+-}\rangle$ state stays unmixed at energy $2\eta - \beta$, while $|Z_{+-}\rangle$ and $|Z_{--}\rangle$, of different symmetry, remain degenerate at energy $2\eta + \beta$. The molecule possesses inversion symmetry, therefore only *ungerade* states are accessible *via* OPA. According to symmetry, the transition towards the B_{2u} state is polarized along the main molecular axis (coinciding with y), while B_{3u} is polarized perpendicularly (along x). Transitions towards the remaining states are instead 2PA-allowed. B_{1g} is degenerate with the OPA-allowed B_{3u}, while the other states possess both A_g symmetry. One of them coincides with the highest-energy excited state, while the position of the other depends on the choice of the model parameters.

It is clear that, compared to the three-state model, this six-state model has the capability of describing more details, affording higher complexity. Indeed, the B_{3u} state is bright in OPA and has the right polarization to describe the dip in anisotropy. Moreover, the presence of three 2PA-active states allows for a much more detailed description of 2PA spectra.

To address bandshapes, the electronic model was extended to include intramolecular vibrations, in a similar way to quadrupolar chromophores [85]. Two independent vibrational coordinates q_1 and q_2 with harmonic frequency ω_v describe nuclear motion along the two equivalent molecular arms $D - A_2$ and $A_2 - D$, with vibrational relaxation energy ε_v. The $|ZZ\rangle$ state couples with both coordinates, and the vibrational Hamiltonian $\hat{H}_v$

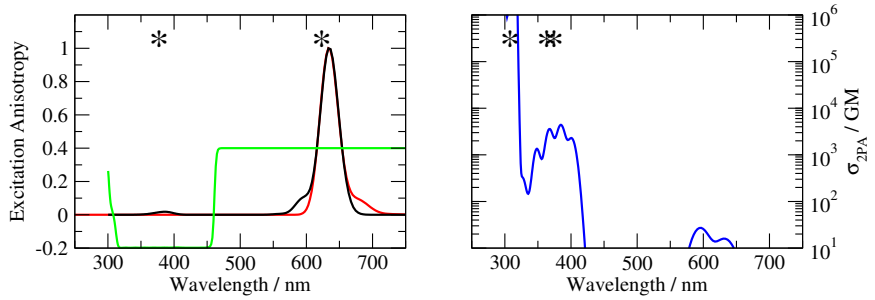

Figure 1.14: Spectra of **SQ0** calculated with the six-state model. Left panel: normalized absorption (black) and emission (red), and excitation anisotropy (green). Right panel: 2PA spectrum. Model parameters: $\eta = 0.35$ eV, $\tau = 0.97$ eV, $\tau' = 0.2$ eV, $\beta = 0.65$ eV, $\varepsilon_v = 0.11$ eV, $\omega_v = 0.13$ eV, $\mu_0^x = 4.0$ D, $\mu_0^y = 24.0$ D, $\gamma = 0.05$ eV. We set $\varepsilon_{or} = 0.1$ eV for toluene (absorption, emission and 2PA spectra) and $\varepsilon_{or} = 0.2$ eV for polytetrahydrofuran (anisotropy). Asterisks mark transition energies obtained from the diagonalization of the electronic problem.

reads

$$\begin{aligned}\hat{H}_v = &- \sqrt{2\varepsilon_v}\omega_v\hat{q}_1\big(\,|Z_{1u}\rangle\langle Z_{1d}| + |Z_{1d}\rangle\langle Z_{1u}| + |ZZ\rangle\langle ZZ|\,\big)\\ &- \sqrt{2\varepsilon_v}\omega_v\hat{q}_2\big(\,|Z_{2u}\rangle\langle Z_{2d}| + |Z_{2d}\rangle\langle Z_{2u}| + |ZZ\rangle\langle ZZ|\,\big)\\ &+ \frac{1}{2}\big[\omega_v^2(\hat{q}_1^2+\hat{q}_2^2)\big] + \frac{1}{2}(\hat{p}_1^2+\hat{p}_2^2)\end{aligned} \tag{1.39}$$

Polar solvation was introduced in a reaction-field approach, and diagonalization of the complete problem was performed non adiabatically, as was already described for quadrupolar chromophores.

Results reported herein for **SQ0** were obtained setting 10 vibrational states. We fixed $\varepsilon_{or} = 0.1$ eV to compare with experimental data in toluene, while a higher value of ε_{or} (0.2 eV) was chosen for the calculation of anisotropy, to compare with more polar polytetrahydrofuran. The parameters μ_0^x and μ_0^y were tuned to reproduce the molar extinction coefficient in toluene.

Spectra of **SQ0** obtained with the six-state model are reported in Figure 1.14. In order to better locate the states responsible for the various spectral features, the position of the purely electronic states obtained from the diagonalization of $\hat{H}_e$ are shown on the panels with asterisks.

According to the model, the intense and narrow absorption peak at $\lambda \approx 635$ nm corresponds to the transition towards the B_{2u} state, polarized along the main molecular axis. The same state is responsible for emission.

Fluorescence spectrum is the mirror image of the main absorption peak and compares favourably with experiment, also in terms of bandshape.

Concerning 2PA, the correspondence between experimental and simulated spectra is satisfactory in the high-energy region. The most intense band peaks at $\lambda < 320$ nm, outside the experimentally accessible window, in agreement with experiment. The state involved in this transition is the highest-energy A_g state, which contains a significant contribution from the doubly-excited $|ZZ\rangle$ state. Another, less intense 2PA band ($\sigma \approx 3.5 \times 10^3$ GM), mainly due to the other A_g state, is predicted in between 350 and 400 nm, acting as a shoulder of the main 2PA peak, and possess a partial doubly-excited character as well. B_{1g} is bright in 2PA with small cross-section and overlaps with the A_g bands. Another 2PA signal was found at $\lambda \approx 600$ nm and corresponds to a vibronically-activated transition towards the lowest B_{2u} state, as found experimentally, however both its intensity and width are underestimated.

The modelling of fluorescence excitation anisotropy is instead more delicate. The calculated anisotropy amounts to 0.4 inside the main OPA band and decreases abruptly to the lower limit -0.2 at $\lambda \approx 470$ nm. This result is trivial, considering that the two OPA transitions are mutually perpendicular. Indeed, the dip is due to the presence of the B_{3u} state, polarized along x.

Two main issues are related to the calculated anisotropy. The first concerns the width of the dip, that is too wide compared to experiment. The second is related to the weak peak at $\lambda \approx 385$ nm, that compares well with the one found in the OPA spectrum in terms of spectral position, shape and intensity, but has a very different polarization. According to the model, this peak is due to the B_{3u} state, the same state responsible for the anisotropy dip. Conversely, in the experimental spectrum, anisotropy corresponding to this band is high ($r \approx 0.3$) rather suggesting a y-polarization. In our model, anisotropy dip and weak OPA band are correlated features, and cannot be adjusted to match experiment, for any set of parameters. At the same time, having only two states contributing to anisotropy, an improvement of its shape is difficult to achieve.

The state responsible for the weak OPA band in the UV could be most probably another B_{2u} state, that is not included in our model. To improve

these features, addition of more states could be a possibility, and will be explored in the next section.

The eight-state model

We describe the target squaraine as a DA_2D molecule of symmetry D_{2h}, as in the six-state model. However, in this case, we take into account the possibility of the stabilization of the negative charge by the squaric ring itself. Thus, the eight states depicted in Figure 1.15 (a) are required to describe the system.

Starting from the neutral $|N\rangle$ state, the charge can be transferred from either of the external D groups to the squaric ring, obtaining the two zwitterionic states $|Z_1\rangle$ and $|Z_2\rangle$, having both a dipole moment aligned along the y axis. $|N\rangle$, $|Z_1\rangle$ and $|Z_2\rangle$ correspond to the same basis set adopted in the original three-state model for typical quadrupolar DAD chromophores, where the ring behaves as acceptor.

Here we also take into account the displacement of the negative charge from the ring to either of the Oxygen atoms, treated as acceptor sites. This requires the addition of four zwitterionic states, coinciding to those introduced in the six-state model, $|Z_{1u}\rangle$, $|Z_{1d}\rangle$, $|Z_{2u}\rangle$ and $|Z_{2d}\rangle$.

In principle, three double-zwitterionic states can be obtained, one ($|ZZ\rangle$) corresponding to the situation in which all D and A groups are charged, and two where one of the negative charges resides on the squaric ring. To keep the model simple, only $|ZZ\rangle$ will be accounted for in the model, in analogy with the six-state model.

As before, we set 2η as the energy gap between the neutral state and the zwitterionic states $|Z_{1u}\rangle$, $|Z_{1d}\rangle$, $|Z_{2u}\rangle$ and $|Z_{2d}\rangle$, and 4η as the energy of $|ZZ\rangle$. A different diagonal energy $2(\eta + k)$ was assigned to the states $|Z_1\rangle$ and $|Z_2\rangle$, introducing a new model parameter, k. Moreover, the matrix element τ describes charge transfer from the donors to the squaric ring, while β describes charge resonance between the squaric ring and the acceptor groups. The parameter τ' mixes the four degenerate zwitterionic states with the double-zwitterionic state.

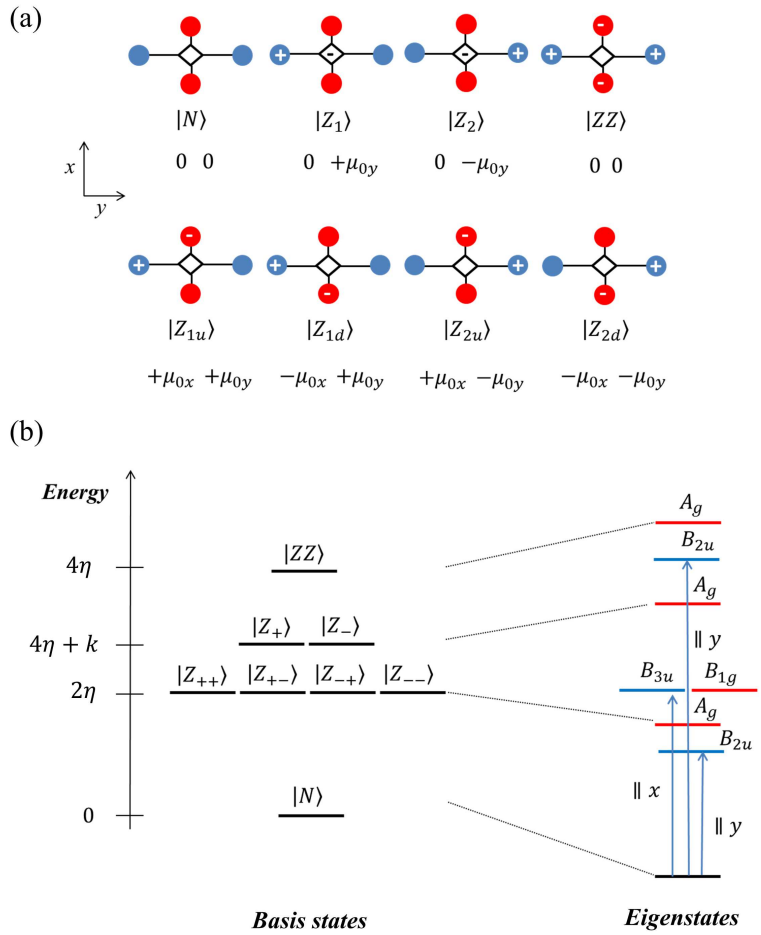

Figure 1.15: The eight-state model for a DA_2D squaraine. (a) Schematic representation of the eight basis states. Red and blue dots represent electron acceptor and electron donor groups respectively. Components of the dipole moment of the states (direction from the positive to the negative charge) are shown according to the Cartesian axes sketched on the left. (b) Left: energy of the symmetrized basis states. Right: the electronic eigenstates. States in blue (red) are accessible via one photon (two photon) absorption.

On this basis the electronic Hamiltonian $\hat{H}_e$ is the following eight-dimensional matrix:

$$\hat{H}_e = \begin{pmatrix} 0 & -\tau & -\tau & 0 & 0 & 0 & 0 & 0 \\ -\tau & 2(\eta+k) & 0 & -\beta & -\beta & 0 & 0 & 0 \\ -\tau & 0 & 2(\eta+k) & 0 & 0 & -\beta & -\beta & 0 \\ 0 & -\beta & 0 & 2\eta & 0 & 0 & 0 & -\tau' \\ 0 & -\beta & 0 & 0 & 2\eta & 0 & 0 & -\tau' \\ 0 & 0 & -\beta & 0 & 0 & 2\eta & 0 & -\tau' \\ 0 & 0 & -\beta & 0 & 0 & 0 & 2\eta & -\tau' \\ 0 & 0 & 0 & -\tau' & -\tau' & -\tau' & -\tau' & 4\eta \end{pmatrix} \tag{1.40}$$

Exploiting symmetry, the four degenerate zwitterionic states can be combined into the symmetrized $|Z_{++}\rangle$, $|Z_{-+}\rangle$, $|Z_{+-}\rangle$ and $|Z_{--}\rangle$ wavefunctions, as described by Eqs. 1.34-1.37, while the states $|Z_1\rangle$ and $|Z_2\rangle$ can be combined in one A_g and one B_{2u} state:

$$|Z_+\rangle = \frac{1}{\sqrt{2}}(|Z_1\rangle + |Z_2\rangle) \quad (A_g) \tag{1.41}$$

$$|Z_-\rangle = \frac{1}{\sqrt{2}}(|Z_1\rangle - |Z_2\rangle) \quad (B_{2u}) \tag{1.42}$$

The four A_g states, $|N\rangle$, $|Z_+\rangle$, $|Z_{++}\rangle$ and $|ZZ\rangle$ are mixed to give the ground state and three excited states, $|Z_-\rangle$ mixes with $|Z_{-+}\rangle$ giving two B_{2u} excited states, while the remaining $|Z_{+-}\rangle$ and $|Z_{--}\rangle$ stay unmixed at energy 2η (Figure 1.15 (b)). Thus, we expect three OPA transitions, two of them (B_{2u}) polarized along the long molecular axis and one (B_{3u}) polarized in the perpendicular direction. Four states are contributing to 2PA, three of them possessing A_g symmetry and one of B_{1g} symmetry, degenerate with the x-polarized OPA transition.

As in the six-state model, two independent vibrational coordinates q_1 and q_2 with harmonic frequency ω_v and vibrational relaxation energy ε_v describe nuclear motion along the two equivalent molecular arms, leading to the following vibrational Hamiltonian $\hat{H}_v$

$$\begin{aligned} \hat{H}_v = &- \sqrt{2\varepsilon_v}\omega_v\hat{q}_1\big(\,|Z_1\rangle\langle Z_1| + |Z_{1u}\rangle\langle Z_{1d}| + |Z_{1d}\rangle\langle Z_{1u}| + |ZZ\rangle\langle ZZ|\,\big) \\ &- \sqrt{2\varepsilon_v}\omega_v\hat{q}_2\big(\,|Z_2\rangle\langle Z_2| + |Z_{2u}\rangle\langle Z_{2d}| + |Z_{2d}\rangle\langle Z_{2u}| + |ZZ\rangle\langle ZZ|\,\big) \\ &+ \frac{1}{2}\big[\omega_v^2(\hat{q}_1^2+\hat{q}_2^2)\big] + \frac{1}{2}(\hat{p}_1^2+\hat{p}_2^2) \end{aligned} \tag{1.43}$$

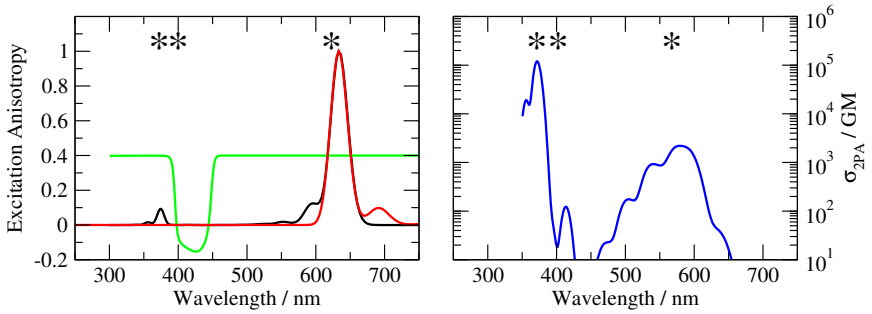

Figure 1.16: Spectra of **SQ0** calculated with the eight-state model. Left panel: normalized absorption (black) and emission (red) spectra, and excitation anisotropy (green). Right panel: 2PA spectrum. Model parameters: $\eta = 1.05$ eV, $\tau = 1.03$ eV, $\tau' = 0.75$ eV, $k = -0.42$ eV, $\beta = 0.38$ eV, $\varepsilon_v = 0.1$ eV, $\omega_v = 0.17$ eV, $\mu_0^x = 4.0$ D, $\mu_0^y = 28.0$ D, $\gamma = 0.045$ eV. We set $\varepsilon_{or} = 0.01$ eV for toluene (absorption, emission and 2PA spectra) and $\varepsilon_{or} = 0.1$ eV for polytetrahydrofuran (anisotropy). Asterisks mark transition energies obtained from the diagonalization of the electronic problem.

Spectra of **SQ0** obtained with the eight-state model are collected in Figure 1.16. Calculations were performed in solution with different values of the orientational relaxation energy ($\varepsilon_{or} = 0.01$ eV for toluene and 0.1 eV for polytetrahydrofuran). Asterisks on the panels indicate the transition energies obtained from diagonalization of the electronic Hamiltonian. Only six states were found inside the experimental spectral range, while the transition towards the highest (A_g) excited state was predicted below 210 nm. The best fit was obtained for negative k, i.e. for $|Z_1\rangle$ and $|Z_2\rangle$ having low energy with respect to the other four zwitterionic states.

Linear absorption and emission spectra are well reproduced by the model in terms of position and bandshapes. In the OPA spectrum we accurately retrieve the main absorption peak at $\lambda \approx 640$ nm, due to a B_{2u} state, and also the weak peak at $\lambda \approx 380$ nm, ascribed to the other B_{2u} state. The intensity of the latter transition is however slightly overestimated compared to experiment. The remaining state that should be active in OPA, B_{3u}, is found on the red side of the secondary absorption band and has a lower oscillator strength, making it invisible in the absorption spectrum.

Conversely, the transition towards the very same B_{3u} state, polarized along x, is responsible for the narrow anisotropy dip at $\lambda \approx 425$ nm. Aniso-

tropy returns back to 0.4 in the region corresponding to the secondary OPA peak, that has y polarization, in very good agreement with experiment.

Concerning 2PA, the most intense band peaks at $\lambda \approx 370$ nm, outside the spectral range accessed in the experiment. It corresponds to an A_g transition, whose red-edge tail adds to the nearby and less intense B_{1g} transition. Another band, assigned to the lowest-energy A_g transition, spans the region between 550 and 600 nm, and overlaps with the small contribution at the vibronic shoulder of the OPA spectrum. Although the shape of the 2PA spectrum is quite accurate, and transition energies are well reproduced, the cross-section of the shoulder at $\lambda \approx 400$ nm is underestimated by one order of magnitude. At the same time, the intensity of the low-energy 2PA band is considerably overestimated, with $\sigma \approx 2.5 \times 10^4$ GM, compared to the experimental $\sigma \approx 600$ GM.

Six-state *versus* eight-state model

We are now in the position to summarize and compare the performance of the two models introduced in this section.

Both of them are accurate in the description of the shape and position of the main OPA band, assigned to a B_{2u} transition. Indeed, all first principle methods tested on **SQ0** agree with this assignment [187]. The emission spectrum is also nicely reproduced by the two models, which are consistent in the description of the shape and the small Stokes shift.

The performance of the two models is however very different as far as anisotropy and 2PA are concerned. Both of them assign the experimental dip in excitation anisotropy to a transition towards a B_{3u} state, polarized along the short molecular axis and hence perpendicular to the main OPA band. This state coincides with the $|Z_{+-}\rangle$ basis state and, according to both methods, is degenerate with a B_{1g} state, bright in 2PA. However, the six-state model fails in the description of excitation anisotropy, predicting a dip too wide compared to experiment. Moreover it fails in the description of the weak OPA band in the UV, predicting the wrong polarization. On the opposite, the eight-state model was found to be more accurate in reproducing both anisotropy and linear absorption in the high-energy region. According to the eight-state model, the secondary OPA band is due to a B_{2u} state not included in the six-state model.

Concerning anisotropy and OPA, a few questions may arise on the assignment of the spectral features by the eight-state model. According to first principle calculations on **SQ0** reported in Ref. [187], many methods agree with our model in predicting the degeneracy of the B_{3u} and B_{1g} states, however there are large uncertainties concerning their location. Some methods locate them outside the experimental spectral window (> 4 eV), ruling out their involvement in anisotropy. Nonetheless, in [187] calculations were performed in gas phase, so that interactions with the solvent may stabilize the B_{3u} state to lower energies. Although in our models it has an electronic origin, the vibronic origin of the anisotropy dip could be an alternative and effective hypothesis, but cannot be either definitively confirmed or excluded by our results.

Indeed, a B_{2u} state could be responsible for the weak OPA band, as in the eight-state model. However, the main drawback of this model is that it only describe CT transitions, while some high-energy transitions could be instead localized on the donor moieties.

Concerning 2PA, the addition of the $|ZZ\rangle$ state is effective in improving the agreement with experiment in the high-energy side of the spectrum. The six-state model compares well with experimental data and gives a balanced description of band position and intensity. The main 2PA bands in the UV were assigned to two A_g states, as predicted by other methods [187], and have doubly-excited character. Conversely, the eight-state model performs poorly. Not only the absolute intensities are incorrect, but an additional A_g state is predicted at low energy, that does not have a theoretical or experimental counterpart.

From the computational point of view, addition of more basis states implies the increase of the number of model parameters. While only two parameters enter the electronic Hamiltonian in the three-state model, three parameters are needed in the five-state model, four in the six-state model (η, τ, τ' and β), five in the eight-state model (η, τ, τ', β and k). Moreover, the number of parameters is expected to increase when the symmetry of the system is lowered, requiring more specific strategies for the parametrization.

As more states are included, the greater is the level of detail that can be achieved in the modelling of the spectra. However, the states become highly correlated and it is difficult to disentangle the effect of each single

parameter. Adding many states is against the spirit of ESMs, and the risk is the overproliferation of degrees of freedom, resulting in complex models difficult to parametrize and analyze, and leading to unrealistic description of the chromophores.

1.4.2 Core-substituted squaraines

So far we challenged ESMs with the small and highly symmetric structure of **SQ0**. In this Section we will deal with more complex yet very interesting structures belonging to the squaraine family, **SQ1** and **SQ2** (Figure 1.11). They are both members of the class of indolenine-based squaraine dyes, and possess similar molecular structures, however, while **SQ1** is a typical symmetric squaraine [217], in **SQ2** one Oxygen atom of the squaric core was substituted with a dicyanovinyl group, a strong electron acceptor [207]. The COOH groups on the indole moieties, designed as anchoring groups to the semiconductor in OPV cells, are intrinsically electron withdrawing, but it was demonstrated that their effect is limited to a red shift of the main absorption band by a few nm [204,206]. Dyes were synthesized and provided by Dr. Nadia Barbero and Prof. Claudia Barolo from University of Torino, Italy.

Functionalization of the central group with a bulky substituent forces the molecule to adopt a *cis* conformation [204,210,211], blocking conformational motion and preventing isomerization. Diffraction studies on a few core-substituted squaraines revealed that they adopt planar structures in which, due to steric hindrance, the indoles point to opposite sides with respect to the substituent, creating enough space to host the long alkyl chains linked to the Nitrogen atoms [211]. It is well-known that this kind of substitution affects the spectroscopic properties of the dye, promoting a red shift of the main absorption peak, and the appearance of one (or more) bands in the UV, which are absent in non-substituted analogues [201, 203–210].

While some reports relate these bands to the substituent [182, 203, 207, 214], this phenomenon was never addressed in detail neither from the experimental nor from the theoretical point of view. In this Work we attempted a more in-depth study of the effect of core-substitution, starting from a detailed spectroscopic investigation of **SQ2** (**SQ1** will serve as a reference) and then undertaking, for the first time, theoretical modelling with ESMs.

Spectroscopic characterization of SQ1 and SQ2

The target squaraines were characterized in different solvents, spanning a wide polarity range. Linear absorption and emission spectra are shown in Figure 1.17 (a-d), while main spectroscopic data are summarized in Table 1.4.

SQ1 features the typical cyanine-like OPA band at $\lambda \approx 650$ nm, and a very weak absorption below 400 nm. The narrow emission band peaks at $\lambda \approx 660$, with a quantum yield $\approx 40\%$ in toluene which decreases in more polar solvents. Emission lifetimes are in between 1 and 2 ns in all the solvents considered, in agreement with literature data [217]. Solvent polarity plays a minor effect both on absorption and emission spectra. The corresponding maxima are found within a very narrow spectral range ($\sim$ 10 nm-width) and the small shifts can be justified by differences in the refractive index of the solvents.

Absorption and emission spectra of **SQ2** are broadened with respect to **SQ1** and are red-shifted by more than 40 nm, depending on the solvent. Moreover, **SQ2** features additional absorption signals in the 300-500 nm region, with a peak at $\lambda \approx 380$ nm and a more flat band between 400 and 500 nm, both absent in **SQ1**. The emission maximum is found at $\lambda > 700$ nm, with larger Stokes shifts compared to **SQ1** which increases with solvent polarity. Core-substitution marginally affects fluorescence quantum yields, leading to a slight increase in low-polarity solvents only. A more important effect concerns emission lifetimes, ranging from ~ 2 to more than 4 ns [207].

SQ2 absorption and emission are solvatochromic. Specifically, the main OPA band blue-shifts by 560 cm^{-1} from toluene to acetonitrile, while no solvatochromic effects are seen for the band at 385 nm. Also the portion in the 450-500 nm range is sensitive to solvent polarity, undergoing a blue-shift similarly to the main band. Emission is subject to negative solvatochromism as well, with a displacement of the maximum of approximately 440 cm^{-1} from toluene to acetonitrile.

Negative solvatochromism indicates a higher polarity of the ground state compared to the fluorescent state. Indeed, electro-optical measurement performed on a parent dicyanovinyl-substituted squaraine revealed a permanent dipole moment $\mu_g \approx 4$ D, that decreases by ~ 2 D upon $S_0 \rightarrow S_1$ absorp-

Table 1.4: Spectroscopic properties of **SQ1** and **SQ2** in solvents of different polarity: absorption and emission maxima (λ_{abs}^{max} and λ_{em}^{max}), Stokes shift (SS), fluorescence quantum yields (QY), emission lifetimes (τ). Solvents are labelled as following: TOL: toluene, CTC: carbon tetrachloride, CHL: chloroform, 2-MeTHF: 2-methyltetrahydrofuran, ACN: acetonitrile, DMSO: dimethyl sulfoxide. The reference standard for fluorescence quantum yield measurements was cresyl violet in ethanol at 23°C (QY = 51%). [a]poorly soluble. [b]not measured. [c]in ACN two components were found whose amplitudes are reported in brackets.

Compound	Solvent	λ_{abs}^{max}/nm	λ_{em}^{max}/nm	SS/cm^{-1}	QY/%	τ/ns
SQ1	TOL	657	665	183	43	1.76
	CTC	652	665	300	-[a]	1.79
	CHL	652	660	186	36	1.89
	2-MeTHF	652	660	186	26	-[b]
	ACN	648	657	211	10	0.76[94]; 2.11[4][c]
	DMSO	659	669	227	24	1.47
SQ2	TOL	720	734	265	48	3.69
	CTC	720	735	283	40	4.26
	CHL	709	726	330	57	3.52
	2-MeTHF	710	725	291	43	-[b]
	ACN	692	711	386	13	1.93
	DMSO	699	716	340	25	2.49

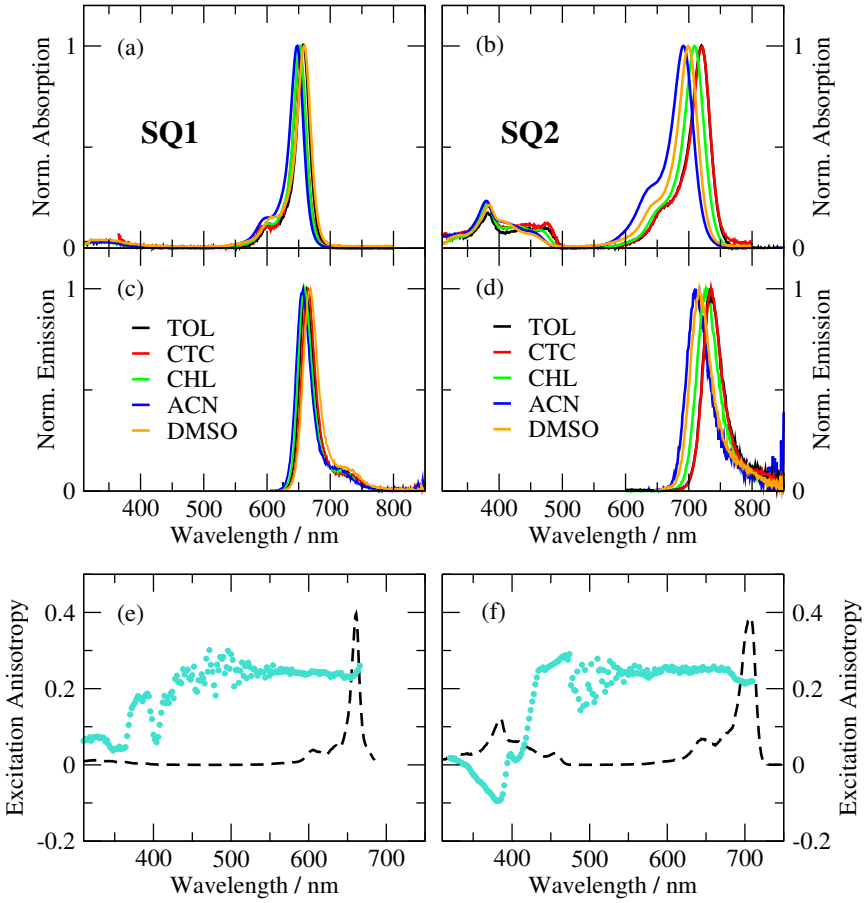

Figure 1.17: Optical spectra of **SQ1** (left) and **SQ2** (right). (a-b) Normalized absorption and (c-d) emission spectra in solvents of different polarity (TOL: toluene, CTC: carbon tetrachloride, CHL: chloroform, ACN: acetonitrile, DMSO: dimethyl sulfoxide). Absorption spectrum of **SQ1** in CTC, too noisy because of the low solubility of the dye, was replaced by its excitation spectrum. (e-f) Excitation anisotropy in glassy 2-methyltetrahydrofuran at 77 K (dots). Excitation spectra collected under the same experimental conditions (dashed lines) are shown as a guide to the eye.

tion [211]. The same study revealed that core-substituted squaraines, quite independently of the identity of the donor groups, are close to the cyanine limit from the side of betaine-like dyes. Crystallographic studies further supported this finding, giving a low bond-length alternation (BLA) on the chain connecting the Nitrogen atoms (BLA = 0.02-0.03) [211].

Another interesting property to look at is fluorescence anisotropy (Figure 1.17 (e,f)), which was collected in vitrified 2-methyltetrahydrofuran. Excitation anisotropy of **SQ1** amounts to $r \approx 0.25$ in the red-edge of the spectral window and remains flat within the main OPA band. In the 450-500 nm range the measurement becomes challenging because of small absorption oscillator strength, however, anisotropy still oscillates around its maximum value. At $\lambda \approx 400$ nm we found the characteristic dip of squaraines, with a minimum anisotropy close to 0.05. Anisotropy increases to $r \approx 0.2$ at $\lambda \approx 380$ nm, and then decreases again in the region corresponding to weak signal(s) in the absorption spectrum.

Anisotropy of **SQ2** amounts to 0.25 inside the main absorption band, and remains flat until $\lambda \approx 450$ nm, on the red-side of the group of high-energy signals. Anisotropy decreases steeply to $r \approx 0$ at $\lambda \approx 400$ nm, and reaches a negative value ($r \approx -0.1$) at $\lambda \approx 380$ nm, corresponding to the secondary peak in the absorption spectrum. These data suggest that at least two different transitions contribute to the UV absorption band of **SQ2**: one at $\lambda \approx 455$ nm, with the same polarization of the main OPA band, and another at $\lambda \approx 380$ nm, polarized along the direction of the substituent. The minimum at which $r \approx 0$ could correspond to another transition, forming an angle of $\sim 54°$ with emission, or could originate from the overlap of the other two bands. This minimum could, instead, correspond to the dip observed for **SQ1**.

We will not investigate 2PA spectra of the squaraines here. 2PA spectra of structural analogues of **SQ1** and **SQ2** can be found in the paper by Ceymann *et al.* [215], however the acquisition was limited in the range 400-800 nm, in which 2PA of the two squaraines is very similar, with a weak peak ($\sigma \approx 100$ GM) at the vibronic shoulder of the main absorption band and a tail at high-energy, peaking outside the accessible range and is not informative in our case.

From experiment to the model

Spectroscopic data of the two indolenine-based squaraines invite to the essential-state modelling. We will start from the simplest model, the three-state model, that is known to be the minimal model working for the description of the basic properties of unsubstituted squaraines like **SQ1** [85], but has never been tested for core-substituted squaraines such as **SQ2**.

According to the three-state model, squaraines are described as DAD dyes. To account for the centrosymmetric structure of **SQ1**, we assumed a linear arrangement of the donor and acceptor moieties ($\alpha = 180°$). Accordingly, selection rules predict that only the $|g\rangle \rightarrow |c\rangle$ transition is OPA allowed, while $|g\rangle \rightarrow |e\rangle$, expected at higher energies, is dark. Therefore, only the low-energy region of the calculated spectra can be compared to experiment (Figure 1.18). Nevertheless, the model reproduces accurately the position and shape of the OPA band, as well as the emission spectrum. Neither absorption nor emission is solvatochromic, according to the nonpolar nature of the ground and the excited state. Indeed, symmetric squaraines belong to class II, which includes quadrupolar chromophores not prone to symmetry-breaking effects.

Parametrization of **SQ2** is instead more challenging. We assume a slightly bent structure ($\alpha = 170°$), accounting for the *cis* conformation induced by core-substitution. This lowers the symmetry of the system, making $|g\rangle \rightarrow |e\rangle$ a bright transition too. However, there is uncertainty about the location of this transition in the absorption spectrum. For this transition we expect a polarization perpendicular to the main OPA band, a requirement that is met for the peak at $\lambda \approx 380$ nm, which is however insensitive to solvent polarity, as instead would be expected for CT transitions. Another feature that we want to reproduce is the negative solvatochromism, and we know that this system is close to the cyanine limit ($\rho \rightarrow 0.5$) [211].

A plausible parametrization of **SQ2** is shown in Figure 1.18 (b,d). The choice of model parameters can be intuitively rationalized from the comparison with **SQ1**. The parameter η is related to the energy difference between the resonating forms, and is in general expected to be dependent on the relative strength of the D/A groups [113]. Substitution with the dicyanovinylene, a strong electron acceptor, increases the electron withdrawing capabil-

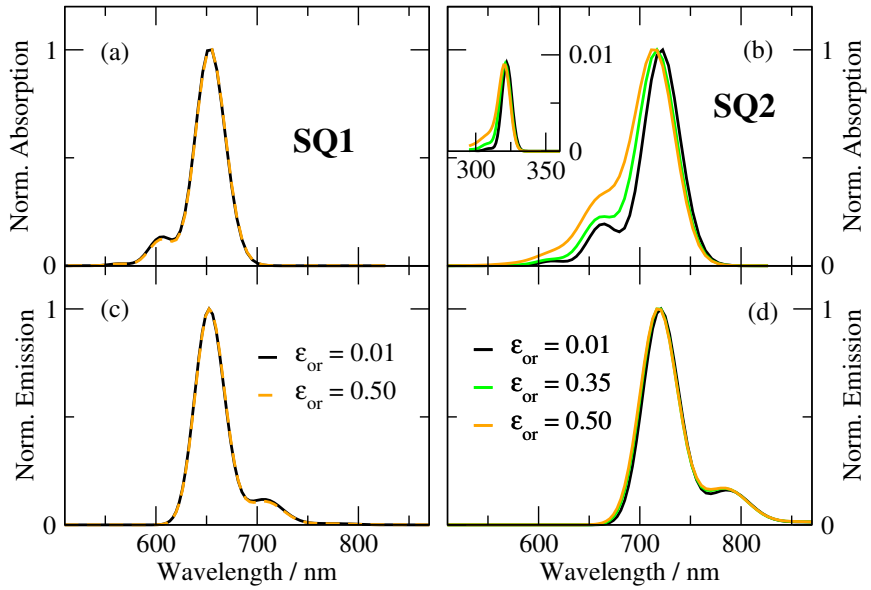

Figure 1.18: Absorption (a-b) and emission (c-d) spectra of **SQ1** (left) and **SQ2** (right) calculated with the three-state model. For clarity, only the region corresponding to the main OPA band is shown. The inset in the **SQ2** absorption spectrum contains a magnification of the secondary OPA peak. Model parameters for **SQ1**: $\eta = 0.35$ eV, $\sqrt{2}t = 1.10$ eV, $\omega_v = 0.15$ eV, $\varepsilon_v = 0.11$ eV, $\gamma = 0.05$ eV, $\alpha = 180°$. Model parameters for **SQ2**: $\eta = -0.10$ eV, $\sqrt{2}t = 1.35$ eV, $\omega_v = 0.15$ eV, $\varepsilon_v = 0.29$ eV, $\gamma = 0.05$ eV, $\alpha = 170°$. For clarity, spectra of **SQ1** are shown for two solvents only (a nonpolar and a highly polar solvent), and spectra of **SQ2** for only three solvents of different polarity. Values of ε_{or} are displayed on the panels and are in eV.

ity of the squaric core (A moiety in the model), stabilizing the zwitterionic structures with respect to the neutral one, hence it is not surprising that the charge-separated states become more stable than the neutral state ($\eta < 0$). On the opposite, the $\sqrt{2}t$ parameter is mostly related to the conjugating capability of the $D - A$ bridge and increases for higher conjugation. This parameter is very similar for the two squaraines, as the bridge connecting the donor moieties with the central site is the same. With the selected values of η and $\sqrt{2}t$ we obtained $\rho = 0.53$, very close to the cyanine limit.

The parameters ω_v and ε_v depend on the coupled vibrational modes, which in turn are related to the molecular backbone. The two squaraines possess the same skeleton, so that the same value of ω_v was chosen. The model only accounts for two vibrational degrees of freedom which takes into account the average effect of all the coupled modes: probably in **SQ2** there is a higher number of coupled modes, leading to a larger ε_v.

With this parametrization we got a satisfactory reproduction of the main OPA band, while the secondary band ($|g\rangle \rightarrow |e\rangle$ transition) is predicted at $\lambda \approx 320$ nm, i.e. blue-shifted by more than 60 nm (0.6 eV) with respect to the high-energy experimental band(s). Moreover, the relative intensity of the two bands is underestimated compared to experiment. Only a slight blue-shift of the absorption spectrum with solvent polarity could be reproduced, amounting to ~ 10 nm (160 cm^{-1}). On the opposite, the calculated emission spectrum was insensitive to solvent polarity. This behaviour is related to incipient ground-state symmetry breaking, favoured by polar solvents, locating **SQ2** at the boundary between class II and class III.

Making a step further, we also applied the five-state model described in Ref. [139] to both squaraines.

Spectra of **SQ1** calculated with the five-state model are shown in Figure 1.19. With respect to the three-state model, we do not loose in accuracy concerning the position and shape of the main OPA band, as well as in the fluorescence spectrum. Also the lack of solvatochromic effects over a wide polarity range is well accounted for, both in absorption and emission.

The new feature introduced by the five-state model consists in the ability to describe the short-wavelength region of the spectrum. A weak OPA peak is found below 400 nm, due to the presence of an OPA transition polarized along the short molecular axis. This state is also responsible for the decrease

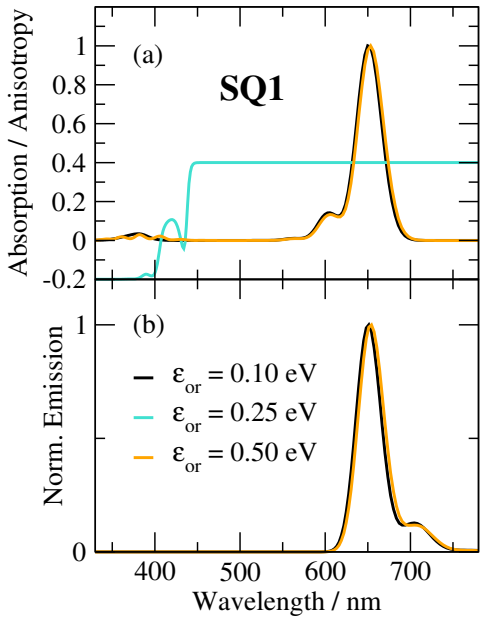

Figure 1.19: Spectra of **SQ1** calculated with the five-state model. (a) Room temperature absorption spectra (black and orange lines) and excitation anisotropy (turquoise line) calculated in frozen solvent at 90 K. (b) Room temperature emission spectra. Model parameters: $\eta = 0.78$ eV, $\tau = 0.73$ eV, $\beta = 0.70$ eV, $\omega_v = 0.15$ eV, $\varepsilon_v = 0.11$ eV, $\gamma = 0.05$, $\mu_0^x = 5.4$ D, $\mu_0^y = 24.4$ D. Absorption and emission spectra were calculated in a low polarity solvent ($\varepsilon_{or} = 0.1$ eV) and a highly polar solvent ($\varepsilon_{or} = 0.5$ eV), while anisotropy was calculated for an intermediate polarity, to mimic 2-methyltetrahydrofuran ($\varepsilon_{or} = 0.25$ eV).

of fluorescence excitation anisotropy from 0.4, inside the main OPA band, to -0.2 in the UV region. The dip is wide and too deep compared to experiment, where a positive anisotropy was found. These observations stress the limits of the five-state model already pointed out in Ref [139] and detailed in the previous section for **SQ0**. The main source of deviation from experiment could be the origin of the anisotropy dip (electronic or vibronic), but also the nature of the states in the UV, that could be one (or more) states localized on the donor units.

In order to be applied to **SQ2**, the five-state model has to be generalized to account for the nonequivalence of the acceptor groups (Figure 1.20).

A core-substituted squaraine can be described by the general $DAA'D$ formula, where A and A' correspond to the Oxygen atom and the substituent

of the squaric ring respectively. Five basis states are introduced to describe this system, a neutral state $|N\rangle$ and four charge-separated states. The states in which the electron resides on the same acceptor site are degenerate, thus, we have two pairs of degenerate states, $|Z_1\rangle$ and $|Z_2\rangle$, with a negative charge on A, of energy 2η with respect to $|N\rangle$, and $|Z'_1\rangle$ and $|Z'_2\rangle$, with a negative charge on A', of energy $2\eta'$. The matrix elements τ and τ' mix the neutral state with the zwitterionic states, indicating the degree of hopping from the donor to the A or A' site respectively. An additional parameter, β, accounts for charge resonance between the acceptor sites. On this basis the electronic Hamiltonian $\hat{H}_e$ can be written as

$$\hat{H}_e = \begin{pmatrix} 0 & -\tau' & -\tau & -\tau' & -\tau \\ -\tau' & 2\eta' & -\beta & 0 & 0 \\ -\tau & -\beta & 2\eta & 0 & 0 \\ -\tau' & 0 & 0 & 2\eta' & -\beta \\ -\tau & 0 & 0 & -\beta & 2\eta \end{pmatrix} \tag{1.44}$$

When $A' = A$, i.e. in an unsubstituted squaraine, $\eta' = \eta$ and $\tau' = \tau$ so that the four zwitterionic states become degenerate and the model collapses to the one described in Ref. [139]

Exploiting C_{2v} symmetry of the system, the $|Z_1\rangle$ and $|Z_2\rangle$ states can be combined into the symmetry-adapted $|Z_+\rangle = \frac{1}{2}(|Z_1\rangle + |Z_2\rangle)$ and $|Z_-\rangle = \frac{1}{2}(|Z_1\rangle - |Z_2\rangle)$ states of A_0 and B_0 symmetry respectively. In the same way $|Z'_1\rangle$ and $|Z'_2\rangle$ give the symmetric combination $|Z'_+\rangle = \frac{1}{2}(|Z'_1\rangle + |Z'_2\rangle)$ and the antisymmetric combination $|Z'_-\rangle = \frac{1}{2}(|Z'_1\rangle - |Z'_2\rangle)\rangle$. According to symmetry, $|N\rangle$, $|Z_+\rangle$ and $|Z'_+\rangle$ are mixed to give the ground state and two excited states, while $|Z_-\rangle$ and $|Z'_-\rangle$ give two B_0 excited states. All four electronic transitions are allowed with different polarization, as depicted in Figure 1.20 (b).

Given the equivalence of the D groups, the absolute value of the y component of the dipole moment operator is the same (μ_0^y) for all the charge-separated states. On the opposite, we assumed different $D - A$ and $D - A'$ distances, defining different x components of the dipole moment operators for the two pairs of degenerate states, μ_0^x for $|Z_1\rangle$ and $|Z_2\rangle$, and $\mu_0'^x$ for $|Z'_1\rangle$ and $|Z'_2\rangle$.

As usual, we introduced two mutually decoupled vibrational coordinates q_1 and q_2, describing nuclear motion along the two equivalent molecular

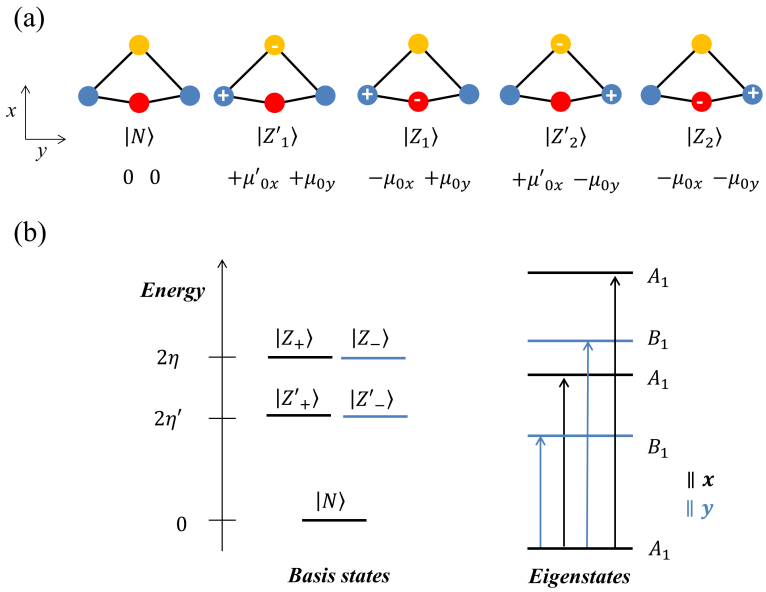

Figure 1.20: The five-state model for a core-substituted $DAA'D$ squaraine. (a) Sketch of the five basis states and their dipole moment components. Blue circles stand for D groups, red and orange circles for A and A' respectively. (b) Energies of the electronic basis states (left) and the eigenstates (right), labelled with their symmetry species. States of the same colour have the same symmetry. All transitions are active in both OPA and 2PA and are polarized either along the y axis (blue arrows) or the x axis (black arrows).

arms. The coordinates are characterized by the harmonic frequency ω_v and the vibrational relaxation energy ε_v. The vibrational Hamiltonian reads:

$$\begin{aligned}\hat{H}_v = &-\sqrt{2\varepsilon_v}\omega_v\hat{q}_1\left(\left|Z'_1\right\rangle\left\langle Z'_1\right| + \left|Z_1\right\rangle\left\langle Z_1\right|\right)\\ &-\sqrt{2\varepsilon_v}\omega_v\hat{q}_2\left(\left|Z'_2\right\rangle\left\langle Z'_2\right| + \left|Z_2\right\rangle\left\langle Z_2\right|\right)\\ &+\frac{1}{2}\left[\omega_v^2(\hat{q}_1^2+\hat{q}_2^2)\right] + \frac{1}{2}(\hat{p}_1^2+\hat{p}_2^2)\end{aligned} \tag{1.45}$$

Several attempts of parametrization of **SQ2** with the five-state model were unsuccessful. The main issue concerns the simultaneous reproduction of anisotropy and OPA spectrum in the UV range and solvatochromism. Chemical intuition suggests that $\eta' < \eta$, being A' a stronger acceptor than A, as shown in Figure 1.20. Excluding symmetry-breaking effects, the ground state contains a contribution of the neutral state, giving a dipole moment that is always lower than the one of the first excited-state, originating from

the mixing of charge-separated states only, always resulting in positive solvatochromism. According to anisotropy, the first transition in the 300-500 nm range should have the same polarization of the main absorption band, i.e. it should have B_0 symmetry. However, the order of the states cannot be modified, at least for realistic parametrization, and an A_0 state is always in-between the ground-state and the first B_0 state, of which there is no experimental evidence.

The transitions in the 300-500 nm region could instead be localized on the squaric core. Indeed, the substituent may act as an acceptor with respect to the whole molecule pointing to a completely different electronic structure. The shape and intensity of this band changes with the nature of the substituent, further supporting this hypothesis [182, 203, 209].

Summarizing, our work confirmed that the three-state model provides a fairly good description of standard unsubstituted squaraines, as far as absorption and emission spectra are concerned. For these dyes, the five-state extension allows for a more detailed description, however it requires a careful interpretation of experimental data and introduces more degrees of freedom.

Both models are inadequate to describe core-substituted squaraines. Substitution heavily perturbs the electronic structure of the system bringing about new issues to solve. For example, it is necessary to distinguish between CT and local excitations, and eventually to look at structural variations following photoexcitation. The univocal interpretation of the processes involved is fundamental for developing a suitable, and possibly simple, model. Indeed, for substituted squaraines, an increase of the basis set dimension prevents the analytical solution of the problem, resulting in more difficult parametrization, overproliferation of adjustable parameters and more complex analysis.

1.5 Conclusion

Spectroscopic properties of multipolar dyes in solution are dictated by the interplay between the intrinsic electronic structure, electron-phonon coupling and medium effects. The understanding of the photophysics of this class of dyes requires a balanced description of these elements and relies

on the synergy between experimental techniques and advanced theoretical models.

Essential-state models, briefly reviewed in the first part of the Chapter, are an effective theoretical tool for the description of multipolar chromophores, combining all the factors mentioned above. ESMs describe optical properties of fairly large ad complex structures in terms of only a few states, providing a unifying interpretative scheme. Moreover, in the ESM approach, the limited number of parameters entering the Hamiltonian can be readily extracted from experiment and, once fixed, can be used to predict other properties of interest.

In this Chapter we challenged the ESMs with the description of two complex chromophoric systems in solution, exploring the strengths and also the limits of the essential-state approach.

The first system under study was a novel aza-nanographene dye characterized by a butterfly-shaped three-dimensional architecture obtained by the π-expansion of the electron rich pyrrolo[3,2-*b*]pyrrole building block. Spectroscopic properties of this dye are quite interesting: good emission quantum yield in a wide polarity range and a pronounced emission solvatochromism, typical of quadrupolar dyes undergoing excited-state symmetry breaking, in spite of the lack of electron-withdrawing groups. At the same time, detailed spectroscopic investigation pointed out that fluorescence emission is almost completely depolarized for excitation inside the main absorption band(s), indicating a more complex picture with respect to prototypical quadrupolar dyes.

A coherent interpretation of experimental data was achieved resorting to extensive theoretical analysis based on two complementary theoretical frameworks: TDDFT and ESMs. TDDFT analysis disclosed the underlying quadrupolar nature of the dye, in which the PP acts as electron donor towards the peripheral wings. It also demonstrated the presence of a symmetry-broken first excited state, responsible for emission solvatochromism, identifying the dye as a class I quadrupolar chromophore, in spite of its unique structure.

The complexity of the absorption spectrum and excitation anisotropy was fully rationalized as a consequence of the proximity of CT and localized excited states with different polarization and oscillator strengths.

The intense localized transitions dominate absorption and anisotropy, while CT transitions, because of their low oscillator strengths, are hidden in the absorption spectrum but are responsible for intense emission and solvatochromism. Moreover, the fluorescent CT state could mix with nearby intense localized excitations, borrowing emission intensity from them.

These observations were confirmed by the fact that it was possible to isolate CT transitions in the experimental data, and reproduce quantitatively their features with a simple ESM, accounting for only three states (three-state model), as for typical ADA quadrupolar dyes.

These results open a new perspective in the design of heterocyclic nanographenes, exploiting the charge polarization induced by the electron-richness of the PP moiety. This dye is also an example of the combination between a quadrupolar character, generating solvatofluorochromism, and an extended π-structure originating several intense overlapping transitions leading to a wide absorption range from the UV to the visible spectrum.

The last part of the Chapter was devoted to the well-known family of squaraine dyes. In spite of their long history, the understanding of their main spectroscopic properties is still debated. Theoretical modelling of squaraines with standard (TD)DFT is limited by their biradicaloid character, which is the source of large inaccuracies. On the other hand, high-level first principle methods are time-consuming, and to date, are unsuitable for the size of the majority of structures.

In this context, ESMs are promising candidates for the theoretical study of this dye family. Indeed, a simple three-state model was adequate for the description of the main optical properties of squaraines, including the main OPA band, the intense 2PA band and emission spectra, and was effective in explaining the lack of solvatochromism, due to the absence of symmetry-breaking phenomena.

This simple model has however some limits, concerning the detailed description of optical spectra, including the fine structure of the 2PA spectrum and the accurate description of excitation anisotropy, and more recently a five-state model was proposed, describing a squaraine like a DA_2D dye.

Here, we extended the three-state and five-state pictures, with the aim of achieving a more detailed and sound description of squaraine dyes. We proposed two different ESMs, which account for the inner degree of freedom of

the squaric ring, namely a six-state and an eight-state model. Both models were tested against literature data on a simple aniline-based squaraine, however, in spite of some improvements, none of them provided an exhaustive description of the spectroscopic properties.

We also addressed, for the first time, the extensive spectroscopic investigation and essential-state modelling of a core-substituted squaraine. The key features arising from substitution of the squaric core are the appearance of a set of absorption signals in the UV, and a negative solvatochromism of absorption and emission bands, indicating a polar ground state. These features could not be reproduced by the standard three-state model, so that also the five-state model was tested, that was redefined to account for different A groups ($DAA'D$).

The failure of the modelling has mostly to be related to the complex electronic structure of squaraines, that cannot be fully captured by the standard essential-state approach. The complexity increases in the high-energy region of the spectrum, where CT and localized excitations may be close in energy, and significant mixing of the relevant states may occur, reducing the CT character of the states. Moreover, the origin of the characteristic dip in the excitation anisotropy spectrum was not clarified and needs confirmation from experiment or other reliable theoretical models.

Besides these issues applying to the entire family of squaraine dyes, other questions have to be solved for core-substituted dyes, in which substitution substantially affects the charge distribution of the molecule pointing to a more complex scenario. Also in this case, further extensive and systematic spectroscopic investigation on a wider variety of molecules with different substituents are highly desirable to focus on the key phenomena involved.

Nevertheless, the study proposed herein provided a focus on squaraine spectroscopy, disclosing all the critical points in the modelling of this interesting family of chromophores. Moreover, these results do not undermine our confidence in the three-state model concerning the ability to describe the main CT-related properties of squaraine dyes, but rather claims for more in-depth investigation.

Chapter 2

Interacting chromophores: models and spectroscopy

2.1 Introduction

Optical properties of molecular materials depend crucially on intermolecular interactions. The occurrence of inter- and supramolecular interactions is responsible for the formation of aggregates, namely dimers, multichromophores, clusters and crystals, and may give rise to unique responses which cannot be achieved from isolated (solvated) molecules [218–222]. Cooperative and collective effects depend on the mutual orientation and distance of the molecular units, and the unfavourable molecular packing may be detrimental for the device performance [219, 222–225]. Thus, the design of smart molecular materials requires the simultaneous control over two different aspects: the chemical structure of the chromophoric units and their supramolecular organization [26, 226].

From the chemical point of view, the molecular backbone of the chromophore can be optimized through the choice of the building blocks and the type of linkers, tailoring orbital energies and molecular conformation [37, 227–230], while the spatial arrangement of the dyes may be controlled by the insertion of suitable scaffolds or through self-assembly governed by chemical substitution and/or the choice of external conditions, such as temperature or solvent [231–238].

Quantum chemical models relating the optical properties of aggregates to their supramolecular architecture are fundamental for the full knowledge-based exploitation of the nonadditive behaviour of supramolecular assemblies for the design of materials and devices [239].

A popular model for the description of the optical properties of molecular aggregates is the so-called excitonic model, which represents the intermolecular interactions as electrostatic interactions between transition dipole moments of the monomeric units [81, 240]. The excitonic picture well describes typical changes of the optical properties following aggregation, such as the splitting or the shift of the absorption bands, as well as the enhancement or suppression of fluorescence [56].

However, the validity of the excitonic model is limited to aggregates of nonpolar and hardly polarizable molecules. Indeed, polar molecules are characterized by fairly large permanent dipole moments in the ground as well as in the excited states, which can interact *via* electrostatic forces of the same order of magnitude, or even larger, than their excitation energies [44, 45, 241]. A polarizable molecule in a cluster feels the electric field generated by the neighbouring molecules and readjusts its polarity in a feedback mechanism, a phenomenon known as mean-field effect. The mean-field effect is responsible for the cooperative behaviour of the aggregate, and adds to the effects of the excitonic coupling, therefore it has to be carefully considered when dealing with supramolecular assemblies of multipolar (and polarizable) chromophores [46, 61, 242, 243].

In this Chapter we will give an overview both at the theoretical and experimental level of the effect of intermolecular interactions on the spectroscopy of molecular materials, through the presentation of selected case studies on systems of different complexity.

After a short introduction to the excitonic model, we will describe the detailed TDDFT investigation of a model dimeric structure obtained by covalent bonding of two N-substituted naphthalimides, which, due to its electronic structure, can be satisfactorily rationalized based on the excitonic scheme.

Moving on, we will address the effect of aggregation on phosphorescence of molecular materials based on polar chromophores, which cannot be understood without properly considering mean-field effects.

Finally, we will present an experimental work investigating the intriguing self-aggregation behaviour of a family of near-IR emitting multipolar dyes decorated with alkyl chains, highlighting the interplay between chemical substitution, solvation and mechanical effects on molecular packing and optical properties.

2.2 The excitonic model

Suppose a collection of identical molecules, each one behaving like a two-level system, i. e. described by the ground state $|g\rangle$ and an excited state $|e\rangle$, separated by the energy $E = \hbar\omega_0$ (Figure 2.1 (a)). In a dilute solution we can assume the lack of intermolecular interactions and we expect only one peak in the absorption spectrum centered at $\omega = \omega_0$, corresponding to the $|g\rangle \rightarrow |e\rangle$ transition.

If we increase the concentration of the solution, the molecules will start experiencing intermolecular (Van der Waals) forces, which will induce the formation of aggregates. For now we will consider the simplest aggregate: a dimer of equivalent species, each one described by the two-level picture introduced above. For convenience we label the two molecules with numbers 1 and 2, and we assume that their transition energy is ω_0 ($\hbar = 1$). We also assume that their transition dipole moments, $\overrightarrow{\mu}_1$ and $\overrightarrow{\mu}_2$, are of the same magnitude and are oriented in the aggregate to form an angle α.

This two-molecule system is described *via* four basis states which, in the absence of intermolecular interactions, coincide with the eigenstates: the ground state $|gg\rangle$, describing both molecules in the $|g\rangle$ state, two degenerate state at energy ω_0, $|eg\rangle$ and $|ge\rangle$, describing one molecule in the ground state and the other in the excited state, and the state $|ee\rangle$, of energy $2\omega_0$, describing both molecules in the excited state (Figure 2.1 (b), middle panel).

The interaction between the molecules is responsible for the mixing of the basis states. As a first approximation, the intermolecular interactions can be regarded as a weak perturbation, so that the only relevant mixing is the one between the degenerate states $|eg\rangle$ and $|ge\rangle$. The eigenstates of the coupled system, $|+\rangle$ and $|-\rangle$, are given by the following linear combinations [56]:

$$|\pm\rangle = \frac{1}{\sqrt{2}}(|eg\rangle \pm |ge\rangle) \tag{2.1}$$

and their energy is

$$E_{\pm} = \omega_0 \pm J \tag{2.2}$$

where J is the interaction matrix element $J = \langle eg| \hat{V} |ge\rangle$. $\hat{V}$ is the Hamiltonian describing the electrostatic interaction and, within the dipole approximation, it is proportional to the interaction between the transition dipole moments of the molecules. The states $|+\rangle$ and $|-\rangle$ are called monoexcitonic states, since they describe a single excitation delocalized over both molecules.

The dipole moment operator $\hat{M}$ of the dimer reads $\hat{M} = \overrightarrow{\mu}_1 + \overrightarrow{\mu}_2$. It follows that the transition dipole moments relevant to the $|gg\rangle \rightarrow |+\rangle$ and $|gg\rangle \rightarrow |-\rangle$ transitions, μ_{gg+} and μ_{gg-}, are

$$\mu_{gg\pm} = \langle \pm| \hat{M} |gg\rangle = \frac{(\overrightarrow{\mu}_1 \pm \overrightarrow{\mu}_2)}{\sqrt{2}} \tag{2.3}$$

Thus, in the absorption spectrum of the aggregate we expect two bands, separated by a $2|J|$ energy gap, whose relative intensity depends on the angle α, i. e. on the geometrical arrangement of the molecules:

$$\frac{I_+}{I_-} = \left(\frac{1+\cos\alpha}{1-\cos\alpha}\right)^2 \tag{2.4}$$

The transition towards the $|ee\rangle$ state is instead forbidden.

We will now focus on two specific geometries of the dimer, as sketched in Figure 2.1 (b). In a face-to-face arrangement of the chromophores (left panel of Figure 2.1 (b)), the transition dipoles are parallel ($\alpha = 0$) and only the symmetric monoexcitonic state $|+\rangle$ can be populated in absorption, while $|-\rangle$ is dark. Thus, the absorption spectrum of the aggregate features a single signal at higher energy compared to the isolated molecule. Aggregates whose absorption is shifted at higher frequency with respect to the constituting monomers are usually called H-aggregates [244, 245]. These aggregates are poorly fluorescent, since after photoexcitation they quickly relax towards the lowest excited state $|-\rangle$, which is dark.

Conversely, when the molecules are arranged in a head-to-tail geometry ($\alpha = 180°$, right panel of Figure 2.1 (b)), only the $|-\rangle$ state can be accessed upon absorption, while $|+\rangle$ is dark. In this case aggregation is responsible for a red-shift of the absorption spectrum, and aggregates are usually called J-aggregates [246, 247]. Intense fluorescence emission characterizes

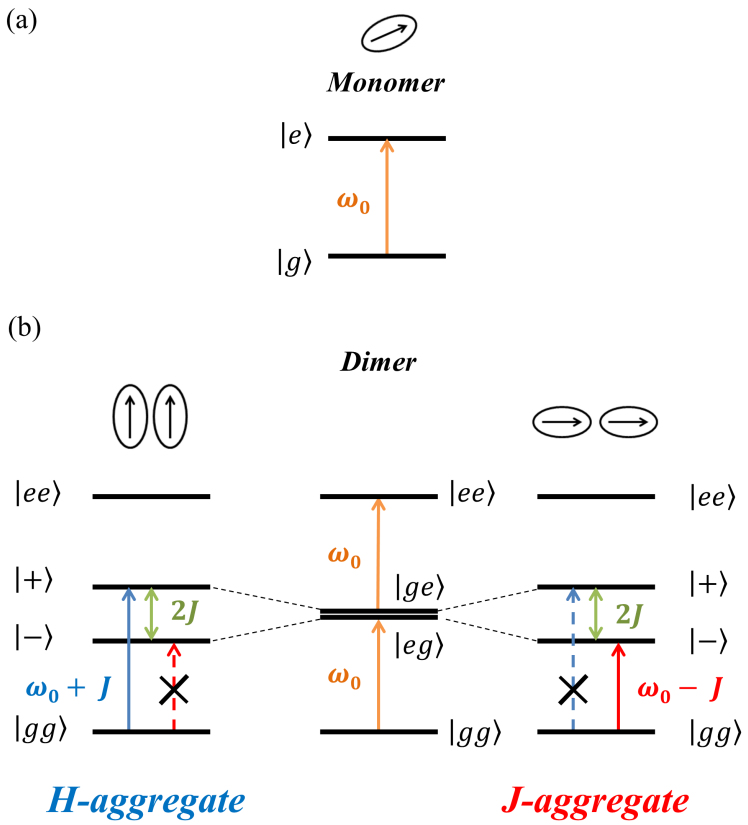

Figure 2.1: The excitonic model. (a) A two-level model for the monomer. (b) Excitonic model for a dimer: unperturbed states (middle) and eigenstates of the coupled system (left and right panels). The intermolecular interactions described by the coupling J induce a splitting of the degenerate basis states $|eg\rangle$ and $|ge\rangle$ into the monoexcitonic states $|+\rangle$ and $|-\rangle$ at energies $\omega_0 + J$ and $\omega_0 - J$ respectively. In the limiting case of H-aggregates (face-to-face transition dipoles, left), only the transition at energy $\omega_0 + J$ is allowed, while the $|-\rangle$ state is dark. In the limiting case of J-aggregates (head-to-tail transition dipoles, right), only the transition at $\omega_0 - J$ is allowed, while the $|+\rangle$ state is dark.

J-aggregates, since their lowest-energy state ($|-\rangle$) possess a non vanishing transition dipole moment towards the ground state.

The exciton model for a dimer can be easily extended to a cluster of N molecules [56]. In this case, diagonalization of the coupled Hamiltonian yields 2^N eigenstates, which can be classified according to the number of excitations shared by the molecules. We will have a ground state, describing the situation in which all the molecules are in their ground state, N monoexcitonic states, describing the delocalization of one excitation and forming a band centered at ω_0, $0.5N(N-1)$ bi-excitonic states describing two excitations delocalized over the aggregate, forming another band at higher energy and so on.

Only transitions between neighbouring bands are allowed in linear spectroscopy, so that for a system initially in its ground state, only the monoexcitonic band can be populated in (linear) absorption. It can be demonstrated that only a few monoexcitonic states possess a finite transition dipole moment and contribute to the absorption spectrum. The position of the brightest state into the monoexcitonic band depends on the sign of J. For $J > 0$ most of the oscillator strength is shared by the states on the top of the excitonic band, so that a blue-shift of the absorption spectrum is predicted compared to the monomer and also the fast relaxation towards the lowest-energy excited states, which is dark and responsible for fluorescence quenching. This is the case of H-aggregates, as mentioned above. Conversely, for $J < 0$, the largest oscillator strength is associated to transitions towards the lowest-energy states of the monoexcitonic band, resulting in a red-shift of the absorption spectrum and also bright emission, which denote J-aggregation.

2.3 Excitonic interactions in naphthalimide dimers

1,8-naphthalimide (NI) is an attractive electron-deficient building block in organic chemistry, and its derivatives found widespread applications, for example as fluorescent probes and anticancer drugs [248]. The properties of these derivatives can be tuned by proper substitution of the NI moiety, either at the N-imide site or on the aromatic core, leading to large families of NI-based materials with different optical and electrochemical behaviour [249].

For instance, while unsubstituted NIs are characterized by $\pi - \pi^*$ transitions in the UV, the substitution at the 4-position with electron donating units promotes the appearance of low-energy CT bands, shifting the absorption spectrum to the visible or near-IR [250].

Because of their planar structure, most NI-based dyes prepared in the past decades showed the tendency to form $\pi - \pi$ stacks in the solid state (H-type aggregates), which suppressed emission intensity and posed a serious limit to their application in light-emitting devices. More recent works instead demonstrated that the appropriate functionalization of the NI core could prevent H-type aggregation promoting instead aggregated induced emission (AIE) behaviour [251]. Moreover, it was found that nonplanar architectures in which the NI moiety is substituted at the 4-position and through a single covalent bond with an electron donating aromatic group tilted with respect to the NI plane are able to form self-assembled structures capable of stabilizing long-lived CT states [252, 253].

Another interesting application of NIs is as fully organic phosphorescent materials in optoelectronic devices [254–256]. Also in this case, the understanding of how the electronic structure of NI is affected by chemical substitution and supramolecular interactions deserves special attention.

In this Work, performed in collaboration with Prof. Mahesh Hariharan (Indian Institute of Science Education and Research, Trivandrum, India), we focused on a dimeric structure obtained by covalent linkage of two identical NI moieties. This essential architecture will allow to gain a deeper understanding of the coupling between the NI units as well as the effect of their geometrical arrangement.

The molecular structures of investigated chromophores are displayed in Figure 2.2. The two monomers, **NI-pr** and **NI-DIPA**, are constituted by a NI moiety *N*-substituted with groups of increasing electron donating ability, respectively propyl (pr) and 2,6-diisopropyl phenyl (DIPA). The corresponding dimers, **NINI-pr** and **NINI-DIPA**, are obtained joining two monomers at the 4-position through a covalent C-C bond. The comparative study between the four structures in Figure 2.2 allows to simultaneously assess both the effect of *N*-substitution and the coupling between the monomers.

While *N*-substituted NIs have been extensively investigated through steady-state and time resolved techniques [257–261] and theoretical mod-

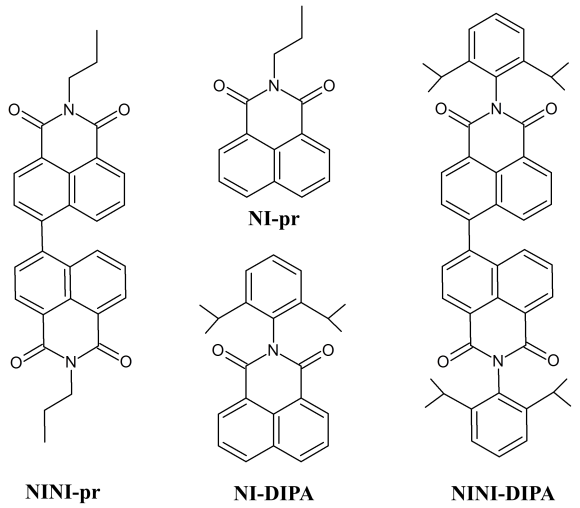

Figure 2.2: Molecular structure of the target NI derivatives: monomers **NI-pr** and **NI-DIPA** and corresponding dimers **NINI-pr** and **NINI-DIPA**.

els [256, 262, 263], to the best of our knowledge, only few reports on dimeric NI-based systems are available to date [264, 265]. In this work we will tackle the theoretical description of the electronic structure of the target NI-based dimers, exploring for the first time their triplet manifold.

2.3.1 NI-pr and NINI-pr

Propyl-substituted compounds, **NI-pr** and its related dimer **NINI-pr**, have the same skeleton of **NI-DIPA** and **NINI-DIPA**, and are a good starting point to analyze the effects of the covalent linkage between two identical molecular fragments. Their smaller size, compared to their DIPA-substituted counterparts, make them easier to attack with TDDFT computations. Moreover, the low electron-donating ability of the propyl fragment should exclude its participation in the low-energy photophysics of the dimer, allowing us to focus on the NI-NI interaction only. Only as the last step we will consider the effect of substitution with DIPA.

From the experimental point of view, the spectroscopic features of the propyl-substituted dyes are analogous to those of the related DIPA-containing compounds (see Subsection 2.3.2), suggesting a similar ground and excited-

state scenario. In chloroform, the absorption spectrum of the monomeric species peaks below 350 nm, while absorption of the dimers is red-shifted by $\sim$ 25 nm (0.2 eV). Emission of **NINI-pr**, more intense compared to **NI-pr**, spans the 400-500 nm spectral window and undergoes a moderate positive solvatochromic shift from cyclohexane to dimethyl formamide ($\lambda_{em}^{max} = 407$ and 435 nm respectively).

Calculations were performed with the Gaussian16 package [159]. Ground state calculations were performed at DFT level of theory [155–157], while excited state properties were computed with its time-dependent extension (TDDFT) [162–165]. To achieve an accurate description of CT states, all calculations were performed with the long-range corrected ωB97XD functional [266], together with the 6-31+G(d,p) basis set. Stationary points were characterized by frequency analysis, and solvent effects were described according to the PCM approach [160, 267]. Standard equilibrium solvation was adopted in geometry optimizations, while default nonequilibrium solvation was assumed in the calculation of vertical excitation energies, unless otherwise stated.

For model compounds **NI-pr** and **NINI-pr** all calculations were performed in chloroform. Frontier molecular orbitals (FMOs) of **NI-pr** are shown in Figure 2.3 (a). According to our results, the HOMO-LUMO gap of **NINI-pr** amounts to 7.5 eV, and the LUMO is well separated (by more than 2 eV) from the rest of unoccupied orbitals. All FMOs are localized on the NI moiety, and the propyl chain is involved in low-energy occupied orbitals only. Therefore, we expect a marginal effect of the alkyl substituent on the low-energy spectroscopy of **NI-pr**.

Vertical excitation energies obtained from TDDFT calculations are collected in Table 2.1. The most intense transition ($f = 0.410$), the $S_0 \rightarrow S_1$ transition, is predicted at 3.9 eV and is polarized along the C_2 axis of the NI. This transition has mainly (98%) a HOMO $\rightarrow$ LUMO character and is localized on the NI moiety. Another weakly allowed transition, the $S_0 \rightarrow S_2$ transition, is predicted at 4.2 eV, has a dominant contribution (82%) from HOMO-1 $\rightarrow$ LUMO, and is localized on the NI group as well.

Inspection of the FMOs and the density difference plots provided in Figure 2.4 (a) suggest that both the aforementioned transitions are $\pi - \pi^*$ in nature, as well as $S_0 \rightarrow S_5$ and $S_0 \rightarrow S_6$. Conversely, $S_0 \rightarrow S_3$ and $S_0 \rightarrow S_4$,

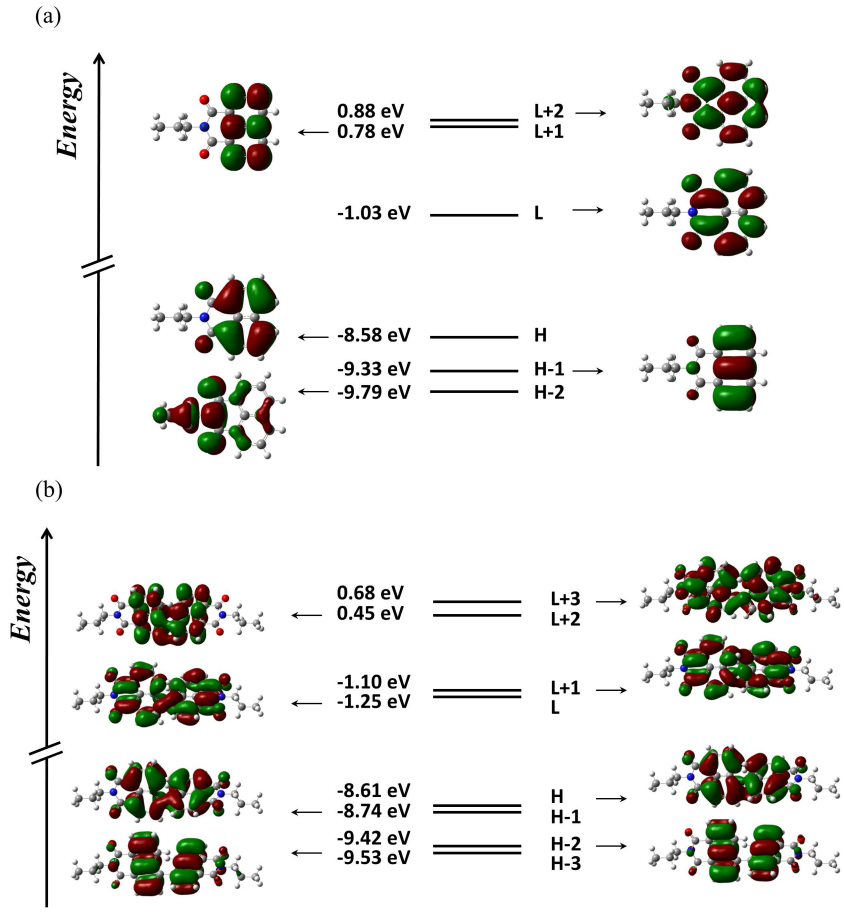

Figure 2.3: Frontier molecular orbitals (FMOs) of (a) **NI-pr** and (b) **NINI-pr**. Energies and contour plots (isovalue 0.02) calculated at DFT level (ωB97XD/6-31+G(d,p)) in chloroform.

Table 2.1: The lowest-energy $S_0 \rightarrow S_n$ transitions of **NI-pr** and **NINI-pr**: transition energy and wavelength, oscillator strength (f) and main excitations calculated at TDDFT level (ωB97XD/6-31+G(d,p)) in chloroform. Data in italic were obtained with state-specific solvation.

NI-pr				
S_n	Energy/eV	Wavelength/nm	f	Type (> 20%)
S_1	3.931 (*4.004*)	315.4 (*309.6*)	0.410	H → L (98%)
S_2	4.249 (*4.233*)	291.8 (*292.9*)	0.092	H-1 → L (82%)
S_3	4.433 (*4.471*)	279.7 (*277.3*)	0.000	H-3 → L (82%)
S_4	4.748 (*4.784*)	261.1 (*259.2*)	0.010	H-4 → L (60%)
S_5	5.005 (*4.979*)	247.7 (*249.0*)	0.034	H-2 → L (58%)
S_6	5.510 (*5.583*)	225.0 (*222.1*)	0.153	H → L+1 (26%)
				H → L+2 (46%)
NINI-pr				
S_n	Energy/eV	Wavelength/nm	f	Type (> 20%)
S_1	3.793 (*3.864*)	326.9 (*320.9*)	1.095	H-1 → L+1 (32%)
				H → L (65%)
S_2	3.970 (*4.036*)	312.3 (*307.2*)	0.002	H-1 → L (48%)
				H → L+1 (48%)
S_3	4.230 (*4.221*)	293.1 (*293.7*)	0.103	H-3 → L+1 (32%)
				H-2 → L (48%)
S_4	4.243	292.2	0.062	H-3 → L (40%)
				H-2 → L+1 (39%)
S_5	4.400	281.8	0.000	H-7 → L+1 (39%)
				H-6 → L (42%)
S_6	4.400	281.8	0.000	H-7 → L (40%)
				H-6 → L+1 (39%)

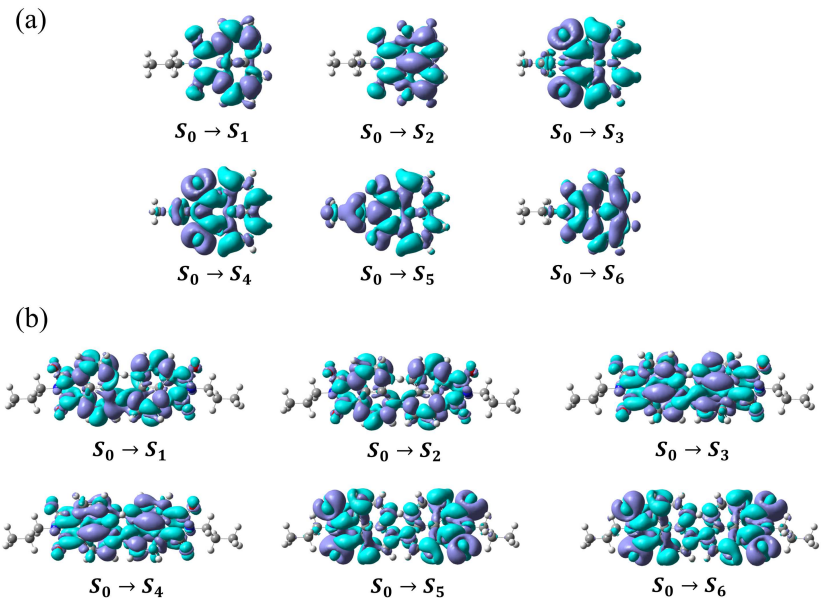

Figure 2.4: Density difference plots for the six lowest-energy singlet transitions of (a) **NI-pr** and (b) **NINI-pr** computed at TDDFT level in chloroform. Upon excitation, electron density moves from the regions in purple to the regions in blue.

also localized on the NI moiety, possess a prominent $n-\pi^*$ character, as they involve the lone pairs on the Oxygen atoms. The alkyl group participates in $S_0 \rightarrow S_5$ only, which has a low oscillator strength and mainly LE character, as evinced from density difference plots. We also remark that state-specific corrections [166] have a small effect (< 0.07 eV) on the estimated transition energies, as expected for LE transitions.

In the optimized ground state geometry of **NINI-pr**, the two NI moieties are tilted by $\sim 73°$ because of the steric repulsion between the hydrogen atoms on the naphthalene subunits. FMOs of **NINI-pr** are provided in Figure 2.3. In the energy diagram, the FMOs are distributed in pairs, and each pair is constituted by the in-phase and out-of-phase combinations of the same **NI-pr** orbitals. Indeed, the orbitals of **NI-pr** are only slightly distorted in **NINI-pr**, indicating that the coupling of the NI moieties is weak, as due to the almost orthogonal arrangement of the monomeric subunits. In more detail, the combination between HOMO-1 orbitals of **NI-pr** originates HOMO-2 and HOMO-3 of **NINI-pr**, the combination of **NI-pr** HOMOs

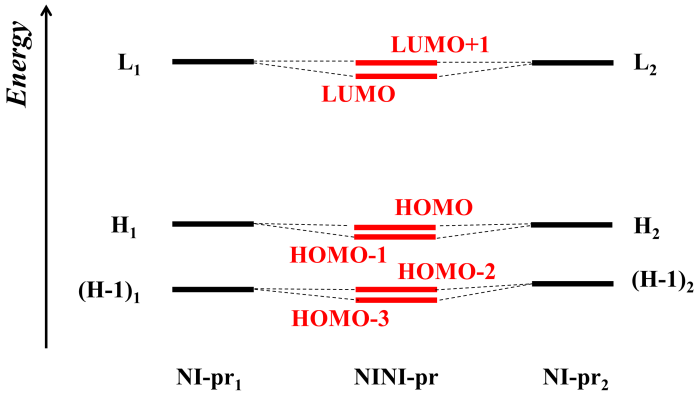

Figure 2.5: Energy scheme of **NINI-pr** orbitals (middle) and two equivalent **NI-pr** molecules. Degenerate **NI-pr** orbitals combine into pairs of **NINI-pr** orbitals. Subscripts 1 and 2 denote the two molecules in the dimer.

originates HOMO and HOMO-1, and the combination of **NI-pr** LUMOs originates LUMO and LUMO+1, as sketched in Figure 2.5.

TDDFT results on **NINI-pr** are collected in Table 2.1. The highest oscillator strength ($f = 1.095$) is associated to the $S_0 \rightarrow S_1$ transition, which is predicted below 3.8 eV, i. e. red shifted by 0.14 eV compared to **NI-pr**. The $S_0 \rightarrow S_2$ transition is dark, while a weakly allowed transition ($S_0 \rightarrow S_3$) is expected at 4.2 eV. Because of the high computational cost, the energies corrected for state-specific solvation were computed for the three lowest-energy transitions only, and are in agreement with those obtained with default nonequilibrium solvation.

All singlet transitions of **NINI-pr** are combinations of two electronic excitations with similar weight. Density difference plots in Figure 2.4 (b) may help in the identification of their character. Their analysis suggests that all transitions are combinations of excitations on both **NI-pr** units possessing the same character. Indeed, each transition of **NI-pr** splits into two equivalent transitions in **NINI-pr**: $S_0 \rightarrow S_1$ and $S_0 \rightarrow S_2$ **NINI-pr** correspond to a $S_0 \rightarrow S_1$ transition on each **NI-pr** unit, $S_0 \rightarrow S_3$ and $S_0 \rightarrow S_4$, almost degenerate, correspond to a $S_0 \rightarrow S_2$ transition on each **NI-pr**, while $S_0 \rightarrow S_5$ and $S_0 \rightarrow S_6$ correspond to $S_0 \rightarrow S_3$ on isolated **NI-pr**.

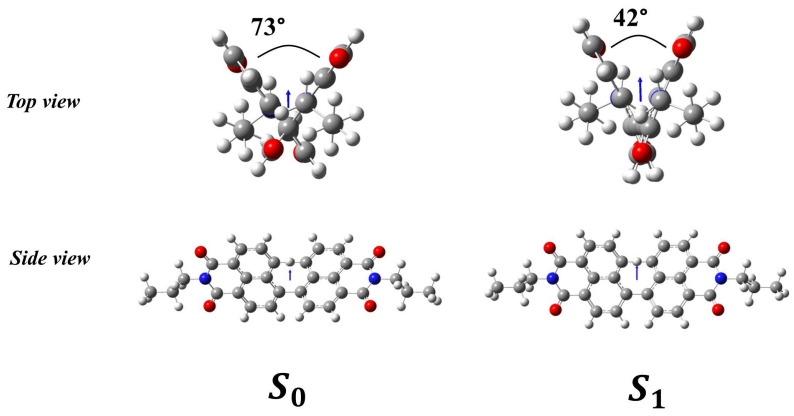

Figure 2.6: Optimized geometry of **NINI-pr** in the ground state (left) and first excited state (S_1, right). Dipole moments are shown as blue vectors. The angle between the NI moieties is decreased in the relaxed excited state.

These results support a purely exciton model for **NINI-pr**. The head-to-head arrangement of the **NI-pr** units induces the J-coupling between them [265]. The $S_0 \rightarrow S_1$ transition dipole moments of the two **NI-pr** molecules, aligned along the direction of the C-C bond connecting them, originates a splitting into a lower-energy transition ($S_0 \rightarrow S_1$) with a three-fold enhanced oscillator strength, and a higher-energy transition ($S_0 \rightarrow S_2$) which is dark. The effect is a red shift of the absorption spectrum of **NINI-pr** compared to **NI-pr**.

Significant geometrical rearrangements occur during the relaxation of **NINI-pr** in the first excited state. The main modifications concern the angle between the NI moieties, decreasing from 73.35° in the ground state to 41.96° in the relaxed S_1 state, leading to a more planar structure (Figure 2.6). At the same time, the length of the bond connecting the two subunits decreases from 1.49 to 1.43 Å, indicating an increase of conjugation between the monomers. Moreover, NI groups slightly deviate from planarity in relaxed S_1 state. The permanent dipole moment of **NINI-pr** amounts to 0.296 D in the ground state and increases to 0.406 D in the relaxed excited state.

The large structural modifications in the excited state justify a sizeable Stokes shift in mildly polar solvents. Indeed, emission is predicted at

3.10 eV (399.4 nm) with nonequilibrium solvation, and is mainly (95%) a HOMO ← LUMO transition, where the orbitals are only slightly distorted with respect to the ground state.

2.3.2 NI-DIPA and NINI-DIPA

Steady-state spectra of DIPA-substituted dyes collected in chloroform are reported in Figure 2.7 (a). **NI-DIPA** features a well resolved absorption band in the region between 300 and 350 nm peaking at $\lambda = 335$ nm. Absorption of **NINI-DIPA** is red-shifted by ~ 25 nm (0.2 eV) and spans the 300-400 nm region ($\lambda_{abs}^{max} = 359$ nm).

Emission of **NI-DIPA** is too weak to be estimated (typically QY $\leq 3\%$ for alkyl *N*-substituted NIs [268]), conversely, **NINI-DIPA** is characterized by brighter emission, with fluorescence quantum yields amounting to 14% in toluene, 15% in chloroform and 39% in acetonitrile. It also features sub-nanosecond fluorescence lifetimes (0.85 ns) in toluene and chloroform and 1.71 ns lifetime in acetonitrile. Fluorescence emission occurs between 400 and 500 nm, and, contrary to absorption, is sensitive to solvent polarity. The emission maximum is red-shifted by ~ 50 nm (0.2 eV) from nonpolar cyclohexane to more polar dimethyl formamide, and experiences concomitant band broadening. Large Stokes shifts are found in mildly polar solvents, e. g. 3800 cm^{-1} in chloroform. **NINI-DIPA** is also characterized by good triplet quantum yield (45%), estimated relative to the standard $[Ru(bpy)_3]Cl_2$ with the method of triplet-triplet energy transfer towards β-carotene [269, 270].

TDDFT results: singlet states

Geometry optimization and TDDFT calculations of **NI-DIPA** and **NINI-DIPA** were performed in chloroform and acetonitrile, a mildly and strongly polar solvent respectively. However, geometrical parameters and TDDFT results are barely affected by solvent polarity and in the following we will focus on results in chloroform only, to get a direct comparison with experiment.

When **NI-DIPA** is in its ground state, the NI and DIPA moieties lie on almost perpendicular planes, due to steric hindrance provided by the

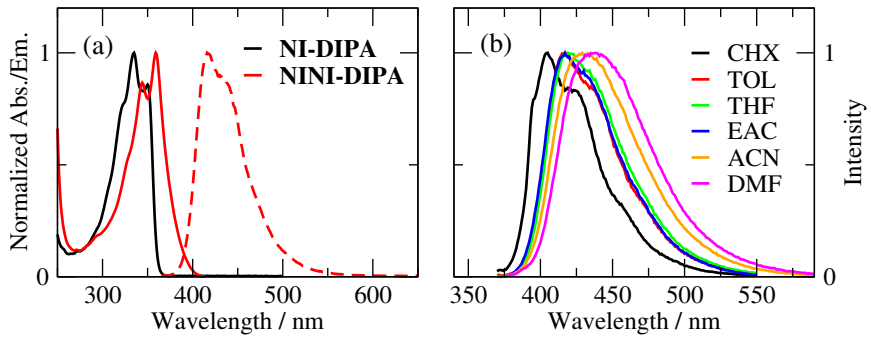

Figure 2.7: Optical spectra of **NI-DIPA** and **NINI-DIPA** in solution. (a) Absorption spectra of **NI-DIPA** and **NINI-DIPA** (continuous lines) and emission spectrum of **NINI-DIPA** (dashed line) in chloroform. (b) Emission spectrum of **NINI-DIPA** in solvents of different polarity (CHX: cyclohexane, TOL: toluene, THF: tetrahydrofuran, EAC: ethyl acetate, ACN: acetonitrile, DMF: dimethyl formamide).

isopropyl groups on the DIPA (Table 2.2). The length of the bond connecting the NI to the DIPA (1.4 Å) is close to the typical length of a single C-N bond. This should reduce the conjugation between the two fragments, disfavouring intramolecular CT.

FMOs of **NI-DIPA** can be localized on the NI moiety, on the DIPA, or both of them (Figure 2.8 (a)). As for **NI-pr**, the HOMO-LUMO gap of **NI-DIPA** amounts to 7.5 eV, however, while the LUMO has the same shape and is localized on the NI, the HOMO, as well as HOMO-1, is delocalized over the whole molecule.

TDDFT results are summarized in Table 2.3. The brightest transition of **NI-DIPA** is the $S_0 \rightarrow S_1$, predicted at ~ 3.9 eV as for **NI-pr**, and blue shifted by ~ 0.4 eV (35 nm) with respect to the experimental absorption. This transition corresponds to a combination with similar weights of two excitations, HOMO-1 $\rightarrow$ LUMO (42%) and HOMO $\rightarrow$ LUMO (54%) and is polarized along the direction of the C-N bond connecting the DIPA to the NI. In order to get a more readable picture of the transition character we generated the electron density difference plots in Figure 2.9 (a), from which it emerges that the redistribution of electron density occurring upon the $S_0 \rightarrow S_1$ process is confined on the NI group, making this transition a local excitation, as for **NI-pr**. Indeed, HOMO-1 and HOMO of **NI-DIPA**

Table 2.2: Geometrical parameters and dipole moment (μ) of the ground state (S_0) and relaxed excited states of **NI-DIPA** and **NINI-DIPA** computed in chloroform at ωB97XD/6-31+G(d,p) level of theory. $\delta_{NI-DIPA}$: dihedral angle between the plane of NI and the plane of DIPA; $d_{NI-DIPA}$: length of the C-N bond connecting NI to DIPA; δ_{NI-NI}: dihedral angle between the NI planes of the two monomers; d_{NI-NI}: length of the C-C bond connecting the NI units. [a]The S_1 geometry of **NINI-DIPA** was optimized with TDA. [b]Not calculated.

NI-DIPA				
	S_0	S_1	S_5	T_1
$\delta_{NI-DIPA}$/deg	89.60	89.54	72.88	89.72
$d_{NI-DIPA}$/Å	1.44	1.44	1.42	1.44
μ/D	5.95	7.71	10.40	6.36
NINI-DIPA				
	S_0	S_1[a]	S_5[b]	T_1
δ_{NI-NI}/deg	73.52	40.42	–	63.94
$\delta^1_{NI-DIPA}$/deg	90.86	91.05	–	90.61
$\delta^2_{NI-DIPA}$/deg	89.35	90.75	–	90.71
d_{NI-NI}/Å	1.49	1.43	–	1.48
$d^1_{NI-DIPA}$/Å	1.44	1.44	–	1.44
$d^2_{NI-DIPA}$/Å	1.44	1.44	–	1.44
μ/D	0.436	0.547	–	0.754

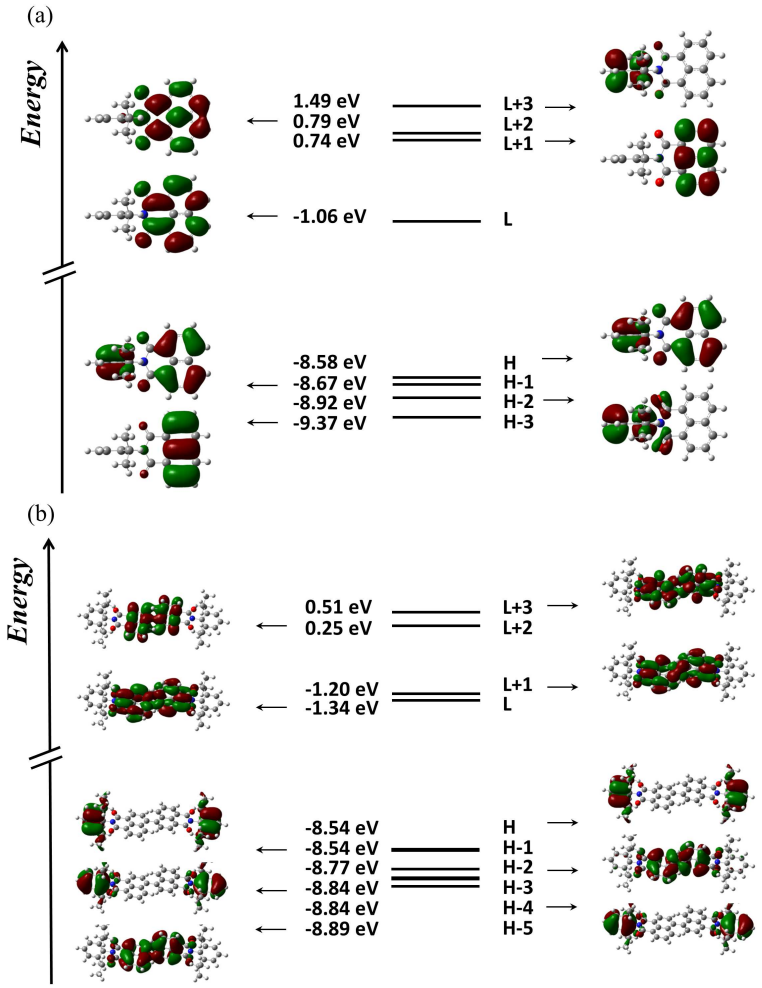

Figure 2.8: Frontier molecular orbitals (FMOs) of (a) **NI-DIPA** and (b) **NINI-DIPA**. Energies and contour plots (isovalue 0.02) calculated at DFT level (ωB97XD/6-31+G(d,p)) in chloroform.

are characterized by the same phase on the NI group and opposite phase on the DIPA, cancelling out the contribution of DIPA to excitation.

The $S_0 \rightarrow S_2$ transition is allowed with a lower oscillator strength, is predicted at 4.26 eV (291 nm) and possess a LE character as well. From the plots in Figure 2.9, we recognize that the first two transitions are $\pi - \pi^*$ in nature, while the third and the fourth are $n - \pi^*$, matching with the corresponding lowest-energy transitions of **NI-pr**. Conversely, $S_0 \rightarrow S_5$ and $S_0 \rightarrow S_6$ transitions of **NI-DIPA** possess a marked intramolecular CT character from the electron-rich DIPA to the electron withdrawing NI.

As expected, the magnitude of state-specific corrections to excitation energies increases with increasing the CT character of the transitions. While the energy of the LE transitions is basically independent of the solvation method, the $S_0 \rightarrow S_5$ transition is stabilized by ~ 0.8 eV with SS solvation, i. e. shifted to ~ 0.1 eV above the SS-corrected $S_0 \rightarrow S_1$ transition. However, both CT transitions are dark, excluding their contribution to the absorption spectrum.

The optimized geometry of the first excited state (S_1) of **NI-DIPA** is almost indistinguishable from the ground-state geometry. Its dipole moment lies along the C-N direction as in the ground state and becomes larger by 1.8 D (Table 2.2). Indeed, as already pointed out in previous theoretical studies [262], only the $\pi - \pi$ bonding pattern of the Carbon atoms on the naphthalene subunit is changed going from the S_0 to the S_1 state, while the imide moiety remains unaffected.

Conversely, the optimized geometry of the lowest-energy CT state (S_5) is characterized by a twist of the DIPA with respect to the NI plane, yielding a more planar structure. Indeed, the dihedral angle between the two units is decreased by 17° (Table 2.2). At the same time, the length of the bond connecting NI to DIPA is also slightly decreased, coherently with the increase of conjugation between the two moieties. The relaxed S_5 state is also characterized by a large dipole moment, almost twice as large as the ground state's.

The energy difference between relaxed S_1 and S_5 states amounts to ~ 0.9 eV, suggesting that the CT state is not involved in emission. The emission energy predicted with standard nonequilibrium solvation is 3.402 eV (364.4 nm), corresponding to a HOMO $\leftarrow$ LUMO (95%) de-excitation.

Table 2.3: The lowest-energy $S_0 \rightarrow S_n$ transitions of **NI-DIPA** and **NINI-DIPA**: excitation energy and wavelength, oscillator strength (f) and main excitations calculated at TDDFT level (ωB97XD/6-31+G(d,p)) in chloroform. Data in italic were obtained with state-specific solvation.

NI-DIPA				
S_n	Energy/eV	Wavelength/nm	f	Type (> 20%)
S_1	3.933 (*3.996*)	315.2 (*310.3*)	0.461	H-1 → L (42%)
				H → L (54%)
S_2	4.258 (*4.242*)	291.1 (*292.3*)	0.097	H-3 → L (82%)
S_3	4.351 (*4.397*)	284.9 (*282.0*)	0.000	H-4 → L (63%)
S_4	4.774 (*4.847*)	259.7 (*255.8*)	0.000	H-6 → L (70%)
S_5	4.917 (*4.096*)	252.2 (*302.7*)	0.000	H-1 → L (54%)
				H → L (42%)
S_6	4.973 (*5.575*)	249.3 (*271.0*)	0.000	H-2 → L (72%)
NINI-DIPA				
S_n	Energy/eV	Wavelength/nm	f	Type (> 20%)
S_1	3.809 (*3.410*)	325.5 (*363.6*)	1.235	H-3 → L+1 (29%)
				H-2 → L (23%)
				H → L (40%)
S_2	3.987	310.9	0.002	H-3 → L (42%)
				H → L+1 (30%)
S_3	4.245	292.1	0.106	H-7 → L+1 (32%)
				H-6 → L (46%)
S_4	4.257	291.2	0.064	H-7 → L (40%)
				H-6 → L+1 (37%)
S_5	4.356	284.6	0.000	H-9 → L (34%)
				H-8 → L+1 (30%)
S_6	4.356	284.6	0.001	H-9 → L+1 (30%)
				H-8 → L (34%)

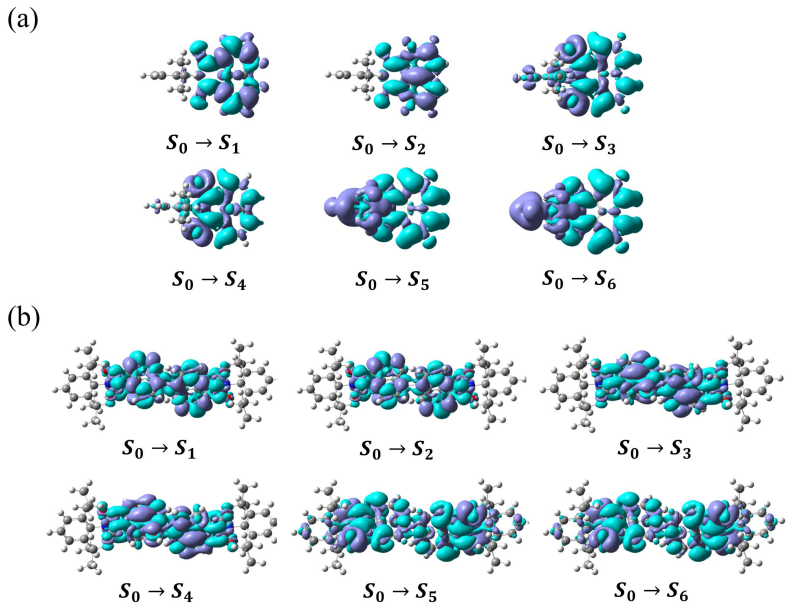

Figure 2.9: Density difference plots for the six lowest-energy singlet transitions of (a) **NI-DIPA** and (b) **NINI-DIPA** computed at TDDFT level in chloroform. Upon excitation, the electron density moves from the regions in purple to the regions in blue.

In the ground state of **NINI-DIPA** the planes of the two NI moieties are twisted by approximately 74°, and the bond joining them is a typical single C-C bond, disfavouring electron transport between the monomers, as it happens in **NINI-pr**. The two monomeric units retain the geometry of the isolated **NI-DIPA** molecule, with perpendicular NI and DIPA planes and same C-N bond length (Table 2.2).

FMOs of **NINI-DIPA** (Figure 2.8 (b)) can be regarded as linear combinations of the corresponding **NI-DIPA** orbitals. In more detail, LUMO and LUMO+1, separated by 0.14 eV, are the in-phase and out-of-phase combinations of **NI-DIPA** LUMOs, and are localized on the NI groups of the two equivalent monomers. Occupied orbitals are closer in energy and are localized either on the NIs (e.g. HOMO-2 and HOMO-5) or on the DIPAs (e.g. HOMO, HOMO-1, HOMO-3 and HOMO-4). Linear combinations of orbitals localized on the DIPA moieties (i.e. the pair HOMO/HOMO-1 and the pair HOMO-3/HOMO-4), which are spatially separated, are almost degenerate, while combinations of orbitals localized on the NI groups, which are in close proximity, undergo a splitting amounting to ~ 0.12 eV for the HOMO-2/HOMO-5 pair.

Singlet transition energies of **NINI-DIPA** computed at TDDFT level are reported in Table 2.3. The brightest transition is predicted at 3.8 eV and coincides with $S_0 \rightarrow S_1$, as for **NINI-pr**. The predicted energy is overestimated by ~ 0.3 eV with respect to experiment when default nonequilibrium solvation is assumed, while the agreement with experimental data significantly improves adopting state-specific corrections. The main transition of **NINI-DIPA** is red shifted by 0.12 eV compared to **NI-DIPA**, in good agreement with experiment (~ 0.2 eV).

Inspection of the density difference plots of **NINI-DIPA** (Figure 2.9 (b)) points out that, as in **NINI-pr**, the $S_0 \rightarrow S_1$ and the $S_0 \rightarrow S_2$ transitions originate from the $S_0 \rightarrow S_1$ transition of the monomer, the $S_0 \rightarrow S_3$ and $S_0 \rightarrow S_4$ transitions originate from the $S_0 \rightarrow S_2$ transition, and the $S_0 \rightarrow S_5$ and $S_0 \rightarrow S_6$ transitions from $S_0 \rightarrow S_3$. None of them possess neither an intermolecular nor an intramolecular CT character, and the participation of DIPA is ruled out.

Optimization of the S_1 geometry of **NINI-DIPA** with full TDDFT becomes computationally demanding because of the large number of atoms.

Therefore, we replaced the lenghty full TDDFT optimization with the Tamm-Dancoff approximation [271]. Calculated geometrical distortions of relaxed S_1 are in agreement with those observed for **NINI-pr**, as expected by their structural similarity. In the S_1 minimum, the dimer assumes a more planar conformation, as the dihedral angle between the NI planes is reduced from 73° in the ground state to $\sim 40°$ in the relaxed excited state. Within each monomeric unit, the NI and the DIPA lie on perpendicular planes, as in the ground state, inhibiting conjugation between the two fragments. As the geometry rearranges, the dipole moment, pointing perpendicularly to the direction of the C-C bond joining the monomers, increases by ~ 0.1 D, and may contribute to the solvatochromic shift observed in emission. The large structural variations accompanying excited-state relaxation are also compatible with the large Stokes shift experimentally observed also in mildly polar solvents. Fluorescence emission is predicted at ~ 3 eV (~ 410 nm) with nonequilibrium solvation, in good agreement with experimental data.

In summary, the electronic structure of DIPA-substituted compounds is very similar to that of their propyl-substituted analogues, notwithstanding the different electron donating ability of the substituent. Thanks to its electron richness, the DIPA can be involved in intramolecular CT towards the electron-deficient NI moiety, however the CT transitions are dark and they are located at higher energy with respect to $\pi-\pi^*$ excitations of the NI core, which dominate absorption and emission spectroscopy. N-substitution of the NI with stronger electron-donating groups may stabilize the CT states, giving rise to interesting LE/CT interplays [256, 263].

The connection of two NIs at the 4-position through a covalent single C-C bond, independently of the substituent, induces the J-coupling between the monomers, which are arranged in a head-to-head geometry, and the $S_0 \rightarrow S_1$ transition of the monomer is split in two transitions, a lower-energy bright transition with high oscillator strength (approximately three times the oscillator strength of the monomer), and a dark transition at higher energy.

TDDFT results: triplet states

Various non-radiative de-excitation mechanisms follow photoexcitation events. For example, internal conversion (IC) is the non-radiative transition

between two states of the same multiplicity. Typically IC is effective on fast timescales, and is the reason behind Kasha's rule for which when we photoexcite a chromophore, fluorescence usually stems from the lowest (singlet) excited state.

Conversely, intersystem crossing (ISC) consists in a non-radiative transition between states with different multiplicity [272]. While IC is a fast and common spin-allowed process, ISC is spin-forbidden. To achieve sizeable ISC rates, significant spin-orbit coupling us necessary, as induced, for example, by the presence of heavy atoms such as Br and I, or transition metals [273]. However, small purely organic phosphors are highly desirable and many efforts were devoted in the last years to the synthesis and optimization of heavy-atom free organic chromophores with efficient ISC ability [274].

The ISC rate k_{ISC} can be described by the following equation:

$$k_{ISC} \propto \frac{\langle T_1 | \hat{H}_{SO} | S_1 \rangle^2}{(\Delta E_{S_1 - T_1})^2} \tag{2.5}$$

where $\hat{H}_{SO}$ is the spin-orbit coupling Hamiltonian [275] and $\Delta E_{S_1-T_1}$ is the energy gap between the states involved in ISC (here we assumed that ISC occurs from S_1 to T_1, even if in some cases higher-energy singlet and triplet states may be involved [276]). Therefore, large spin-orbit matrix elements and small energy gaps are required to enhance ISC [277]. The latter requirement is also referred to as the energy gap law [278].

Another qualitative rule is the so-called El-Sayed rule [279], stating that ISC is enhanced if it involves a change of orbital type, for example $^1(\pi - \pi^*) \rightarrow {}^3(n - \pi^*)$. The $^1(\pi - \pi^*) \rightarrow {}^3(\pi - \pi^*)$ or $^1(n - \pi^*) \rightarrow {}^3(n - \pi^*)$ transitions are instead disfavoured.

Aromatic carbonyl compounds, that can benefit from closely spaced $n - \pi^*$ and $\pi - \pi^*$ transitions, are prone to ISC, representing promising all-organic phosphorescent materials [280]. NI derivatives are among the mostly investigated structures possessing these features as their intersystem crossing quantum yield can reach unity [281]. It follows that the exploration of the triplet manifold of NI dimers adds valuable information to our study, and could pave the way to new applications.

Energies of the $S_0 \rightarrow T_n$ transitions were computed adopting the Tamm-Dancoff approximation [271] at ωB97XD/6-31+G(d,p) level of theory. Cal-

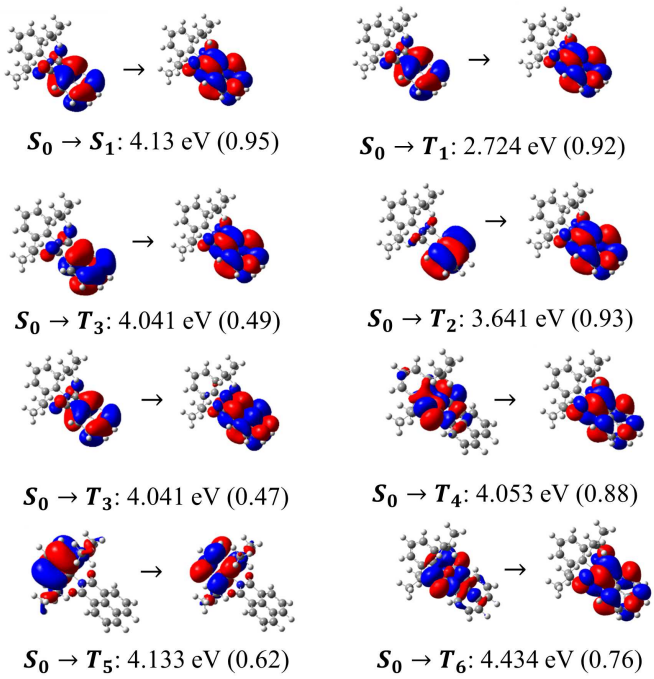

Figure 2.10: Natural transition orbitals for the lowest-energy singlet transition ($S_0 \rightarrow S_1$) and the lower $S_0 \rightarrow T_n$ transitions of **NI-DIPA**, and corresponding transition energies. Contribution of each NTO pair is given in brackets. Calculations performed in chloroform with TDA-TDDFT at ωB97XD/6-31+G(d,p) level of theory.

culations were performed in chloroform with default nonequilibrium solvation, given the LE nature of the transitions.

To provide a graphical information on the transition character at a low computational cost, Natural Transition Orbitals (NTOs) [282] were generated for the first singlet state and the lowest-energy triplet states. Indeed, NTOs offer a compact and more readable representation of electronic transitions, in which each transition is collapsed into excitations between one (or sometimes two) pair(s) of fictitious molecular orbitals called the NTOs. This representation is particularly useful for the characterization of the excited states, especially when several excitations are found with similar coefficients and no one is dominant, as it is our case.

The $S_0 \rightarrow T_1$ transition of **NI-DIPA** is predicted at 2.7 eV, i.e. the T_1 state lies $\sim$ 1.4 eV below the S_1 state. The transition possesses the

same $\pi - \pi^*$ nature of $S_0 \rightarrow S_1$, as argued from the corresponding NTOs (Figure 2.10). $S_0 \rightarrow T_2$ and $S_0 \rightarrow T_3$ are also $\pi - \pi^*$ transitions localized on the NI, while $S_0 \rightarrow T_5$ is still a $\pi - \pi^*$ transition but is localized on the DIPA moiety. According to the El-Sayed rule, ISC from S_1 to all the aforementioned triplet states is negligible. Conversely, $S_0 \rightarrow T_4$, as well as $S_0 \rightarrow T_6$, possess a $n - \pi^*$ character, as they involve the lone pairs of the oxygen atoms on the NI unit, and can thus provide an ISC channel.

ISC is favoured for small singlet-triplet energy gaps (Eq. 2.5). Two different energy gaps can be defined [283]. The so-called adiabatic singlet-triplet energy gap ΔE_{ST}^{ad} is obtained as the energy difference between the singlet and triplet states at their equilibrium positions. Due to the computational cost required by excited-state optimizations, ΔE_{ST}^{ad} were computed only for the T_1 state. Conversely, the vertical singlet-triplet energy gap ΔE_{ST}^{v} is calculated as the difference between the vertical transition energies from S_0 to the target singlet and triplet states. The energy gap relevant to the ISC from S_1 to T_1 of **NI-DIPA** calculated with the two approaches are in agreement (Table 2.4).

Spin-orbit coupling matrix elements (SOCMEs) relevant to ISC from the S_1 state towards the lowest-energy triplet states were computed on the S_1 optimized geometry with the ORCA package [284], adopting the Zero-Order Regular Approximation (ZORA) for relativistic effects [285], and the TDA. The ωB97X-D3 [286] functional was adopted together with def2-SVP basis set [287, 288]. Chloroform was introduced in the calculations with C-PCM model, as implemented in the ORCA code [289].

As expected, the SOCMEs are vanishing for the triplet states having the same nature ($\pi - \pi^*$) of the S_1 state, i.e. T_1 and T_3 (Table 2.4). Conversely, a fairly large coupling is found between the S_1 state and the T_4 state (> 13 cm^{-1}), which is instead $n - \pi^*$. This state is also almost degenerate with S_1, therefore, the $S_1 \rightarrow T_4$ could be the main ISC channel of **NI-DIPA**, as demonstrated elsewhere through dynamics simulations on a parent N-substituted NI [290]. Phosphorescence of **NI-DIPA** was predicted at 2.029 eV (611.0 nm), as typical of N-substituted NI derivatives [258].

NINI-DIPA is characterized by closely spaced $S_0 \rightarrow T_n$ transitions. $S_0 \rightarrow T_1$ and $S_0 \rightarrow T_2$ are predicted at ~ 2.7 eV, more than 1 eV below the $S_0 \rightarrow S_1$ transition. Corresponding NTOs (Figure 2.11) are the in-

Table 2.4: Adiabatic and vertical singlet-triplet energy gaps (ΔE_{ST}^{ad} and ΔE_{ST}^{v} respectively) and SOCMEs calculated for **NI-DIPA** and **NINI-DIPA** in chloroform (TDA-TDDFT, ωB97X-D3/def2-SVP). [a]energy of S_1 computed with TDA.

NI-DIPA			
Transition	ΔE_{ST}^{ad}/eV	ΔE_{ST}^{v}/eV	SOCME/cm^{-1}
$S_1 \rightarrow T_1$	1.235	1.411	0.00
$S_1 \rightarrow T_2$	–	0.4941	0.01
$S_1 \rightarrow T_3$	–	0.0939	0.01
$S_1 \rightarrow T_4$	–	0.0818	13.19
$S_1 \rightarrow T_5$	–	0.0017	0.01
$S_1 \rightarrow T_6$	–	-0.2989	6.53
NINI-DIPA			
Transition	ΔE_{ST}^{ad}/eV	ΔE_{ST}^{v}/eV	SOCME/cm^{-1}
$S_1 \rightarrow T_1$	1.145[a]	1.2815	0.16
$S_1 \rightarrow T_2$	–	1.2539	0.45
$S_1 \rightarrow T_3$	–	0.3319	0.09
$S_1 \rightarrow T_4$	–	0.3269	0.16
$S_1 \rightarrow T_5$	–	0.0308	0.46
$S_1 \rightarrow T_6$	–	-0.0626	0.14
$S_1 \rightarrow T_7$	–	-0.0771	5.25
$S_1 \rightarrow T_8$	–	-0.0772	9.52
$S_1 \rightarrow T_9$	–	-0.1628	0.06

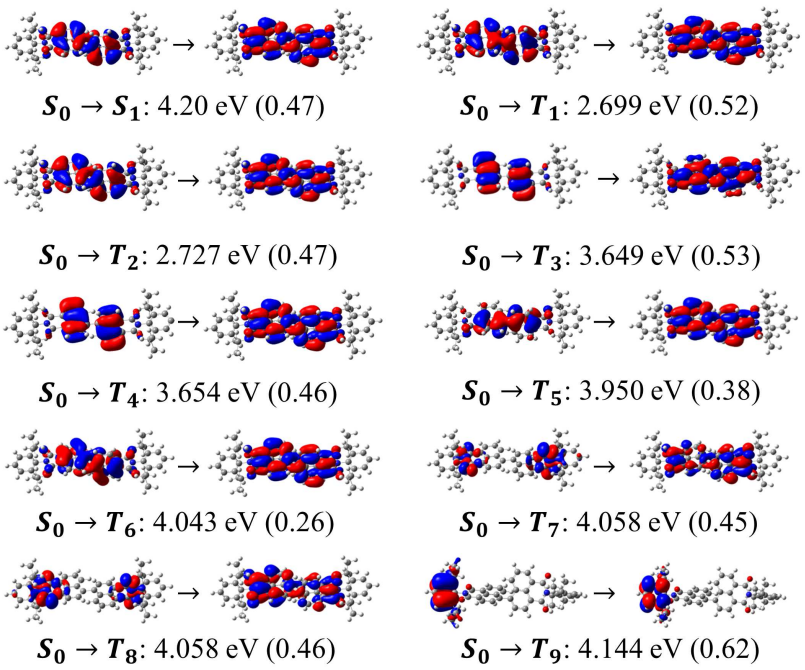

Figure 2.11: Natural transition orbitals for the lowest-energy singlet transition ($S_0 \rightarrow S_1$) and the lower $S_0 \rightarrow T_n$ transitions of **NINI-DIPA** and corresponding transition energies. The contribution of each NTO pair is given in brackets. Only one pair is shown for each transition; another pair with similar contribution differs only for the phase. Calculations were performed in chloroform with TDA-TDDFT at ωB97XD/6-31+G(d,p) level of theory.

phase and out-of phase combinations of $\pi - \pi^*$ transitions localized on the monomeric units, matching to the $S_0 \rightarrow T_1$ transition of **NI-DIPA**. A closer inspection to the NTOs indicates that each triplet transition of **NI-DIPA** is doubled in the dimer and both transitions are degenerate with the monomer transition. This result is in agreement with the excitonic theory, since triplet transitions are characterized by vanishing transition dipole moments, and therefore cannot interact.

SOCMEs of **NINI-DIPA** are sizable only for the two degenerate states T_7 and T_8. Indeed, $S_0 \rightarrow T_7$ and $S_0 \rightarrow T_8$ possess a $n - \pi^*$ character and are localized on the NI (Table 2.4). The small energy gap (< 0.1 eV) makes $S_1 \rightarrow T_{7-8}$ possible ISC channels for **NINI-DIPA**, explaining the sizeable experimental triplet quantum yield (45%).

The fact that the lowest-energy triplet state is located almost midway between the ground state and S_1 makes these systems promising candidates for triplet-triplet annihilation (TTA) applications [291–293]. TTA is one of the most attracting upconversion strategies, consisting in the population of an excited state at higher energy with respect to the incident photons. Some of the advantages of TTA are the low excitation power requirements, the use of incoherent excitation sources, the high upconversion efficiencies, and the possibility to exploit the tunability and light-harvesting ability of organic dyes over a wide spectral range.

The key process of TTA is the collision between two molecules M in the triplet state, $M^*(T_1)$, promoting one of them into the S_1 state ($M^*(S_1)$), while the other returns to its ground state:

$$M^*(T_1) + M^*(T_1) \rightarrow M^*(S_1) + M(S_0) \tag{2.6}$$

This process requires the fullfilment of the following relationship between the energy levels of M: $2E_{T_1} > E_{S_1}$, where E_{T_1} and E_{S_1} are the energies of the T_1 and S_1 states, respectively [292].

In **NI-DIPA** and **NINI-DIPA**, the sum of the energy of the triplet states is larger than the energy of the singlet state, making the process expressed by Eq. 2.6 exoergonic, and thermodynamically favoured. Moreover, the fluorescence properties of **NINI-DIPA** could be exploited to obtain upconverted emission in the blue spectral range, under appropriate conditions. More experimental studies will be planned to assess the TTA ability of **NINI-DIPA**.

2.4 Phosphorescent aggregates of polar chromophores: beyond the excitonic approximation

Thanks to their long emission lifetimes and high triplet quantum yields, phosphorescent materials attracted growing interest from various technological areas, for example light emitting devices, optical sensing, imaging and biomedical applications [294–300].

Because of the spin-orbit coupling requirements, transition metal complexes are among the most investigated phosphorescent materials [301].

However, the synthesis of metal-free phosphorescent molecules, highly desirable in view of the reduced toxicity and better tunability, represents a rich research field, and many fully organic phosphorescent dyes were prepared and studied in the last decades [300, 302–304]. To date, only a few studies were considering CT chromophores as phosphorescent materials [302, 305–307], however, the possibility to achieve long lasting luminescence at room temperature from custom-designed donor-acceptor systems makes them likely to be the focus of material sciences in the near future.

Since many applications of phosphorescent materials are in the solid state, the understanding of the effects of molecular packing and intermolecular interactions on the luminescence properties of the molecular assembly sets the basis for the engineering of efficient devices [226,308–311]. It is well known that different polymorphs may exhibit different emission intensities and/or wavelengths [312, 313]. Indeed, polymorphism represents an opportunity to obtain different luminescence properties from the same molecular structure and, if the polymorphs can be interconverted by external stimuli, it can be exploited in luminescent switches [226, 305, 306, 314, 315].

From the theoretical side, the popular exciton approximation works well for interacting nonpolar dyes, but can be misleading when applied to aggregates of polar and polarizable molecules, which can readjust their charge distribution according to the local electrostatic field generated by the neighbouring molecules, leading to additional cooperative (mean-field) effects completely overlooked in the excitonic picture [118].

In this context, ESMs represent a flexible tool for the description of aggregates of CT chromophores, incorporating excitonic and mean-field effects in a coherent and physically sound picture [242]. ESMs for aggregates can be readily built in a bottom-up approach starting from the corresponding single-molecule Hamiltonians, and the model parameters extracted for the solvated molecule can be rigidly transferred to the aggregate without re-optimization, implying a great predictive impact. So far, ESMs have been developed and validated for dimers, aggregates and clusters of dipolar [45, 59, 61, 118, 231, 241, 243, 316] and quadrupolar [46, 128–131] dyes, and were successful in describing not only spectral shifts but also more intriguing phenomena such as bistability [243], multielectron transfer [241] and the amplification of NLO responses [46, 61].

In the following, we will introduce an ESM describing simple aggregates of phosphorescent dipolar dyes, which will allow us to draw general considerations on the effects of intermolecular interactions on phosphorescence, and offer guidelines to experimentalists about the design of new phosphorescent materials based on CT dyes.

Although fully organic dyes are preferable to their organometallic counterparts, the achievement of intense emission from the triplet states of metal-free dyes is a challenging issue, dealing with the unfavourable selection rules for the singlet-to-triplet transitions, and the concomitant effects of intermolecular interactions in the solid state. For these reasons, the in-depth investigation of purely organic phosphors is still in its infancy, while metal complexes, coming in a variety of well-characterized structures, are good benchmarks for theoretical models.

In this Section, we will discuss a specific case study consisting in a dinuclear Rhenium(I) complex featuring two highly luminescent concomitant polymorphs characterized by different emission colours [317]. Notwithstanding its complex electronic structure, which cannot be captured by a simple few-state model, this dye represents an example of a polar CT system, and will give us the opportunity to extend the conclusions drawn from ESMs to a wider family of molecular materials.

2.4.1 Aggregates of push-pull dyes: the ESM approach

As described in the previous Chapter, the basic electronic ESM for a push-pull dye relies on the choice of two basis states corresponding to its limiting resonance structures: a neutral state $|N\rangle$ representative of the DA structure, and a zwitterionic $|Z\rangle$ state describing the charge-separated D^+A^- structure [42,83,84]. However, to model phosphorescence emission, we must take into account spin multiplicity. Specifically, the unpaired electrons in the $|Z\rangle$ state can be combined into one singlet $|Z_S\rangle$ and three degenerate triplet states $|Z_{T_i}\rangle$, thus, the minimal basis set required to reproduce both absorption and phosphorescence spectra of this system consists of three electronic states: $|N\rangle$, $|Z_S\rangle$ and $|Z_T\rangle$, where only one out of the three triplet states is accounted for, without loosing generality.

On this basis, the electronic Hamiltonian $\hat{H}_e$ describing the isolated dye is the following 3×3 matrix:

$$\hat{H}_e = \begin{pmatrix} 0 & -\sqrt{2}t & -V_{SO} \\ -\sqrt{2}t & 2\eta & 0 \\ -V_{SO} & 0 & 2\eta \end{pmatrix} \tag{2.7}$$

where we set 2η as the energy gap between the zwitterionic states and the $|N\rangle$ state. The matrix element $-\sqrt{2}t$ mixes the states with the same spin multiplicity ($|N\rangle$ and $|Z_S\rangle$), and describes the probability of electron hopping from the D to the A site. The mixing between states of different multiplicity ($|N\rangle$ and $|Z_T\rangle$) is introduced by the spin-orbit coupling term V_{SO}. Typically, the spin-orbit coupling only represents a small perturbation, i. e. $V_{SO} \ll t$.

Diagonalization of $\hat{H}_e$ returns the eigenstates of the system: the ground-state $|g\rangle$, and two excited states, $|e_1\rangle$ and $|e_2\rangle$. Since V_{SO} is small, $|g\rangle$ and $|e_2\rangle$ originate mainly from the mixing of the singlet states, while $|e_1\rangle$ is almost coincident with $|Z_T\rangle$. In the limit of $V_{SO} = 0$, $|Z_T\rangle$ stays unmixed, and the eigenstates collapse into the following:

$$|g\rangle = \sqrt{1-\rho}\,|N\rangle + \sqrt{\rho}\,|Z_S\rangle \tag{2.8}$$

$$|e_1\rangle = |Z_T\rangle \tag{2.9}$$

$$|e_2\rangle = \sqrt{\rho}\,|N\rangle - \sqrt{1-\rho}\,|Z_S\rangle \tag{2.10}$$

As before, the ionicity ρ in the equations above measures the weight of $|Z_S\rangle$ in the ground state and can be regarded as an indicator of the dye polarity. In more quantitative terms, $\rho = \langle g|\,\hat{\rho}\,|g\rangle$, where $\hat{\rho}$, the ionicity operator, is defined as

$$\hat{\rho} = \begin{pmatrix} 0 & 0 & 0 \\ 0 & 1 & 0 \\ 0 & 0 & 1 \end{pmatrix} \tag{2.11}$$

and is related to model parameters η and t as given by

$$\rho = \frac{1}{2}\left(1 - \frac{\eta}{\sqrt{\eta^2 + 2t^2}}\right) \tag{2.12}$$

Neglecting all off-diagonal elements, the dipole moment operator $\hat{\mu}$ relevant to the system is written as

$$\hat{\mu} = \mu_0 \hat{\rho} \tag{2.13}$$

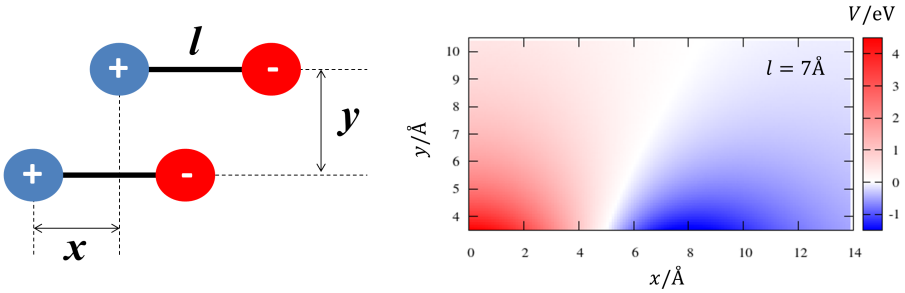

Figure 2.12: Left: the model geometry for a dimer of dipolar chromophores (the electron donor is in blue, the electron acceptor in red). Molecules are fixed at a distance y and horizontally shifted by x. The molecule length is l. Right: dependence of the intermolecular interaction V on geometrical parameters x and y (we set $l = 7$Å). Repulsive interactions are indicated in red, attractive interactions in blue.

where μ_0 is the magnitude of the dipole moment of each of the zwitterionic states.

Starting from this simple three-state model for the non-interacting molecule, we can easily build up a model for aggregates, following a bottom-up approach. Here, we will consider the simple yet instructive case of a dimer of DA molecules, each one described by the Hamiltonian in Eq. 2.7.

The Hamiltonian describing a dimer of push-pull dyes can be written as follows [44, 241]:

$$\hat{H} = \sum_{i=1}^{2} \hat{h}_i + V\hat{\rho}_1\hat{\rho}_2 \tag{2.14}$$

where $\hat{h}_i$ are the Hamiltonians of the non-interacting molecules (Eq. 2.7), $\hat{\rho}_i$ is the ionicity operator of the i-th molecule and V is the electrostatic intermolecular interaction between the two molecules in a purely zwitterionic state.

Different approximation schemes can be adopted for the calculation of V. The dipolar approximation is not suitable for aggregates of push-pull dyes, where the intermolecular distance is usually of the same order of magnitude of the molecular length. In a better approach [44, 46, 241], the dipolar approximation is relaxed and V is calculated as the sum of Coulombic interactions between point charges located on the D (positive charge) and A

(negative charged) sites:

$$V = \frac{e^2}{4\pi\varepsilon_0}\left(+ \frac{1}{d_{++}} + \frac{1}{d_{--}} - \frac{1}{d_{+-}} - \frac{1}{d_{-+}}\right) \tag{2.15}$$

where e is the elementary charge, ε_0 is the vacuum permittivity and $d_{+(-)+(-)}$ is the distance between the positive (negative) charge on the first molecule and the positive (negative) charge on the second one.

The distances entering in Eq. 2.15 are dependent on the geometry of the aggregate. For example, let us considering the ladder structure presented in Figure 2.12. Each molecule is treated as a segment of length l connecting the point-like D and A moieties. The molecules are parallel, with both A groups pointing in the same direction. Two geometrical parameters are required to quantitatively describe this configuration: the distance y between the molecules and the lateral shift x.

For this geometry, the following relations can be written:

$$d_{++} = d_{--} = \sqrt{x^2 + y^2} \tag{2.16}$$

$$d_{+-} = \sqrt{(l - x)^2 + y^2} \tag{2.17}$$

$$d_{-+} = \sqrt{(l + x)^2 + y^2} \tag{2.18}$$

Thus, the electrostatic potential V is univocally determined by the distances x, y and the molecular length l. In Figure 2.12 (right) we mapped the values assumed by V as a function of the intermolecular distances for a model chromophore with $l = 7$Å. The intermolecular distance y mainly affects the magnitude of V, while the lateral shift x also affects its sign. When the molecules are in a face-to-face arrangement (small x) the repulsive interactions are dominant, resulting in positive V, conversely, when the lateral shift is large enough, the dominant interactions become negative and the sign of V is reversed.

The total dipole moment of the dimer is given by the sum of the dipole moments of the individual molecules: $\hat{\mu} = \hat{\mu}_1 + \hat{\mu}_2$, being $\hat{\mu}_i$ the dipole moment operator of the i-th molecule, aligned with the molecular axis.

The ESM introduced above naturally accounts for typical excitonic effects arising from the relative orientation of the transition dipole moments of the interacting chromophores. Moreover, it also introduces the effects of

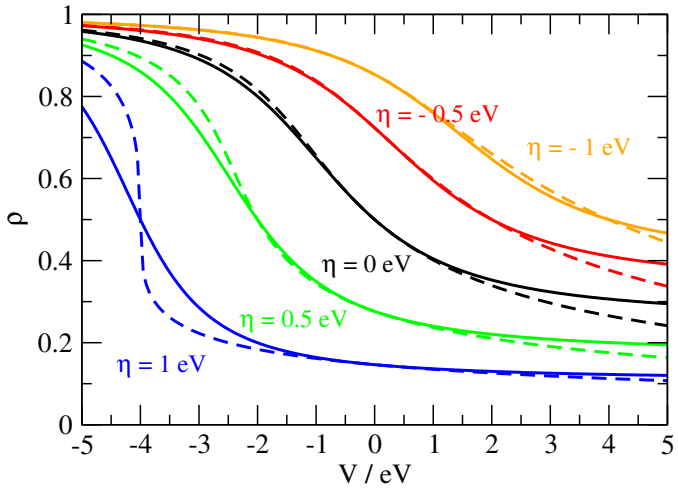

Figure 2.13: Ground-state ionicity ρ of a molecule in the dimer calculated as a function of the intermolecular interaction V for different values of η ($\sqrt{2}t = 1$ eV). Continuous lines were obtained with the full model, dashed lines were obtained with the *mf* approach.

the interaction between the charge distribution of each molecule and the electric field generated by the other molecule [44].

The latter phenomenon alone can be captured by the mean-field (*mf*) approximation [318], a simple approximation scheme collapsing the description of the aggregate into the solution of a single-molecule Hamiltonian with renormalized parameters accounting for the effects of the electrostatic potential generated by the surroundings [44].

To our purposes, the *mf* scheme consists in the diagonalization of the Hamiltonian in Eq. 2.7 in which the energy η is replaced by the effective energy η_{eff} computed as

$$\eta_{eff} = \eta + M\rho \tag{2.19}$$

where M is the Madelung energy, which for a dimer simply reads $M = \frac{1}{2}V$. The ground-state ionicity ρ depends itself on η_{eff}, so that Eq. 2.19 can be solved imposing self-consistency.

In Figure 2.13 we reported the evolution of the ground-state ionicity as a function of the intermolecular interaction V for selected values of η, corresponding to different polarities of the monomer (for simplicity we set $\sqrt{2}t = 1$ eV, as for typical push-pull dyes). Results obtained with the ESM, i. e. from the diagonalization of Eq. 2.14, hereafter referred to as

full model, are compared with those calculated applying the *mf* approximation (Eqs. 2.7 and 2.19). The two approaches give quantitatively consistent results, at least when the interactions are not too large. Attractive interactions ($V < 0$) favour ionic lattices, and molecules being mostly neutral in their ground state ($\eta > 0$) can become ionic ($\rho > 0.5$) when paired together. Conversely, repulsive interactions ($V > 0$) reduce the degree of charge separation, favouring instead a neutral regime. The appearance of discontinuous charge crossovers, as detailed elsewhere [44], confirms the cooperative behaviour of aggregates of polar and polarizable dyes and the dependence of the materials properties on the supramolecular organization (e. g. intermolecular distances).

More interesting to our purposes are the spectroscopic effects summarized below. We selected three different values of η, corresponding to different ionicities, chosen in the range in which the two models (full model and *mf*) are in good agreement, at least for realistic strengths of intermolecular interactions: $\eta = 0.5$ eV, describing a neutral dye ($\rho \approx 0.28$), $\eta = -0.5$ eV, describing an ionic molecule ($\rho \approx 0.72$) and $\eta = 0$, corresponding to $\rho = 0.5$ (in all calculations we set $\sqrt{2}t = 1$ eV). To reduce the number of adjustable parameters, absorption and phosphorescence spectra were computed for different values of V, disregarding its specific dependence on the aggregate geometry and yielding more general results.

The absolute maxima of the absorption spectra calculated as a function of V are reported in the upper panels of Figure 2.14. Large shifts of the absorption band are expected, depending on the sign and magnitude of the intermolecular interaction. For $\eta = 0$ or -0.5 eV ($\rho \geq 0.5$), the absorption band of the dimer is always shifted to higher energy compared to the non-interacting molecule, while for $\eta = 0.5$ eV ($\rho < 0.5$) the absorption band is blue-shifted for repulsive interactions and red-shifted for attractive potential. Of course, the absorption shift vanishes for $V \to 0$.

More instructive is the comparison between the exact results (full model) and the *mf* results. Indeed, the spectral shifts obtained with the full model arise from the interplay between two qualitatively different contributions. The first one is due to the interaction between transition dipole moments of the dyes, which is also at the heart of the excitonic theory. The second one is the mean-field effect, which is completely neglected in the excitonic

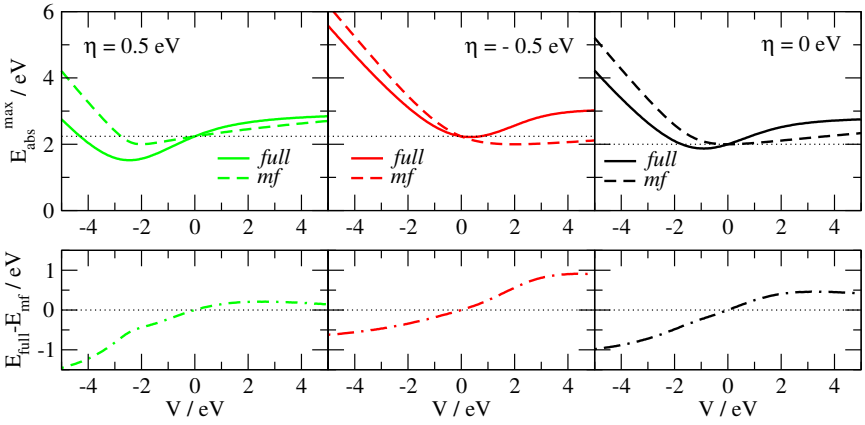

Figure 2.14: Top panels: the absorption maximum of a dimer (E_{abs}^{max}) of push-pull dyes as a function of the intermolecular interaction V calculated for selected values of η ($\sqrt{2}t = 1$ eV) with the full model (continuous lines) and the mean-field approach (*mf*, dashed lines). The black dotted lines mark the energies obtained for $V = 0$ (isolated molecule). Bottom panels: difference between the exact energy (E_{full}) and the *mf* energy (E_{mf}).

picture. Thus, the comparison between the two approaches, as reported in Figure 2.14, allows to separate and quantify the mean-field contribution to the exact results.

The two models provide qualitatively different results, also for small intermolecular interactions. For $\rho = 0.5$, for example, the *mf* approach overestimates and underestimates the transition energy for $V < 0$ and $V > 0$ respectively. For $\rho > 0.5$ the *mf* model shifts the spectrum to the red for repulsive interactions, where a blue-shift is instead expected based on the exact results. Also for $\rho > 0.5$ large deviations are found. As expected, the difference between the exact and *mf* transition energies, reported in the lower panels of Figure 2.14, increases moving away from $V = 0$, and can be as large as 1 eV for $V \approx 4$ eV, which can be reached for short intermolecular contacts (e. g. $x \approx 0$ and $y \leq 4$Å, Figure 2.12).

In Figure 2.15 (upper panels) we reported the energy of the phosphorescent state as a function of the interaction term V. Independently of the sign of η, large shifts of the phosphorescence spectrum are expected for the interacting molecules, whose direction depends on the sign of V. When the interactions are repulsive ($V > 0$) the aggregate emits at higher energy compared to the isolated molecule, conversely, when attractive interactions

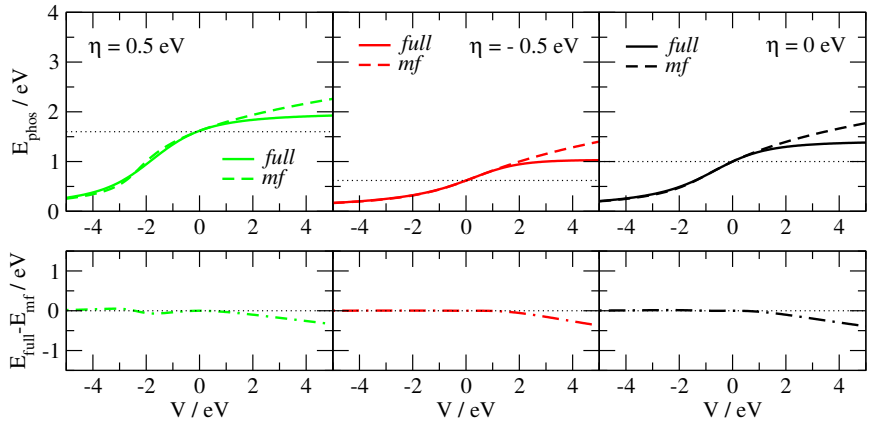

Figure 2.15: Top panels: energy of the phosphorescent state(s) of a dimer (E_{phos}) of push-pull dyes as a function of the intermolecular interaction V calculated for selected values of η ($\sqrt{2}t = 1$ eV) with the full model (continuous lines) and the mean-field approach (*mf*, dashed lines). In all calculations we set $V_{SO} = 1 \times 10^{-4}$ eV. The black dotted lines mark the energies corresponding to $V = 0$ (isolated molecule). Bottom panels: difference between the exact energy (E_{full}) and the *mf* energy (E_{mf}).

dominate ($V < 0$), the phosphorescence of the aggregate is shifted to lower energy. It follows that the control of molecular packing can be exploited not only to tune the absorption spectral window, but also the phosphorescence colour. Moreover, the curves obtained with the mean-field approach are coinciding over a wide range of V values with the exact curves, demonstrating that the phosphorescence shifts have a mean-field origin, while excitonic effects are negligible.

In other words, in clusters of push-pull dyes, as far as absorption is concerned, the mean-field effect cooperates with excitonic interactions, at least for large enough V, and both effects must be carefully considered. Conversely, the mean-field effects alone are responsible for quite impressive phosphorescent shifts which, due to their intrinsic nature, are peculiar of aggregates of largely polar and polarizable chromophores.

In summary, we demonstrated not only that phosphorescence tuning through aggregation is possible for push-pull chromophores, making this family of molecules worth exploring for application in real devices, but also that for this class of materials relying on the excitonic scheme alone can be misleading.

In the following we will present experimental evidence of a metal-containing luminophore which, notwithstanding the complex electronic structure requiring a different theoretical approach, owes the different emission colours of its polymorphs to mean-field effects, corroborating the general conclusions drawn above.

2.4.2 Phosphorescent polymorphs of a dinuclear Rhenium(I) complex

Transition metal complexes, in view of their fairly large spin-orbit coupling favouring fast ISC, are among the most investigated phosphorescent emitters, for example in light emitting diodes [319].

Here we will focus on **2**, a dinuclear Rhenium(I) complex recently reported by Panigati and coworkers [317, 320], in which two Re atoms are bridged by a pyridazine ligand (Figure 2.16). **2** belongs to the family of complexes of general formula $Re_2(\mu\text{-}X)_2(CO)_6(\mu\text{-}1,2\text{-diazine})$ (X = halogen), many of them characterized by intense emission from triplet metal-to-ligand charge transfer (^{3}MLCT) states [321, 322].

Complex **2** is characterized by the combination of few interesting properties, among which the intense emission in the solid state, about one order of magnitude higher with respect to solution, and the concomitant formation of two polymorphs, the so-called yellow polymorph **2Y** and the orange polymorph **2O**, characterized by markedly different absorption and emission properties, and undergoing a clean single-crystal-to-single-crystal transition [317].

The **2Y** polymorph is monoclinic, and is characterized by only half a molecule in the asymmetric unit. It can be described as a collection of closely spaced layers of equally oriented molecules containing the pyridazine planes. The 3D structure originates from the parallel stacking of these layers alternating the direction of the molecular dipoles (Figure 2.16). Conversely, the **2O** polymorph is orthorombic and contains two molecules in the asymmetric unit. The 3D organization of the molecules consists of layers of molecules in a zig-zag arrangement, which are stacked alternating the macroscopic polarity every two layers.

2O is more densely packed than **2Y**, indeed **2O** is the thermodinamically favoured polymorph at low temperatures, while **2Y** corresponds to the ki-

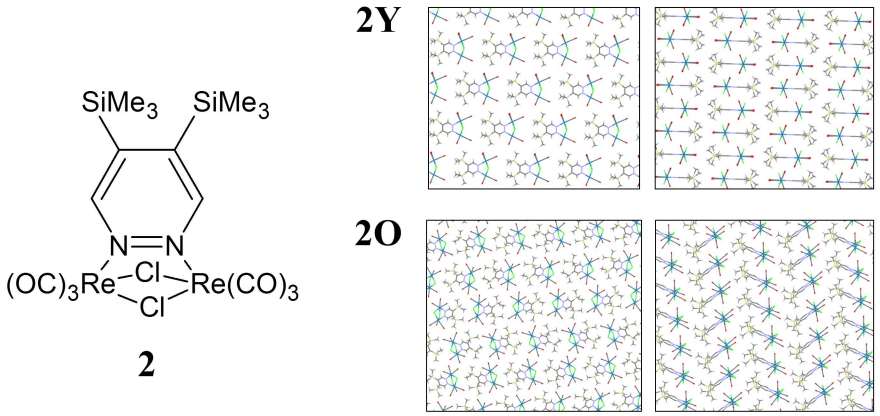

Figure 2.16: Left: molecular structure of the target dinuclear Rhenium(I) complex **2**, $Re_2(\mu\text{-}Cl)_2(CO)_6(\mu\text{-}4,5\text{-}(Me_3Si)_2$pyridazine). Right: views of the layers in polymorphs **2Y** and **2O**.

netically favoured phase. Therefore, acting on the crystallization rate, it was possible to obtain selectively one of them. The **2O**→**2Y** phase transition is an irreversible process occurring at 443 K [317].

Absorption spectra of **2** in solution feature a low-energy CT band ($\lambda \approx$ 400 nm), assigned to a ^{1}MLCT transition [317]. This broad and featureless band is sensitive to solvent polarity, and blue-shifts by $\sim$ 0.3 eV from nonpolar toluene to more polar acetonitrile (Table 2.5), indicating that the ground-state is more polar than the CT excited state. Phosphorescence emission of **2** occurs below 600 nm with monoexponential microsecond decay times, and was assigned to a ^{3}MLCT transition. The emission band undergoes a slight positive solvatochromic shift amounting to $\sim$ 0.1 eV.

The two polymorphs **2Y** and **2O** are characterized by different spectroscopic signatures. The absorption maximum of **2O** is almost coincident with the absorption maximum of toluene solution, while the absorption band of **2Y** is blue-shifted by $\sim$ 0.2 eV. The phosphorescence spectrum of both polymorphs is blue-shifted compared to solution, but while the shift amounts to $\sim$ 0.15 eV for **2O**, it is considerably larger for **2Y** ($\sim$ 0.3 eV). It is worth noticing that the crystalline phases are more efficient emitters compared to the solutions, with quantum yields exceeding 50%. This interesting phe-

Table 2.5: Spectroscopic data of **2** in solution and in the two crystal polymorphs **2Y** and **2O**: absorption and emission maxima (λ_{abs}^{max} and λ_{em}^{max}), emission quantum yield (QY) and emission lifetime (τ). Data in solution are referred to solvents of different polarity: toluene (TOL), dichloromethane (DCM) and acetonitrile (ACN). Data are taken from Ref. [317]

Sample	λ_{abs}^{max} / nm	λ_{em}^{max} / nm	QY / %	τ / μs
2 (TOL)	394	612	6	0.7
2 (DCM)	384	625	4	–
2 (ACN)	361	663	1	–
2Y	370	534	56	5.8
2O	393	570	52	4.1

nomenon was attributed to the restricted roto-vibrational motion of the Me_3Si groups in the solid state [317, 323].

The data above suggest that the crystal packing is responsible for the spectroscopic differences observed between the two polymorphs. Given the polar nature of **2**, we could expect the emission shifts of the crystals to be induced by mean-field effects, as demonstrated in the previous Section for prototypical push-pull systems. However, the complexity of the electronic structure of **2**, mostly related to the presence of two metal centers, as detailed below, cannot be accurately described by few-state models. Nevertheless, resorting to DFT calculations, we were able to unambiguously demonstrate the key role played by mean-field effects in the luminescence properties of **2** in the solid state.

Modelling the solvated dye

(TD)DFT calculations were performed with the Gaussian16 package [159], including the solvent with the standard PCM model [160,267]. Calculations were run with the long-range corrected CAM-B3LYP functional [170], and the selected basis set was 6-31G(d,p) for all elements except Re, for which the Stuttgart-Dresden effective core potentials (ECPs) were included together with the corresponding basis set [324].

Excitation energies computed on the optimized geometry with TDDFT are collected in Table 2.6.

Table 2.6: TDDFT data on the vertical $S_0 \rightarrow X_n$ electronic transitions of **2** in dichloromethane: transition energies and wavelengths, oscillator strengths (f), polarization (p) and main excitations. For the individuation of the polarization, the x direction coincides with the C_2 axis of the molecule. The level of theory was CAM-B3LYP/6-31G(d,p), and Stuttgart-Dresden ECPs were employed for Re atoms. Triplet energies were computed within Tamm-Dancoff approximation. Data in brackets were obtained with state-specific solvation.

X_n	Energy / eV	Wavelength / nm	f	p	Type (> 25%)
S_1	3.624 (3.826)	342.1 (324.1)	0.000	x	H→L (94%)
S_2	3.756 (3.998)	330.1 (310.1)	0.150	yz	H-1→L (93%)
S_3	3.787 (3.972)	327.4 (312.1)	0.006	yz	H-2→L (94%)
S_4	3.972 (4.248)	312.3 (291.9)	0.376	x	H-3→L (83%)
S_5	3.994 (4.206)	310.4 (294.8)	0.003	yz	H-4→L (59%)
T_1	3.429 (3.645)	361.5 (340.1)	–	–	H-1→L (73%)
T_2	3.568 (3.783)	347.5 (327.7)	–	–	H→L (71%)
T_3	3.570 (3.751)	347.3 (330.5)	–	–	H-3→L (60%)

As argued from the inspection of the NTOs in Figure 2.17, the lowest-energy singlet and triplet transitions possess a CT character and correspond to a charge migration from the region of the Re atoms and the inorganic ligands (CO and Cl^-) to the pyridazine ligand. Indeed, all excitations involve the LUMO, which is localized over the pyridazine ring.

Only few transitions are allowed in absorption: the $S_0 \rightarrow S_1$, $S_0 \rightarrow S_3$ and $S_0 \rightarrow S_5$ transitions are dark, while $S_0 \rightarrow S_2$ and $S_0 \rightarrow S_4$ are symmetry allowed. The $S_0 \rightarrow S_2$ transition is weaker and is mainly polarized in the Re−Re direction, while $S_0 \rightarrow S_4$ is characterized by a higher oscillator strength and is polarized along the C_2 axis of the complex. As evidenced in Figure 2.17, the two transitions differ for the phase of the occupied orbitals. Given the small energy difference between these two transitions, they could both contribute to the experimental absorption band at $\lambda \approx 380$ nm.

According to DFT, the permanent dipole moment of **2** in the ground state lies along the C_2 molecular axis and amounts to 17.05 D. Upon vertical excitation to S_2 and S_4 it decreases to 5.622 and 8.911 D respectively, explaining the experimental negative solvatochromic shift.

While two states are responsible for absorption, we can assume that phosphorescence emission stems from the lowest-energy triplet state at its

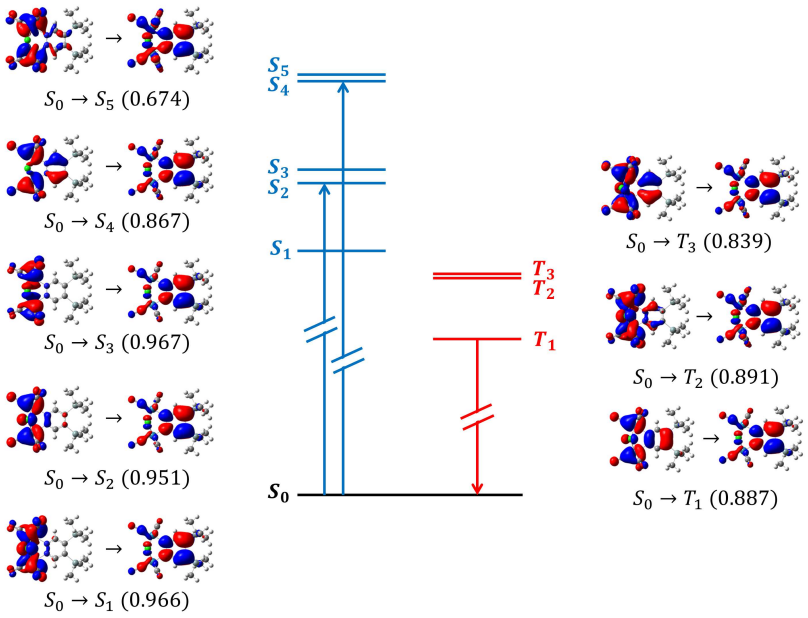

Figure 2.17: Vertical electronic transitions of **2** and corresponding NTOs (isovalue 0.02) computed in dichloromethane. Energies are on scale. Blue arrows indicate the transitions allowed in absorption, the red arrow indicates phosphorescence originating from the lowest-energy triplet state. Numbers in brackets refer to the contribution of the NTO pair to the total excitation.

equilibrium geometry. The NTOs in Figure 2.17 suggest that the $S_0 \rightarrow T_1$ transition possess the same nature as the lowest-energy transition allowed in absorption ($S_0 \rightarrow S_2$), conversely, the brightest state in absorption, S_4, is characterized by the same nature of T_3. In order to identify the one responsible for emission, we relaxed the geometry of both triplet states. We found that the energy of T_1 amounts to 2.846 eV, while the predicted energy of T_3 is 3.171 eV. Thus, even if the energy difference is moderate (< 0.35 eV), T_1 is likely to be the phosphorescent state of **2**. The $S_0 \leftarrow T_1$ transition is predicted at 2.212 eV (560.4 nm) with standard nonequilibrium solvation, and to 1.696 eV (731.0 nm) according to state-specific solvation [166]. The dipole moment of the relaxed T_1 state amounts to 9.27 D, and increases to 15.04 D after de-excitation.

Mean-field effects in clusters of 2

The complex electronic structure evinced from the TDDFT study detailed above, in which at least two different CT states are involved in absorption and phosphorescence, makes **2** unsuitable for the modelling through a simple ESM approach. At the same time, the full DFT treatment of aggregates becomes computationally demanding as the dimension of the aggregate increases, becoming unfeasible for a representative number of molecules.

Nevertheless, moving from the general conclusions made in the previous Section, we could expect mean-field effects being responsible for the different phosphorescence energies of the two polymorphs. To verify this hypothesis, we selected a representative substructure of the crystal lattice containing 21 molecules for **2Y** and 36 molecules for **2O**, as shown in Figure 2.18. These clusters are the smallest structures obtained surrounding the molecules in the unit cell (one molecule for **2Y** and two molecules for **2O**) by the nearest-neighbour molecules. To mimic mean-field effects, only the molecule in the asymmetric unit (depicted in blue or red in Figure 2.18) were treated explicitly with TDDFT, while the neighbouring ones were replaced by point charges located at the atom positions reflecting their charge distribution. In this way, all the spectroscopic effects observed on the target molecule can be attributed to the interaction with the electrostatic field generated by the surroundings, allowing to quantify mean-field effects. For this purpose, a self-consistent approach was adopted to estimate the equilibrium charge dis-

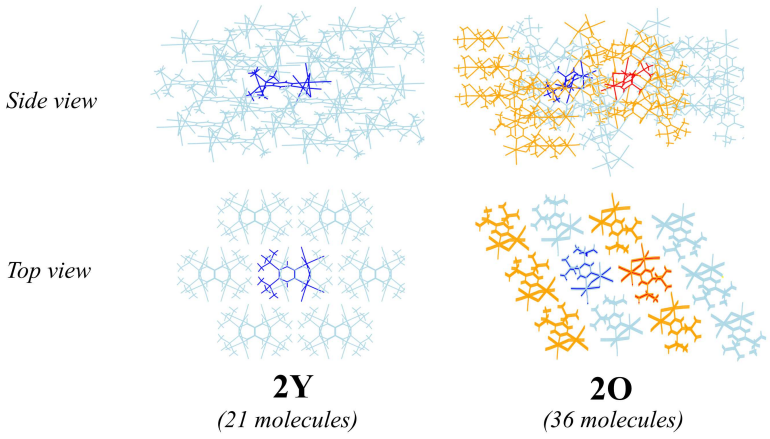

Figure 2.18: Views of the representative clusters of the **Y** and **O** polymorphs. The molecules in dark blue/red are those explicitly considered in the TDDFT calculations of the spectroscopic properties. The other molecules were accounted for as distributions of atomic point charges located at the atom positions. For **2O**, different colours reflect a different symmetry: light blue (orange) molecules have the same symmetry of the molecule in blue (red).

tribution in the crystal. Starting from the gas phase values, atomic charges were updated in an iterative series of computational steps, until convergence was achieved.

Comparison between ESP charges of the isolated molecule in gas phase and those of the molecule in the cluster (Table 2.7) gives a hint of the effect of the electrostatic interactions on the charge distribution. Indeed, charge separation between the $Re_2(CO)_6Cl_2$ fragment and the pyridazine ligand increases by $\sim$ 25% from gas phase to both polymorphs. Moreover, the two nonequivalent molecules of **2O** are characterized by different charge distributions, as a consequence of their different environment.

Spectroscopic properties of the isolated molecule in gas phase and in the clusters were addressed at the same level of theory adopted for the description of the solvated molecule and were computed on the non-optimized crystallographic geometry. Main TDDFT results are collected in Table 2.8, together with corresponding experimental data.

Absorption transitions of the clusters match those obtained in dichloromethane solution. The most intense transition ($f \gtrsim 0.2$) is the one towards

Table 2.7: Cumulative ESP charges on selected regions of **2** in gas phase and in a cluster of 21 (**2Y**) or 36 (**2O**) molecules, calculated on the crystallographic geometry. ESP charges of the clusters were obtained from an iterative process in which, starting from the gas-phase values, the charge distribution calculated in each step was adopted for the calculation of the charges in the subsequent step. Up to 5-6 steps were performed to reach convergence. For the **O** polymorph the two numbers refer to the two nonequivalent molecules in the unit cell.

	2Y		**2O**	
	gas phase	crystal	gas phase	crystal
$Re(CO)_3Cl$	-0.2549	-0.3193	-0.2831/-0.2457	-0.3752/-0.2723
$Re(CO)_3Cl$	-0.2565	-0.3258	-0.2615/-0.2781	-0.2307/-0.2940
$(Me_3Si)_2$pyridazine	0.5113	0.6452	0.5446/0.5240	0.6059/0.5663

Table 2.8: Comparison of experimental and calculated transition energies (in eV) of noninteracting **2** molecule (in gas phase or toluene solution) and in a **Y**/**O** cluster. [a]Data taken from Ref. [317] [b]values reported in the experimental column is reported the maximum of the absorption spectrum, in the calculated column the energy of the transition with higher oscillator strength. [c]vertical transition from the ground state. [d]calculated on the relaxed T_1 geometry.

		Experimental[a]		Calculated	
	Transition	toluene	crystal	gas phase	crystal
Y	$S_0 \rightarrow S_n$ (S_n)[b]	3.15	3.35	3.57 (S_5)	4.15 (S_4)
	$S_0 \rightarrow T_1$[c]	–	–	2.80	3.43
	$T_1 \rightarrow S_0$[d]	2.02	2.32	1.97	2.20
O	$S_0 \rightarrow S_n$ (S_n)[b]	3.15	3.15	3.59/3.51 (S_5)	3.80/3.67 (S_5)
	$S_0 \rightarrow T_1$[c]	–	–	2.82/2.71	3.04/2.88
	$T_1 \rightarrow S_0$[d]	2.02	2.17	1.97	1.97/2.03

the S_4 or S_5 state and corresponds to a CT from the metal atoms to the organic ligand. Absorption of **2Y** is blue-shifted by $\sim$ 0.58 eV compared to the molecule in gas phase, to be compared with an experimental shift of 0.2 eV in the same direction from solution (in nonpolar solvents) to the crystal. In gas phase, the two monomers of the **2O** polymorph absorb at slightly different energies ($\Delta E \approx 0.08$ eV) due to their different crystallographic geometry, which is the result of the different environment felt in the crystal. The interaction with the charge distribution of the neighbouring molecules in the crystal amplifies this difference, which becomes 0.13 eV. Also in this case, mean-field interactions are responsible for a blue-shift of the main absorption transition, amounting to less than 0.2 eV with reference to gas phase results.

Excitation energies relevant to the vertical $S_0 \rightarrow T_1$ process follow the same trend, with the interactions in the crystal displacing the transitions to higher energy, specifically by $\sim$ 0.6 eV for **2Y** and $\sim$ 0.2 eV for **2O**.

To get a better estimate of phosphorescence energies, we optimized the geometry of **2** in the T_1 state, both in gas phase and in the clusters. The phosphorescence energy, i. e. the energy of the $S_0 \leftarrow T_1$ process at T_1 equilibrium geometry, amounts to 1.97 eV for the monomer in gas phase, and can be affected by the electrostatic field of the cluster, depending on the packing. Indeed, the phosphorescence of **2Y** is predicted at 2.20 eV, i. e. blue-shifted by $\sim$ 0.2 eV compared to gas phase. Conversely, in **2O**, only the molecules occupying one of the nonequivalent positions of the unit cell feel an effect on phosphorescence, consisting in a small blue-shift ($\Delta E \approx 0.06$ eV).

Comparison with experiment is tricky, and requires some premises. Firstly, experimental data of the noninteracting molecule are collected in solution, where solvent effects cannot be suppressed even in nonpolar solvents and contribute to the measured absorption. Secondly, experimental absorption spectra of **2**, both in solution and in the crystal, are broad and their information cannot be collapsed into a single wavelength. As emerged from the TDDFT study in solution, at least another CT transition polarized along the direction connecting the two metal centers supplies intensity to the absorption band in the low-energy side, but its contribution cannot be recognized and quantified in the experimental spectrum. Furthermore, for the **O** polymorph, the two nonequivalent molecules in the unit cell con-

tribute with different energies, and the broad experimental bands also take this into account.

Another issue is related to the approximations introduced by the theoretical method itself, among which the choice of the functional (CAM-B3LYP) which, as argued from the data on the solvated dye, shows an intrinsic tendency to overestimate transition energies. Moreover, the experimental absorption energies could also contain the contribution of excitonic effects, which are not accounted for in the modelling.

Notwithstanding these limitations, meaningful considerations can be driven based on the relative predicted emission energies. Indeed, emission of **2Y** is found at higher energy with respect to **2O**, and the energy difference between the transition energies of the two polymorphs amounts to 0.17-0.23 eV, in very good agreement with the experimental value (0.15 eV). Moreover, both polymorphs emit at higher energy with respect to the noninteracting molecule and, even if the phosphorescence shift of **2O** seems to be underestimated compared to experiment, the same trend is predicted by TDDFT, corroborating our hypothesis.

In summary, replacing the nearest neighbouring molecules of the crystal with the electrostatic field generated by their charge distribution, we quantitatively accounted for the difference in the emission energies of the two polymorphs, confirming that their origin is due to mean-field effects, which become relevant in view of the polar/polarizable nature of the dye, and whose magnitude is related to the specific molecular packing of each polymorph. Further work will examine the effect of the size and shape of the selected model cluster on the computed properties, in order to generalize these findings.

2.5 Spectroscopy and aggregation of benzothiadiazole-based multipolar chromophores

The appropriate introduction of substituents at the periphery of the conjugated backbone may assist the formation of ordered assemblies. Alkyl substituents are characterized by high absorption energies, which makes them irrelevant to the spectroscopic properties of the isolated chromophores, conversely, they can be actively involved in supporting the formation of ag-

gregates, governing molecular orientation, interchromophoric distances and strength of the intermolecular interactions [237, 325, 326]. Thus, side-chain engineering can be exploited not only for the enhancement of the dye solubility, which should improve the processability of the materials, but also to achieve a control over the aggregation process of the chromophores, leading to nanostructured self-assembled architectures possessing the desired properties [327, 328].

Even more interestingly, the competition between the interactions between side chains (typically Van der Waals interactions) and those occurring between the π-conjugated skeleton of the chromophores (typically $\pi-\pi$ stacking) sometimes leads to multistable aggregates, opening the possibility of achieving a switching effect [66]. Indeed, the occurrence of metastable states that, when subject to an external input, can be interconverted or driven towards the thermodynamically stable state, is one of the prerequisites for stimuli-responsive materials [329–336].

The understanding of the relationship between the molecular structure and the aggregation pattern, as well as the effect promoted by external stimuli, is fundamental for the exploitation of supramolecular organization as a tool to design molecular materials with tailored properties [222, 247, 337–339].

In this Work we focused on the family of multipolar chromophores presented in Figure 2.19, synthesized and provided by Dr. Kathleen I. Moineau-Chane Ching and coworkers (Laboratory of Coordination Chemistry, CNRS-UPR8241, Toulouse, France). They are all based on the same molecular backbone, characterized by a dithienylsilyl core, a well-known electron-donating group, symmetrically disubstituted with two 2,1,3-benzothiadiazole (BDT) units, two strong electron acceptors [340]. Each branch of the molecule is elongated *via* a thiophene group end-capped with an alkyl cyanoacetate moiety. Thus, each molecule can be described as a $A'D'ADAD'A'$ system, where we considered the thiophene and the cyanoacetate as additional electron donors and electron acceptors respectively (D' and A'). Conjugation is extended over the entire network, and should grant for the planarity of the backbone [341].

The π-conjugated skeleton of the chromophores is decorated with C_8 alkyl chains grafted to the dithienylsilyl core and to the terminal cyanoac-

etate moieties. Two types of alkyl chain were considered for each of the grafting sites, a linear (octyl, O) chain and a branched (2-ethylhexyl, EH) chain, yielding four different alkyl-substituted dyes: **SilOCAO**, **SilOCAEH**, **SilEHCAO** and **SilEHCAEH**.

Recent studies on parent BDT-based chromophores end capped with alkyl groups demonstrated that the nature of the alkyl chains is irrelevant as far as the optical properties of the solvated dyes are concerned, but affects the supramolecular assembly in the solid state and in nanoparticle suspensions, promoting the partial ordering into J-aggregates and sometimes the occurrence of liquid crystalline behaviour [130, 342]. Moreover, thanks to the competition between intermolecular contacts driven by the side chains and those promoted by the molecular backbone, different aggregated phases could be obtained, whose relative abundancy could be modified by mild mechanical or thermal treatments, such as grinding and annealing, with an impressive effect on the optical properties [131].

Here, the introduction of the central D group extends the conjugation of the system, shifting the emission to the near-IR, but also allows for the introduction of alkyl substituents at the core of the π-conjugated skeleton, which may affect the supramolecular organization of the molecules.

In the following we report on the detailed spectroscopic investigation of the target chromophores and their aggregation behaviour, with the aim of finding useful structure-property relationships.

2.5.1 Solution and solid state spectroscopy

Steady-state absorption and emission spectra of the target dyes were collected in different solvents, spanning a wide polarity range (Figure 2.20). Main spectroscopic properties are summarized in Table 2.9. Measurements were performed on diluted solutions ($c \approx 10^{-6}$ mol L^{-1}) to avoid inner filter effects, self-absorption and aggregation.

All chromophores display similar spectral features, indicating that the nature of the alkyl chains is irrelevant in solution, where the spectroscopic behaviour is dominated by the π-conjugated backbone. Absorption spectra are characterized by two bands covering most of the UV/vis spectral window: an intense featureless band ($\varepsilon > 7 \times 10^4$ mol^{-1} L cm^{-1}) is centered at $\lambda \approx 600$ nm, while another less intense peak is found in the UV,

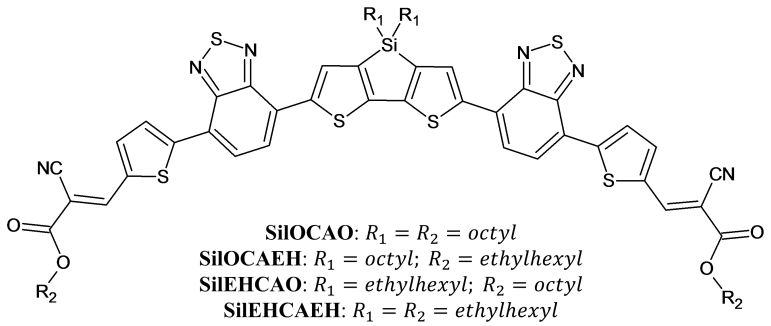

Figure 2.19: Molecular structure of the target BDT-based chromophores.

at $\lambda \approx 400$ nm. The two bands are broad and are basically unaffected by solvent polarity.

Fluorescence occurs in the red-NIR region, and the emission maxima shift from $\lambda \approx 660 - 670$ nm in nonpolar cyclohexane to $\lambda > 800$ nm in polar solvents like dimethyl formamide and dimethyl sulfoxide. The solvatochromic shift amounts to more than 2500 cm^{-1}, indicating a polar emissive state. The vibronic structure of the emission band is partially resolved in nonpolar environments (cyclohexane and toluene) and is progressively blurred upon increasing the solvent polarity. Fluorescence quantum yields amount to $20 - 30\%$ in nonpolar solvents and drop to $\sim 7 - 10\%$ in polar solvents, following a similar trend for all the compounds.

Fluorescence anisotropy of two selected dyes, **SilOCAO** and **SilEHCAEH**, was collected in vitrified 2-methyltetrahydrofuran solutions, and is shown in Figure 2.21. Anisotropy amounts to $\sim 0.2 - 0.3$ in the red-edge of the main absorption band and smoothly decreases to $r \approx 0$ in the region between 450 and 500 nm, corresponding to the minimum between the two absorption bands. Anisotropy increases again in the UV, reaching $r \approx 0.1 - 0.15$ at the maximum of the secondary band.

The smoothness and the limited range of anisotropy, which never assumes negative values, is qualitatively different with respect to parent BDT-based dyes characterized by a quadrupolar-like behaviour [130]. Indeed, the complex structure of the π-conjugated backbone of the dyes, alternating

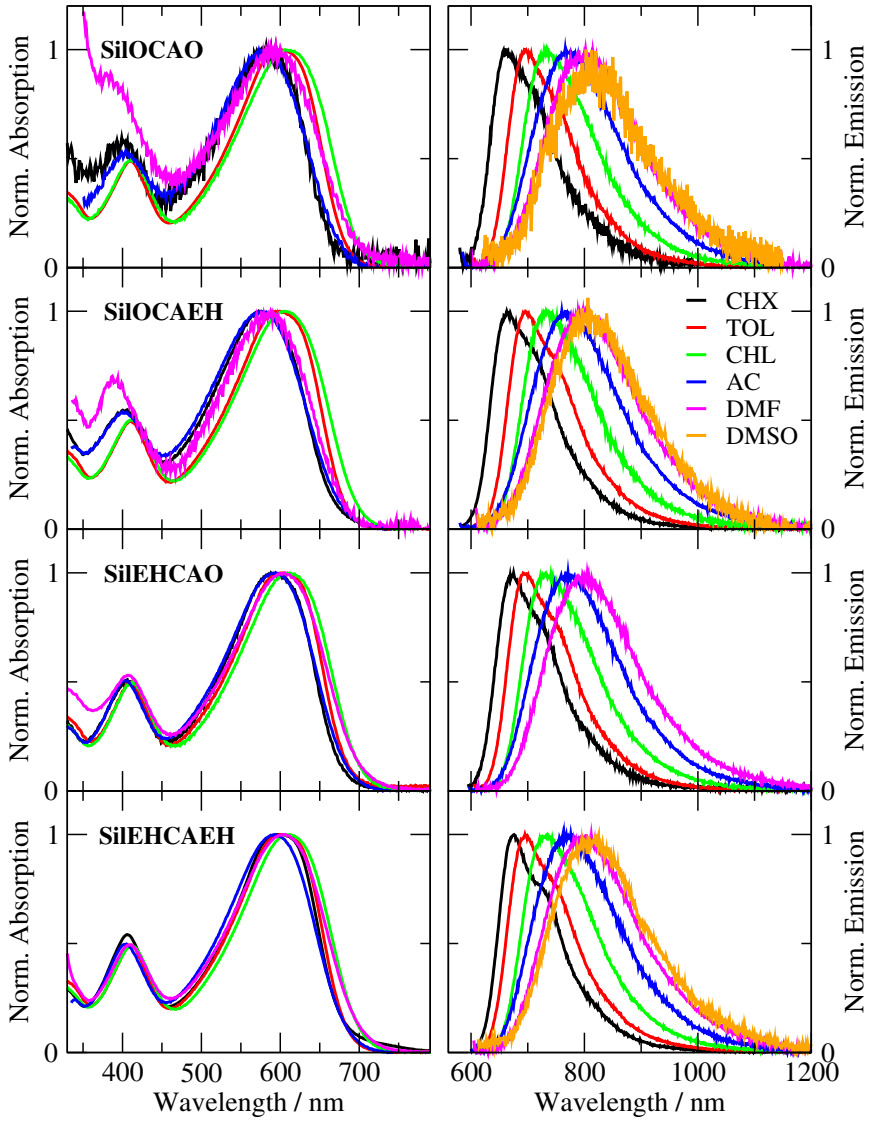

Figure 2.20: Normalized absorption (left panels) and emission (right panels) of **SilOCAO**, **SilOCAEH**, **SilEHCAO** and **SilEHCAEH** in solvents of different polarity (CHX: cyclohexane, TOL: toluene, CHL: chloroform, AC: acetone, DMF: dimethyl formamide, DMSO: dimethyl sulfoxide). Absorption spectra in DMSO could not be obtained because of the low solubility of the dye.

Table 2.9: Spectroscopic properties of the investigated BDT-based chromophores in solvents of different polarity (CHX: cyclohexane, TOL: toluene, CHL: chloroform, AC: acetone, DMF: dimethyl formamide, DMSO: dimethyl sulfoxide). λ_{abs}^{max}: absorption maximum, λ_{em}^{max}: emission maximum, QY: fluorescence quantum yield. The standard for fluorescence quantum yield measurements was cresyl violet in ethanol (QY = 51% for λ_{exc} = 550 nm). Quantum yields were estimated for excitation in proximity of the absorption maximum. [a]not determined (sample poorly soluble).

Compound	Solvent	λ_{abs}^{max}/nm	λ_{em}^{max}/nm	Stokes shift/cm^{-1}	QY %
SilOCAO	CHX	581	661	2083	27
	TOL	600	694	2257	30
	CHL	606	729	2784	25
	AC	582	766	4127	16
	DMF	594	802	4366	9
	DMSO	578	>800	>4800	-[a]
SilOCAEH	CHX	573	663	2369	22
	TOL	599	696	2327	24
	CHL	606	732	2840	21
	AC	576	760	4203	13
	DMF	588	802	4538	7
	DMSO	590	808	4573	-[a]
SilEHCAO	CHX	588	675	2192	23
	TOL	606	692	2051	25
	CHL	612	732	2679	20
	AC	594	771	3865	12
	DMF	605	805	4106	8
	DMSO	-[a]	-[a]	-[a]	-[a]
SilEHCAEH	CHX	597	676	1957	23
	TOL	600	695	2278	28
	CHL	612	734	2716	21
	AC	594	776	3948	12
	DMF	606	803	4048	7
	DMSO	609	808	4044	-[a]

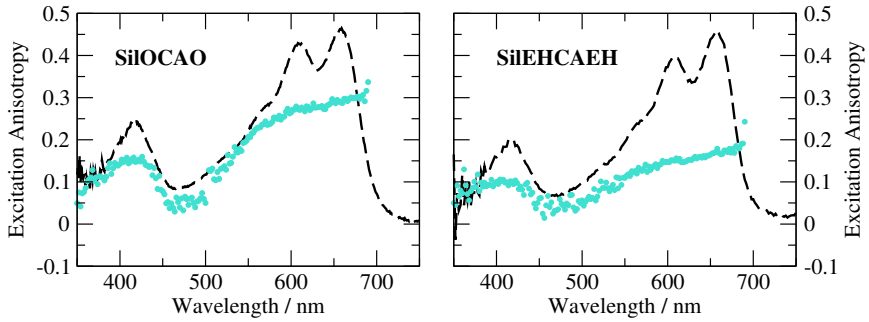

Figure 2.21: Excitation anisotropy (dots) of **SilOCAO** and **SilEHCAEH** collected in 2-methyltetrahydrofuran undercooled at 77K. Excitation spectra collected under the same experimental conditions (dashed lines) are reported as a guide to the eye.

multiple D and A groups gives rise to many CT transitions which are responsible for the large and featureless absorption bands even in low polarity solvents. Given the additivity of anisotropy [151], the experimental value of r may be the result of the superposition of absorption bands relevant to transitions with different intensity and polarization.

Emission spectra in the solid state were collected both on pristine powders, i. e. without pre-treatment of the sample, and after gentle grinding in a mortar (Figure 2.22). Conversely, absorption spectra could be collected on ground powders only, due to the sizeable scattering of the pristine samples.

Emission spectra of pristine powders are independent of the excitation wavelength and feature a broad band in the near-IR spanning the 800-1400 nm range. The emission maximum of the dyes depends on the nature of the alkyl chains grafted to the molecular core: fluorescence of octyl-substituted dyes (**SilOCAO** and **SilOCAEH**) peaks at $\lambda \approx 1000$ nm, while fluorescence of ethylhexyl substituted dyes (**SilEHCAO** and **SilEHCAEH**) is shifted to higher energy ($\lambda \approx 940$ nm).

To characterize ground powders, a small amount of sample was manually ground and stuck to a quartz plate forming a thin transparent film. Absorption measurements were performed in transmission, with the incident beam perpendicularly directed through the plate. As in solution, absorption spectra of ground powders (Figure 2.22 (a)) feature two bands: one band is found in the UV ($\lambda \approx 430$ nm) while a broader and more intense band covers the whole visible range, with an offset at $\lambda \approx 900$ nm. The former

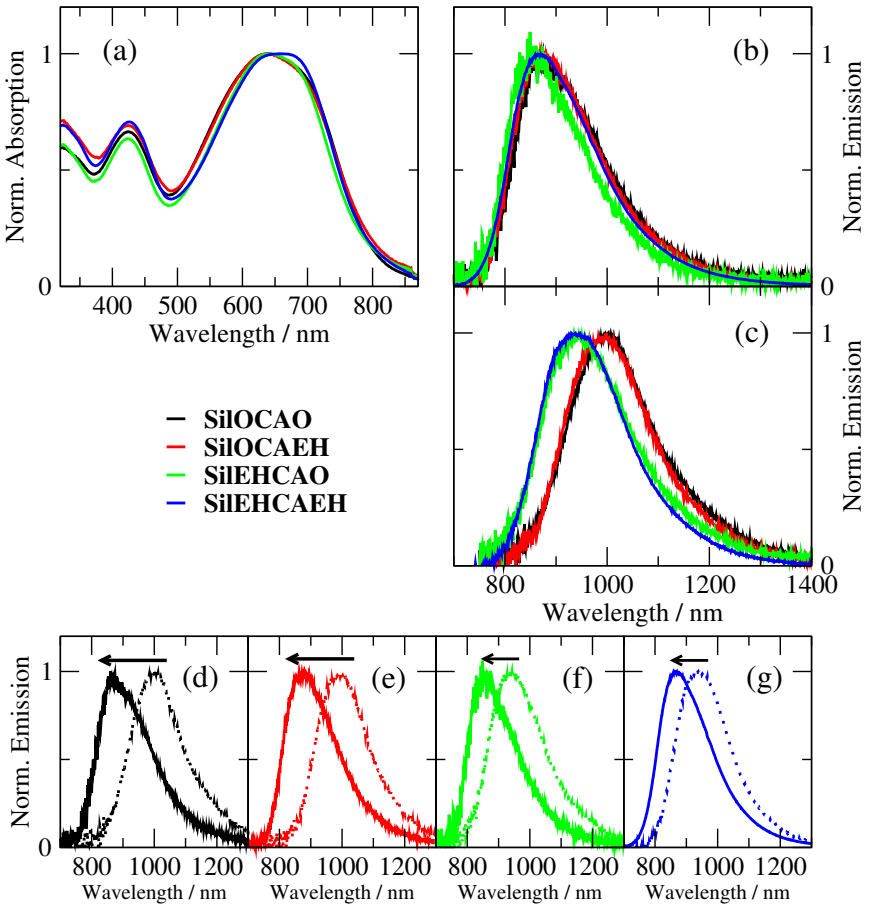

Figure 2.22: Spectroscopic properties in the solid state. (a) Absorption and (b) emission of ground powders. (c) Emission spectra of pristine powders. (d-g) Mechanochromism of the powders: gentle grinding induces a displacement of the emission spectrum in the direction indicated by the arrow (dotted lines: pristine powders, continuous lines: ground powders).

band is slightly red-shifted (by $\sim$ 10 nm) compared to solution, while the latter is characterized by a broad shoulder extending over the red side of the spectrum, in the 700-800 nm region. In this case, the spectra of the four target compounds are indistinguishable.

Emission of ground samples (Figure 2.22 (b)) is independent of the excitation wavelength and occurs in the 800-1400 nm range. The spectra of the four compounds are very similar in terms of position and shape, and emission maxima are confined in a narrow spectral range (850-875 nm).

Comparison between emission spectra of pristine and ground powders reveals the mechanofluorochromic behaviour of the target dyes (Figure 2.22 (d-g)). Indeed, grinding induces a blue-shift of the emission spectrum, amounting to $\sim$ 130 nm for **SilOCAO** and **SilOCAEH**, $\sim$ 90 nm for **SilEHCAO** and $\sim$ 60 nm for **SilEHCAEH**.

2.5.2 Aggregation study in solvent/antisolvent mixtures

To pursue an in-depth study of the aggregation behaviour of the target dyes, while maintaining a sample concentration suitable for spectroscopic analysis, we forced the aggregation of the chromophores through the addition of an antisolvent to a solution of the dye. We chose tetrahydrofuran (THF) as the organic solvent and water as the antisolvent, as the two liquids are miscible in all proportions under ambient conditions, and we characterized the chromophores in mixtures with different THF/water ratios.

The samples were prepared as follows. A 2.5×10^{-4} mol L^{-1} stock solution of the dye in THF was prepared and stored in the dark. Then, 40.0 μL of stock solution were added to 5.0 mL of a THF/water mixture with given composition, achieving a nominal 2.0×10^{-6} mol L^{-1} concentration of the dye in the final mixture (maximum absorbance $\approx$ 0.1). Mixtures with different water content (% volume) were investigated, from 0 (THF only) to 100% (40.0 μL of THF stock solution in 5.0 mL of water under vigorous stirring). The stability of the samples was monitored *via* absorption spectroscopy, and the characterization was completed within one day. The suspensions remained clear and stable under working conditions for few days.

Absorption and emission spectra are markedly affected by the composition of the mixture (Figure 2.23). When water is added to THF, both absorption maxima (the absolute maximum at $\lambda \approx$ 600 nm and the sec-

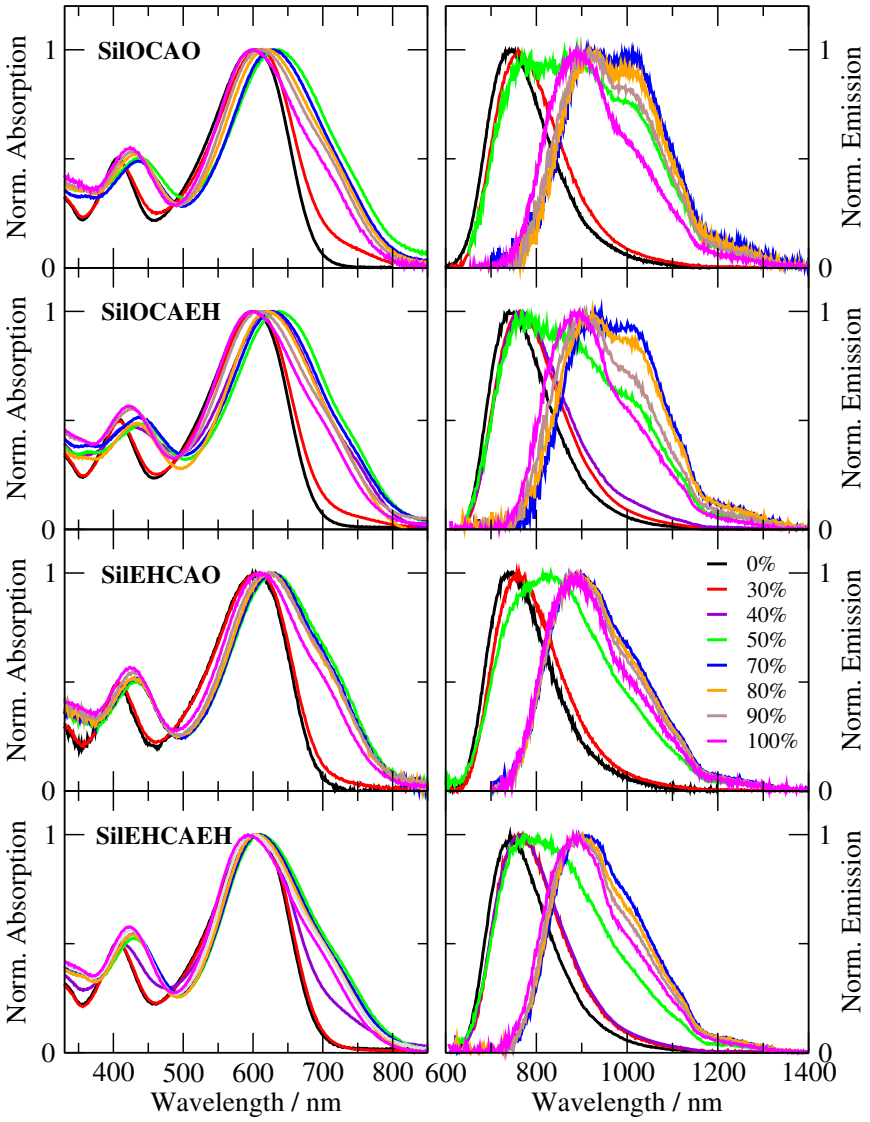

Figure 2.23: Normalized absorption (left panels) and emission (right panels) spectra of the target compounds in THF/water mixtures with different water content (the legend reports % water). Emission spectra were collected for excitation at the absorption maximum. The concentration of the samples was 2.0μM.

ondary one at $\lambda \approx 400$ nm) shift to the red, and a shoulder appears in the region between 700 and 800 nm. As the water fraction exceeds 50%, the absorption maxima are shifted back towards their initial values, while the red-sided shoulder undergoes a slight variation of intensity.

In emission, the behaviour of the dyes is more intriguing (Figure 2.23, right panels). In 30-40% water mixtures we still recognize the emission band of THF solution, even if slightly shifted to the red, probably as a consequence of the increase of solvent polarity. Indeed, the dielectric constant of pure THF amounts to 7.39 and increases up to 31.97 in a 40% water mixture [343]. When the water content reaches 50%, the emission spectrum becomes broader (600-1400 nm) and characterized by three maxima: one at $\lambda \approx 770$ nm, still corresponding to emission in THF solution, and other two at $\lambda \approx 900$ nm and $\lambda \approx 1000$ nm. When the water fraction is increased further the 770 nm emission band vanishes, and the ratio between the remaining bands changes, with the 1000 nm component decreasing as the amount of water increases. We can tentatively assign the three emission bands to different emitting species, that we call for convenience phase I (emitting at 770 nm), II (emitting at 900 nm) and III (emitting at 1000 nm), respectively.

The behaviour described above applies to all the investigated dyes. Indeed, the only difference concerns the relative intensities of the emission maxima in the 50-90% mixtures which depends on the alkyl substituents at the core position. Dyes differing for the nature of the terminal chains only yield superimposable spectra, following the same trend of pristine powders.

Fluorescence quantum yields are strongly dependent on the mixture composition (Figure 2.24). The dyes are good emitters in THF (QY$\approx$ 20%), as in the majority of low/medium polarity solvents (Table 2.9), but undergo sizeable fluorescence quenching upon the addition of water. Indeed, their quantum yield is halved in 30% mixtures and drops to $\sim 0.5 - 1\%$ in 50% mixtures. At higher water fractions the quantum yields are well below 1% and become independent of the mixture composition, in the limit of experimental uncertainty.

Dynamic light scattering (DLS) measurements were performed on samples rich in water (70 to 100%) only (Table 2.10). Indeed, when the organic component is dominant the samples are not scattering and therefore not

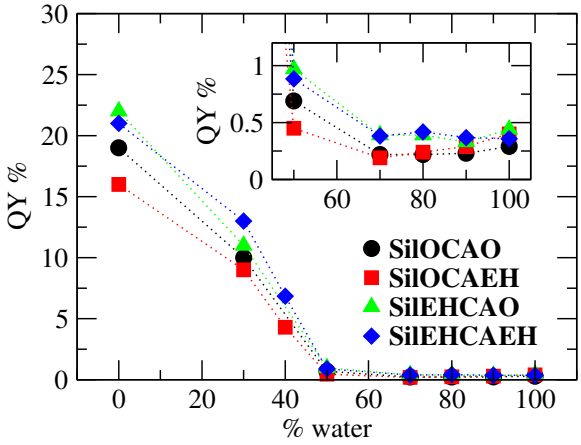

Figure 2.24: Fluorescence quantum yields (QY) of the samples as a function of the mixture composition. QYs were estimated for excitation near the absorption maximum, and a dilute solution of HITCI in ethanol was used as reference (QY = 28.3%, λ_{exc} = 680 nm). The inset is a magnification of the region with low QY.

suitable for DLS analysis. This indicates that when the water fraction is lower than 50% the principal species is the solvated monomer, while aggregates, if present, are less abundant. Conversely, an excess of water promotes the formation of nanosuspensions.

All the investigated samples are highly polydisperse (the polydispersity index obtained from cumulant analysis is higher than 0.25) revealing the formation of heterogeneous particles. The experimental autocorrelation function was fitted with a multi-exponential distribution, yielding a dominant population with a diameter ranging between 40 and 130 nm, as reported in Table 2.10, and sometimes a minor population of smaller particles (< 10 nm). The mean diameter of the dominant population is sensitive to the mixture composition and decreases as the water content is increased from 70% to 90%, before increasing again in 100% water mixtures, in a similar trend for all the chromophores. Under the same conditions, the two dyes bearing branched chains on the dithienylsilyl core (**SilEHCAO** and **SilEHCAEH**) undergo self-assembly into bigger aggregates of similar size, indicating the key role played by the central site on the morphology of the system.

More information on the aggregated species was gathered from the comparison between excitation and emission spectra collected at different emis-

Table 2.10: Mean diameter of the particles formed in the THF/water mixtures obtained from DLS measurements on freshly prepared samples. Only the main component of the (multimodal) distribution is shown, and the corresponding amplitude is reported in brackets.

Compound	%water	Mean diameter/nm (%)
SilOCAO	70	90 ± 1 (87%)
	80	61 ± 3 (88%)
	90	44 ± 2 (95%)
	100	64.0 ± 0.6 (96%)
SilOCAEH	70	84 ± 1 (90%)
	80	58 ± 1 (91%)
	90	48.1 ± 0.9 (100%)
	100	59.4 ± 0.6 (97%)
SilEHCAO	70	119 ± 5 (93%)
	80	76 ± 3 (95%)
	90	58 ± 3 (98%)
	100	87 ± 5 (97%)
SilEHCAEH	70	125.7 ± 0.5 (96%)
	80	76 ± 4 (96%)
	90	61 ± 4 (98%)
	100	76 ± 2 (100%)

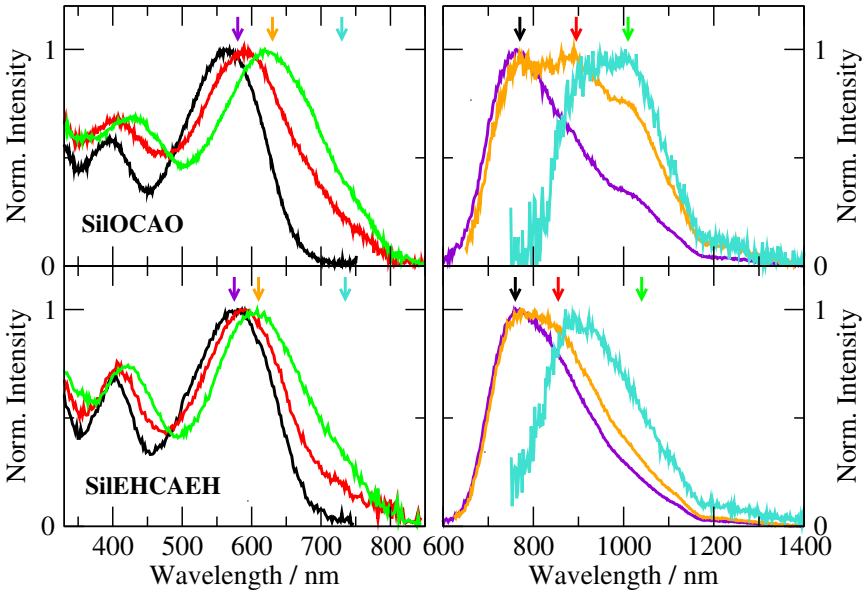

Figure 2.25: Excitation (left panels) and emission (right panels) spectra of **SilOCAO** and **SilEHCAEH** in 50:50 THF:water mixtures collected for different emission/excitation wavelengths, indicated by the coloured arrows.

sion/excitation wavelengths. For clarity we will focus on the spectra of two representative dyes differently core-substituted, **SilOCAO** and **SilEHCAEH** in 50% water mixtures, where all three emission features are present (Figure 2.25).

When emission is detected at the lowest-energy maximum ($\lambda \approx 770$ nm) the excitation spectrum almost coincides with the excitation spectrum of THF solution, and suggests the presence of free (solvated) monomer (phase I). Upon detection on the intermediate maximum ($\lambda \approx 900$ nm), the excitation spectrum contains the absorption of THF solution plus a shoulder on the red edge, characterizing the aggregated phase(s). Indeed, in this region, even if we are detecting in proximity of the fluorescence maximum of phase II, there is a significant contribution from the neighbouring emission of phase I and III. Finally, when emission is collected on the lowest-energy maximum ($\lambda \approx 1000$ nm) or at lower energies, the excitation spectrum coincides with the absorption spectrum of the sample. For mixtures with water content higher than 50% (not shown) excitation spectra are basically independent of the emission wavelength and coincide with the corresponding absorption

spectra. This could be due to efficient energy transfer from phase II to phase III, which requires the cohexistence of both phases inside the same particle and the spectral overlap between the emission spectrum of II and the absorption spectrum of III or, more trivially, it can be a consequence of the similar quantum yield and the proximity of the emission spectra of the fluorophores which prevents the selective collection of the emission from one of them.

The contributions of the emissive species to the absorption/excitation spectrum are more difficult to resolve because of the very large and overlapping bands. For excitation on the maximum of the solution-like excitation band ($\lambda < 600$ nm) the emission spectrum features the dominant emission of phase I with a tail at longer wavelengths, due to the partial excitation of phase II and/or III. For excitation in the 600-650 nm range, in proximity of the absolute absorption maximum of the mixture, all the emission bands are recovered. Finally, for excitation below 700 nm, only the emission contributions at $\lambda \approx 900$ and $\lambda \approx 1000$ nm are retrieved with similar intensity, while the contribution at $\lambda \approx 770$ nm vanishes. This wavelength-dependence of emission suggests that the absorption of phases II and III occur at lower energy with respect to the absorption of phase I.

In order to separate the contributions of the emitting species and investigate their evolution with the mixture composition we performed a fit of fluorescence spectra of two dyes (**SilOCAO** and **SilEHCAEH**) collected for excitation at the maximum of absorption (Figure 2.26 and 2.27) [131].

Each spectrum was fitted on the wavenumber scale adopting the least squares method with a sum of Gaussian functions of the form

$$I(\tilde{\nu}) = \sum_{i=1}^{n} G_i(\tilde{\nu}) \tag{2.20}$$

with

$$G_i(\tilde{\nu}) = a_i \exp \frac{(\tilde{\nu} - b_i)^2}{2c_i^2} \tag{2.21}$$

All parameters (a_i, b_i and c_i) were allowed to readjust freely in order to minimize the error. We fixed $n = 1 - 3$ depending on the mixture, obtaining good quality results. Inspection of the fits suggests that the emission spectrum at any composition can be decomposed in the sum of three types of Gaussian functions: G0, peaking at ~ 12700 cm^{-1} (~ 790 nm), which is

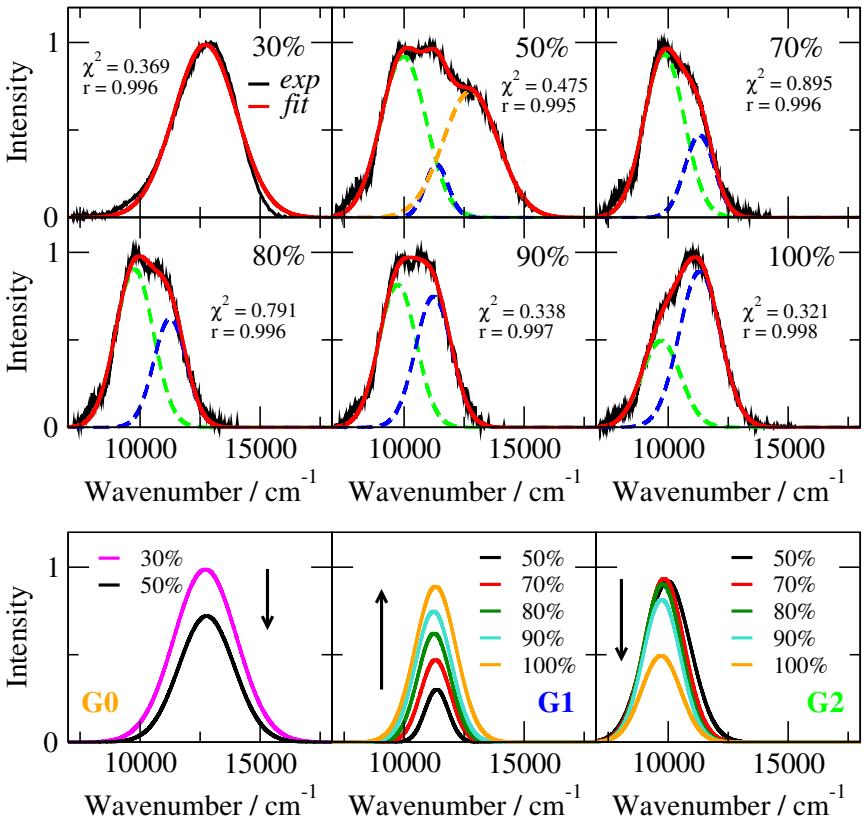

Figure 2.26: Deconvolution of **SilOCAO** emission spectra in selected THF/water mixtures (on the panels the % of water). Top panels: experimental spectra (black lines) were deconvoluted as the sum of three Gaussian functions, G0 (orange), G1 (blue) and G2 (green). Results of the fit are reported in red and labelled with the corresponding chi-squared value (χ^2) and correlation coefficient (r). Bottom panels: evolution of G0, G1 and G2 following an increase of %water, as indicated by the arrow.

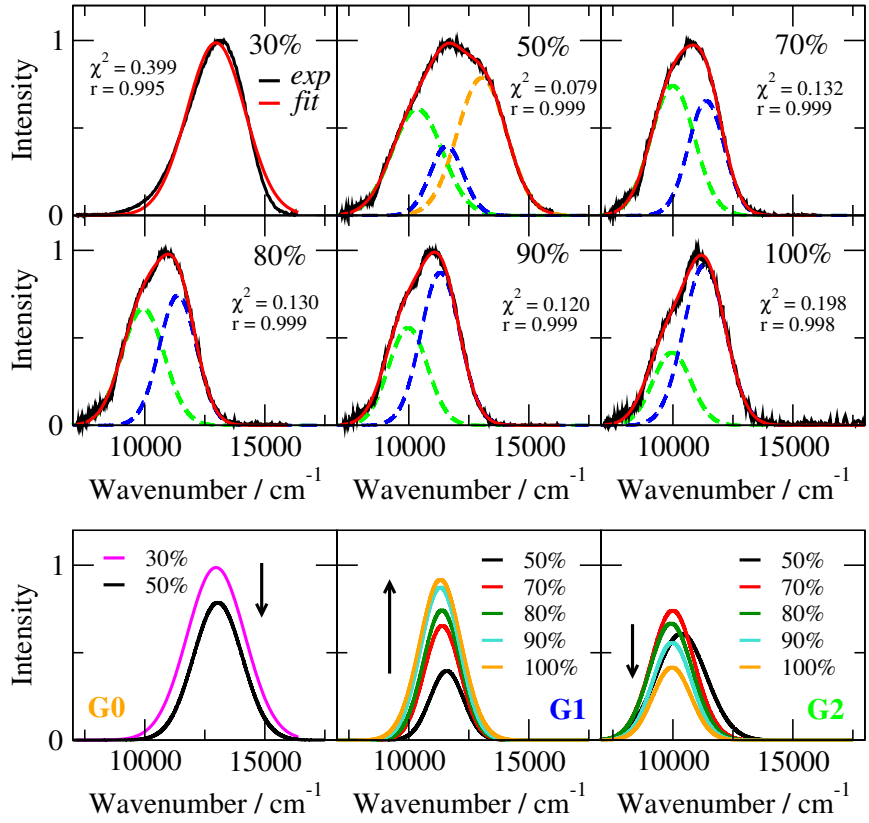

Figure 2.27: Deconvolution of **SilEHCAEH** emission spectra in selected THF/water mixtures (on the panels the % of water). Top panels: experimental spectra (black lines) were deconvoluted as the sum of three Gaussian functions, G0 (orange), G1 (blue) and G2 (green). Results of the fit are reported in red and labelled with the corresponding chi-squared value (χ^2) and correlation coefficient (r). Bottom panels: evolution of G0, G1 and G2 following an increase of %water, as indicated by the arrow.

only contributing to 30% and 50% mixtures and roughly corresponds to the emission of phase I, G1, peaking at $\sim$ 11300 cm^{-1} ($\sim$ 890 nm) and G2, peaking at $\sim$ 9900 cm^{-1} ($\sim$ 1010 nm), which are both present in the mixtures with more than 30% water and correspond to phase II and III, respectively.

As the water fraction increases, the peak of phase I looses intensity and vanishes, while at the same time the peak related to phase II increases and that of phase III decreases concomitantly, indicating a different stability of the phases. Indeed, the composition of the mixture can be tuned to modify the relative abundancy of the aggregated species.

Similarities and differences between spectroscopic properties of the dyes in the various aggregation states can be appreciated looking at Figure 2.28. Aggregation either in the solid state or in the water/THF mixtures is responsible for the broadening and the batochromic shift of both absorption bands, with the appearance of a shoulder in the 700-800 nm range.

Most notably, fluorescence properties are strongly dependent upon the aggregation state. The emission bands of phases II and III characterizing the THF/water mixtures match the emission spectra of ground and pristine powders respectively, suggesting that the aggregates which are spontaneously formed in presence of a nonsolvent are characterized by the same packing motifs of the solid state.

Summarizing, starting from non-interacting molecules in THF solution, the addition of water leads to the spontaneous formation of aggregates. When the water fraction is the minor component ($\leq$ 50%) there is a residual solution-like (solvated) phase, called phase I, in addition to two aggregated phases, phases II and III, whose formation is induced by the presence of water. Compared to the solvated monomer in THF, both phases are characterized by red-shifted absorption and emission spectra. These two phases cannot be distinguished in absorption because of the broad absorption bands, however they emit at different wavelengths ($\lambda \approx 900$ and $\lambda \approx 1000$ nm respectively) with a low quantum yield ($< 1\%$).

The spectroscopic signatures of II and III are independent of the mixture composition, indeed the composition affects their relative abundancy, with II being favoured in mixtures richer in water. Considering the spectral features of phases II and III, we found similarities with the solid state: II has the same emission of ground powders (and probably also absorbs in the

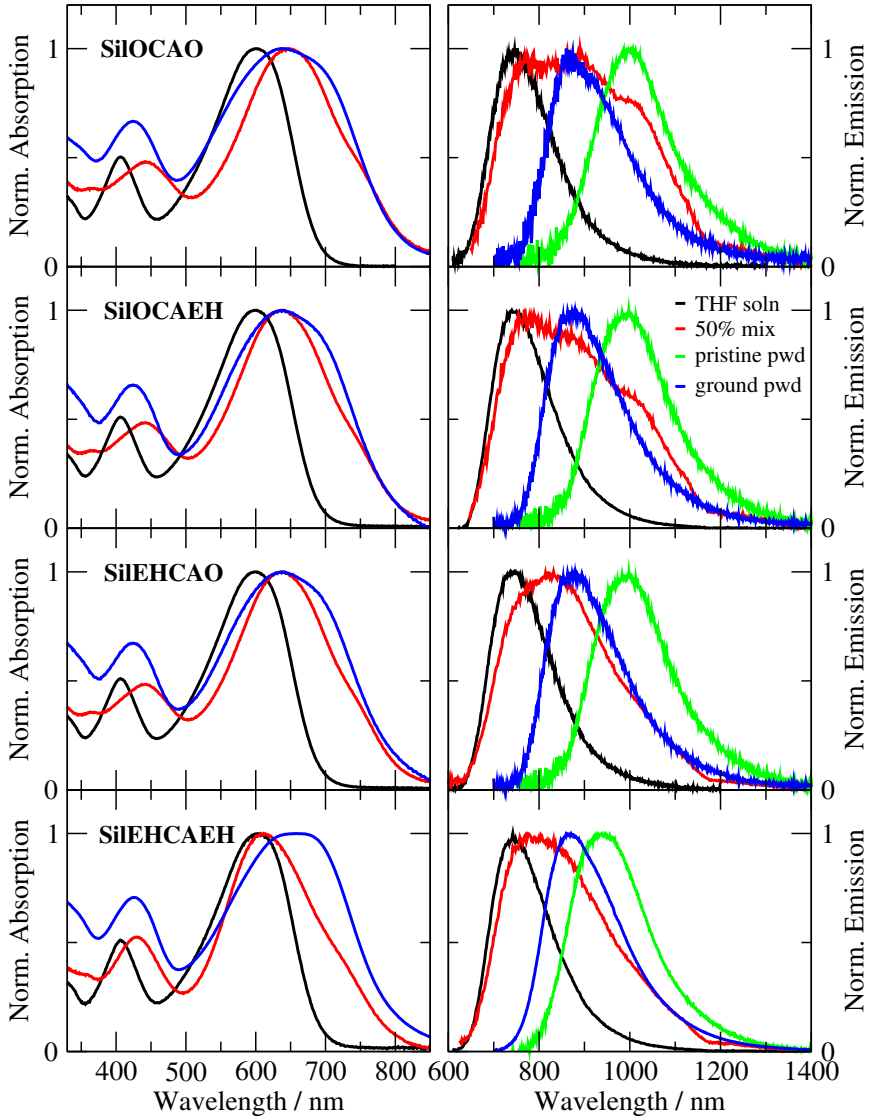

Figure 2.28: Absorption and emission spectra of the dyes in different aggregation states: THF solution (black line), THF/water mixture (50:50 ratio, red line), pristine and ground powders (green and blue lines, respectively).

same region), while emission of III is more similar to that of pristine powders. Accordingly, III may be more crystalline or characterized by longer and/or 3D extended stacks with respect to II, and gentle grinding of the powders converts almost quantitatively III into II, breaking the weak intermolecular interactions. Moreover, the organic solvent (THF) could play a role in assisting the formation of phase III, exerting a sort of template effect, and thus explaining why phase III is less abundant in mixtures rich in water. X-ray diffraction studies on pristine and ground powders could add more information in support of this hypothesis.

We can also conclude that the nature of the alkyl chains is irrelevant in solution but assists the aggregation of the dyes in the solid state and in the nanosuspensions. In the aggregated states **SilOCAO** behaves like **SilOCAEH**, while **SilEHCAEH** shows the same properties of **SilEHCAEH**, suggesting that intermolecular interactions are driven by the chains on the central moiety.

We can envisage that the central chains play a more strategic role in self-assembly: they are linked to the same atom and their bulkiness is crucial in the definition of the intermolecular contacts and distances. Indeed, the main differentiation in the solid state concerns the crystalline phase (phase III), which could be characterized by different interplanar distances, according to the different space required for accommodating linear (**SilOCAO** and **SilOCAEH**) or branched (**SilEHCAO** and **SilEHCAEH**) alkyl chains.

Phases II and III can be considered an example of the so-called non-fluorescent J-aggregates (or, equivalently, red-shifted H-aggregates) [129–131, 344]. Indeed, aggregation is accompanied by a batochromic shift of the absorption band, as it occurs for standard J-aggregates, however they undergo fluorescence quenching, which is instead a typical feature of H-aggregates.

This phenomenon was already pointed out in aggregates of quadrupolar and quadrupolar-like chromophores [130, 131, 345, 346]. Theoretical models including ESMs unraveled the electronic origin of this intriguing behaviour, relating emission quenching to the presence of a low-energy dark state [129,130,344]. Non-fluorescent J-aggregates are not expected based on the standard excitonic approximation and are peculiar of polar and polarizable chromophores, as this family of multipolar dyes.

2.6 Conclusion

The design and preparation of molecular materials with improved optical responses require both the development of reliable predictive models relating the optical properties of collections of molecules, e. g. nanoclusters or crystals, to the supramolecular organization of the aggregate and the specific intermolecular interactions, and the mastering of experimental techniques to induce the self-assembly of the molecular synthons into the sought architecture. Both aspects were covered in this Chapter, through the presentation of selected case studies of different complexity.

In the first one we examined a dimeric structure obtained by covalent linkage of two equivalent NI derivatives, and we established a connection between its optical properties in solution, its electronic structure and geometrical arrangement of the monomeric units. Through a detailed (TD)DFT study we demonstrated that the spectroscopy of this system is dominated by localized excitations, and the coupled NI-NI system can be satisfactorily described within the excitonic scheme as a standard J-dimer, explaining the batochromic shift in absorption and the increase of emission quantum yield.

As expected based on the excitonic picture, the triplet manifold is unaffected by the intermolecular interactions, which are approximated with interactions between the corresponding transition densities, and are vanishing for forbidden singlet-to-triplet excitations. Interestingly, according to our calculations, the NI-NI dimer, characterized by sizeable triplet quantum yield, possess two degenerate triplet states (T_1 and T_2) at almost half the energy of the $S_0 \rightarrow S_1$ transition. This property, together with the good emission intensity in the blue region, makes the dimeric NI-NI an interesting candidate for energy upconversion through TTA, and future work will explore in more detail its suitability.

As the following step, we explored the limits of the exciton approach, focusing on aggregates of polar and polarizable molecules, which strongly interact through electrostatic forces which are typically larger than their excitation energies. For the first time we addressed the effect of aggregation on phosphorescence of CT chromophores, combining two complementary theoretical approaches: DFT and ESMs.

Following the ESM strategy, we built a simple three-state model describing absorption and phosphorescence spectra of an ideal push-pull chromophore and, in a bottom up strategy, we extended it to account for the intermolecular electrostatic interactions in a molecular dimer. For the dimer, fairly large deviations of phosphorescence energy are predicted compared to the noninteracting monomers, whose magnitude and sign depend upon the geometrical arrangement of the molecules in the aggregate. The phosphorescence energies obtained with this model could be quantitatively reproduced following a mean-field approach, i. e. solving a single-molecule problem in the self-consistent field generated by the surrounding molecules, indicating this phenomenon is the dominant effect as far as phosphorescence spectra are concerned. This general result applies to every polar/polarizable chromophore, and suggests how phosphorescence tuning can be achieved through the control over molecular packing.

In this framework, we also examined a specific case study which, in spite of the intrinsic complexity of the system preventing the application of the ESM approach, offered a valid demonstration of the statements above. The target chromophore was a dinuclear Rhenium(I) complex undergoing MLCT and featuring two polymorphs characterized by high phosphorescence intensity and different emission colours. Through TDDFT calculations on a single molecule surrounded by the charge distribution of the nearest-neighbour molecules we were able to accurately reproduce the phosphorescence shift between the two polymorphs, confirming its mean-field origin.

In a broader perspective, we can conclude that mean-field effects, completely neglected in the standard excitonic scheme, are a fundamental ingredient for the correct understanding of the spectroscopy of aggregates made of CT dyes, and must be included in the theoretical models to set the correct scenario for the full understanding and exploitation of the cooperative effects arising from aggregation.

The last part of this Chapter discussed the experimental work on a family of multipolar near-IR emitting dyes decorated with different alkyl groups and designed to study the relationship between chemical structure, supramolecular organization, and optical properties. We found that, both in the solid state and in solvent/antisolvent mixtures, these dyes arrange spontaneously into two phases characterized by different absorption/emission spectra and

low fluorescence quantum yield. Most interestingly, the abundancy of these phases can be easily controlled by external stimuli, such as gentle grinding of the powders or a variation of the mixture composition, allowing to get a control over the spectroscopic properties. This intriguing behaviour is related to the subtle balance between the intermolecular interactions promoted by the rigid conjugated skeleton of the chromophores and those driven by the bulky and flexible side chains, and offers an interesting design strategy for the modulation of the materials optical properties through supramolecular engineering.

Chapter 3

Energy and electron transfer in calixarene-based dyads

3.1 Introduction

Energy and electron transfer are fundamental processes in chemistry and life sciences [151, 152, 347–349]. They occur in a variety of materials, from organic dyes to metal complexes, from nanoparticles and nanocrystals to dendrimers and polymers, including biomolecules and proteins, and are relevant both in natural and technological applications [350].

Excitation energy transfer (EET) and electron transfer (eT) constitute the essential steps of photosynthesis, a process converting sunlight into chemical energy naturally occurring in plants, algae and some bacteria [67, 351]. These organisms possess specific units fitted for the purpose, the photosynthetic units (PSU), consisting in a reaction center (RC), devoted to the photochemical reactions, surrounded by arrays of light-harvesting (LH) complexes containing hundreds of chlorophylls. Only few of them are directly involved in the chemical transformations, while the majority play the role of light-harvesting antennae, absorbing solar energy and funnelling the electronic excitation towards the RC [352]. Light-harvesting antennae of the external LH complexes initiate a cascade energy-transfer process towards the inner complexes, eventually conveying the excitation to the RC, where a sequence of electron-transfer events stabilizes a long-lived charge-separated state, creating an electrochemical gradient which provides the

driving force to the chemical reactions. Overall, excitation energy transfer as performed within a PSU is a well-organized process whose efficiency approaches unity [353].

The quest for clean and renewable energy sources on a global scale motivated an increasing interest on the study of natural photosynthesis, as a model for solar energy conversion. Indeed, biomimetic systems, mimicking the supramolecular organization and function of natural PSU are promising artificial systems for the conversion of sunlight [354].

So far, research focused on the synthesis of artificial models based on covalent or supramolecular architectures simulating light-harvesting antennae, or more complex systems combining an antenna and a reaction centre [355–357].

Artificial systems are not only candidate to work as active units in optoelectronic devices [358, 359], but are also simplified models to study the physical and chemical factors affecting EET and eT processes, as well as their interplay in the photosynthetic route, with the aim of finding guidelines for the design and optimization of efficient devices [360, 361].

Research is not only devoted to improve the optical properties of chromophores, but also to optimize the molecular architecture of the network, paying attention to the type of interconnections, distance and orientation between the dyes, which also have a fundamental impact on the performance of EET and eT [362]. Moreover, also the medium in which the system is embedded perturbs EET and eT processes, and its effect has to be carefully investigated [134, 363].

The simplest model systems for the investigation of EET and/or eT are dyads or triads [364–373]. A dyad is a bichromophoric system in which a pair of active units (chromophores), an energy and/or electron donor and an energy and/or electron acceptor, are covalently bridged by a suitable scaffold. This essential architecture allows to play with the identity of the chromophores but also with the nature of the bridge, which is of paramount importance in defining the intermolecular interactions [374–376].

In this Work, we considered model dyads for EET and eT studies in which the role of the bridge is played by a calix[4]arene. Covalent linkage of the chromophores to a calix[4]arene scaffold offers several advantages. Firstly, calix[4]arenes are highly versatile structures, as they can be eas-

ily functionalized at specific sites, guaranteeing good control on interchromophoric distance and orientation [377]. Moreover, calix[4]arenes can be immobilized in one out of four different conformations (cone, partial cone, 1,2-alternated and 1,3-alternated) affecting the mutual orientation of the substituents as well [378]. The residual conformational mobility of the calix modulates the distance between the substituents on the upper rim [379], according to the specific attractive or repulsive interactions [380], and can be triggered by external stimuli such as a variation of temperature or solvent polarity [381].

Calixarene-based systems undergoing EET and/or eT were largely investigated as fluorescent probes for ions [382], however only a few examples of calix[4]arene-based dyads especially designed for EET and eT studies are reported in the literature [381, 383–386].

In this Chapter we will offer a detailed investigation of EET and eT in a series of novel calixarene-based dyads developed in collaboration with Prof. Laura Baldini and Prof. Francesco Sansone from University of Parma, who were in charge of the chemical synthesis. After providing a brief and general introduction to EET and eT, we will describe the characterization of a few bichromophoric systems explicitly designed for EET, based on pairs of boron-dipyrromethene (BODIPY) dyes, that will allow the investigation of the effect of solvent polarity and calix conformation on EET efficiency [387]. Moving on, we will examine the interplay between EET and eT in a Nile Red - fullerene bichromophoric system. Finally, we will focus on an application of EET in a molecular dyad in which the conformational mobility of the calix scaffold can be exploited for temperature sensing [388].

3.2 Energy transfer

Excitation energy transfer (EET) is a process in which electronic excitation migrates from an excited chromophore, called energy donor ($\mathcal{D}$), to another chromophore, the energy acceptor ($\mathcal{A}$), initially in its ground-state. $\mathcal{D}$ and $\mathcal{A}$ can be identical chemical species, in this case the process is called homotransfer, or different species, and in this case it is called heterotransfer. Similarly, $\mathcal{D}$ and $\mathcal{A}$ can belong to the same molecule or to different molecules, and EET is referred to as intramolecular or intermolecular transfer, respec-

tively. Also multiple donor/multiple acceptor systems may be involved in the process, however, in the following, we will focus on a single $\mathcal{D} - \mathcal{A}$ pair, as relevant to this Work.

EET can occur either radiatively or non-radiatively. Radiative EET is the simplest process, and follows two sequential steps. The first step corresponds to the de-excitation of $\mathcal{D}$ with concomitant emission of a photon, while the second step consists in the absorption of the emitted photon by $\mathcal{A}$, as described by the following:

$$\mathcal{D}^* \rightarrow \mathcal{D} + h\nu_{\mathcal{D}} \tag{3.1}$$

$$\mathcal{A} + h\nu_{\mathcal{D}} \rightarrow \mathcal{A}^* \tag{3.2}$$

In the chemical equations above $\mathcal{D}^*$ labels the excited donor and $h\nu_{\mathcal{D}}$ is the energy of the photon emitted by the donor.

Radiative transfer does not require an interaction between $\mathcal{D}$ and $\mathcal{A}$; the only conditions are that the emitted photons reach the acceptor and their energy match its transition energy, i.e. a finite overlap must exist between the emission spectrum of $\mathcal{D}$ and the absorption spectrum of $\mathcal{A}$. This kind of EET is of no practical interest and belongs to the so-called inner filter effects which one wants to avoid in spectroscopic measurements, for example, operating on diluted solutions.

More interesting to our purposes is nonradiative energy transfer, which takes place under near field conditions, i.e. when the distance between $\mathcal{D}$ and $\mathcal{A}$ is shorter than the wavelength of the photon. Under this condition, de-excitation of $\mathcal{D}$ and excitation of $\mathcal{A}$ occur in a single step, without the emission of real photons (a so-called virtual photon is exchanged):

$$\mathcal{D}^* + \mathcal{A} \rightarrow \mathcal{D} + \mathcal{A}^* \tag{3.3}$$

where the asterisks mark excited species. Nonradiative EET occurs at distances typically shorter than 10 nm, and requires an interaction between the partners involved. At very short distances, where a finite overlap is present between the electronic wavefunctions of donor and acceptor, EET occurs *via* electron exchange, according to the so-called Dexter mechanism. When the distance is larger and intermolecular orbital overlap can be neglected, EET is mainly due to Coulombic interactions.

The strength of the interaction determines the mechanism of EET. In the strong coupling regime, occurring when the interchromophoric coupling is larger than the exciton-bath coupling, the electronic states of the donor and those of the acceptor are largely mixed, and the resulting states are delocalized over both units. In this case the excitation oscillates between $\mathcal{D}$ and $\mathcal{A}$ in a coherent process. Coherent EET was experimentally found in photosynthetic organisms, even if its role in photosynthesis is still subject to debate [389–392].

When the coupling between $\mathcal{D}$ and $\mathcal{A}$ is much weaker than the coupling to the bath and EET is slower than vibrational relaxation of the donor and the bath, we are in the so-called weak coupling regime. The theory describing EET in the weak coupling regime was originally proposed by Förster [393], and was validated by experimental findings on a few model systems [394–396]. Förster theory relates the mechanism of EET to experimental observables, and is widely adopted today. EET is sometimes known as FRET, as the acronym of Förster (or fluorescence) Resonance Energy Transfer, and will be described in detail in the following.

3.2.1 Förster theory for energy transfer

In the weak coupling limit EET (hereafter FRET) occurs on a nanosecond timescale, i.e. much slower than the internal conversion processes, typically characterized by picosecond dynamics. This means that $\mathcal{D}^*$ relaxes to the lowest excited-state through internal conversion before transferring the excitation to $\mathcal{A}$, as sketched in Figure 3.1. This implies that the virtual photons absorbed by $\mathcal{A}$ are those associated with the fluorescence of $\mathcal{D}$. After energy transfer has been completed, the acceptor itself relaxes to the ground-state through its characteristic radiative and/or nonradiative channels.

According to Förster, the interaction between donor and acceptor is described adopting the perturbative theory. The rate of the process described by Eq. 3.3, k_{FRET}, can be expressed through the Fermi golden rule:

$$k_{FRET} = \frac{1}{\hbar^2} |\langle \psi_{\mathcal{D}^*}(1)\psi_{\mathcal{A}}(2)| \hat{H}' |\psi_{\mathcal{D}}(1)\psi_{\mathcal{A}^*}(2)\rangle|^2 \delta(\nu_{\mathcal{D}} - \nu_{\mathcal{A}}) \tag{3.4}$$

In the equation above $\psi_{\mathcal{D}^*}(1)\psi_{\mathcal{A}}(2)$ and $\psi_{\mathcal{D}}(1)\psi_{\mathcal{A}^*}(2)$ are the initial and final wavefunctions of the coupled system respectively, with numbers 1 and 2 labelling the electrons, while $\nu_{\mathcal{D}}$ and $\nu_{\mathcal{A}}$ are the frequencies of the virtual

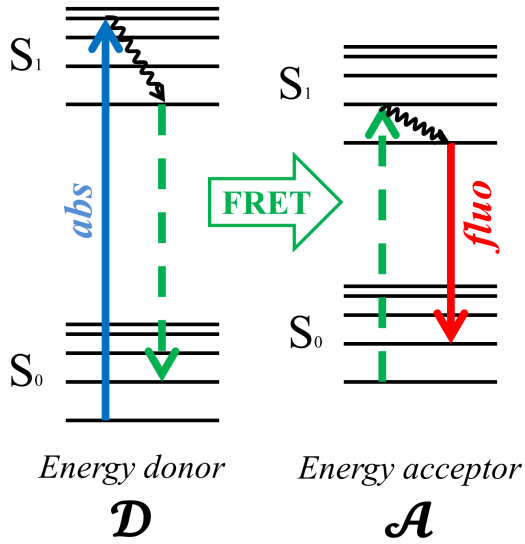

Figure 3.1: Excitation energy transfer (FRET) in the weak coupling regime. Scheme of the process: after photoexcitation, the energy donor $\mathcal{D}$ transfers its excitation energy to the energy acceptor $\mathcal{A}$, which then relaxes to the ground state e.g. through fluorescence emission. The energy of the virtual photon emitted by $\mathcal{D}$ (dashed green arrow) must correspond to a transition energy of $\mathcal{A}$.

photon emitted by $\mathcal{D}$ and absorbed by $\mathcal{A}$, respectively. Accordingly, FRET can occur only if de-excitation of $\mathcal{D}$ and excitation of $\mathcal{A}$ are isoenergetic. $\hat{H}'$ is the Hamiltonian describing the electrostatic interaction between the FRET partners:

$$\hat{H}' = \frac{1}{4\pi\varepsilon_0 n^2}\frac{e^2}{r} \tag{3.5}$$

where ε_0 is the vacuum permittivity, n is the refractive index of the medium, e is the charge of the electron and r is the distance between the donor and the acceptor. The matrix element

$$V = \frac{e^2}{4\pi\varepsilon_0 n^2}\left\langle \psi_{\mathcal{D}^*}(1)\psi_{\mathcal{A}}(2)\right| \frac{1}{r} \left|\psi_{\mathcal{D}}(1)\psi_{\mathcal{A}^*}(2)\right\rangle \tag{3.6}$$

describes the electrostatic interaction between the transition charge density of the donor and the transition charge density of the acceptor.

In the classical picture, the excited donor is associated to an electric dipole oscillating at frequency $\nu_{\mathcal{D}}$, which generates an electric field in the surrounding. The oscillating field can drive into resonance a molecule of $\mathcal{A}$ which is located close enough, provided that it matches one of its natural frequencies $\nu_{\mathcal{A}}$. If the strength of the electric field generated by $\mathcal{D}$ is sufficient and the species are nearby, conditions for FRET are met, and $\mathcal{A}$ starts oscillating as well.

When the interchromophoric distance r is larger than the dimension of the FRET partners, as it is often the case in the weak coupling regime, the interaction V can be written in the dipolar approximation, i.e. as the interaction between the transition dipole moments of $\mathcal{D}$ and $\mathcal{A}$:

$$V = \frac{1}{4\pi\varepsilon_0 n^2}\frac{\vec{\mu}_{\mathcal{D}} \cdot \vec{\mu}_{\mathcal{A}} - 3(\vec{\mu}_{\mathcal{D}} \cdot \hat{\boldsymbol{R}}_{\mathcal{D}\mathcal{A}})(\vec{\mu}_{\mathcal{A}} \cdot \hat{\boldsymbol{R}}_{\mathcal{D}\mathcal{A}})}{r^3} \tag{3.7}$$

where we indicated with $\vec{\mu}_{\mathcal{D}}$ and $\vec{\mu}_{\mathcal{A}}$ the emission dipole moment of $\mathcal{D}$ and the absorption dipole moment of $\mathcal{A}$ respectively, and $\hat{\boldsymbol{R}}_{\mathcal{D}\mathcal{A}}$ is the versor defining the line connecting their origins (Figure 3.2). Based on geometrical arguments, Eq. 3.7 can be recast as:

$$\begin{aligned} V &= \frac{1}{4\pi\varepsilon_0 n^2}\frac{|\vec{\mu}_{\mathcal{D}}||\vec{\mu}_{\mathcal{A}}|}{r^3}(\cos\theta_T - 3\cos\theta_{\mathcal{D}}\cos\theta_{\mathcal{A}}) \\ &= \frac{1}{4\pi\varepsilon_0 n^2}\frac{|\vec{\mu}_{\mathcal{D}}||\vec{\mu}_{\mathcal{A}}|}{r^3}k \end{aligned} \tag{3.8}$$

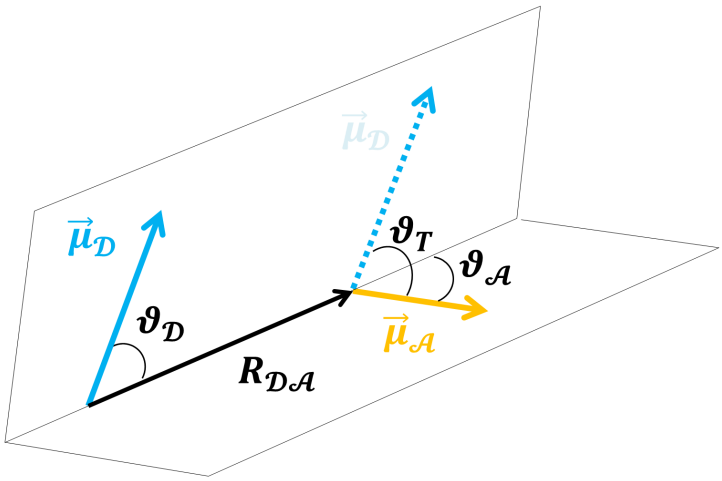

Figure 3.2: Transition dipole moments related to the de-excitation of the energy donor ($\vec{\mu}_{\mathcal{D}}$) and the excitation of the energy acceptor ($\vec{\mu}_{\mathcal{A}}$) and definition of the angles entering the expression for the orientational factor k (Eq. 3.8).

with the angles θ_T, $\theta_{\mathcal{D}}$ and $\theta_{\mathcal{A}}$ defined as in Figure 3.2. The term k is called orientational factor and only depends on the relative orientation of the dipoles.

A more convenient expression relating k_{FRET} to experimental observables can be derived from Eq. 3.4 exploiting the definition of absorption and emission spectra. Omitting the demonstration, the expression for the FRET rate reads:

$$k_{FRET} = \frac{Q_{\mathcal{D}} k^2}{\tau_{\mathcal{D}} r^6} \left(\frac{9000(\ln 10)}{128\pi^5 N n^4} \right) \int_0^\infty F_{\mathcal{D}}(\lambda) \varepsilon_{\mathcal{A}}(\lambda) \lambda^4 d\lambda \tag{3.9}$$

where $Q_{\mathcal{D}}$ and $\tau_{\mathcal{D}}$ are the fluorescence quantum yield and lifetime of the donor in the absence of FRET, r is the donor-acceptor distance, N is the Avogadro number and n is the refractive index of the medium. $F_{\mathcal{D}}(\lambda)$ is the fluorescence spectrum of the donor (on the wavelength scale) normalized to unit area, while $\varepsilon_{\mathcal{A}}(\lambda)$ is the molar extinction coefficient of the acceptor in units of mol^{-1} L cm^{-1}. All wavelengths are expressed in nm.

The last term of Eq. 3.9 is also called overlap integral, J:

$$J = \int_0^\infty F_{\mathcal{D}}(\lambda) \varepsilon_{\mathcal{A}}(\lambda) \lambda^4 d\lambda \tag{3.10}$$

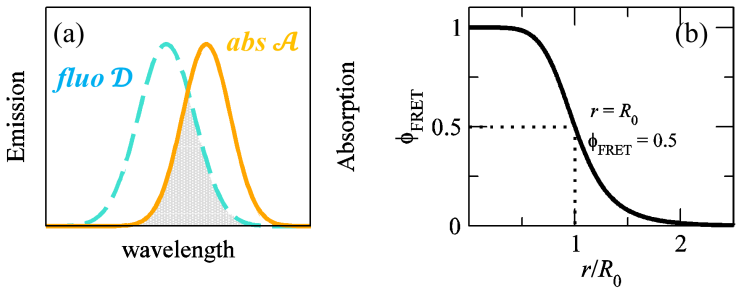

Figure 3.3: Requirements for FRET. (a) Representation of the spectral overlap (greyed area) between emission of $\mathcal{D}$ and absorption of $\mathcal{A}$. (b) Relationship between FRET efficiency ϕ_{FRET} and interchromophoric distance r. The Förster radius R_0 is the distance at which $\phi_{FRET} = 0.5$.

and is in units of mol^{-1} L cm^{-1} nm^4. Practically, it expresses the degree of spectral overlap between the emission of the donor and the absorption of the acceptor.

Eq. 3.9 summarizes all the requirements for FRET. Even if the process does not imply emission of real photons, k_{FRET} is proportional to the fluorescence quantum yield of the donor and the inverse of its lifetime, so that the ideal donor should be a bright emitter with fast decay kinetics. Moreover, a finite and possibly large overlap between the donor emission and the acceptor absorption must exist in order to guarantee high energy transfer rate (Figure 3.3 (a)), and acceptors with high molar extinction coefficient also favour FRET, through the increase of J. The term k^2 depends on the relative orientation of the transition dipole moments of $\mathcal{D}$ and $\mathcal{A}$. It can range from 0, for perpendicular dipoles, to 4 for head-to-tail parallel dipoles. In solution, rotational diffusion of the fluorophores during the excited-state lifetime causes a randomization of their orientation, and under this condition $k^2 = 2/3$, which is usually assumed for chromophores which are free to rotate in solution. In some special cases, e.g. in rigid matrixes or constrained $\mathcal{D} - \mathcal{A}$ pairs, $k^2 = 0$ may occur leading to $k_{FRET} = 0$. Finally, the interchromophoric distance enters as the inverse of the sixth power, implying a large effect on k_{FRET}.

The quantities $Q_{\mathcal{D}}$, $\tau_{\mathcal{D}}$ and J are easily accessible from basic spectroscopic investigation of the isolated donor and acceptor. However, the in-

terchromophoric distance and the FRET rate k_{FRET} are more difficult to estimate.

The problem can be simplified introducing the Förster radius R_0, defined as the distance at which the FRET rate equals the decay rate of the isolated donor. Substitution of $r = R_0$ and $k_{FRET} = \tau_{\mathcal{D}}^{-1}$ into Eq. 3.9 allows to write R_0 as a function of k^2, $Q_{\mathcal{D}}$ and J:

$$R_0^6 = \frac{9000(\ln 10)}{128\pi^5 N n^4} k^2 Q_{\mathcal{D}} J \tag{3.11}$$

It follows that, for a given FRET pair, the Förster radius can be easily extracted from experiment in the absence of energy transfer. Typical values of R_0 range from 20 to 60 Å [151]. Accordingly, the rate of FRET can be rewritten as

$$k_{FRET} = \frac{1}{\tau_{\mathcal{D}}} \left(\frac{R_0}{r} \right)^6 \tag{3.12}$$

which highlights its dependence on the ratio between the Förster radius and the donor-acceptor distance.

Another useful quantity is the efficiency of energy transfer, ϕ_{FRET}, indicating the fraction of photons absorbed by the donor which are transferred to the acceptor. ϕ_{FRET} is defined as the ratio of the FRET rate to the total decay rate of the donor in presence of the acceptor, which includes energy transfer and all other decay processes:

$$\phi_{FRET} = \frac{k_{FRET}}{\tau_{\mathcal{D}}^{-1} + k_{FRET}} \tag{3.13}$$

Combination of Eq. 3.12 and 3.13 gives

$$\phi_{FRET} = \frac{R_0^6}{R_0^6 + r^6} = \frac{1}{1 + (\frac{r}{R_0})^6} \tag{3.14}$$

The dependency of ϕ_{FRET} on the interchromophoric distance is shown in Figure 3.3 (b). The efficiency is sensitive to distance in proximity of R_0. When $r = R_0$ the efficiency amounts to 50%, while it quickly increases to 1 for $r < R_0$ becoming the main decay channel of the donor. On the opposite ϕ_{FRET} decreases steeply to 0 for $r > R_0$. Once R_0 is known, the experimental measurement of ϕ_{FRET} (see below) allows to estimate the interchromophoric distance, exploiting FRET as a 'spectroscopic ruler' [71, 397]. However, because of the strong dependence on distance, measurements of r can be considered reliable only in the range $0.5R_0 < r < 2R_0$ [151].

3.2.2 Measurement of FRET efficiency

Within the Förster theory, a few methods can be exploited for the measurement of ϕ_{FRET} in $\mathcal{D}-\mathcal{A}$ pairs separated by a fixed distance. The most widely adopted methods include a time-resolved and three steady-state methods, and will be briefly reviewed in the following [151, 152].

Method I. The time-resolved method is based on the observation that the lifetime of the energy donor is reduced in presence of FRET. This method requires the measurement of the donor lifetime in the absence and in presence of the acceptor, and estimates the efficiency as follows:

$$\phi_{FRET} = 1 - \frac{\tau_{\mathcal{D}(\mathcal{A})}}{\tau_{\mathcal{D}}} \tag{3.15}$$

where $\tau_{\mathcal{D}(\mathcal{A})}$ ($\tau_{\mathcal{D}}$) denotes the lifetime of the donor measured in presence (absence) of the acceptor.

Method II. The FRET efficiency can also be estimated evaluating the FRET-induced quenching of the donor, from the comparison between emission intensities (or quantum yields) of the donor in presence and in absence of transfer:

$$\phi_{FRET} = 1 - \frac{F_{\mathcal{D}(\mathcal{A})}}{F_{\mathcal{D}}} = 1 - \frac{\phi_{\mathcal{D}(\mathcal{A})}}{\phi_{\mathcal{D}}} \tag{3.16}$$

where $F_{\mathcal{D}(\mathcal{A})}$ ($\phi_{\mathcal{D}(\mathcal{A})}$) and $F_{\mathcal{D}}$ ($\phi_{\mathcal{D}}$) are the fluorescence intensities (quantum yields) of the donor in presence or in absence of the acceptor respectively.

Methods I and II are direct methods, i.e. they are based on the direct observation of the FRET effect on the energy donor. However, in order to apply them, the residual emission of the donor must be intense enough to guarantee a reliable measurement of fluorescence intensity or lifetime. Similarly, the donor lifetime in presence of the acceptor must be within the time resolution of the instrumental setup, to allow for its measurement. In other words, these methods can be adopted only when $\phi_{FRET} < 1$.

If the acceptor is also fluorescent, other two indirect methods can be applied, which focus on the emission from the acceptor.

Method III. FRET constitutes a source of excitation energy for the acceptor, increasing its fluorescence intensity. Sensitization of the acceptor emission allows for the estimation of ϕ_{FRET} upon selective excitation of the donor according to the following:

$$\phi_{FRET} = \frac{\varepsilon_{\mathcal{A}}(\lambda_{\mathcal{D}}^{ex})}{\varepsilon_{\mathcal{D}}(\lambda_{\mathcal{D}}^{ex})}\left[\frac{I_{\mathcal{A}(\mathcal{D})}}{I_{\mathcal{A}}} - 1\right] \tag{3.17}$$

where $\varepsilon_{\mathcal{A}/\mathcal{D}}$ is the molar extinction coefficient of the acceptor/donor at the excitation wavelength $\lambda_{\mathcal{D}}^{ex}$, $I_{\mathcal{A}}$ is the emission intensity of the energy acceptor in the absence of the energy donor, and $I_{\mathcal{A}(\mathcal{D})}$ is the emission intensity of the acceptor in presence of the donor.

Method IV. The last method relies on the comparison between the absorption and the excitation spectra of the $\mathcal{D}-\mathcal{A}$ system, where the excitation spectrum is collected for detection of the photons emitted by the sole acceptor. Absorption and excitation spectra are normalized at the absorption band of the acceptor. In the limiting case of $\phi_{FRET} = 1$ the spectra should perfectly match, conversely, in the absence of transfer, only the acceptor band should be observed in the excitation spectrum. In the intermediate situations the FRET efficiency can be obtained from the ratio between the excitation and absorption intensities of the donor in the region in which only the donor absorbs. In more quantitative terms:

$$\phi_{FRET} = \frac{I(\lambda_{\mathcal{D}})}{A(\lambda_{\mathcal{D}})} \tag{3.18}$$

where I and A denote excitation and absorption spectra at wavelength $\lambda_{\mathcal{D}}$ at which the absorption of the acceptor can be neglected. If the absorption bands of donor and acceptor are largely overlapped, a fitting procedure is required to extract the donor contribution to the spectra of the bichromophoric system.

3.3 Electron transfer

Electron transfer (eT) is a reaction in which an excess of charge initially localized on the electron donor, $\mathbb{D}$, spontaneously migrates on the electron acceptor $\mathbb{A}$, as expressed by the following:

$$\mathbb{D}^- + \mathbb{A} \rightarrow \mathbb{D} + \mathbb{A}^- \tag{3.19}$$

Donor and acceptor may be separate chemical entities or belong to the same species, accordingly, the process is named intermolecular or intramolecular eT, respectively. In both cases, the structure formed by $\mathbb{D}$ and $\mathbb{A}$ undergoing eT is called donor-acceptor ($\mathbb{D}-\mathbb{A}$) complex. Independently of the mechanism and the species involved, eT requires the overlap between the

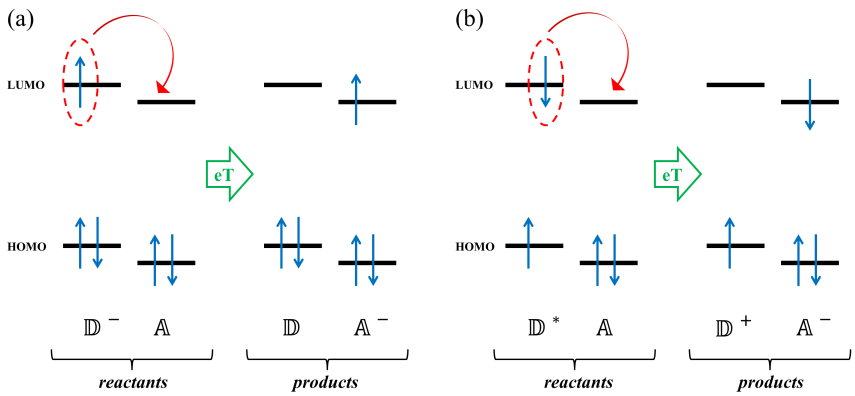

Figure 3.4: Sketch of the electron transfer (eT) process. (a) An electron migrates from the LUMO of the donor to the LUMO of the acceptor. (b) Photoinduced eT: the excited electron of the donor moves to the LUMO of the acceptor.

frontier orbitals of donor and acceptor, so that short distance between the eT partners is a prerequisite for the process [398].

A representation of the eT reaction expressed by Eq. 3.19 is provided in Figure 3.4 (a) where, for simplicity, only the frontier molecular orbitals (HOMO and LUMO) of the $\mathbb{D}-\mathbb{A}$ complex are shown. The excess charge initially occupies the LUMO of $\mathbb{D}$ and then migrates on the LUMO of $\mathbb{A}$. A favourable alignment of the energy levels of donor and acceptor, with the LUMO of $\mathbb{A}$ at a lower energy than the LUMO of $\mathbb{D}$, guarantees the spontaneity of the process.

Another eT mechanism, more relevant to this Thesis work, is the so-called photoinduced eT (Figure 3.4 (b)). In this case the donor is initially in an excited-state before donating one electron to the acceptor, as described by:

$$\mathbb{D}^* + \mathbb{A} \rightarrow \mathbb{D}^+ + \mathbb{A}^- \tag{3.20}$$

where the asterisk marks the excited species. The way in which the excitation on $\mathbb{D}$ is created, for example irradiation with an external energy source or, as in photosynthesis, energy transfer, is irrelevant to the eT process. Photoexcitation of the donor creates a bound electron-hole pair, usually called *exciton*, characterized by its binding energy which, for organic materials, is typically on the order of 0.4 eV. eT occurs spontaneously only if the energy difference between the LUMO of the donor and the LUMO of the

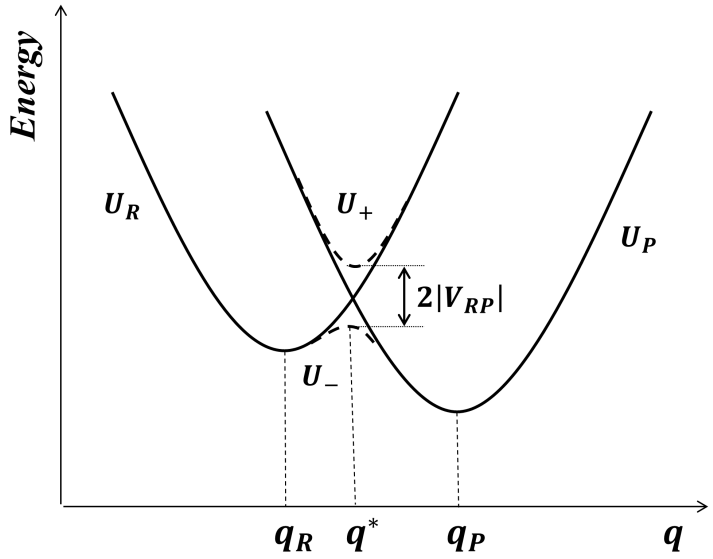

Figure 3.5: Potential energy surfaces (PES) relevant to the eT process along coordinate q. U_R and U_P are the diabatic PES of reagents and products, characterized by equilibrium positions at q_R and q_P, respectively. U_+ and U_- (dashed lines) are the adiabatic PES originated from the mixing of the diabatic curves. The adiabatic states are split by $2|V_{RP}|$ at the crossing point of the diabatic curves, q^*.

acceptor is larger than the exciton binding energy, guaranteeing an energy gain. At the same time, the HOMO of the acceptor must be lower in energy than the HOMO of the donor to avoid a backward eT, that would lead to charge recombination. To this aim, the lifetime of the exciton should be long enough to allow eT from $\mathbb{D}$ to $\mathbb{A}$ and the kinetics of the forward and backward processes must occur on different timescales.

An intermolecular eT reaction may occur at several distances and orientations between $\mathbb{D}$ and $\mathbb{A}$, requiring the averaging over all the possible configurations of the $\mathbb{D}-\mathbb{A}$ complex. Conversely, intramolecular eT occurs at fixed $\mathbb{D}-\mathbb{A}$ distance and can be treated within a more simple formal description. In the following, we will focus on intramolecular eT only, which is the process applying to the dyads presented in this Work.

The variation of charge distribution occurring during the eT reaction affects the electrostatic field of the $\mathbb{D}-\mathbb{A}$ complex, driving the nuclei to a

new equilibrium position. At the same time, if the complex is embedded in a polarizable environment, for example a polar solvent, eT may induce a rearrangement of the configuration of the surrounding medium as well. Therefore, an eT process is coupled to all vibrational modes and all solvation coordinates of the system. For simplicity we will focus on a single generic coordinate q (Figure 3.5).

The energy of the reactants as a function of q defines the potential energy surface (PES) U_R, characterized by a minimum at $q = q_R$, corresponding to the equilibrium configuration of the reactants. The PES for the products, U_P, is characterized by the equilibrium position q_P. In the most general case $q_R \neq q_P$ and the two PES cross at $q = q^*$. The curves U_R and U_P correspond to the diabatic representation of the problem, i.e. to the representation in the absence of interaction between donor and acceptor. The interaction leads to the mixing of the diabatic states, resulting in a splitting of $2|V_{RP}|$ at $q = q^*$ (see the adiabatic curves U_+ and U_- in Figure 3.5), where V_{RP} is the interaction energy between the states of reactants and products.

V_{RP} is a key quantity in the eT theory, since its magnitude defines the mechanism of the process. In more quantitative terms, we should compare the characteristic time of the transfer τ_e, with the characteristic time of nuclear motion τ_v. The former is proportional to the time needed for the displacement of the electronic wavefunction from the reactant state to the product state at the crossing point q^*, and is related to V_{RP}:

$$\tau_e = \frac{h}{|V_{RP}|} \tag{3.21}$$

where h is the Planck constant. The latter depends on the vibrational frequency ω_v:

$$\tau_v = \frac{2\pi}{\omega_v} \tag{3.22}$$

For $\tau_e \ll \tau_v$, eT is faster than nuclear vibration, therefore it occurs at a frozen nuclear configuration. This process, also called adiabatic eT, occurs when V_{RP} is large enough to induce a sizeable splitting of the curves U_+ and U_-. In this case the whole process occurs on the lowest PES only (U_-) which features a double minimum. It is the typical case of a thermally activated reaction evolving from the reactant minimum to the product minimum through the crossing of a barrier, whose rate k_{eT} is described by the

standard Arrhenius equation:

$$k_{eT} \propto \exp\left(\frac{-E_{act}}{k_B T}\right) \tag{3.23}$$

where E_{act} denotes the activation energy of the process, k_B is the Boltzmann constant and T is the temperature.

On the opposite, if nuclear vibrations are much faster than eT ($\tau_e \gg \tau_v$), we are in the so-called nonadiabatic regime, typical of small V_{RP}. This case can be described resorting to a perturbative treatment, where the diabatic states coincide with the unperturbed states. At the lowest order (Fermi golden rule), eT occurs when the energy levels of the reactants and products are degenerate, i.e. at $q = q^*$, with a probability $|V_{RP}|^2$. At the same time, we have to take into account the probability of reaching the crossing region q^*, which is given by the exponential in Eq. 3.23. Combining the two requirements we obtain:

$$k_{eT} \propto |V_{RP}|^2 \exp\left(\frac{-E_{act}}{k_B T}\right) \tag{3.24}$$

3.3.1 Marcus theory for electron transfer

A formal description of eT was developed by Marcus in the 50's and correlates the activation energy of the transfer reaction with quantities easily accessible from experiment [399, 400]. These quantities are ΔE, also called driving force of the reaction, and the reorganization energy E_λ. Both quantities are depicted in Figure 3.6. The driving force is defined as the energy difference between products and reactants at their equilibrium position, while the reorganization energy is the energy gained by the system upon relaxation from q_R to q_P after the transfer is completed.

Following a classical treatment of vibrational motion, the relationship between E_{act}, ΔE and E_λ can be derived analytically from geometrical arguments, considering harmonic potentials. A more general quantum mechanical approach requires instead the distinction between high-temperature and low-temperature case.

The high-temperature case is defined for $k_B T \gg \hbar\omega_\alpha$ for all coordinates of the system, being ω_α the vibrational frequency of coordinate α. Under this assumption the eT rate is given by the Marcus equation

$$k_{eT} = |V_{RP}|^2 \sqrt{\frac{\pi}{\hbar^2 k_B T E_\lambda}} \exp\left(-\frac{(\Delta E + E_\lambda)^2}{4 E_\lambda k_B T}\right) \tag{3.25}$$

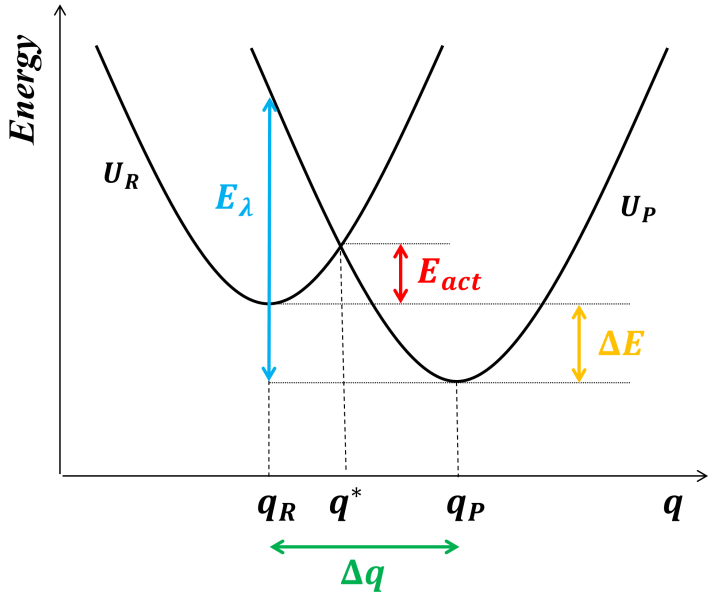

Figure 3.6: Potential energy surfaces of reactants and products and definition of the activation energy E_{act}, the driving force ΔE and the reorganization energy E_λ.

which has the form of the equation for a thermally-activated reaction (Eq. 3.23). Three unknown quantities enter the Marcus equation: V_{RP} and ΔE, related to the chemical structure of $\mathbb{D}$ and $\mathbb{A}$ and E_λ, mainly dependent on the medium. Usually a fit of experimental data is performed through an Arrhenius plot, i.e. plotting $\log k_{eT}$ versus $1/T$. Otherwise, ΔE and E_λ can be obtained from indirect methods. When many vibrational modes are coupled to eT, the total driving force of the process can be obtained as the energy difference between reactants and products, which can be gathered from thermodynamic measurements. At the same time, the total reorganization energy can be retrieved summing up the individual quantities for all the coupled modes: $E_\lambda = \sum_\alpha \frac{1}{2}\omega_\alpha^2(\Delta q_\alpha)^2$. In the solid state, the terms ω_α and Δq_α can be accessed from the resolution of the crystallographic geometry or, more conveniently, they can be extracted from resonant Raman measurements, which provide direct information on the modes coupled to eT.

Supposing fixed values of V_{RP} and E_λ, the dependence of the eT rate upon ΔE is shown in Figure 3.7. For $|\Delta E| < E_\lambda$ we are in the so-called

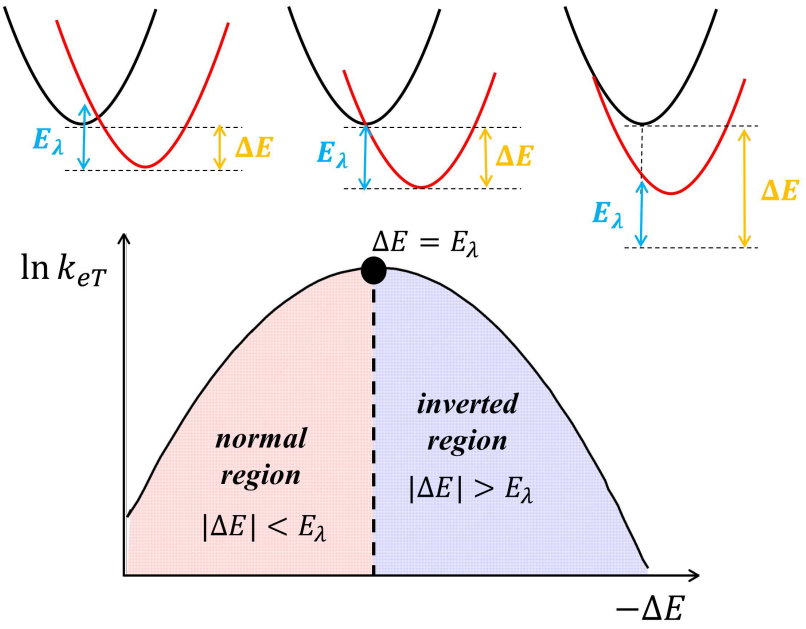

Figure 3.7: Top: sketch of the PES of reactants (black curves) and products (red curves) in different regimes for fixed E_λ: normal region (left), activationless case (centre) and inverted region (right). Bottom: plot of $\ln k_{eT}$ versus $-\Delta E$.

normal Marcus region. In this region the intersection point between the curve of the reactants and the curve of the products, q^*, occurs at the right side of q_R and the eT reaction requires the crossing of an energy barrier. An increase of ΔE shifts q^* to the left, reaching $q* = q_R$ for $|\Delta E| = E_\lambda$. This point corresponds to the activationless case, for which the energy barrier vanishes and the eT rate becomes independent of temperature. A further increase of $|\Delta E|$ brings the system in the inverted Marcus region, where the activation energy increases again.

It follows that the eT rate increases in the normal region as $|\Delta E|$ (and also E_{act}) is increased, it reaches a maximum at $\Delta E = E_\lambda$, when $E_{act} = 0$, and decreases again in the inverted region with increasing $|\Delta E|$ (E_{act}) (Figure 3.7, bottom).

When $k_B T \ll \hbar\omega_\alpha$ for all the coupled modes, we are in the low-temperature regime, characterized by a different mechanism. In this case the formal treatment of eT requires the quantum mechanical description of vibrational motion. It can be demonstrated that the expression for the eT rate in this

regime is

$$k_{eT} = \frac{2\pi}{\hbar^2\omega}|V_{RP}|^2|\left\langle \chi_{R_0} \,|\, \chi_{Pn_{res}} \right\rangle|^2 \tag{3.26}$$

where $|\chi_{R_0}\rangle$ is the vibrational ground state of the reactants and $|\chi_{Pn_{res}}\rangle$ is the vibrational state of the products which is degenerate with the vibrational ground state of the reactants. In the low-temperature regime, the rate of the transfer is independent of temperature, as it does not involves thermal activation. Indeed, the only requirement for the process is a finite overlap between the initial vibrational wavefunction of the reagents and the final wavefunction of the products. In other words, the eT transfer is due to nuclear tunnelling and does not require the crossing of a barrier. This process becomes competitive with thermally activated eT in the Marcus inverted region, where the overlap becomes sizeable, while it is the only mechanism working at low temperature where there is not enough energy for thermal activation.

A more general case is the so-called mixed quantum-classical case, where the low-frequency modes, for example those of the solvent, are in the high-temperature limit while the others are in the low-temperature limit. The generalization of the Marcus formula accounting for both regimes reads as follows:

$$k_{eT} = |V_{RP}|^2\sqrt{\frac{\pi}{\hbar^2 k_B T E_\lambda}}\sum_n |\left\langle \chi_{R_0} \,|\, \chi_{P_n} \right\rangle|^2 \exp\left[-\frac{(\Delta E + n\hbar\omega + E_\lambda)^2}{4E_\lambda k_B T}\right] \tag{3.27}$$

where n runs over all the vibrational states of the products. At low temperature the dominant effect is nuclear tunnelling, while as the temperature is increased, thermal activation becomes more important and dominates at high temperatures.

Another distinction between eT mechanisms is based on the role played by the bridge connecting the $\mathbb{D}$ and $\mathbb{A}$ entities. eT is called *through space* transfer if the bridge is not involved in the process. In this case short distances (typically less than 20 Å) are required in order to guarantee orbital overlap. Conversely, in the so-called *through bond* or *bridge assisted* eT reactions, the bridge B is actively involved in the transfer making it possible at longer distances. A typical bridge-assisted reaction can be represented as follows:

$$\mathbb{D}^- B\mathbb{A} \rightarrow \mathbb{D}B^-\mathbb{A} \rightarrow \mathbb{D}B\mathbb{A}^- \tag{3.28}$$

There are at least two ways in which the bridging unit can assist eT. If the energy levels of the bridge are well separated from those of the active units, eT proceeds through a *super-exchange* mechanism. The states of the bridge act as a perturbation to the energy levels of donor and acceptor, and the initial state of the system becomes delocalized over the bridge states, modifying the $\mathbb{D} - \mathbb{A}$ coupling.

On the opposite, if the bridge states are almost resonant with the LUMOs of $\mathbb{D}$ and $\mathbb{A}$, ET follows the so-called *hopping* or sequential mechanism, in which the electron moves stepwise from the donor to the acceptor through the bridge states, residing temporarily on the bridge.

3.4 Energy transfer in BODIPY-decorated calixarenes

Simplified systems acting as artificial antennae allow to study the factors affecting the first steps of the photosynthetic pathway, namely light harvesting and excitation energy transfer. The model bichromophoric systems investigated in this Thesis were obtained by covalent linkage of two suitable EET partners, an energy donor and an energy acceptor, at the 1,3-distal positions of the upper rim of a calix[4]arene scaffold.

Boron-dipyrromethene (hereafter BODIPY) dyes are a family of fluorescent dyes containing the 4,4-difluoro-4-bora-3a,4a-diaza-*s*-indacene unit, characterized by high chemical stability and interesting optical properties such as sharp and intense absorption and emission bands whose position can be tuned by appropriate chemical functionalization [401, 402]. The high fluorescence quantum yield and the possibility of tailoring their spectral properties makes BODIPY dyes ideal candidates as active units in model systems for EET [357].

We considered two couples of BODIPY dyes specifically designed to act as energy donor-energy acceptor pairs. The first couple was linked to a calix[4]arene in the cone conformation through flexible spacers, ensuring a residual mobility of the system [387]. Conversely, for the second EET pair we devised a more constrained arrangement through the choice of rigid linkers, and we also compared the conformationally flexible cone calix[4]arene scaffold with the more rigid 1,3-alternated isomer to assess the effect of

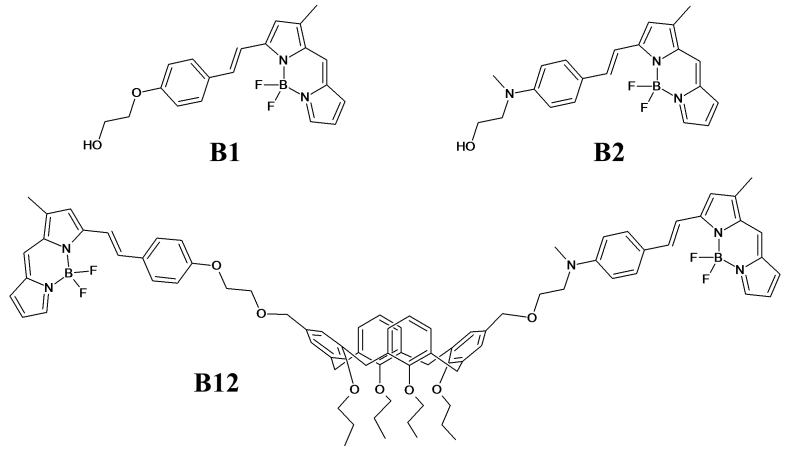

Figure 3.8: First couple of BODIPY dyes. Molecular structure of the dyad **B12** and reference compounds **B1** and **B2**.

the calix conformation on the interchromophoric interactions and EET efficiency.

3.4.1 First couple of BODIPY dyes

Dyes **B1** and **B2** (Figure 3.8) belong to the family of 3-stiryl BODIPYs [401,403]. Substitution with an electron donor group at the *p*-position of the phenyl ring increases π-conjugation, red-shifting the absorption and emission bands compared to unsubstituted dyes, at wavelengths longer than 500 nm [403,404]. The electron-donating strength of the substituent largely affects the optical properties of the dyes, differentiating their spectroscopic behaviour. **B1** and **B2** meet the basic requirements for EET [401] and were selected as the first EET pair in our study, also acting as reference dyes in the spectroscopic analysis.

The target dyad **B12** was obtained anchoring the selected fluorophores at the distal positions of the upper rim of a calix[4]arene in the cone conformation [387]. A ^{1}H NMR study of **B12** in solution revealed that, irrespectively of the solvent, the system possess a C_{4v} symmetry, resulting from fast interconversion between two opposite flattened cone conformations characterized by similar stability [379]. Their stability is probably the result of a balance between steric repulsion between the substituents, that should favour an

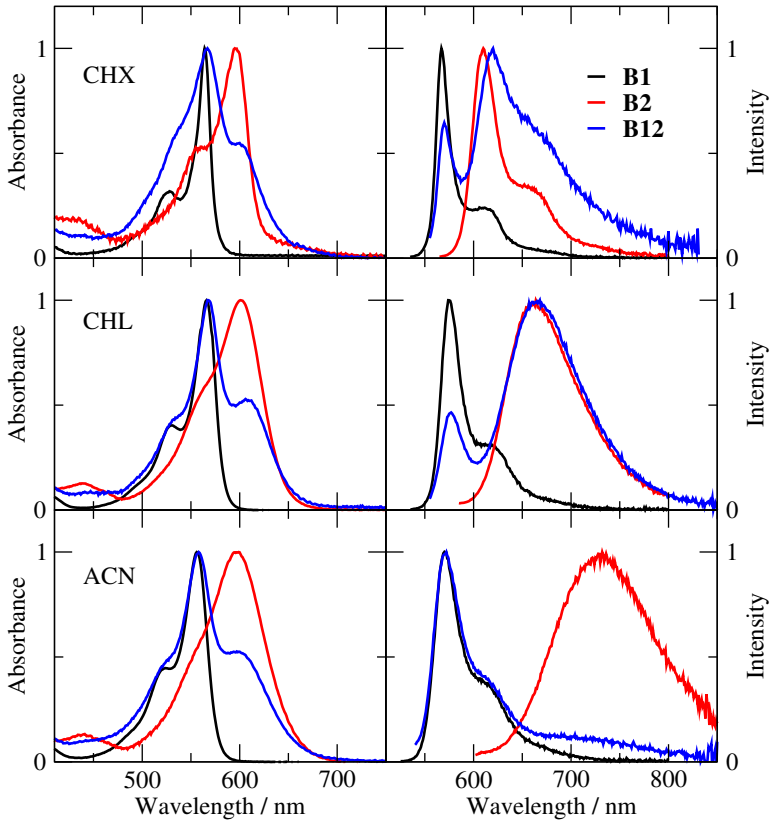

Figure 3.9: Normalized absorption (left) and emission (right) spectra of **B12** and the reference dyes in solvents of different polarity: cyclohexane (CHX), chloroform (CHL) and acetonitrile (ACN). For the dyad, the excitation wavelengths were 550 nm in CHX and CHL, 535 nm in ACN.

open flattened cone conformation, and weak $\pi - \pi$ interactions between the BODIPY units, which should stabilize a closed flattened cone conformation. This hypothesis was validated by theoretical analysis (see below).

Steady-state spectroscopy

The bichromophoric system **B12** and reference dyes were characterized in solvents of different polarity, namely cyclohexane, chloroform and acetonitrile (Figure 3.9 and Table 3.1).

B1 is characterized by sharp absorption and emission peaks, which are almost insensitive to solvent polarity. Its emission quantum yield, approaching unity in cyclohexane, remains high ($> 80\%$) in more polar solvents.

Table 3.1: Spectroscopic properties of **B1**, **B2** and **B12** in different solvents (CHX: cyclohexane, CHL: chloroform, ACN: acetonitrile): absorption and emission maxima (λ_{abs}^{max} and λ_{em}^{max}), fluorescence quantum yield (QY) and emission lifetime (τ). The standard for fluorescence quantum yield measurements was fluorescein in NaOH(aq) 0.1 M (QY = 90%).

Solvent	Compound	λ_{abs}^{max}/nm	λ_{em}^{max}/nm	QY%[λ_{exc}/nm]	τ/ns [λ_{em}/nm]
CHX	**B1**	564	567	100 [530]	3.92
	B2	595	610	73 [560]	3.34
	B12	567	619	20 [535]; 21 [550]	3.55 [570]
CHL	**B1**	566	574	91 [530]	3.82
	B2	601	661	55 [565]	3.05
	B12	568	664	32 [530]; 32 [550]	3.27 [575]
ACN	**B1**	556	570	87 [520]	3.9
	B2	597	730	< 1 [560]	-
	B12	558	571	8 [527]; 7 [535]	3.12 [610]

Absorption of **B2** is red-shifted by more than 30 nm compared to **B1** and is characterized by broad bands, which are marginally affected by solvent polarity. Conversely, emission of **B2** is strongly solvatochromic and moves from $\lambda \approx 600$ nm in cyclohexane to $\lambda > 730$ nm in acetonitrile. Moreover, as the solvent polarity increases, the emission band broadens and looses intensity. This behaviour suggests that the ground and excited states of **B1** are non-polar (or slightly polar), while fluorescence of **B2** comes from a polar state.

Emission of **B1** and absorption of **B2** occur within the same spectral window, guaranteeing good spectral overlap over all the solvent polarity range (Figure 3.10). This should grant for efficient EET from **B1**, acting as the energy donor, to **B2**, acting as the energy acceptor, in all the solvents considered.

As for the reference dyes, absorption of **B12** is marginally affected by solvent polarity. On the opposite, its emission spectra are solvent-dependent. For excitation on the short-wavelength side of the absorption spectrum, in the region between 500 and 550 nm, emission of **B12** features two maxima, corresponding to the emission maxima of **B1** and **B2**. Indeed, while the short-wavelength maximum is unaffected by solvent polarity, the long-

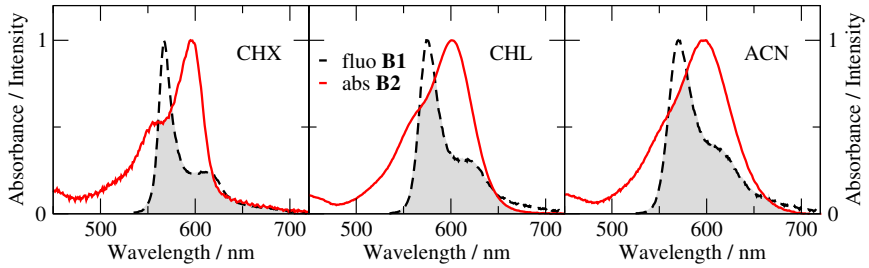

Figure 3.10: Emission spectra of **B1** and absorption spectra of **B2** in different solvents (CHX: cyclohexane, CHL: chloroform, ACN: acetonitrile). The greyed area indicates the spectral overlap. The overlap between the normalized spectra expressed in wavenumbers (Eq. 3.30) amounts to 244×10^{-6} cm in CHX, 281×10^{-6} cm in CHL and 262×10^{-6} cm in ACN.

wavelength maximum moves to the red from cyclohexane to chloroform, and vanishes in acetonitrile due to the small quantum yield of **B2** in this solvent compared to **B1**. Fluorescence quantum yield of the dyad is considerably lower than the quantum yield of the isolated chromophores, suggesting the activation of new decay paths among which energy transfer.

Unfortunately, the amount of synthesized compound did not allow for the measurement of molar extinction coefficients. Therefore, in order to verify if absorption spectra of the bichromophoric system correspond to the sum of the absorption spectra of the isolated chromophores, we resorted to a fitting procedure (Figure 3.11, top panels). Absorption spectra of **B12** in chloroform and acetonitrile were recovered as the sum of the absorption spectra of **B1** and **B2** weighted for appropriate coefficients. Conversely, the experimental absorption spectrum of **B12** in cyclohexane is broader compared to the weighted sum of the reference spectra. The broadening could be ascribed to conformational disorder, which has a larger effect in non-polar solvents, where the bands are narrower. Overall, the possibility of retrieving the spectrum of the dyad roughly as the sum of the absorption spectra of its constituting units suggests that the electronic coupling between the EET partners is weak and we are in the weak coupling regime.

The efficiency of EET in **B12** was estimated from the evaluation of the donor quenching (Method II, Eq. 3.16). Because of the large overlap between absorption spectra of **B1** and **B2**, it is not possible to selectively excite the donor into the dyad. Therefore, additional data processing is required prior

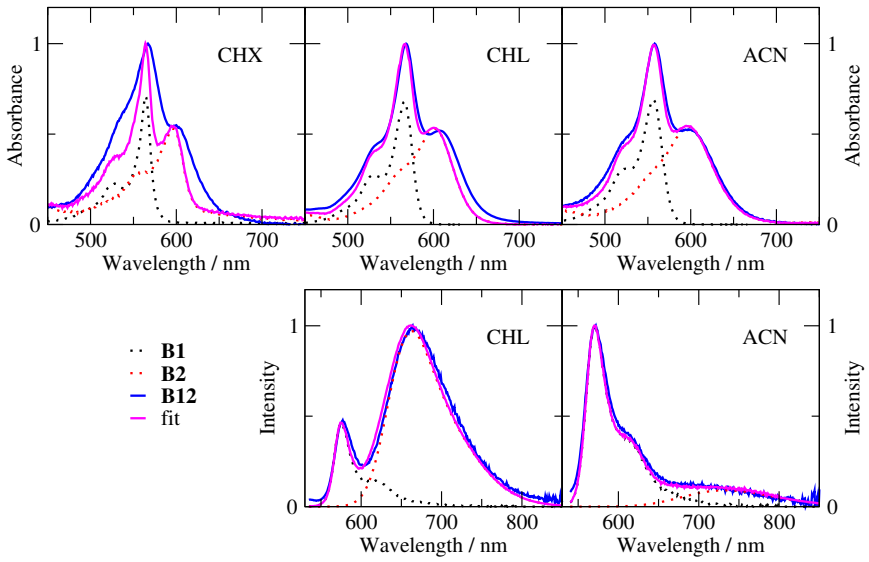

Figure 3.11: Experimental spectra of **B12** (blue lines) and best fit (magenta lines) as the weighted sum of the corresponding spectra of references **B1** and **B2** (black and red dotted lines respectively). Top panels: absorption spectra. Bottom panels: emission spectra. Emission spectra of **B12** in chloroform (CHL) and acetonitrile (ACN) were collected for excitation at 530 and 535 nm respectively.

to apply Eq. 3.16, in order to extract the quantum yield of the donor in presence of the acceptor ($\phi_{\mathcal{D}(\mathcal{A})}$). The results of the fit of the absorption spectra in Figure 3.11 were rescaled to get the experimental value of absorbance at the excitation wavelength. Then, the contribution of the donor to the total absorption of the dyad was retrieved from the coefficients of the fit and was used in the calculation of quantum yield. Similarly, a fitting procedure on the emission spectra (Figure 3.11, bottom panels) allowed for the separation of the donor contribution to the emission intensity of **B12**, which was employed for the estimate of $\phi_{\mathcal{D}(\mathcal{A})}$. Quantum yields were estimated in chloroform and acetonitrile only, since in cyclohexane we did not obtain a satisfactory fit of the absorption spectrum. The procedure was applied for different excitation wavelengths, obtaining consistent results (Table 3.2).

The residual quantum yield of the donor in **B12** amounts to less than 10%, indicating a strong quenching effect. Indeed, EET efficiencies calculated through Eq. 3.16 are high ($\phi_{EET} \approx 90\%$) and are unaffected by solvent polarity.

Table 3.2: Energy transfer in **B12** estimated from donor quenching in chloroform (CHL) and acetonitrile (ACN) at two different excitation wavelengths. $\phi_{\mathcal{D}}$: quantum yield of isolated donor (**B1**), λ_{exc}: excitation wavelength, $\phi_{\mathcal{D}(\mathcal{A})}$: quantum yield of the donor in presence of the acceptor (i.e. in **B12**) estimated from a fitting procedure, ϕ_{EET}: estimated EET efficiency.

Solvent	$\phi_{\mathcal{D}}$	λ_{exc}/nm	$\phi_{\mathcal{D}(\mathcal{A})}$	ϕ_{EET}
CHL	0.91	530	0.08	0.91
		550	0.08	0.91
ACN	0.87	535	0.09	0.89
		527	0.09	0.89

Fluorescence anisotropy experiments provide information about the relative orientation of absorption and emission dipole moments of fluorophores (see also Appendix A). In presence of EET, absorption and emission come from different fluorophores, so that anisotropy could reveal information on the relative orientation between them.

Fluorescence excitation and emission anisotropies of the dyad, as well of the reference compounds, were measured in a glassy 2-methyltetrahydrofuran dilute solution undercooled at 77 K (Figure 3.12). Under these conditions absorption and emission bandshapes are more resolved compared to room temperature spectra because of the reduction of thermal disorder (inhomogeneous broadening).

Anisotropy of **B1** and **B2** is trivial. For both of them we obtained $r \approx 0.4$ inside the main absorption/emission band, as expected for parallel absorption and emission dipole moments. Indeed, the very same state responsible for intense absorption in the visible range is also responsible for emission. Excitation anisotropy of **B2** decreases to the limiting -0.2 value in the UV, corresponding to less intense transitions polarized perpendicularly to the $S_0 \rightarrow S_1$ transition.

Fluorescence excitation anisotropy of **B12** was collected at $\lambda_{em} = 670$ nm, i.e. collecting emission from the sole acceptor. In the 600-650 nm region, where only the acceptor absorbs, anisotropy is flat and close to the maximum 0.4 value, indeed the very same state is involved in absorption and emission. Conversely, anisotropy decreases abruptly to $r \approx 0.05 - 0.1$ at $\lambda \approx 575$ nm, corresponding to the absorption maximum of the donor, and

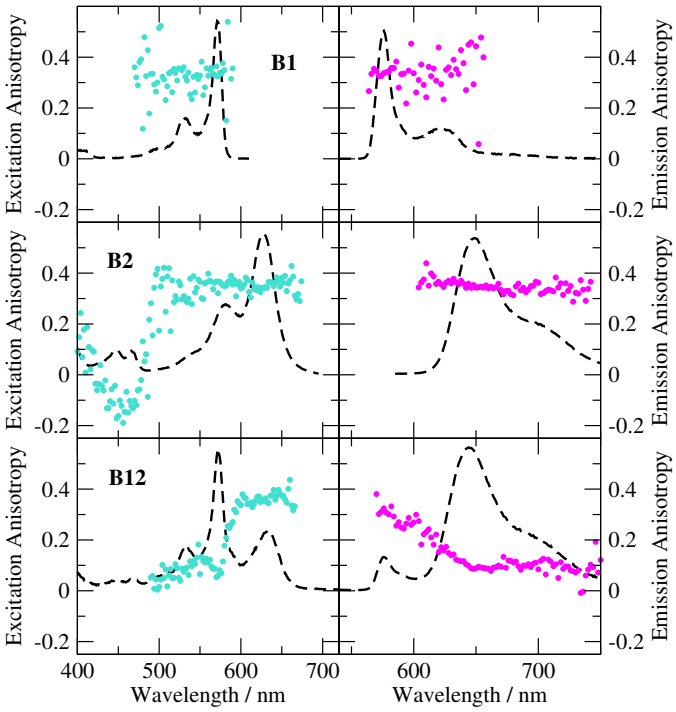

Figure 3.12: Fluorescence excitation (left panels) and emission (right panels) anisotropy in frozen 2-methyltetrahydrofuran at 77 K (dots). Corresponding excitation and emission spectra measured under the same experimental conditions (dashed lines) are reported as a guide to the eye. Excitation anisotropy of **B12** was collected at $\lambda_{em} = 670$ nm, emission anisotropy at $\lambda_{exc} = 565$ nm.

remains flat across the whole donor band. This result suggests that at low temperature the chromophores are arranged to form an average angle of $45-50^{\circ}$ (or an angle with the same squared cosine) between the absorption dipole moment of the energy donor and the emission dipole of the energy acceptor. An alternative hypothesis could be the presence of a distribution of configuration with similar energy giving an average anisotropy close to 0. Emission anisotropy, collected for excitation at the absorption maximum of the donor, is consistent with excitation anisotropy and suggests similar considerations.

Transient absorption measurements

To gain more insights into the dynamics of EET in **B12**, a transient absorption study was performed in collaboration with Dr. Mariangela Di Donato and coworkers at LENS (European Laboratory for Non-Linear Spectroscopy), Florence, Italy. Transient absorption measurements with subpicosecond resolution were performed in all the investigated solvents for the dyad (Figure 3.13) and for reference chromophores (not shown). Experimental kinetic traces were processed by a global analysis procedure, consisting in the simultaneous fit of the data at all wavelengths with combinations of exponential functions. The output of the procedure are the time constants of the excited-state processes and the corresponding spectral components, called Evolution Associated Difference Spectra (EADS) [405, 406].

A satisfactory fit of experimental data on **B12** was achieved with four kinetic components in acetonitrile and three kinetic components in the other solvents. Corresponding EADS are reported in the left panels of Figure 3.13. Selective excitation of the donor moiety is impossible because of the large overlap between the absorption spectra of donor and acceptor. Thus, irrespective of the solvent, the dyad was excited at $\lambda = 520$ nm, where the absorbance of the donor dominates over the absorbance of the acceptor. Nevertheless, direct excitation of the acceptor cannot be avoided, as seen from the presence of the signals of both dyes in the transient spectra at early times. Indeed, the two negative bands found in all solvents immediately after excitation peaking at $\lambda \approx 560$ nm and $\lambda \approx 620$ nm can be assigned to bleaching/stimulated emission of the donor and acceptor, respectively.

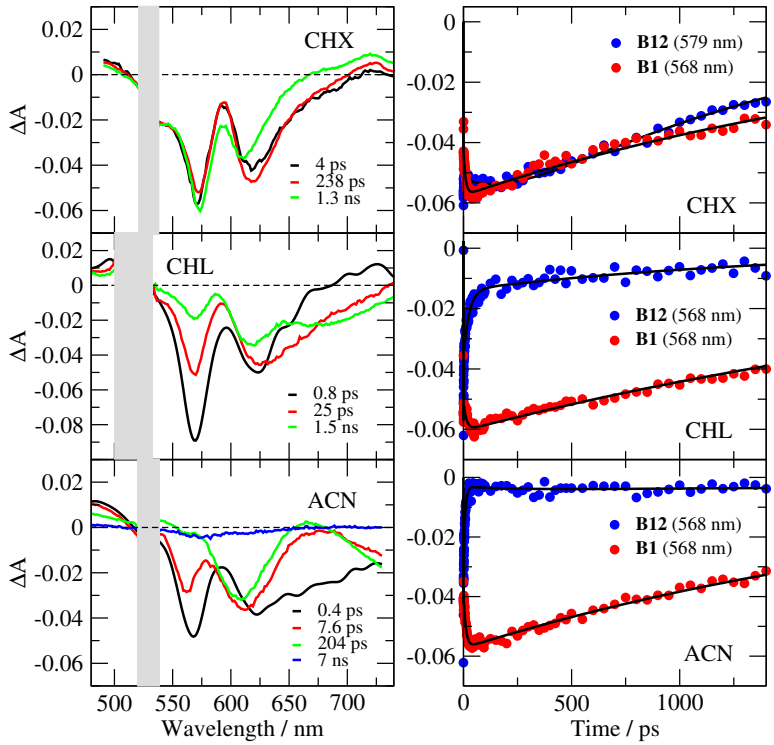

Figure 3.13: Transient absorption data collected for **B12** in different solvents (CHX: cyclohexane, CHL: chloroform, ACN: acetonitrile). Left panels: EADS retrieved from global analysis of transient absorption spectra ($\lambda_{exc} = 520$ nm). Right panels: kinetic traces recorded at the maximum of the bleaching/stimulated absorption band of the donor in **B12** (blue dots) and isolated donor **B1** (red dots). Wavelengths are reported in the legends. Black traces indicate the fits obtained from global analysis.

The absence of transient signals of BODIPY ions allows to safely exclude the occurrence of electron transfer in **B12** [407, 408].

In chloroform and acetonitrile, the signal of the donor undergoes a rapid decrease, suggesting fast and efficient energy transfer with multi-exponential kinetics. In acetonitrile, almost one half of the donor signal recovers in less than 1 ps, while the residual part decays within 7.6 ps. Overall, the transient signal of the dyad decays on a 200 ps timescale and even if a fourth ns-lifetime (7 ns) improves the quality of the fit, only a small residual signal is present on this long timescale. This fast decay is in agreement with the short lifetime measured in this solvent.

Also in chloroform, global analysis suggests a multi-exponential EET with a sub-picosecond component, an intermediate component (25 ps) and a longer (ns) lifetime. The overall signal recovers almost completely after 1.5 ns. The residual donor emission on the nanosecond timescale, amounting to approximately 15% of the initial value, suggests that energy transfer is highly efficient but not quantitative, in agreement with steady-state data.

A different scenario was found in non polar cyclohexane. In this solvent, a less pronounced time evolution of the transient signals was observed compared to the other more polar solvents, and a significant contribution of the donor survives on a long timescale. A slight decrease of the donor band and the concomitant increase of the acceptor band occurring within the first 4 ps suggest the occurrence of energy transfer at early times. However, in the following 238 ps the donor band increases again and the acceptor band looses intensity, indicating the concomitant presence of backtransfer.

More information on the transfer rates can be gained from the comparison between the decay of the donor band in **B12** and the decay of the donor alone (**B1**, Figure 3.13, right panels). In polar solvents (chloroform and acetonitrile) the donor signal in the dyad decays faster with respect to the isolated molecule, indicating fast EET. Conversely, in cyclohexane, the decay traces of the donor in presence and in absence of acceptor are comparable, suggesting a different process.

In order to verify the hypothesis of backward energy transfer in cyclohexane, transient absorption measurements were repeated for excitation at $\lambda = 600$ nm, with the aim of achieving a preferential exitation of the acceptor. Corresponding EADS obtained from global analysis (Figure 3.14) show

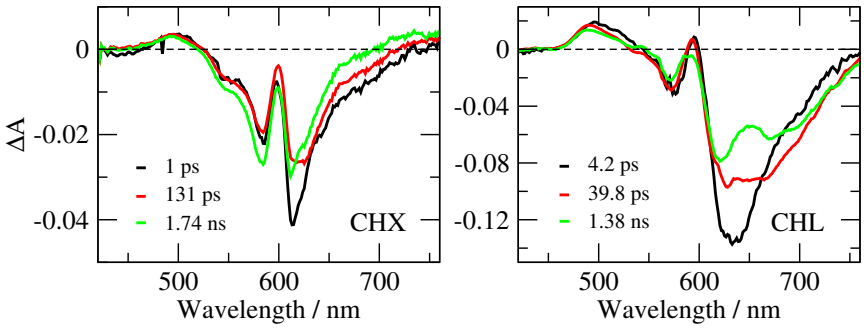

Figure 3.14: EADS obtained for **B12** upon excitation at $\lambda = 600$ nm in cyclohexane (CHX) and chloroform (CHL).

however the characteristic signals of both units at early times, indicating a partial direct excitation of the donor. On a short timescale ($\sim$ 1 ps) both signals of donor and acceptor loose intensity, however, at $\sim$ 130 ps, the band of the donor increases again, signalling energy transfer from **B2** to **B1**. The observation of a significant fraction of donor signals on the ns-timescale and the overall decrease of EET rate can be explained by the instauration of an equilibrium between forward and backward processes.

The aforementioned increase of the donor band is not taking place in chloroform, suggesting that backtransfer is negligible in this solvent. Indeed, the overlap between emission of **B2** and absorption of **B1** in cyclohexane, a requirement for the occurrence of backtransfer, is more than one order of magnitude larger compared to chloroform (Figure 3.15). However, in cyclohexane, the overlap relevant to backtransfer is approximately 60 times smaller than the overlap relevant to the direct transfer, explaining the slower kinetics of backtransfer compared to direct EET emerging from transient absorption data.

The ultrafast kinetic component obtained from global analysis (4 ps, 0.8 ps and 0.4 ps in cyclohexane, chloroform and acetonitrile respectively) can be attributed to vibrational and solvent relaxation, while the intermediate kinetic constant (238 ps, 25 ps and 7.5 ps in the three solvents) correlates with energy transfer. The high value obtained in cyclohexane can be explained with the concomitant occurrence of backward energy transfer and, because of that, it is not directly related to the EET rate. Finally, the ns-component (respectively 1.3 ns and 2.1 ns in cyclohexane and chlo-

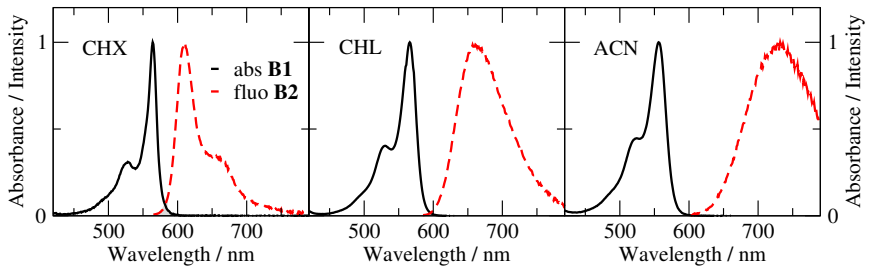

Figure 3.15: Emission spectra of **B2** and absorption spectra of **B1** in different solvents (CHX: cyclohexane, CHL: chloroform, ACN: acetonitrile). The greyed area indicates the spectral overlap. The overlap between the normalized spectra expressed in wavenumbers (Eq. 3.30) amounts to 4.14×10^{-6} cm in CHX, 5.72×10^{-7} cm in CHL and is vanishing in ACN.

roform) as well as the 204 ps / 7 ns components retrieved in acetonitrile, are related to the excited-state lifetime of the fluorophore and are in reasonable agreement with emission lifetime values measured in the various solvents.

Theoretical study

A complementary insight into the photophysics of **B12** was achieved through theoretical modelling, performed in collaboration with Prof. Chiara Cappelli and coworkers (Scuola Normale Superiore, Pisa, Italy).

Absorption and emission spectra of reference dyes, computed in acetonitrile at TDDFT level (CAM-B3LYP/6-31+G), indicated closely spaced transitions at 2.57 eV (482 nm) with oscillator strength 0.95 for **B1** and at 2.50 eV (496 nm) with oscillator strength 1.39 for **B2**.

In principle, many conformers of **B12** may exist in solution because of the flexibility of the calix scaffold. Only two of them were selected for theoretical investigation, corresponding to the most representative conformations. Calix[4]arenes substituted at the distal positions of the upper rim can assume two *flattened cone* conformations (Figure 3.16 (a)) [380]: an open flattened cone conformation, which minimizes steric repulsion between the substituents and is preferred in the absence of specific attractive interchromophoric interactions, and a closed flattened cone conformation, which is favoured by the presence of attractive interactions between the substituents, in our case the $\pi-\pi$ stacking between the BODIPY units.

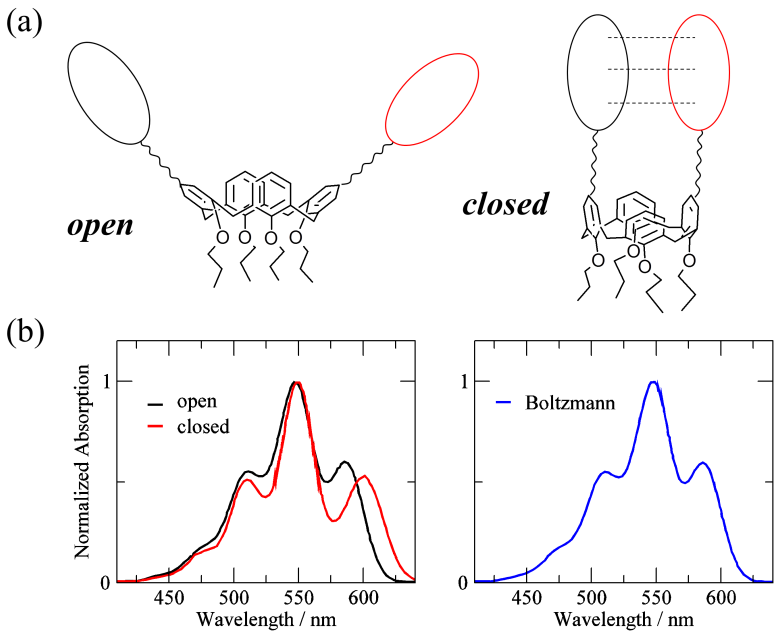

Figure 3.16: Theoretical modelling of bichromophore **B12**. (a) Sketch of the *open* and *closed* flattened cone conformations of a 1,3-substituted calix[4]arene considered in the theoretical study. (b) Left panel: absorption spectra of the two conformations of **B12** in acetonitrile obtained summing up the contributions of the transitions towards S_1 and S_2. Right panel: Boltzmann-weighted spectrum.

From the geometry optimization of the two conformers of **B12** it was found that the closed flattened cone conformer is the most stable (by ~ 13 kcal mol^{-1} only in the gas phase, while in solution the open conformer is favoured, even if the energy difference between the isomers amount to less than 3 kcal mol^{-1}. Indeed, an average conformation of the calix emerged from ^{1}H NMR studies, indicating similar stability. The absorption spectrum of the bichromophoric system computed in acetonitrile with the Vertical Gradient approach [409–411] is shown in Figure 3.16 (b). The energy of the S_1 state of **B12** coincides with the energy of the S_1 state of **B2** (2.50 eV for the open and 2.44 eV for the closed conformation), while the S_2 state of **B12** is close to the energy of the first excited state of **B1** (2.63 eV for the closed and 2.58 eV for the open conformation respectively). It follows that the absorption spectrum of **B12** is roughly the sum of the absorption spectra of **B1** and **B2**, in agreement with experimental findings. Indeed, the Boltzmann-weighted computed spectrum compares well with the experimental spectrum of the dyad. Similar results were obtained in the other solvents (not shown).

The rate of EET was calculated in cyclohexane and acetonitrile according to the following [412]:

$$k_{EET} = \frac{V_{\mathcal{DA}}^2}{\hbar^2 c} J'_{\mathcal{DA}} \tag{3.29}$$

where $V_{\mathcal{DA}}$ is the electronic coupling energy between the transition density of the donor and acceptor, obtained dividing the bichromophoric system in two fragments, one constituted by the donor and the calix scaffold and the other constituted by the acceptor alone, or the other way around [413]. Calculated values were $V_{\mathcal{DA}} = 0.942$ (0.323) cm^{-1} for the open conformer in acetonitrile (cyclohexane) and $V_{\mathcal{DA}} = 217.8$ (186.48) cm^{-1} for the closed conformer. Moreover, in Eq. 3.29, $\hbar$ is the Planck constant divided by 2π, c is the speed of light in vacuum and $J'_{\mathcal{DA}}$ is defined as

$$J'_{\mathcal{DA}} = \int_0^\infty A_{\mathcal{A}}(\tilde{\nu}) F_{\mathcal{D}}(\tilde{\nu}) d\tilde{\nu} \tag{3.30}$$

being $A_{\mathcal{A}}(\tilde{\nu})$ and $F_{\mathcal{D}}(\tilde{\nu})$ the absorption spectrum of the energy acceptor (**B2**) and the emission spectrum of the energy donor (**B1**) both normalized to unit area. Relevant $J'_{\mathcal{DA}}$ integrals were extracted from experiment (see captions of Figures 3.10 and 3.15).

In acetonitrile values of $k_{EET}^{-1} = 6.80 \times 10^{-2}$ ps and $k_{EET}^{-1} = 3.63 \times 10^{3}$ ps were obtained for the closed and open conformer respectively. Indeed, the transfer is faster where the interchromophoric distance is shorter, i.e. in the closed conformation. The Boltzmann-weighted k_{EET}^{-1} derived in acetonitrile amounts to 1.7 ps and compares favourably with the experimental characteristic time of EET in this solvent (7.5 ps). Conversely, the Boltzmann-weighted lifetime calculated in cyclohexane cannot be directly compared with experiment, since the experimental value is influenced by concomitant backtransfer, which slows down the kinetics of EET. The backtransfer rate could be calculated with the same $V_{\mathcal{DA}}$ and the appropriate value of $J'_{\mathcal{DA}}$ obtained exchanging the roles of **B1** and **B2**. The Boltzmann-weighted k_{EET}^{-1} related to the backward EET in cyclohexane was 144 ps, in excellent agreement with the corresponding experimental value (130 ps).

3.4.2 Second couple of BODIPY dyes

Also the second couple of dyes selected for EET studies, **B3** and **B4** (Figure 3.17), belong to the 3-stiryl BODIPY family. However, at difference with the previously investigated EET pair, they are substituted at the *meso* position with an aromatic ring, which will act as the anchoring site in the dyads [414]. Because of the steric hindrance caused by the methyl groups on the BODIPY unit, the phenyl ring lies almost perpendicularly to the plane of the indacene, interrupting the conjugation [415]. Indeed, spectroscopic properties of *meso*-substituted dyes **B3** and **B4** are very similar to those of unsubstituted **B1** and **B2**, respectively (see below).

The two dyes are linked at the 1,3-distal positions of the calix[4]arene scaffold through a triple bond, ensuring a better rigidity of the spacers, compared to the previous structure. In this case, two conformations of the calixarene were selected: the more flexible cone conformation (**B34c**) and the 1,3-alternated conformation (**B34a**) [416], which should induce a different interchromophoric distance.

Steady-state spectroscopy

Absorption and emission spectra of the target compounds at room temperature were recorded in solvents of different polarity: toluene, dichloromethane

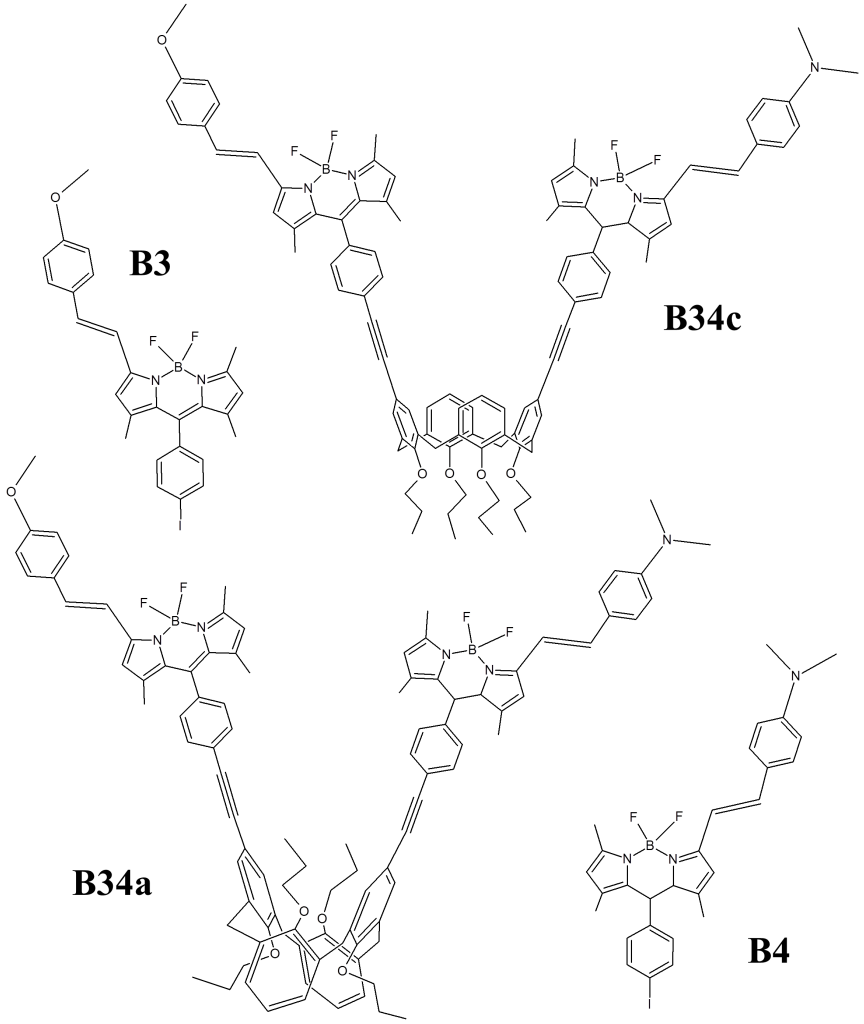

Figure 3.17: Second couple of BODIPY dyes. Molecular structure of dyads **B34c** and **B34a** and reference dyes **B3** and **B4**.

and acetonitrile (Figure 3.18 and Table 3.3). Both reference compounds are characterized by narrow absorption bands in the green-orange region of the visible spectrum, with high molar extinction coefficients ($\varepsilon \approx 1.0 - 1.5 \times 10^5$ mol^{-1} L cm^{-1}). Other less intense transitions are found in the UV, below 450 nm. Solvent effects on the peak position are marginal and only inhomogeneous broadening takes place upon increasing solvent polarity. **B3** features sharp emission bands peaking at $\lambda < 700$ nm, small Stokes shift and high quantum yields approaching unit in non-polar environments and is barely affected by the solvent. Conversely, **B4** is strongly solvatofluorochromic, and the emission maximum is shifted from $\lambda \approx 650$ nm in toluene to $\lambda \approx 730$ nm in acetonitrile, with concomitant broadening of the emission band. Also its fluorescence quantum yield is highly sensitive to solvent polarity and, starting from $\sim$ 85% in toluene, it drops to less than 10% in acetonitrile. Both dyes are characterized by monoexponential fluorescence decays with lifetimes in the range $3.5 - 4.0$ ns for **B3** and decreasing from 3.42 ns to less than 1 ns according to the solvent for **B4**.

Spectral features of the dyads are reminiscent of those of the reference compounds, whose contributions can be easily recognized both in absorption and emission. The absorption maximum at $\lambda \approx 570$ nm observed for **B34c** and **B34a** corresponds to the maximum of **B3** absorption, while the long-wavelength shoulder at $\lambda \approx 610$ nm corresponds to the maximum absorption of **B4**. The poor solubility of the dyads in acetonitrile did not allow for a reliable estimate of the molar extinction coefficient in this solvent. In toluene and dichloromethane the absorption spectra of the bichromophoric systems are roughly the sum of the absorption spectra of the reference dyes, suggesting weak interchromophoric interactions. Indeed, absorption spectra of **B34a** and **B34c** are almost superimposable in toluene and dichloromethane, while in acetonitrile only a slight decrease of the **B4** maximum was found in **B34a** compared to **B34c**.

Emission spectra of the bichromophores feature two bands. The first one, at shorter wavelength and almost insensitive to solvent polarity, corresponds to **B3** emission, while the one at longer wavelengths and strongly solvent-dependent is related to emission of **B4**. Comparison between the emission spectra of **B34a** and **B34c** collected at the same excitation wavelength reveals substantial differences in terms of the ratio between the two emission

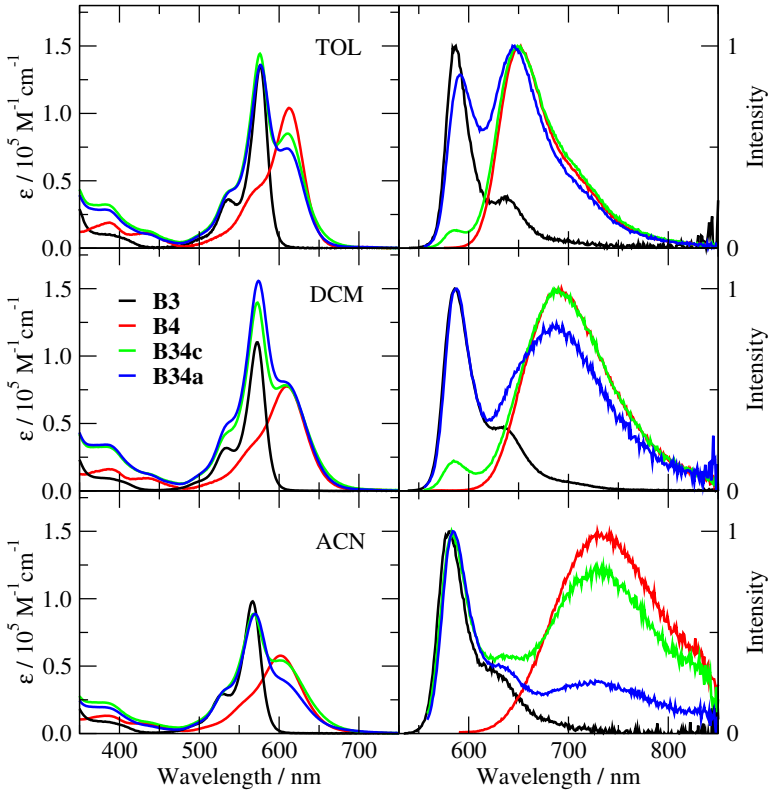

Figure 3.18: Absorption (left) and normalized emission (right) spectra of **B34c**, **B34a**, **B3** and **B4** collected in solvents of different polarity (TOL: toluene, DCM: dichloromethane, ACN: acetonitrile). The absorption spectrum of **B34c** in acetonitrile was normalized to that of **B34a**. Emission spectra of the dyads were collected for excitation at $\lambda = 550$ nm.

bands. In the cone derivative, **B34c**, the intensity of the long-wavelength band is much higher than the short-wavelength one, while the intensities become comparable in the 1,3-alternated isomer, **B34a**. This is true mainly in toluene and dichloromethane, since in acetonitrile the emission of **B4** is vanishing because of the low quantum yield.

The quantum yields of the bichromophores, collected integrating over the whole emission spectrum, are lower than those of the reference dyes, and are smaller for the 1,3-alternated dyad. The reduction of fluorescence quantum yield observed in the bichromophoric systems can be viewed as a hint of EET between the coupled chromophores, which is responsible for the quenching of the donor contribution to the emission spectrum (*vide infra*). Indeed, both dyads undergo bi-exponential decays, suggesting the occurrence of interactions between the active units. The experimental lifetimes, however, point to a more complex scenario.

On general grounds, the emission lifetime of the donor is expected to decrease in presence of the acceptor because of EET, and this effect can be exploited for the determination of the efficiency of the process (Method I, Eq. 3.15). Nevertheless, the experimental decays of the dyads collected for detection on the maximum of the donor band are similar to those of the reference, in contrast with the occurrence of EET. This apparent discrepancy can be explained invoking the conformational disorder of the bichromophores, which is responsible for a distribution of interchromophoric distances/orientations, not equally favourable to EET. Accordingly, the donors participating to efficient EET are almost quantitatively quenched and do not contribute to the dyad's emission, while the residual fraction of donors, not undergoing EET, decays with its characteristic lifetime and is the only fraction that can be detected in the experiments.

Overall, the marked differences between the two bichromophores suggest that the conformation of the calix plays an active role in governing interchromophoric interactions.

In order to evaluate the possibility of EET between the BODIPY moieties, we extracted overlap integrals J (Eq. 3.10) from experimental data of reference compounds and we derived the Förster radius through Eq. 3.11 (Table 3.4). We considered the scenario of direct transfer from **B3** towards **B4**, and also the possibility of backtransfer from **B4** towards **B3**. Emission

Table 3.3: Spectroscopic properties of **B3**, **B4**, **B34c** and **B34a** in different solvents (TOL: cyclohexane, DCM: chloroform, ACN: acetonitrile): absorption and emission maxima (λ_{abs}^{max} and λ_{em}^{max}), fluorescence quantum yield (QY) and emission lifetime (τ). The standard for fluorescence quantum yield measurements was Rhodamine 101 in ethanol (QY = 100%). [a]excitation at $\lambda = 563$ nm.

Solvent	Compound	λ_{abs}^{max}/nm	λ_{em}^{max}/nm	QY%[λ_{exc}/nm]	τ/ns [λ_{em}/nm][a]
TOL	**B3**	576	587	100 [535]	3.62
	B4	613	652	86 [570]	3.42
	B34c	576	588/649	76 [535]	0.20 (27%) 3.29 (73%) [580]
				77 [565]	3.03 (82%) 4.42 (18%) [650]
	B34a	577	591/645	55 [535]	1.82 (63%) 4.55 (37%) [580]
				52 [550]	1.86 (66%) 4.59 (34%) [650]
DCM	**B3**	573	586	95 [534]	3.88
	B4	609	693	73 [550]	3.30
	B34c	573	585/690	51 [534]	0.08 (34%) 3.38 (66%) [580]
				51 [550]	3.18 [688]
	B34a	575	588/684	12 [534]	0.70 (82%) 3.43 (18%) [580]
				12 [550]	0.64 (60%) 2.15 (40%) [690]
ACN	**B3**	567	581	71 [530]	3.93
	B4	601	729	7 [550]	0.77
	B34c	568	583/733	4 [530]	3.09 [583]
				4 [550]	3.06 [600]
	B34a	570	584/730	3 [530]	3.84 (51%) 3.51 (49%) [583]
				3 [550]	

Table 3.4: Data for the **B3**-**B4** EET pair: overlap integral J for forward and backward EET (the direction of EET is indicated by the arrow in the second column), Förster radius R_0 and transfer rate k_{EET} estimated assuming an interchromophoric distance $r = 20$ Å. We assumed $k^2 = 2/3$ in the calculations. TOL: toluene, DCM: dichloromethane, ACN: acetonitrile.

Solvent	Process	$J(\lambda)/\mathrm{M^{-1}cm^{-1}nm^4}$	R_0/Å	$k_{EET}/\mathrm{ns^{-1}}$
TOL	**B3**→**B4**	7.29×10^{15}	66	357
	B3←**B4**	1.37×10^{13}	23	0.68
DCM	**B3**→**B4**	6.37×10^{15}	66	333
	B3←**B4**	5.41×10^{12}	19	0.22
ACN	**B3**→**B4**	4.76×10^{15}	63	248
	B3←**B4**	6.46×10^{13}	21	1.74

of **B3** and absorption of **B4** occur in the same spectral region irrespective of solvent polarity (Figure 3.19, top panels), which should grant for large overlap integrals. Indeed, J for the direct transfer is barely affected by the solvent, and the estimated Förster radius is high (> 60 Å) indicating that energy transfer from **B3** to **B4** should be possible over long distances. Since the chromophores are expected to be at much shorter distance within the dyads (less than 20 Å) [381], this should lead to efficient EET.

The spectral overlap between **B4** emission and **B3** absorption involves only the tails of the corresponding spectra (Figure 3.19, bottom panels). Overlap integrals are two or three orders of magnitude smaller compared to those estimated for direct transfer, and calculated Förster radii are around 20 Å, quite irrespective of the solvent. We should conclude that **B3** and **B4** are a good EET pair and forward transfer between them is the most favoured process. Indeed, supposing that the chromophores are fixed at $r = 20$ Å, the EET rate estimated for the direct transfer is three orders of magnitude larger than the rate estimated for backtransfer. However, the real situation in the dyads is more complex, since the residual conformational mobility of the scaffold could modulate the distance/orientation between the active units, allowing for a distribution of configurations. Moreover, at short distances, also backwards energy transfer can become competitive with direct EET.

In order to verify and quantify EET in the bichromophoric systems, we compared the fluorescence quantum yields of the isolated energy donor

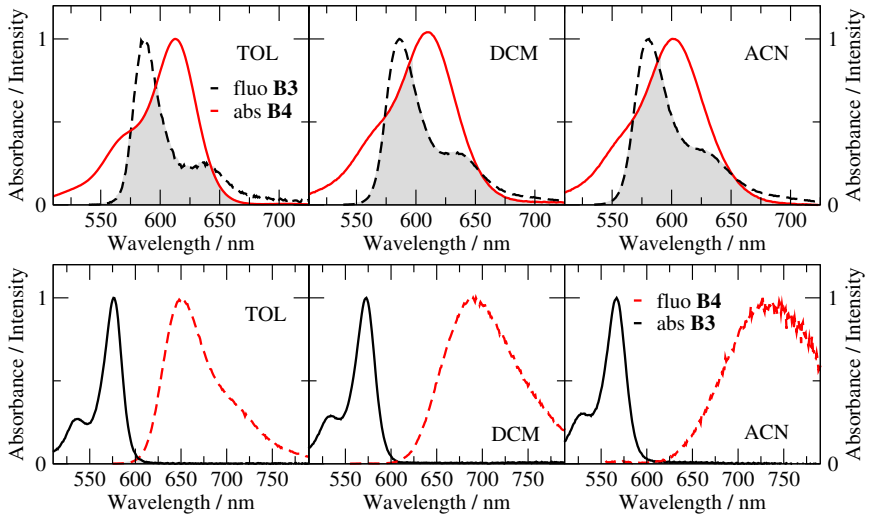

Figure 3.19: Top: emission spectra of **B3** and absorption spectra of **B4**. Bottom: emission spectra of **B4** and absorption spectra of **B3**. Spectra were collected in different solvents: toluene (TOL), dichloromethane (DCM) and acetonitrile (ACN). Greyed areas indicate spectral overlap.

(**B3**) with its quantum yield in presence of the acceptor, i.e. in the dyads. In the dyads the donor cannot be selectively excited because of the spectral overlap between the absorption bands of donor and acceptor, therefore a deconvolution procedure was necessary to extract its quantum yield.

As for the first couple of BODIPY dyes, absorption spectra of the bichromophores were deconvoluted as the weighted sum of the absorption spectra of reference dyes, and rescaled to get the experimental absorbance at the excitation wavelength. The (rescaled) absorbance of the donor at this wavelength provided an estimate of its absorbance in presence of the acceptor. Similarly, emission spectra of the dyads were fitted with the sum of the emission spectra of the references, weighted for appropriate coefficients. The integrated area of the donor emission, rescaled by the coefficients of the fit, was taken as the best estimate of the donor emission in the dyad. Corresponding quantum yields, estimated for two different excitation wavelengths, are reported in Table 3.5 and are in substantial agreement.

In all the investigated solvents the emission of the donor is strongly quenched, pointing to the activation of new efficient decay pathways in the dyes, among which EET. The concomitant occurrence of electron transfer

Table 3.5: Quenching of **B3** emission in the dyads in different solvents (TOL: toluene, DCM: dichloromethane, ACN: acetonitrile). $\phi_{\mathcal{D}}$: quantum yield of isolated donor (**B3**), λ_{exc}: excitation wavelength, $\phi_{\mathcal{D}(\mathcal{A})}$: emission quantum yield of **B3** in the dyads, extracted from a fitting procedure.

Solvent	$\phi_{\mathcal{D}}$	Dyad	λ_{exc}/nm	$\phi_{\mathcal{D}(\mathcal{A})}$
TOL	1	**B34c**	535	0.05
			550	0.06
		B34a	535	0.30
			550	0.33
DCM	0.95	**B34c**	535	0.05
			550	0.05
		B34a	535	0.17
			550	0.20
ACN	0.71	**B34c**	535	0.02
			550	0.02
		B34a	535	0.03
			550	0.06

is unlikely in view of the structural similarity with the other BODIPY pair presented in this Thesis, however it cannot be excluded based on steady-state data and has to be confirmed by future work.

The emission quenching of the donor is larger in **B34c**, in which a reduction of fluorescence of more than 90% was found. A noticeably smaller decrease of donor quantum yield was estimated in **B34a**, especially in toluene and dichloromethane. Assuming that the only process contributing to emission quenching in the dyads is EET, we estimated almost quantitative ϕ_{EET} in **B34c** ($\phi_{EET} \geq 95\%$) irrespective of the solvent, and less efficient transfer in **B34a**.

This result contrasts with chemical intuition, which suggests a shorter interchromophoric distance in the constrained 1,3-alternated isomer, which should make EET even more favoured than in the cone isomer.

For comparison we also estimated the fluorescence quenching of the acceptor (**B4**) when linked to the donor. In this case, the quantum yield of the acceptor inside the bichromophoric systems was estimated by excitation at wavelengths longer than 600 nm, where the absorption of the donor is negligible. Under these conditions we can attribute the whole emission of

Table 3.6: Comparison between the quantum yield of the isolated acceptor (**B4**) and the quantum yield of the acceptor inside the bichromophore in toluene (TOL), dichloromethane (DCM) and acetonitrile (ACN). $\phi_{\mathcal{A}}$: quantum yield of **B4**, $\phi_{\mathcal{A}(\mathcal{D})}$: quantum yield of the bichromophore estimated taking the absorption maximum of the acceptor as the excitation wavelength (where there is formally no absorption from the donor).

Solvent	$\phi_{\mathcal{A}}$	Dyad	$\phi_{\mathcal{A}(\mathcal{D})}$
TOL	0.86	**B34c**	0.61
		B34a	0.31
DCM	0.73	**B34c**	0.40
		B34a	0.10
ACN	0.07	**B34c**	0.03
		B34a	0.02

the dyad to the sole acceptor. We found that emission of the acceptor is quenched inside the bichromophores in all solvents (Table 3.6). The quenching is larger in **B34a**, in which the acceptor quantum yields amount to one half and one fourth of the quantum yields of reference **B4** in toluene and dichloromethane respectively.

Fluorescence quenching of the active units into the dyads can be explained in more general terms with the activation of new decay channels due to the presence of the calixarene scaffold. Indeed, the introduction of the calix increases the dimensions and also the flexibility of the dyads with respect to the small and rigid reference fluorophores, and it can lead to better dissipation of excitation energy through nonradiative processes, for example collisional quenching with solvent molecules. However, other phenomena have to be invoked to explain the different acceptor quenching in the two dyads, which is larger in the conformationally blocked 1,3-alternated isomer. An hypothesis could be backward energy transfer, favoured by the proximity of the dyes in **B34a**, that is also coherent with the reduced quenching of the donor compared to **B34c**.

The considerations above make the analysis of quantum yields trickier, so that a more straightforward method was applied to extract information on EET efficiency. Specifically we applied method IV, relying on the comparison between absorption and excitation spectra of the dyads. Excitation

spectra were recorded for emission at $\lambda = 780 - 790$ nm, where only the acceptor emits, and were normalized at the acceptor band of the absorption spectra. However, since the absorption of the acceptor largely overlaps the absorption of the donor, a fitting procedure was performed to isolate the two contributions to the spectra of the dyads. In more detail, absorption and excitation spectra were fitted independently as the weighted sum of the absorption spectra of reference dyes, and then rescaled to get the same height of the acceptor contribution. The ratio between the coefficients of the fit relative to the donor obtained after rescaling were finally used to extract EET efficiencies through Eq. 3.18.

Experimental spectra are collected in Figure 3.20. In toluene and dichloromethane absorption and excitation spectra of **B34c** are superimposable, suggesting quantitative EET ($\phi_{EET} > 99\%$), while in acetonitrile a slight decrease of the excitation spectrum inside the donor band was detected, indicating less efficient EET ($\phi_{EET} \approx 73\%$). Energy transfer in **B34a** is even less favoured, with estimated efficiencies not exceeding 70% and decreasing with solvent polarity.

This result basically agrees with the different quenching of the donor quantum yield observed in the two bichromophoric systems, indicating that EET is favoured by the cone conformation of the calix. Even if it may seem counterintuitive, because of the larger interchromophoric distance expected in the cone dyad, a few hypothesis can be made explaining these findings.

For example, the closeness of the dyes provided by the 1,3-alternated scaffold may promote competitive backtransfer from **B4** to **B3**, given the corresponding good Förster radius ($R_0 \approx 20$ Å), slowing down the direct EET (from **B3** to **B4**).

An alternative hypothesis is based on the residual conformational mobility of the calix scaffold in the cone conformation, which could modulate the interchromophoric distance/orientation creating preferential channels for EET, in a similar way as the effect of dynamical disorder in polar solvents [134]. Conversely, in the more rigid 1,3-alternated conformation the dyes may be frozen in an unfavourable arrangement, reducing EET efficiency. A distinction between the two scenarios requires further investigation with advanced time-resolved spectroscopic techniques in order to gain information on the excited-state dynamics of these systems.

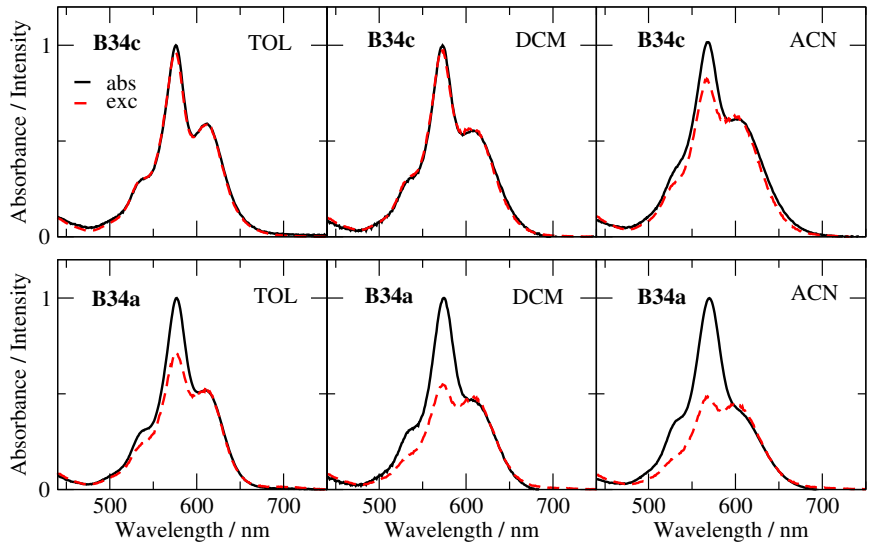

Figure 3.20: Absorption (black) and excitation (red) spectra of the dyads obtained detecting the emission of the sole acceptor: λ_{em} = 780 nm in toluene (TOL) and λ_{em} = 790 nm in dichloromethane (DCM) and acetonitrile (ACN). Spectra are normalized at the acceptor band. Estimated EET efficiencies in **B34c** are 0.99 in TOL and DCM, 0.73 in ACN. EET efficiencies in **B34a** are 0.65 in TOL, 0.43 in DCM and 0.33 in ACN.

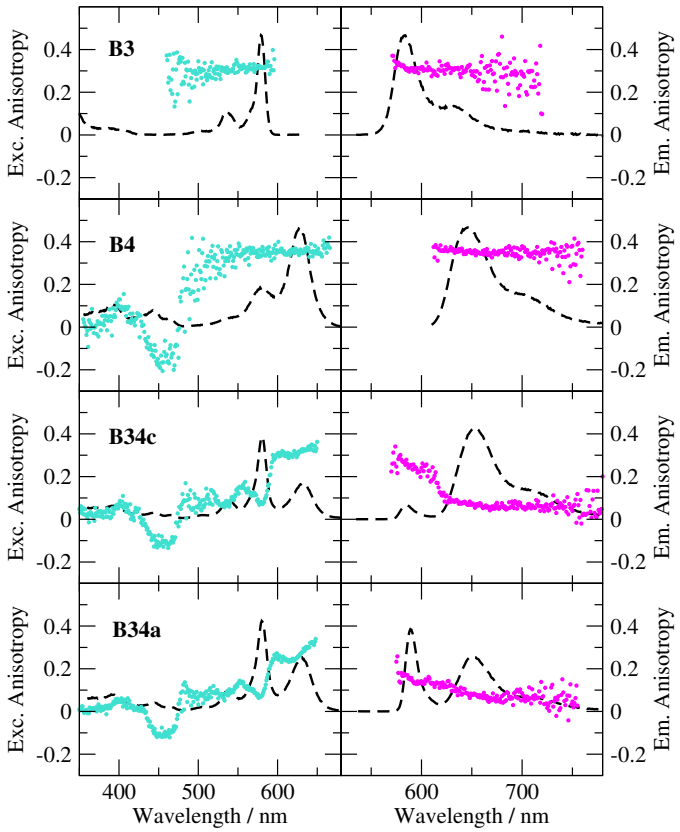

Figure 3.21: Excitation (left panels) and emission (right panels) anisotropy collected in glassy 2-methyltetrahydrofuran at 77 K (dots). Excitation and emission spectra collected under the same experimental conditions are shown as a guide to the eye (dashed lines). Excitation anisotropy of the dyads was collected for detection at $\lambda = 655$ nm, emission anisotropy was collected for excitation at $\lambda = 535$ nm.

Fluorescence anisotropy measurements on the target dyes were performed at 77 K in vitrified 2-methyltetrahydrofuran dilute solutions (Figure 3.21). Anisotropy of reference fluorophores is almost flat and near its upper 0.4 limit inside the main absorption/emission band. Excitation anisotropy of **B4** drops to the lowest -0.2 limit at $\lambda \approx 450$ nm corresponding to other less intense transitions.

Anisotropy of the bichromophores is dependent on the chosen excitation/emission wavelength and can be exploited to retrieve information on the mutual orientation of the fluorophores. Excitation anisotropy was collected for excitation at $\lambda = 655$ nm, where the ratio between the emission of the acceptor to the emission of the donor reaches its maximum. Thus, anisotropy provides information on the orientation of the absorption transition dipole moment of the energy donor relative to the emission dipole moment of the energy acceptor. Indeed, in the low-energy region of the spectrum, where only the acceptor absorbs, a high anisotropy value was found ($r \approx 0.35$), similar to that obtained for **B4**. Moving to shorter wavelengths, anisotropy decreases smoothly to $r \approx 0.3$ (0.25) for **B34c** (**B34a**) at $\lambda \approx 600$ nm, before a sudden decrease to $r \approx 0.05$ takes place at the absorption maximum of the donor. Assuming the absence of depolarization due to a distribution of configurations in solution, this feature indicates a different alignment of the donor and acceptor dipole moments, allowing to roughly estimate an angle of $\sim 50°$ for both dyads.

Emission anisotropy was collected for excitation close to the donor absorption maximum ($\lambda = 535$ nm), to maximize absorption from the donor. Under this conditions we obtained $r \approx 0.05$ inside the emission band of the acceptor, in agreement with excitation anisotropy. On the opposite, anisotropy is lower than the expected ~ 0.4 value within the donor band, and more depolarization occurs for **B34a**.

Essential-state modelling of reference dyes

Reference dyes **B3** and **B4** can be regarded as push-pull dyes, whose intense absorption and emission bands in the visible range originate from a CT transition [417].

Absorption and emission spectra of the two dyes were calculated adopting the standard two-state model for dipolar chromophores, described in

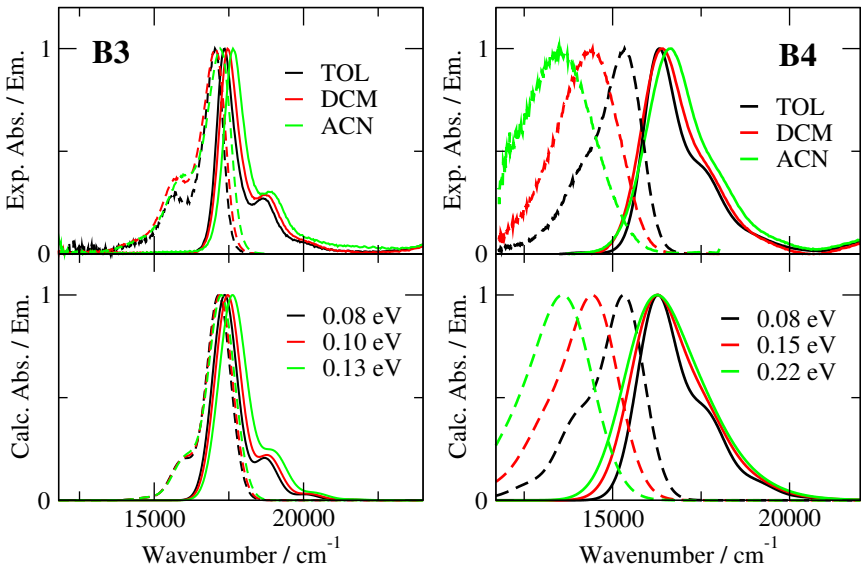

Figure 3.22: Comparison between experimental spectra of **B3** and **B4** (top panels) in different solvents (TOL: toluene, DCM: dichloromethane, ACN: acetonitrile) and spectra calculated with the two-state model (bottom panels). Continuous lines: absorption spectra, dashed lines: emission spectra. Model parameters for **B3**: $\eta = -0.30$ eV, $\sqrt{2}t = 0.97$ eV, $\omega_v = 0.16$ eV, $\varepsilon_v = 0.20$ eV, $\mu_0 = 20.0$ D, $\gamma = 0.05$ eV. Model parameters for **B4**: $\eta = 0.93$ eV, $\sqrt{2}t = 0.50$ eV, $\omega_v = 0.17$ eV, $\varepsilon_v = 0.10$ eV, $\mu_0 = 43.0$ D, $\gamma = 0.05$ eV. Values of the orientational relaxation energy (ε_{or}) corresponding to the various solvents are reported on the panels.

detail in Chapter 1. Model parameters were extracted through the fit of room temperature absorption and emission spectra in the three investigated solvents. The parameter μ_0 was fixed to reproduce the molar extinction coefficient measured in dichloromethane.

Calculated spectra are collected in Figure 3.22 and compared to the corresponding experimental spectra. The quantitative agreement between experimental and theoretical data is impressive, and all characteristic spectral features of the BODIPY dyes are well accounted for, including solvatochromic shifts and inhomogeneous broadening effects.

The different solvatochromic behaviour of **B3** and **B4** is related to a different ground-state polarity. The ground-state ionicity of **B4** is approximately 0.06, while the ionicity of **B3** is larger than 0.7. Indeed, **B4** is a largely neutral dye in the ground-state possessing a highly polar excited state. This state is responsible for fluorescence and is stabilized by polar solvents originating large positive solvatochromism in emission. Conversely, **B3** is mostly zwitterionic, and its ground-state is stabilized by polar solvents, leading to a slight negative solvatochromic shift in absorption.

The transition dipole moment μ_{ge} relevant to the CT transition of the fluorophores can be extracted from model parameters and amounts to ~ 9 D for **B3** and ~ 10 D for **B4**.

The Förster theory is based on the dipole approximation, which works well when the transition dipole moments of the interacting dyes are small compared to their distance. When the transition densities become sizeable, as it is the case of polar CT chromophores, the validity of the dipolar approximation is limited to large interchromophoric distances, while a description based on the extended-dipole approximation is preferable at short distances [132, 418]. This has implications on the dependence of the EET rate on the relative orientation of the dyes and also on its $(R_0/R)^6$ dependence.

In our specific case, the Förster theory may be suitable for the description of **B34c**, assuming a larger interchromophoric distance, but becomes inadequate for the strongly interacting dyes in **B34a**, requiring a more refined theoretical framework. To this aim, future work on these systems will involve the extensive essential-state modelling of the dyads, including the appropriate description of interchromophoric interactions, and will address

the simulation of steady-state spectra as well as the EET dynamics in solution.

3.5 Energy *versus* electron transfer in a Nile Red-fullerene dyad

Molecular dyads are useful structures to investigate a variety of interchromophoric processes other than energy transfer, depending on the choice of the active units. For example, as for energy transfer, calix[4]arene-based dyads could be interesting model systems for electron transfer studies. The construction of a bichromophoric system undergoing eT requires the appropriate choice of an electron donor-electron acceptor pair, with a favourable alignment of the energy levels (i.e. HOMO and LUMO of the acceptor should lie at lower energies compared to the corresponding orbitals of the donor), and also short interchromophoric distance, that should ensure a good overlap between the molecular orbitals. The small calix[4]arene scaffold forces the active units in a confined space, where favourable interactions for eT may arise. To the best of our knowledge, the investigation of eT in a calix[4]arene-based dyad has never been performed in detail and should also provide insights on the role played by the calix in the eT reaction [376].

Thanks to electron delocalization over their large three-dimensional aromatic structure, fullerenes can stabilize up to six negative charges [419], making them ideal electron acceptor candidates [420]. Moreover, several synthetic protocols have been established for their functionalization, allowing for the grafting to many chemical structures [421]. Most importantly, because of their structural rigidity, fullerenes possess small reorganization energies, that should help in achieving large eT rates even with small driving forces, shifting at the same time the undesired charge-recombination process into the inverted Marcus region [422–424]. Indeed, fullerenes have been incorporated as electron acceptor in many multichromophoric systems, paired with a variety of electron donors. Porphyrinoid systems are among the mostly investigated electron donors by virtue of their extended absorption and favourable electrochemical properties [367], but also other organic dyes were able to participate in eT towards fullerenes [407, 425].

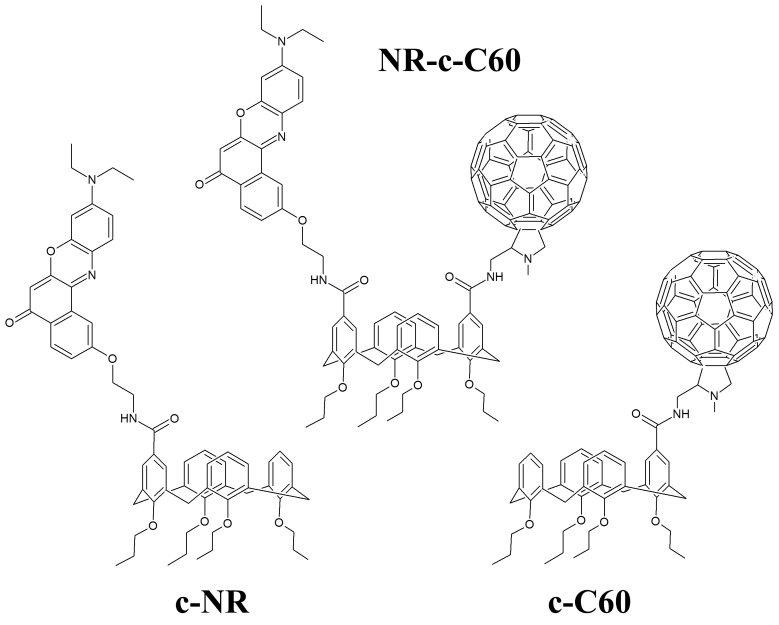

Figure 3.23: Molecular structure of the target dyad **NR-c-C60** and reference compounds **c-NR** and **c-C60**.

The short interchromophoric distance required for eT is however also beneficial to energy transfer and, if appropriate conditions are met, for example a non-vanishing spectral overlap, eT and EET can become competitive processes [426–431].

In this work we coupled fullerene C_{60}, playing the role of electron acceptor, with the well-known laser dye Nile Red, that should act as electron donor [432]. In the target bichromophoric system **NR-c-C60** (Figure 3.23) the two eT partners are linked at the 1,3-distal positions of the upper rim of a tetrapropoxycalix[4]arene blocked in the cone conformation by appropriate alkylation of the lower rim. For better homogeneity, the reference compounds used in this study are monochromophoric systems in which either the Nile Red or the fullerene are anchored to the calix, called **c-NR** and **c-C60** respectively.

3.5.1 Spectroscopic characterization

Spectroscopic characterization of **NR-c-C60** and reference compounds was performed in toluene and chloroform. Experimental spectra at room tem-

perature and main spectroscopic properties are summarized in Figure 3.24 and Table 3.7.

Absorption spectra of **c-NR** feature a broad and intense band in the region between 450 and 600 nm corresponding to the typical absorption band of Nile Red, indicating that the presence of the calix does not affect the electronic properties of the chromophore. Emission peaks at $\lambda > 550$ nm and shows a residual vibronic structure. **c-NR** retains the bright emission of Nile Red, with large fluorescence quantum yields in both the solvents analyzed (QY $\approx$ 80%). Absorption and emission bands of Nile Red are sensitive to solvent polarity and undergo a batochromic shift amounting to more than 0.1 eV ($\sim$ 800 cm^{-1}) from toluene to more polar chloroform [433].

As expected, spectroscopic properties of **c-C60** are reminiscent of those of C_{60} [434]. The characteristic continuous absorption band spans the whole visible range with an offset at $\lambda \approx 750$ nm and intense signals in the UV ($\lambda < 400$ nm). The peak at $\lambda \approx 430$ nm is instead typical of fulleropyrrolidine and its derivatives [371, 435–437]. Fluorescence of **c-C60** features the weak emission band of fullerene at $\lambda \approx 720$ nm, which is independent of the excitation wavelength and polarity of the medium. The emission intensity was too low to reliably estimate the fluorescence quantum yield. Indeed, the quantum yield of C_{60} typically amounts to $\sim 2 \times 10^{-4}$ in nonpolar solvents [438].

Absorption spectra of **NR-c-C60** are roughly the sum of corresponding reference spectra, indicating the absence of strong interactions between the chromophores in the ground state. Because of the large difference between the fluorescence efficiencies of the two dyes, the emission spectrum of the bichromophoric system is dominated by the emission band of Nile Red, while the contribution from C_{60} is recognizeable in toluene only, where it is responsible for a weak shoulder at the long wavelength tail of the spectrum. Nevertheless, fluorescence of Nile Red is strongly quenched into the dyad, indicating the activation of new decay processes.

The molar extinction coefficient of fullerene in the visible range is weak ($\varepsilon \approx 10^3$ mol^{-1} L cm^{-1}) compared to common fluorescent dyes, however its absorption band spans a large region, resulting in a finite spectral overlap with the emission spectrum of Nile Red (Figure 3.25). At the same time Nile

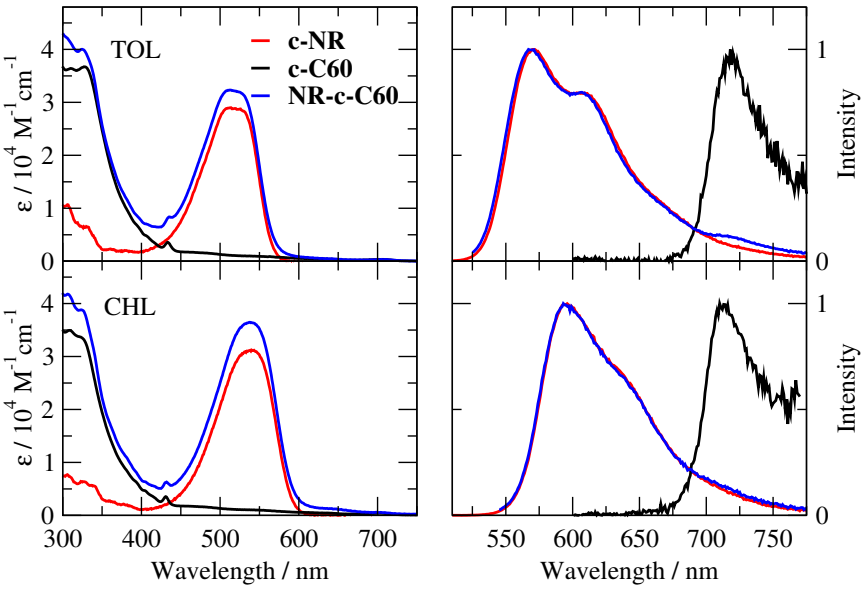

Figure 3.24: Steady-state absorption (left) and emission (right) spectra of **c-NR** (red lines), **c-C60** (black lines) and **NR-c-C60** (blue lines) collected in toluene (TOL, top panels) and chloroform (CHL, bottom panels). Emission spectra of the dyad were collected for excitation at the absorption maximum.

Table 3.7: Spectroscopic properties of **c-NR**, **c-C60** and **NR-c-C60** in toluene (TOL) and chloroform (CHL): absorption and emission maxima (λ_{abs}^{max} and λ_{em}^{max}), molar extinction coefficient at λ_{abs}^{max} (ε_{max}) and fluorescence quantum yield (QY) The standard for fluorescence quantum yield measurements was fluorescein in NaOH(aq) 0.1 M at 23°C (QY = 90%). [a]not determined. [b]data from Ref. [381]

Solvent	Compound	λ_{abs}^{max}/nm	ε_{max}/mol^{-1} L cm^{-1}	λ_{em}^{max}/nm	QY% [λ_{exc}/nm]
TOL	**c-NR**	513	29 000	570	84 [530]
	c-C60	< 350	> 30 000	718	-[a]
	NR-c-C60	514	32 000	567	1.9 [515]
CHL	**c-NR**	540	31 000	596	78[b]
	c-C60	< 350	> 30 000	710	-[a]
	NR-c-C60	538	36 000	593	2.7 [540]

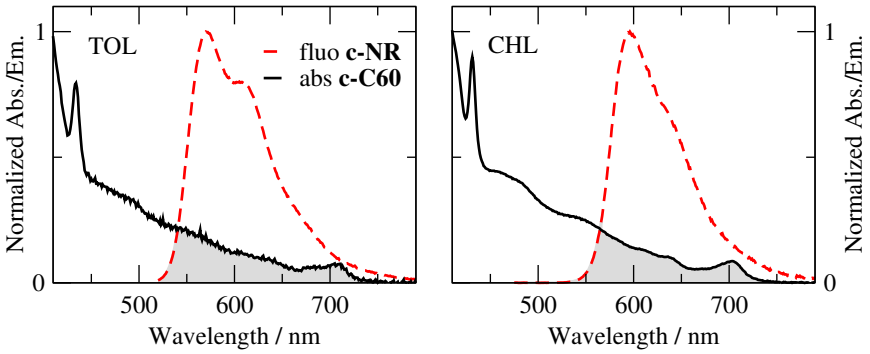

Figure 3.25: Emission spectra of **c-NR** and absorption spectra of **c-C60** in toluene (TOL) and chloroform (CHL). Spectral overlap is indicated by the greyed area.

Red, with its intense emission, represents an ideal energy donor [370, 439]. These elements set the basis for a possible competition between eT and EET in **NR-c-C60**.

We determined the Förster radius for the Nile Red-fullerene pair based on spectroscopic data of references **c-NR** for the energy donor and **c-C60** for the energy acceptor. Assuming a random orientation of the chromophores ($k^2 = 2/3$) we obtained an overlap integral $J = 2.18 \times 10^{13}$ M^{-1} cm^{-1} nm^4 in toluene and $J = 7.56 \times 10^{13}$ M^{-1} cm^{-1} nm^4 in chloroform, corresponding to $R_0 = 25$ Å and $R_0 = 30$ Å respectively. These values of R_0 are lower than those obtained for the BODIPY pair described in the previous Section and especially designed for EET, however they are significant given the proximity of the substituents on the calix scaffold.

Assuming that the huge emission quenching of Nile Red in **NR-c-C60** (Figure 3.26) is entirely due to EET towards fullerene, we can estimate ϕ_{EET} from the comparison between the emission quantum yield of **c-NR** (isolated energy donor) and the emission quantum yield of Nile Red in the bichromophoric system (Method II, Eq. 3.16). In toluene the quantum yield of the donor is decreased from 84% to 1.8%, corresponding to almost quantitative transfer ($\phi_{EET} = 98\%$). Similarly, in chloroform the emission efficiency of the donor is decreased from 78% to 3.5% in the dyad, yielding $\phi_{EET} = 95\%$.

These results, however, do not confirm the occurrence of EET in the target system. Indeed, fluorescence quenching can in principle be related to both EET and eT phenomena. We should therefore devise a method to discriminate between them. A direct proof of EET was obtained focusing

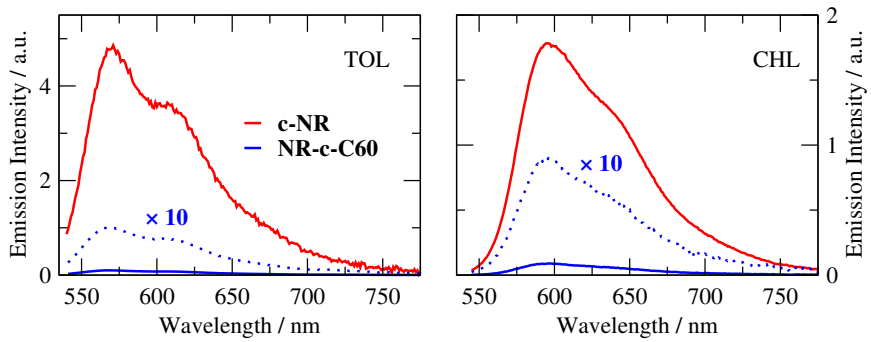

Figure 3.26: Fluorescence quenching of Nile Red in **NR-c-C60**. Emission spectra of equimolar solutions of **c-NR** and **NR-c-C60** collected under the same experimental conditions (λ_{exc} = 530 nm in toluene and 540 nm in chloroform). A magnification of the emission spectrum of the bichromophoric system is shown for clarity.

on fullerene emission (Figure 3.27). The emission spectrum $I_{\mathcal{DA}}(\lambda)$ of **NR-c-C60** was decomposed into the contributions from the two emitting dyes through the fitting with $I_{\mathcal{DA}}(\lambda) = c_{\mathcal{D}} I_{\mathcal{D}}(\lambda) + c_{\mathcal{A}} I_{\mathcal{A}}(\lambda)$, where $I_{\mathcal{D}}(\lambda)$ and $I_{\mathcal{A}}(\lambda)$ are the emission spectra of equimolar solutions of **c-NR** and **c-C60** collected under identical experimental conditions, and the coefficients $c_{\mathcal{D}}$ and $c_{\mathcal{A}}$, representing the weight of the two reference spectra, were adjusted to get the best fit of the experimental spectrum of the dyad. In both solvents the best fit was achieved with $c_{\mathcal{A}} = 23$, indicating a 23-fold enhancement of fullerene emission in **NR-c-C60**.

The EET efficiencies calculated from the results of the fit presented above, according to Method III (Eq. 3.17), are 79% in toluene and 74% in chloroform. While the sensitized emission of fullerene is unambiguously related to EET, fluorescence quenching of Nile Red can result either from EET or eT or both. Indeed, both processes imply the excited-state quenching of the donor but, while EET yields an increase of the excited C_{60} species, the product of the eT reaction, monoanion C_{60}^{-}, emits in the near-IR and cannot be detected in our experiment [440]. The efficiency estimated with Method III, corresponding to the true EET efficiency, is lower than the efficiency estimated with Method II, indicating that a fraction of Nile Red quenching is due to mechanisms other than EET, in our hypothesis eT.

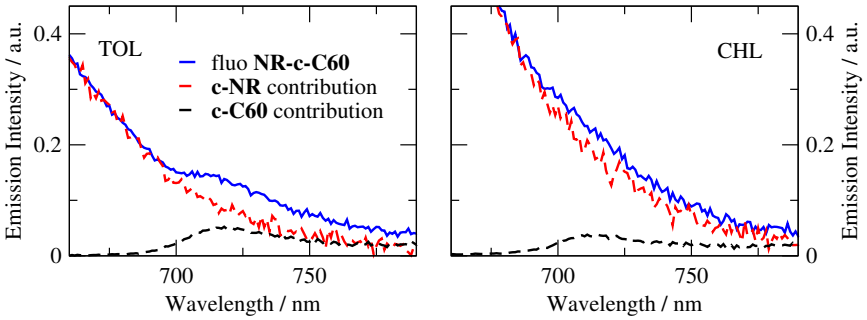

Figure 3.27: Sensitization of fullerene emission in **NR-c-C60**. Deconvolution of the emission spectrum of **NR-c-C60** (blue lines) as the weighted sum of the emission spectra of reference dyes collected under the same experimental conditions (contributions of **c-NR** and **c-C60** to the spectrum of the dyad, rescaled by the coefficient of the fit, are shown as dotted curves). Only the region of fullerene emission is shown for clarity. The contribution of fullerene emission to the fluorescence spectrum of the dyad is 23 times the spectrum of **c-C60**. Deconvolution is shown in both investigated solvents, namely toluene (TOL) and chloroform (CHL).

Results presented above suggest the competition between EET and eT in the target dyad. From one hand, they offered us an explicit proof of EET from Nile Red to C_{60} in **NR-c-C60** together with a reliable estimate of its efficiency ($\phi_{EET} > 70\%$). From the experimental values of ϕ_{EET} we calculated the interchromophoric distance, amounting to ~ 20 Å in toluene and ~ 25 Å in chloroform, which are coherent with the dimension of the bichromophore. Moreover, they provided indirect evidence of eT, even if with a minor contribution, probably because of small orbital overlap between the active units. More studies are mandatory in order to get a direct demonstration of eT, including electrochemical and time-resolved measurements, the latter being also necessary to address the kinetics of the processes and shed light on their competition.

3.6 A fluorescent ratiometric temperature probe

Temperature is a fundamental parameter in many chemical, physical and biological processes. Most cellular functions are accompanied by absorption or release of heat, so that tools for non-invasive and *in situ* measurement of temperature at the sub-micrometric scale are highly desirable for the in-

depth study of cellular metabolism [441]. At the same time, the anomalous increase of temperature is usually an indicator of cell diseases, and the possibility of mapping and monitoring temperature at the nanoscale is crucial for both diagnosis and control of therapeutic effects [442, 443]. In a more broad context, the miniaturization of systems for chemical and biological analysis is highly demanded in view of the construction of portable diagnostic tools, and one of the main concerns about the design of microelectronic and microfluidic devices is the heat control, that requires the development of suitable temperature probes [444].

Conventional thermometry is intrinsically invasive and limited to the study of macroscopic systems. Among the alternative approaches, optical sensors are the most promising, because they do not require physical contact with the sample, they can be easily miniaturized, and provide high resolution over small areas [445, 446]. These sensors are often based on fluorescence, that guarantees high sensitivity and simple readout [447]. The emission properties affected by temperature include intensity [448–450], spectral position [451–453], emission lifetime [448, 454, 455] or anisotropy [456].

A drawback of fluorescence is its sensitivity to external variables, including instrumental factors, dielectric properties, ionic strength and viscosity, which may interfere with the measurement of temperature. This issue is solved by the ratiometric approach, consisting in the comparison between the emission intensities at two different wavelengths. The ratiometric approach requires the variation of emission bandshape with temperature or, as an alternative, the presence of at least two resolved emission bands whose relative intensity is modified by temperature [457]. Because of their multiple emission bands, lanthanides are widely exploited in nanothermometry [458]. Conversely, with the exception of a few systems violating the Kasha rule, undergoing reverse intersystem crossing, or presenting excimers or different isomers [451, 459–467], most organic fluorophores are characterized by a single emission band and their application in ratiometric temperature probes requires the presence of at least two different emitting species [468–473].

Indeed, organic multichromophores are interesting systems for application as nanothermometers, taking advantage of cooperative effects between their components. An interesting strategy consists in the exploitation of EET between fluorophores linked to a thermoresponsive structure

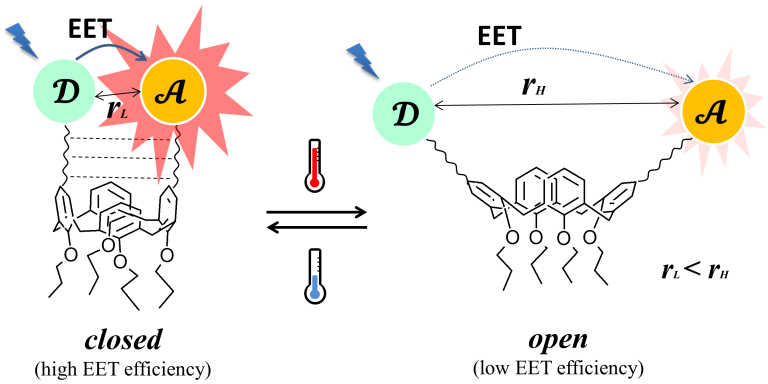

Figure 3.28: Working mechanism of the calix[4]arene-based nanothermometer envisaged in this Work. Thanks to favourable interactions between the substituents, at low temperatures the calix[4]arene scaffold adopts a closed flattened cone conformation bringing the chromophores at short distance, promoting efficient EET; at higher temperatures the open flattened cone conformation is preferred, moving the chromophores far apart and thus decreasing EET efficiency.

that modulates their spatial distribution according to temperature. The occurrence of EET between two (or more) different species implies the presence of distinct interdependent emission signals that can be analyzed in a ratiometric approach. The ratiometric output is accurate and independent of the concentration of the probe and the excitation power [474]. To date, reports on this type of nanosensors are mostly limited to thermoresponsive polymers [469, 470, 473, 475] and DNA-based nanostructures [468, 471, 476].

In this Work we demonstrated that a molecular dyad constituted by two chromophores capable of EET anchored at the upper rim of a cone calix[4]arene is able to work, under appropriate conditions, as a ratiometric temperature probe with good sensitivity and reproducibility [388]. To the best of or knowledge, this is the first example of temperature probe whose driving force consists in the conformational variation of a macrocyclic scaffold.

It is well-known that in solution cone calixarenes interconvert between two equivalent flattened cone structures [379]. When two substituents are grafted at the distal positions of the upper rim, the open flattened cone con-

formation, in which the substituents point outwards, is usually preferred, as it allows to minimize steric repulsions. However, in presence of specific interactions between the substituents, such as $\pi - \pi$ stacking and hydrogen bonds, the closed flattened cone conformation, in which the substituted aromatic rings of the calix are almost parallel, can be stabilized [380, 477, 478]. It follows that an external stimulus, such as a variation of solvent polarity [381, 479, 480] or temperature, can trigger the interconversion between the two conformers. The two flattened cone isomers are characterized by different interchromophoric distance/orientation, whose modulation, thanks to variable EET efficiency, affects the relative emission intensities of the fluorophores, which can be correlated to temperature (Figure 3.28).

Among the advantages of this strategy are the small size of the probe, of the order of a few nanometers, which allows the access to nanoconfined environments such as living cells, at difference with bulkier polymeric probes. At the same time this system is easy to characterize and operates through a well-defined working mechanism. Moreover, with regard to biological applications, this strategy minimizes the risk of hydrolysis and/or aspecific interactions with the internal walls of the cell, which is a typical bottleneck of DNA-based probes [481].

3.6.1 Spectroscopic characterization

The structure of the bichromophoric system **DA** working as temperature probe is shown in Figure 3.29. The selected EET partners are two well-known fluorescent dyes: Coumarin 343, acting as energy donor, and 7-nitrobenz-2-oxa-1,3-diazol-4-yl (NBD), playing the role of the energy acceptor [381, 388]. The aminoethyl spacer used for the connection of the active units to the calix scaffold provides two amide functionalities which, under suitable conditions, can interact via hydrogen bonds stabilizing the closed flattened cone conformation [380, 381]. Monosubstituted calixarenes **D** and **A** were selected as reference compounds mimicking the isolated donor and acceptor respectively.

^{1}H NMR is a powerful technique for the assessment of the calix[4]arene conformation in solution. The preferred conformation of the calix can be inferred by the comparison between the signals of the aromatic protons on the macrocycle. In the flattened cone conformation the aromatic protons

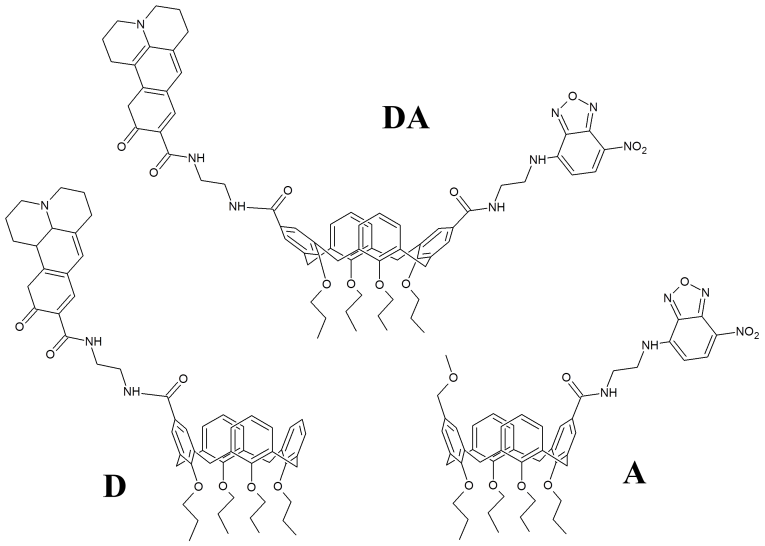

Figure 3.29: Molecular structure of bichromophoric system **DA** and reference dyes **D** and **A**.

on the parallel aromatic rings are shielded by the aromatic rings pointing outwards, and are shifted upfield. In 1,3-disubstituted calix[4]arenes the comparison between the signals of the substituted rings with those of the unsubstituted rings allows to identify the calix conformation.

A ^{1}H NMR study revealed the sensitivity of the calix conformation of **DA** to the solvent. Inspection of the relative position of the signals of the protons on the aromatic rings suggests that in $CDCl_3$ the calixarene is forced to adopt a closed flattened cone conformation, because of the occurrence of an intramolecular hydrogen bonds between the amide NH groups on the linkers. On the opposite, in DMSO-d_6, the amides interact favourably with the solvent, breaking the intramolecular hydrogen bond and favouring an open conformation.

Not only the solvent can modulate the strength of the intramolecular hydrogen bond but, as relevant to our purpose, also temperature plays an important role. In $CDCl_3$ an increase of temperature induces a downfield shift of the signals of the protons *ortho* to the substituents, accompanied by a shift of the signals of the unsubstituted rings in the opposite direction

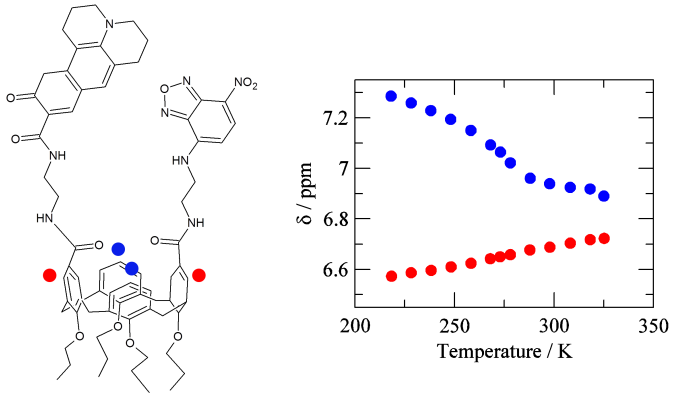

Figure 3.30: Temperature dependent ^{1}H NMR study of **DA** in chloroform. Chemical shift of the aromatic protons of the dyad at selected temperature (for the assignment, see the molecular structure at the left).

(Figure 3.30). These shifts are reversible and are consistent with an opening of the calix upon heating the sample and a closure when the sample is cooled down. This behaviour is independent of concentration, ruling out aggregation effects. Moreover, this phenomenon is absent in the reference dyes, and consistent with the loosening or strengthening of the intramolecular hydrogen bond following a temperature increase or decrease, respectively.

Absorption and emission spectra of **DA** and reference dyes collected in chloroform at room temperature are provided in Figure 3.31, and relevant spectroscopic properties are summarized in Table 3.8. Reference dye **D** features the typical absorption band of Coumarin 343, peaking in the blue with high molar extinction coefficient ($\varepsilon_{max} > 1.7 \times 10^4$ mol^{-1} L cm^{-1}), and sharp and intense fluorescence emission in the 450-550 nm range with quantitative quantum yield. Absorption of **A** is red-shifted compared to **D** and peaks at $\lambda \approx 450$ nm. **A** is also characterized by a broad emission band spanning the whole region between 450 and 700 nm with good emission efficiency. The good spectral overlap between the emission of **D** and the absorption of **A** (Figure 3.32), together with the high emission quantum yield of **D**, satisfy the basic prerequisites for observing efficient EET from Coumarin 343 to NBD in the bichromophoric system.

The absorption spectrum of **DA** is roughly the sum of the absorption spectra of reference dyes, confirming a weak coupling between the chro-

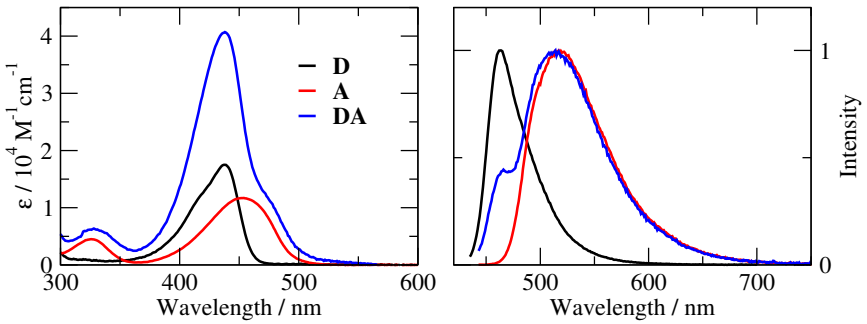

Figure 3.31: Room temperature absorption (left) and emission (right) spectra of **D**, **A** and **DA** in chloroform.

Table 3.8: Spectroscopic properties of **D**, **A** and **DA** in chloroform: absorption and emission maxima (λ_{abs}^{max} and λ_{em}^{max}), molar extinction coefficient at λ_{abs}^{max} (ε_{max}) and fluorescence quantum yield (QY). The standard for fluorescence quantum yield measurements was fluorescein in NaOH(aq) 0.1 M at 23°C (QY = 90%). [a]data are taken from Ref. [381].

Compound	λ_{abs}^{max}/nm	ε_{max}/mol^{-1} L cm^{-1}	λ_{em}^{max}/nm	QY% [λ_{exc}/nm]
D	438	17 500	462	100
A [a]	454	11 700	522	62
DA	438	40 700	514	23 [470]; 22 [438]

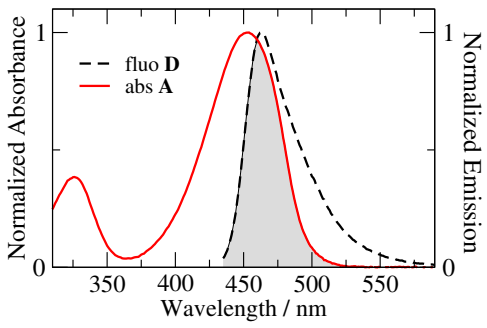

Figure 3.32: Normalized emission spectrum of **D** and absorption spectrum of **A** recorded in chloroform at room temperature. The greyed area indicates spectral overlap.

mophores. The Lambert-Beer law vas verified over a wide concentration range, from $\sim 1 \times 10^{-6}$ to $\sim 5 \times 10^{-4}$ mol L^{-1}, attesting the absence of aggregation phenomena at the investigated concentrations. Emission of **DA** was collected for excitation at its absorption maximum, corresponding to the maximum of the energy donor absorption, and features two partially overlapped bands, assigned to the emission of Coumarin 343 and NBD. The emission intensity of Coumarin 343 in the dyad is largely quenched, suggesting the occurrence of EET.

Absorption and emission spectra of **DA** and reference dyes were collected in chloroform at different temperatures in the range between 240 and 300 K (Figure 3.33). The lower temperature limit is dictated by the crystallization point of the solvent, the upper limit by solvent evaporation. Absorption spectra of **D** and **A** undergo only minor changes with temperature. Cooling down the solution slightly increases the absorbance and shifts the whole spectrum to the red, leaving bandshapes basically unaffected. This shift may be due to the increase of the dielectric constant of chloroform at low temperatures [482]. Also the absorption spectrum of **DA** undergoes small changes and, at any temperature, it roughly corresponds to the sum of Coumarin 343 and NBD absorption bands. The emission band of reference dyes undergoes a shift similar to absorption, and broadens as temperature is increased because of thermal disorder (inhomogeneous broadening). The overall effect is the apparent decrease of the maximum emission intensity, which seems to be more effective in **A**. Fluorescence quantum yields at the various temperatures were estimated taking room temperature solution as the standard. The emission efficiency of **D** is barely affected by temperature, while the efficiency of NBD increases up to 73% as temperature is decreased.

The emission spectrum of **DA**, collected for excitation at the absorption maximum of the energy donor, is instead strongly sensitive to temperature (Figure 3.34). The emission band of Coumarin 343, peaking at $\lambda \approx 465$ nm, and the emission band of NBD, peaking at $\lambda \approx 515$ nm, can be always recognized, however their ratio is strongly influenced by temperature. In the right panel of Figure 3.34 we plotted the ratio of the emission intensity of **DA** at $\lambda = 515$ nm and the emission intensity at $\lambda = 465$ nm. The resulting intensity ratio I_R linearly decreases as temperature increases, with a slope of 0.04 K^{-1}. For comparison we also plotted the values of I_R obtained taking

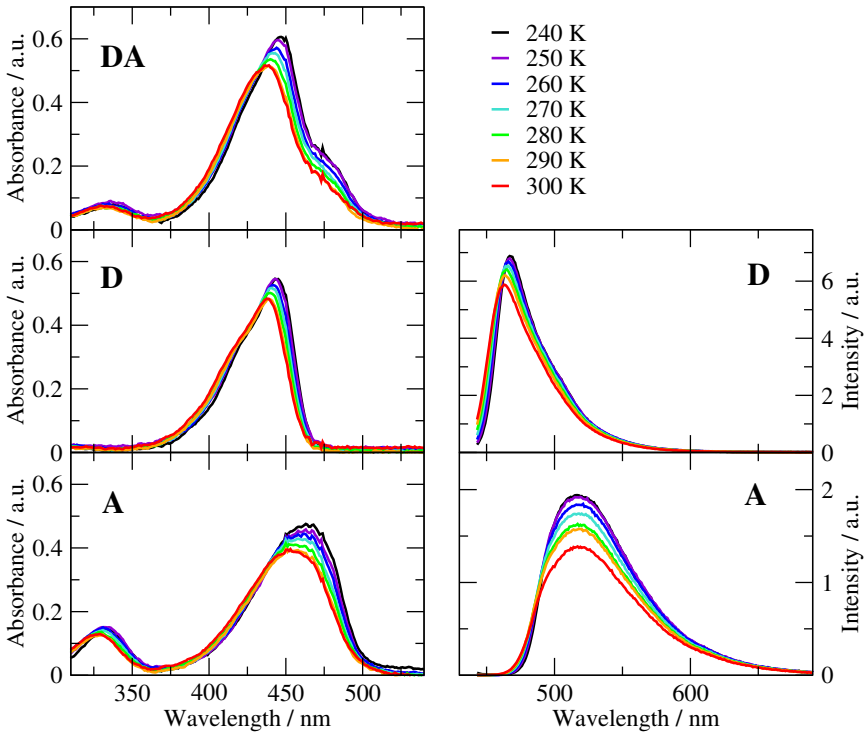

Figure 3.33: Temperature-dependent spectra in chloroform. Left panels: absorption spectra of **DA**, **D** and **A** at selected temperatures. Right panels: emission spectra of reference dyes **D** and **A** at selected temperatures.

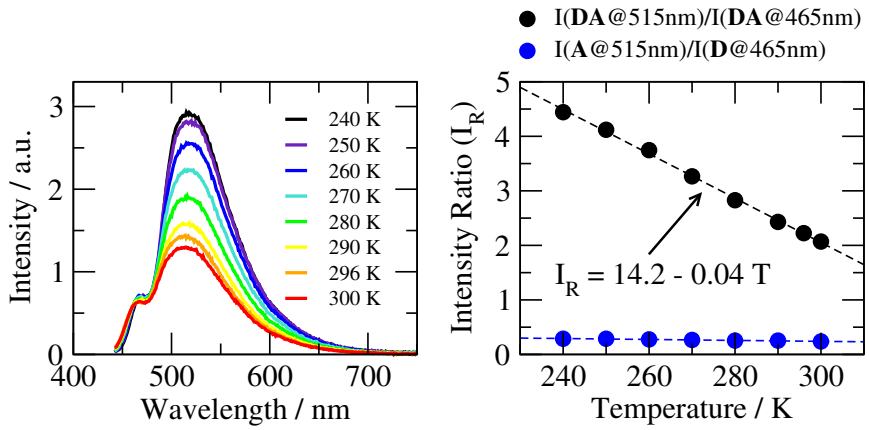

Figure 3.34: Temperature-dependent emission of **DA** in chloroform. Left panel: emission spectra of **DA** at different temperatures collected for excitation at $\lambda = 438$ nm. Right panel: intensity ratio (I_R) between the emission intensity at $\lambda = 515$ nm and the emission intensity at $\lambda = 465$ nm as a function of temperature. Black dots: emission intensities of the bichromophore **DA** spectrum, blue dots: emission intensities of the reference donor **D** ($\lambda = 465$ nm) and reference acceptor **A** ($\lambda = 515$ nm). Dashed lines correspond to the linear fit of experimental data (the equation of the fit is shown on the panel).

the emission intensity of **A** at $\lambda = 515$ nm and the emission intensity of **D** at $\lambda = 465$ nm, obtaining in this case a flat line. This result clearly points out that the thermal responsiveness of **DA** emission is not related to a different temperature dependence of the quantum yields of the two fluorophores, but rather arises from a cooperative interaction between them. Indeed, this phenomenon can be attributed to a temperature-dependent EET, as it will be demonstrated in the following Section.

Results presented above make the dyad **DA** a ratiometric temperature probe, with a sensitivity of 4% K^{-1}. The reversibility of the probe and the repeatability of the measurement was assessed through 12 subsequent cycles of heating and cooling at the limiting temperatures (300 K and 240 K) yielding very precise and consistent results (Figure 3.35). This constitutes a proof of the robustness of **DA** in the investigated temperature range.

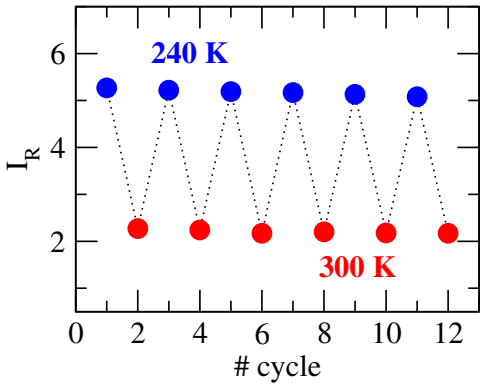

Figure 3.35: Reversibility/repeatability of the ratiometric response of **DA** over 12 heating and cooling cycles at 240 K and 300 K in chloroform. I_R is the intensity ratio between emission at $\lambda = 515$ nm and $\lambda = 465$ nm.

3.6.2 Temperature-dependent EET

The efficiency of the EET process from Coumarin 343 to NBD in the bichromophoric system **DA** was evaluated *via* two different steady-state methods, Method III, considering the EET-induced increase of the acceptor emission, and Method IV, relying on the comparison between absorption and excitation spectra of the dyad.

In Figure 3.36 (a) we compared the absolute emission intensity of the isolated acceptor, i.e. reference dye **A**, with the absolute emission of NBD in an equimolar solution of **DA** recorded under the same experimental conditions. The latter was extracted from the deconvolution of the experimental spectrum of **DA** with the emission spectra of **D** and **A**. At any temperature the emission spectrum of NBD in **DA** is more intense than the spectrum of NBD alone, confirming the occurrence of EET. The sensitization of NBD emission increases as temperature is decreased, suggesting that EET is favoured at lower temperatures.

EET efficiency was estimated through Eq.3.17 (Method III), using the experimental values of the molar extinction coefficients of **D** and **A** and the emission intensity of the acceptor in presence of the donor obtained through the fitting procedure described above. The emission intensity of **A** should be taken as the emission intensity of the acceptor in the absence of EET. However, this is not the best choice in our case. The emission quantum yield of **A** at room temperature amounts to 62%. Conversely,

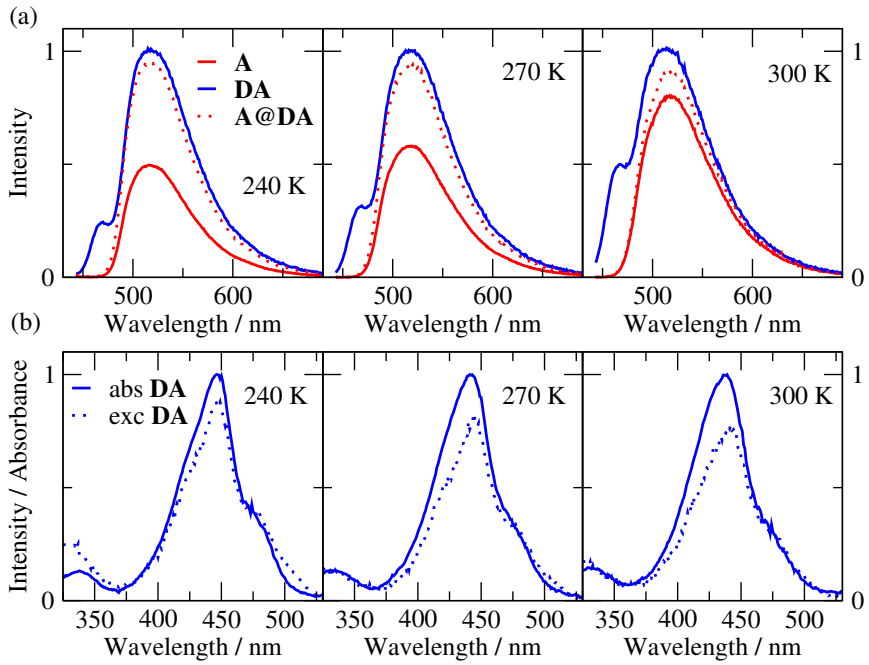

Figure 3.36: Evidences of EET in **DA** and its temperature dependence in chloroform. (a) Sensitization of NBD emission at selected temperatures. The emission spectrum of reference acceptor (continuous red line) is compared to the emission spectrum of NBD obtained from deconvolution of **DA** emission spectrum obtained for $\lambda_{exc} = 438$ nm (blue line: emission of **DA**, red dotted line: contribution of NBD emission to **DA** spectrum). Spectra were collected under the same experimental conditions. (b) Comparison between the absorption spectrum of **DA** (continuous line) and its excitation spectrum obtained collecting the emission from the sole acceptor ($\lambda_{em} = 650$ nm) normalized at the acceptor maximum (dashed line).

considering the emission obtained when selectively exciting NBD in **DA** ($\lambda_{exc} = 480$ nm) we obtained QY = 23%. Backward energy transfer can be ruled out thanks to the negligible overlap between the emission spectrum of **D** and the absorption spectrum of **A**, so that the latter estimate coincides with the quantum yield of the acceptor in the absence of EET. The lower value is an indicator of the activation of new (nonradiative) decay paths in the dyad other than EET. It follows that the best estimate of the acceptor emission in the absence of EET is the one obtained from direct excitation of NBD in **DA**, and was used in the estimation of ϕ_{EET}, after properly rescaling for the absorbance at the excitation wavelength. EET efficiencies obtained with this method are collected in Figure 3.37 and slightly decrease as temperature is increased.

Estimation of ϕ_{EET} through Method IV requires the collection of the excitation spectrum of the bichromophoric system for selective detection of the acceptor emission. The excitation spectrum is rescaled with respect to the absorption spectrum to get the same height of the acceptor band, and the relative heights of the donor bands are compared. Since absorption of NBD overlaps with absorption of Coumarin 343, we resorted again to a fitting procedure to separate the contributions of donor and acceptor.

In more detail, normalized absorption and excitation spectra of **DA** were fitted independently with the sum of normalized absorption spectra of **D** and **A** weighted by appropriate coefficients. Then, the excitation spectrum was rescaled in order to match the acceptor contribution to absorption, and the comparison between the rescaled donor contributions gave an estimate of EET efficiency. In the limit of $\phi_{EET} = 1$ absorption and excitation spectra are expected to perfectly match, on the opposite, for non quantitative transfer, a decrease of the donor band in the excitation spectrum is predicted. For **DA** (Figure 3.36 (b)) a mismatch between absorption and excitation spectra was found at any temperature, suggesting $\phi_{EET} < 1$. Moreover, the donor contribution to excitation decreases as temperature is increased, indicating that EET becomes less efficient as the sample is heated.

Experimental values of ϕ_{EET} estimated over the investigated temperature range are shown in Figure 3.37 and decrease from more than 70% at 240 K to less than 60% at 300 K. These results are in agreement with those obtained with Method III and confirm temperature-dependent EET at the

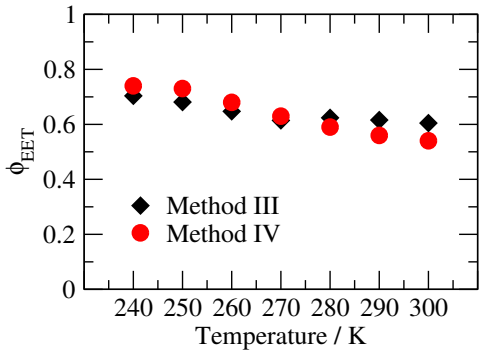

Figure 3.37: EET efficiency (ϕ_{EET}) at different temperatures estimated from sensitization of the emission from the acceptor (Method III) and from the comparison between absorption and excitation spectra of the dyad (Method IV).

basis of the capability of **DA** to work as a temperature probe.

Different factors could be responsible for the variation of EET efficiency with temperature, among which a variation of the overlap integral J between emission of the donor and absorption of the acceptor, the temperature-dependence of the solvent refractive index, a variation of the donor quantum yield or a modification of the donor-acceptor distance/orientation. Spectral overlap, solvent refractive index and quantum yield of the donor, together with the orientational factor, define the Förster radius R_0 for the EET pair (Eq. 3.11).

The quantum yield of **D** is almost constant over the investigated temperature range, while the $\sim 20\%$ decrease of the overlap integral occurring from 240 K to 300 K is compensated by the concomitant decrease of chloroform refractive index (Table 3.9). The orientational factor k is instead more difficult to evaluate, so that we defined an effective Förster distance $R_k = R_0/\sqrt[6]{k^2}$ which incorporates it. R_k values were found to be almost temperature-independent ($R_k \approx 42 - 43$ Å), so that a different origin of the temperature dependence of EET should be invoked.

The relation between EET efficiency and R_k reads as following

$$\phi_{EET} = \frac{R_k^6}{R_k^6 + r_k^6} \tag{3.31}$$

where we indicated with r_k the effective interchromophoric distance incorporating the orientational factor, defined as $r_k = r/\sqrt[6]{k^2}$. Having demonstrated that R_k is constant, the temperature-dependence of ϕ_{EET} should originate

Table 3.9: EET data in chloroform for **DA** at various temperatures. n: solvent refractive index [483, 484], $QY_{\mathcal{D}}$: quantum yield of the isolated donor (**D**), $J(\lambda)$: overlap integral, R_k: effective Förster distance (incorporating the orientational factor), r_k: effective interchromophoric distances calculated from EET efficiencies estimated through Method IV.

T / K	n	$QY_{\mathcal{D}}$%	J / mol^{-1} L cm^{-1} nm^4	R_k / Å	r_k / Å
240	1.4844	106	3.46×10^{14}	42.9	36.1
250	1.4779	97	3.47×10^{14}	43.1	36.5
260	1.4714	99	3.35×10^{14}	43.0	37.9
270	1.4648	97	3.19×10^{14}	42.7	39.1
280	1.4583	98	3.03×10^{14}	42.5	40.0
290	1.4517	100	2.86×10^{14}	42.2	40.1
300	1.4454	64	2.86×10^{14}	42.4	41.2

from a variation of r_k. Indeed, taking experimental values of ϕ_{EET}, we calculated an effective interchromophoric distance increasing from 36 to 41 Å from 240 to 300 K, in agreement with the conformational variations evidenced by ^{1}H NMR spectroscopy.

The typical distance between carbon atoms on the distal positions of the upper rim of a calix[4]arene ranges from $\sim$ 5 to $\sim$ 10 Å [378], so that the variation of r_k becomes significant in view of the small dimension of the bichromophoric system, and also has a large impact on the EET efficiency thanks to its sixth-power dependency.

Finally, we tested the ability of **DA** to work as a ratiometric temperature probe in other solvents: toluene, a nonpolar and non-hydrogen bonding solvent, and two hydrogen bonding solvents, acetone and ethanol (Figure 3.38). The probe performs well in toluene, with the same sensitivity obtained in chloroform (4% K^{-1}). Conversely, in H-bonding solvents, the sensitivity is significantly decreased, according to the specific H-bonding ability of the solvent. The residual sensitivity of the probe amounts to 1% in acetone, a H-bond acceptor, and is further halved in ethanol, a strong H-bond donor and acceptor.

This behaviour provides another proof of the involvement of the intramolecular hydrogen bond between amido functionalities on the spacers in the working mechanism of the probe. Indeed, polar solvents which are able to compete in forming hydrogen bonds destabilize the closed conformation

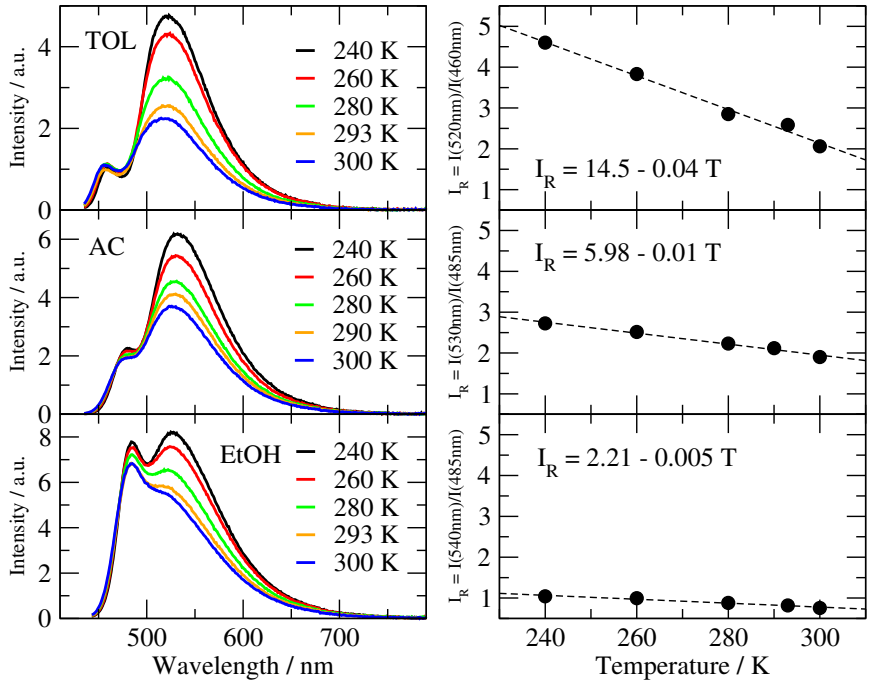

Figure 3.38: Effect of the solvent on the performance of the probe. Left panels: emission spectrum of **DA** as a function of temperature in different solvents (TOL: toluene, AC: acetone, EtOH: ethanol). Right panels: intensity ratio I_R between emission intensity at the maximum of NBD band and the emission intensity at the maximum of Coumarin 343 band (dots). Linear fits (corresponding equations on the panels) are shown as dashed lines.

inhibiting the thermal responsiveness of the scaffold.

In conclusion, we demonstrated that the novel dyad **DA** behaves as a ratiometric temperature probe combining EET between a suitable pair of fluorophores with the thermoresponsive conformational mobility of the scaffold connecting them. The amido groups inserted on the spacers participate in an intramolecular hydrogen bond, which favours a closed flattened cone conformation, in which the fluorophores are brought at short distance. Relevantly to our aims, the strength of the intramolecular H-bond can be modulated by temperature. At low temperatures the amido groups are strongly bonded, and fluorophores are close together, ensuring efficient EET from Coumarin 343 to NBD. An increase of temperature induces the loosening of the H-bond, increasing the interchromophoric distance and decreasing in turn EET efficiency. The temperature-dependent EET is responsible for a variation of the relative intensities of the emission bands of the fluorophores, which allows for a ratiometric readout.

The figures of merit of this nanothermometer are good sensitivity and reproducibility over a 60 K-wide temperature range, short equilibration times and ease of use. Besides the specificity of this system, the exploitation of conformational mobility of cone calix[4]arenes in the design of molecular temperature probes based on EET is presented here for the first time and provides well-controllable structures, easy to characterize and functionalize according to specific needs thanks to the rich chemistry of calixarenes.

Given its low solubility in water, the application of **DA** as a temperature probe is limited to low polarity solvents and non H-bonding environments, making this system unsuitable for biological applications. However, the proposed strategy can be considered for the design of more soluble systems also featuring alternative opening/closure mechanisms of the calix.

3.7 Conclusion

Bichromophoric structures in which a suitable pair of organic fluorophores is covalently anchored at the upper rim of a calix[4]arene are useful and versatile systems for the investigation of the interchromophoric interactions. In this Work we investigated two fundamental phenomena of important technological interest, excitation energy transfer and electron transfer, through

the tailored design and characterization of a series of molecular dyads based on the calix[4]arene scaffold and different organic fluorophores.

A few systems especially designed for EET study were based on two pairs of BODIPY dyes properly chosen to act as energy donor/acceptor pairs. For the first EET couple, anchored at the distal positions of a calix[4]arene in the cone conformation, a fast and efficient EET was observed through steady-state and time resolved spectroscopic techniques and rationalized through theoretical investigation. The dynamics of the process are strongly affected by the solvent polarity and in cyclohexane a sizeable slowdown was noticed, explained by the competition between forward and backward EET, which was experimentally assessed. The different behaviour in cyclohexane is mostly related to emission solvatochromism of the dyes, responsible for a finite overlap between the emission of the energy acceptor and the absorption of the energy donor in this solvent. A regime of weak electronic coupling between the fluorophores emerged both from experimental and theoretical analysis, making Förster theory a suitable theoretical framework to rationalize the EET phenomenon.

For the second couple of BODIPY dyes, two bichromophoric systems characterized by a different conformation of the calix (cone and 1,3-alternated) were investigated and compared in different solvents. The EET efficiency estimated according to the Förster theory for the dyad containing the cone calixarene was unexpectedly higher than the efficiency of the alternated isomer in which the fluorophores, thanks to the constrained mobility of the macrocycle and the rigidity of the spacers, are expected to be at shorter distance. Several hypothesis were made on the origin of this behaviour: the occurrence of backward energy transfer in the alternated isomer, or the adoption of a relative orientation of the fluorophores which is unfavourable for EET. Accordingly, the flexibility of the cone conformation could modulate the interchromophoric interaction accelerating EET. Moreover, from the essential-state modelling of the isolated fluorophores, treated as simple push-pull dyes, large transition dipole moments were obtained, which, for short distances, may lead to the failure of the dipole approximation at the heart of Förster theory. A deeper investigation of this interesting system is required at both experimental and theoretical level, to investigate the dynamics of the process.

We also proposed the study of a bichromophoric system in which the active units, Nile Red and fullerene, can act at the same time as energy donor/energy acceptor and electron donor/electron acceptor pair. The interplay between EET and eT was addressed through steady-state spectroscopy. Preliminary results confirmed the occurrence of EET from Nile Red to fullerene with good efficiency, but also provided indirect evidence of eT, even if to a smaller extent. We suggested more experimental studies to support the hypothesis of eT, including transient absorption and electrochemical measurements.

Calixarene-based dyads are not only ideal model systems for fundamental studies but, after proper design, are promising for applications as well. In the last Section of the Chapter we presented a bichromophoric system acting as a sensible and reversible ratiometric temperature probe over a wide temperature range exploiting EET between a pair of organic fluorophores. The probe relies on the conformational mobility of the calix scaffold and specific (H-bonding) interactions between the spacers which are triggered by heating and allow for a control over the calix conformation, modulating the interchromophoric distance/orientation according to the temperature. As unraveled through extensive spectroscopic investigation, the temperature-induced modulation of interchromophoric distance/orientation affects EET efficiency, modifying the relative emission intensities of the fluorophores, allowing for a ratiometric readout. Although the optimal performance of the probe described herein is restricted to non H-bonding solvents, the basic strategy is more general and paves the way to the exploration of a new class of EET-based nanothermometers exploiting the conformational flexibility of a macrocyclic scaffold as the driving force.

Conclusions and outlook

Optical properties of polar and polarizable chromophores are strongly affected by environmental and interchromophoric interactions. For this reason, the optical properties of molecular materials can be controlled not only by the chemical design of the molecular units, but also at the supramolecular level, exploiting collective and cooperative effects arising from their sensitivity to the surrounding medium. The tunability of the optoelectronic response of molecular and supramolecular systems, which sets the basis for the design of efficient photonic and functional devices, is currently at the frontier of materials science.

To this aim, the investigation of the relationship between the low-energy photophysics and the molecular or supramolecular structure of representative systems is an unavoidable step towards the mastering of physical and chemical engineering, and can benefit from the synergistic exploitation of advanced spectroscopic and computational tools.

In this Thesis, we presented a selection of representative examples, including solvated multipolar dyes, aggregates (dimers, crystals, nanoparticles) and custom-designed heterobichromophoric systems, which allowed us to shed light on the interdependence of optical properties and interactions with the surrounding medium, paving the way to its rational exploitation in functional materials and devices.

Our study combined the experimental characterization with spectroscopic techniques (steady-state and time resolved absorption and emission spectroscopies) and the rationalization of the experimental outcome through extensive theoretical modelling, adopting complementary theoretical frameworks. This analysis allowed to disclose interesting phenomena of broad significance in the field of (multi)polar chromophores for photonic and op-

toelectronic applications.

The investigation of multipolar dyes in solution offered the possibility to address the subtle interplay between their intrinsic electronic structure, electron-phonon coupling, and solute-solvent interactions.

The chemical structure of the chromophore sets the basis of its electronic properties, and the development of innovative chemical designs is a tool to achieve a favourable combination of spectral features. For instance, we demonstrated that it is possible to build a quadrupolar-like dye undergoing excited-state symmetry breaking embedding an electron rich heterocyclic building block into an intrinsically nonpolar graphene-like nanostructure. Noteworthy, the resulting excited-state scenario is unique and originates from the synergy between closely spaced CT and LE transitions, ensuring for example efficient light harvesting over a wide spectral range and good emission quantum yields over a wide solvent polarity range. For these reasons, aza-nanographenes are likely to represent a new interesting class of chromophores deserving further attention.

In this Work we also tested complementary theoretical frameworks, TDDFT and ESMs, against spectroscopic data, indicating that their combined application provides a deeper understanding of complex systems. From one hand, TDDFT does not require a precise *a priori* knowledge of the system under study, and offers a quite detailed insight of the nature of electronic excitations, permitting to identify their LE or CT character. Therefore, it represents a useful starting point to get an overview of the electronic structure of new dyes. On the other hand, ESMs are applicable only to model a subset of dye states, and their application relies on chemical intuition concerning the choice of the most suitable basis set. Nevertheless, after validation against experimental or TDDFT data, ESMs represent a powerful and flexible approach to get a comprehensive and physically sound picture of the low-energy spectroscopy of multipolar dyes, including the description of the coupling with vibrational degrees of freedom and the interactions with polar solvents, which naturally lead to the description of nontrivial phenomena such as symmetry breaking.

Herein, the ESM strategy was challenged with the description of the rich and controversial spectroscopy of squaraines and core-substituted squaraines, pointing out the intrinsic strengths but also the weaknesses of the approach.

In particular, the addition of states to the electronic basis set is a practical way to improve the level of detail on the spectral features, but introduces at the same time more degrees of freedom, and the more difficult parametrization is not compensated by the increased flexibility of the model. In other words, the effectiveness of ESMs is lost with the excessive increase of model parameters, bringing about the risk of an unphysical description of the dyes at hand. Specifically, the failure of ESMs on squaraines has likely to be related to the mixed LE/CT nature of some states, the coupling with vibrations, and electronic effects of the substituents on the squaric core, which have to be properly understood with the help of additional experimental and first principle computations before setting the correct essential-state framework.

In concentrated solutions, in the solid state, or in nanosystems, the interactions between the aggregated molecules are responsible for collective phenomena, which modify their electronic structure with respect to the solvated molecule, leading to sizable spectroscopic effects. Two different kinds of interchromophoric couplings can be recognized in molecular aggregates. The excitonic coupling, which is usually approximated as the interaction between transition dipole moments in the so-called excitonic approximation, and mean-field effects, arising as a consequence of the reciprocal polarization between interacting molecules. In aggregates of nonpolar and hardly polarizable chromophores, the only coupling is excitonic, and the exciton model can be safely adopted as a guide to relate the geometrical arrangement of the aggregate to its spectroscopic features, like a red (or blue) shift of the absorption band and an enhancement (or quenching) of fluorescence, which usually denote J- (or H-) aggregation. Conversely, aggregates of polar and polarizable systems undergo also sizable mean-field effects, which are responsible for cooperative nonadditive behaviour, and need to be carefully included into theoretical frameworks to accurately rationalize experimental data.

The ESM formalism is a powerful tool to explore the effects of interchromophoric interactions in clusters of polar/polarizable molecules. Indeed, once the few model parameters have been fixed, ESMs can be readily extended to model interacting chromophores, accounting for both excitonic and mean-field effects. In this Work, ESMs were applied to disentangle

excitonic and mean-field contributions to absorption and phosphorescence spectra of interacting push-pull dyes, predicting that mean-field effects are responsible for quite impressive variations of the phosphorescence energy with respect to the non-interacting molecule. On the other hand, excitonic coupling only perturbs the energy of the singlet states, leaving the triplet manifold unaffected. These general results were corroborated by a complementary TDDFT analysis on selected examples of a nonpolar system and of a highly polarizable one and suggest, only for the latter, the possibility to tune phosphorescence emission through intermolecular interactions.

This conclusion is significant in and of itself, as it demonstrates, for molecular materials made of polarizable units, the possibility to tailor the phosphorescence energy through supramolecular engineering. For this reason, we expect CT phosphorescent systems to attract more attention in the future, especially if combined with the opportunity to switch between two (or more) metastable aggregated phases with different emission colour through a soft external stimulus such as pressure or heat.

The same strategy is currently exploited in fluorescent dyes characterized by differently packed interconvertible forms. One of the main issues consists in relating the supramolecular organization of the dyes and its variation upon external inputs to the chemical structure of the molecule. Herein we considered side-chain engineering as a tool to direct self-assembly. Indeed, interchain interactions compete with the interactions driven by the conjugated backbone, such as $\pi - \pi$ stacking, originating differently packed species whose relative abundancy is highly sensitive to external conditions.

Intermolecular interactions are also at the basis of scientifically and technologically relevant phenomena like EET and eT. In order to fully exploit the possibilities offered by these processes, for example in the construction of efficient devices for energy conversion, the comprehensive understanding of their mechanism is highly desirable. The design and characterization of simplified model systems, for example molecular dyads obtained from the linkage of two active units through a suitable scaffold, offers the possibility to focus on the interplay of a limited number of factors at a time, and also to define a series of artificial alternatives to biomimetic systems.

Calix[4]arenes are good scaffolds for the connection of donor/acceptor pairs, as they grant for interchromophoric distances small enough to enable

an interaction between the EET/eT partners, they offer the choice between different conformations allowing to control the intermolecular distance and orientation, and their residual conformational mobility can be exploited for functional applications.

In this Thesis, the study of a family of model bichromophoric calix[4]arene-based systems disclosed the role of few significant factors affecting the efficiency and dynamics of EET. In particular, the EET kinetics can be affected by solvent polarity, and in nonpolar solvents a competition between forward and backward EET may occur, repopulating the energy levels of the donor on a long timescale. Interestingly, also the conformation of the calix scaffold is likely to perturb the interchromophoric interactions, setting a more complex scenario for EET, and this aspect will be further investigated in upcoming studies. Moreover, the careful selection of the coupled chromophores, concerning the alignment between their energy levels, the donor quantum yield and the spectral overlap, may enable a competition between EET and eT.

Calix[4]arene-based dyads undergoing EET can be exploited for temperature sensing at the nanoscale. The idea proposed in this Thesis exploits the conformational mobility of cone calix[4]arenes in solution, which modulates the interchromophoric distance of a suitable EET pair. We demonstrated that a calixarene-based bichromophoric system can be engineered to induce the thermal responsiveness of the scaffold, relating the efficiency of EET to temperature, which is exploited for a ratiometric readout. The prototype reported herein offers good sensibility, reproducibility and robustness, and is the first example of a EET-based molecular temperature probe exploiting the conformational mobility of a macrocyclic scaffold as the driving force. We envisage that the same strategy can be implemented with different structural designs and donor/acceptor pairs, to widen the potential area of application, including aqueous and biological media and temperature mapping of nanoconfined environments.

Appendix A

Experimental details

A.1 Absorption and emission spectroscopy

Spectroscopic measurements at room temperature were performed on freshly prepared air-equilibrated solutions. In order to avoid self-absorption processes, inner-filter effects and/or aggregation, the maximum absorbance of the samples was kept lower than 0.1, corresponding to a concentration $c \approx 10^{-6}$ mol^{-1} L^{-1}. Solvents were spectroscopic grade and were used as received.

Absorption spectra were collected with a Perkin-Elmer Lambda 650 UV/vis double-beam spectrophotometer, and the samples were contained in 1 cm^2 quartz cells. Molar extinction coefficients were estimated as the average of independent measurements on solutions of different concentration, obtained by dilution of a stock solution of the sample (typically $c \approx 10^{-4}$ mol^{-1} L^{-1} for the stock solution). The Beer-Lambert law was verified over a concentration range spanning at least three orders of magnitude ($c \approx 10^{-4} - 10^{-6}$ mol^{-1} L^{-1}).

Concerning absorption spectra on ground powders, a small amount of sample was manually ground in a mortar and then spread on the surface of a quartz plate. The plate was then positioned vertically into the sample holder of the spectrometer, and the light transmitted by the sample was detected, using air as reference.

Emission spectra were collected either with a FluoroMax-3 (Horiba Jobin-Yvon) or a FLS1000 (Edinburgh Instruments) fluorometer, both of them

equipped with a Xenon lamp as the excitation source. Emission measurements in the near-IR were performed with the FLS1000 instrument equipped with a PMT-1700 detector in liquid Nitrogen cooled housing. Emission and excitation spectra were corrected for the excitation intensity and detector sensitivity.

Absorption and emission measurements at variable temperature were performed in a OptistatDN (Oxford Instruments) cryostat, equipped with a ITC601 temperature controller (Oxford Instruments). The cryostat was fit into the sample holder of the Lambda 650 spectrophotometer for absorption measurements on concentrated samples, and in the FLS1000 or Fluoromax-3 fluorometers for emission measurements. Qualitative temperature-dependent absorption spectra were also collected with the FLS1000 instrument equipped with an accessory for the detection of transmitted light.

A.1.1 Fluorescence quantum yields

Fluorescence quantum yield ϕ of a fluorophore measures the fraction of molecules following a radiative decay after photoexcitation [151, 152]. It is defined as the ratio of the number of emitted photons to the number of absorbed photons. Practically, it can be expressed as follows

$$\phi = \frac{k_r}{k_r + k_{nr}} \tag{A.1}$$

where the radiative decay rate k_r represents the number of emissive events per unit time, while the nonradiative decay rate k_{nr} accounts for all the other decay processes. The brightest emissions ($\phi \to 1$) are obtained from fluorophores for which $k_{nr} \ll k_r$.

The absolute measurement of ϕ requires the detection of *all* absorbed and emitted photons, and can be done with special equipment, called integrating spheres. Usually, for dilute solutions, a determination of a relative quantum yield is preferred, by comparison with a fluorophore with known ϕ [486]. In this case, the quantum yield of the sample is obtained as

$$\phi = \phi_R \, \frac{I_X}{I_R} \, \frac{OD_R}{OD_X} \, \frac{n_X^2}{n_R^2} \tag{A.2}$$

where ϕ_R is the quantum yield of the reference fluorophore, I is the integrated emission spectrum, OD the absorbance at the excitation wavelength,

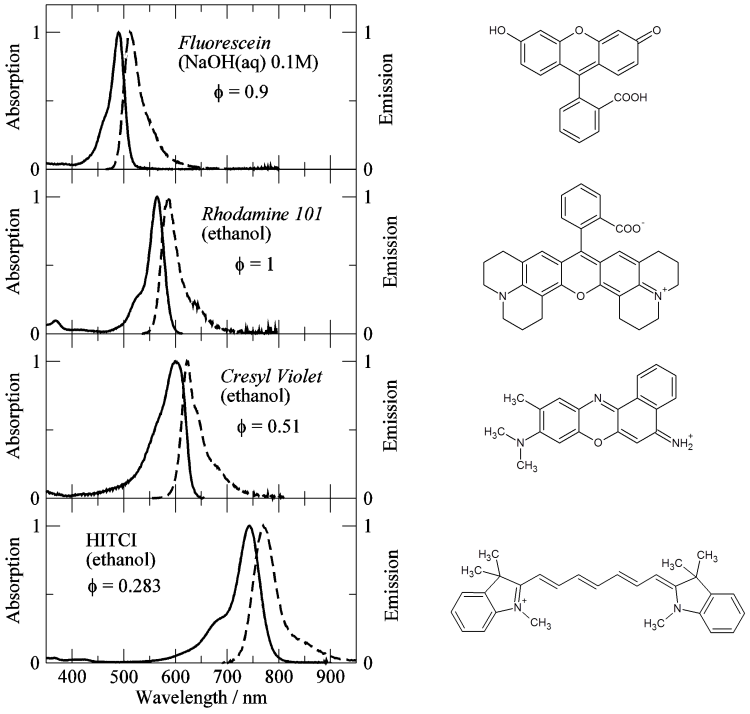

Figure A.1: Some standards for fluorescence quantum yield measurements used in this Work: fluorescein, rhodamine 101, cresyl violet and 1,1',3,3,3',3'-hexa-methyl-indotricarbocyanine iodide (HITCI) [485]. Left panel: normalized absorption (continuous line) and emission (dashed line) spectra. The chemical structure of the fluorophores is reported on the right.

and n the solvent refractive index. The subscripts X and R refer to the sample and the reference respectively. This method allows for the determination of ϕ with an error on the order of 10%.

The ideal standard for fluorescence quantum yield measurements absorbs and emits in the same spectral regions of the sample, and its spectra must be collected under the same experimental conditions. A variety of standards are available in the whole UV/vis spectral range, a selection is presented in Figure A.1.

A.1.2 Emission lifetimes

Together with fluorescence quantum yield, emission lifetime τ is one of the fundamental characteristics of a fluorophore. It measures the average time the fluorophore spends in the excited state before decaying to its ground state. Emission lifetime is quantitatively expressed by

$$\tau = \frac{1}{k_r + k_{nr}} \tag{A.3}$$

and is typically of the order of few ns.

Supposing we are exciting the sample with a pulse of light, the population of fluorophores in the excited state $[F(t)^*]$ follows a first-order decay:

$$\frac{d[F(t)^*]}{dt} = -(k_r + k_{nr})[F(t)^*] \tag{A.4}$$

Being $[F(t)^*]$ proportional to the measured emission intensity $I(t)$, integration between $t = 0$ and t yields the exponential function

$$I(t) = I_0 \exp\left(-\frac{t}{\tau}\right) \tag{A.5}$$

where the lifetime τ is the time at which the emitted intensity amounts to $1/e$ of its initial value I_0.

Emission lifetime and fluorescence quantum yield are related by

$$\tau = \phi \, \frac{1}{k_r} \tag{A.6}$$

It follows that, known ϕ and τ from independent measurements, it is possible to explicitly retrieve k_r and k_{nr} through Eq. A.3 and A.6.

The most common technique for the measurement of excited-state lifetimes is the Time-Correlated Single-Photon Counting (TCSPC), in which

the photons emitted by the sample are detected and counted individually. In this work pulsed NanoLEDs or laser diodes with ps-pulses were used as excitation sources. Electronics for TCSPC measurements were supplied to the Fluoromax-3 instrument by the FluoroHUB module, while were built-in by the manufacturer in the FLS1000 fluorometer. Experimental τ values were extracted from a reconvolution analysis of the decay profiles and the goodness of the fit was judged by the reduced chi-square value ($\chi^2 \leq 1.2$) and by visual inspection of the weighted residuals.

A.2 Fluorescence anisotropy

Fluorescence anisotropy describes the degree of polarization of photons emitted by a sample excited with polarized light. Anisotropy measurements are widely adopted in fluorescence studies of many biochemical systems, allowing to retrieve information on the size and shape of macromolecules and the fluidity of the surrounding medium [151]. At the same time, anisotropy is also a useful spectroscopic tool for accessing more fundamental properties of the excited-states of fluorophores, as we did in this Thesis work. In the following we will summarize the main concepts behind fluorescence anisotropy and provide some practical information on measurement conditions.

A.2.1 Theoretical background

A typical anisotropy experiment requires two polarizers: an excitation polarizer, between the source and the sample, and an emission polarizer, located between the sample and the detector (Figure A.2). The sample is excited with vertically polarized light, and emission intensity is detected along the same direction of polarization ($I_{\parallel}$) and in the perpendicular direction ($I_{\perp}$). Fluorescence anisotropy r is defined as the difference between the measured intensities normalized by the total intensity [151, 152]:

$$r = \frac{I_{\parallel} - I_{\perp}}{I_{\parallel} + 2I_{\perp}} \tag{A.7}$$

r is a dimensionless quantity and depends on both the excitation and emission wavelengths. When it is measured at a fixed excitation wavelength, scanning across the emission wavelengths, it is referred to as emission ani-

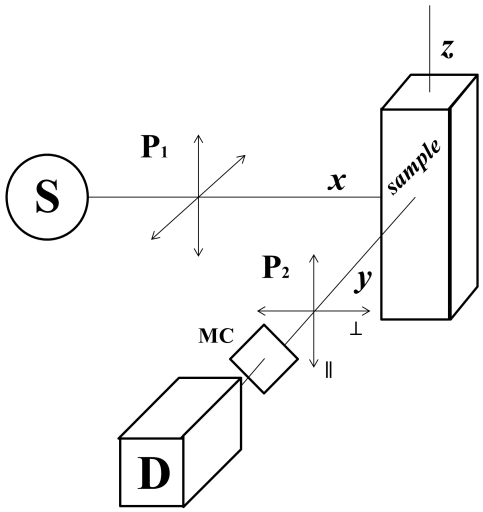

Figure A.2: Schematic view of the anisotropy measurement setup. Light from the source (S) passes through the excitation polarizer P_1, oriented along z, and excites the sample. Emission of the sample is collected by the detector (D) through a second polarizer (P_2), that can be oriented along z (measurement of the parallel component $I_{\parallel}$) or along x ($I_{\perp}$). Emission monochromator is indicated with MC.

sotropy. When it is collected the other way around, at fixed emission wavelength, it is called excitation anisotropy.

In the limiting case of totally depolarized emission $I_{\parallel} = I_{\perp}$, so that $r = 0$. On the opposite, when emission is totally polarized along the direction of the incident light (z), $I_{\perp} = 0$ and $r = 1$. The latter case is never found in practice. Indeed, $r = 1$ would require all the molecules in the sample to be simultaneously oriented with absorption and emission dipole moments along z. In solution the molecules of sample are randomly oriented, so that the angle θ between the electric vector of the incident light and the absorption transition moment of the molecule assumes a distribution of values. The probability of excitation scales with $\cos^2\theta$, so that only a subset of fluorophores, those partially oriented along z, will be photoexcited. This phenomenon, called photoselection, is responsible for the formation of a population of molecules in the excited-state preferentially oriented along

z. It is possible to demonstrate that the maximum value of r that can be obtained in a sample undergoing photoselection is 0.4. $r = 0.4$ occurs when absorption and emission dipole moments are collinear, and there are not depolarization processes.

Rotational diffusion of the solute during its excited-state lifetime is a source of depolarization, and may lead to a decrease of fluorescence anisotropy. Small molecules rotate rapidly, completely depolarizing the signal. On the opposite, for macromolecules with rotational times comparable to their decay time, this phenomenon is exploited for the determination of the size.

In absence of depolarization processes, the measured anisotropy coincides with the so-called fundamental anisotropy, r_0. The fundamental anisotropy of a fluorophore depends on the angle α between the absorption and emission dipole moments, according to

$$r_0 = \frac{2}{5}\left(\frac{3\cos^2\alpha - 1}{2}\right) \tag{A.8}$$

It follows that r_0 is a number between 0.4, for collinear absorption and emission dipole moments ($\alpha = 0$), and -0.2, for perpendicular dipoles ($\alpha = 90°$). The angle for which $r_0 = 0$ ($\alpha = 54.7°$) is called magic angle.

Measurement of the fundamental anisotropy requires the suppression of the solute rotational diffusion. For this reason measurements are typically performed in highly viscous solvents (glycerol, propylene glycol, polytetrahydrofuran are some examples) or in a vitrified solvent. Under these conditions the motion of solute during the excited-state lifetime can be safely neglected.

In this way, anisotropy is a powerful spectroscopic tool for the investigation of the polarization of absorption transitions relative to emission. Usually, according to the Kasha rule, fluorescence occurs from the lowest-energy singlet state S_1, so that the angle α in Eq. A.8 is measured relative to the $S_0 \leftarrow S_1$ transition dipole moment. Thus, in an excitation anisotropy experiment, r is expected to assume different values corresponding to different absorption bands, according to the specific polarization of each $S_0 \rightarrow S_n$ transition.

In the lowest-energy range, corresponding to the $S_0 \rightarrow S_1$ transition, anisotropy is expected to be close to the maximum limiting value 0.4, since in this region the same transition is involved both in absorption and emission, and hence $\alpha = 0$. Conversely, emission anisotropy only depends on the state

populated in absorption, and remains usually flat across the whole emission spectral range.

A.2.2 Measurement methods

Two methods are adopted for anisotropy measurements: the single channel method, also called L-format, in which the intensities $I_{\parallel}$ and $I_{\perp}$ are obtained from different measurements, and the T-format, in which they are collected simultaneously through separate channels. We will consider only the former method, that is the one available for our experimental setup.

The emission monochromator transmits with different efficiencies the $I_{\parallel}$ and $I_{\perp}$ components, leading to $r \neq 0$ also for completely depolarized light. Therefore, the experimental protocol must quantify and remove these artifacts.

The effective intensities measured when both excitation and emission polarizers are vertically oriented (I_{VV}) and when the second polarizer is turned horizontal (I_{VH}) can be written as

$$I_{VV} = kS_V I_{\parallel} \tag{A.9}$$

$$I_{VH} = kS_H I_{\perp} \tag{A.10}$$

where we denoted with S_V (S_H) the sensitivity of instrumental optics for the vertically (horizontally) polarized light, and k is an instrumental constant. Dividing Eq. A.9 by Eq. A.10 one obtains:

$$\frac{I_{VV}}{I_{VH}} = G\frac{I_{\parallel}}{I_{\perp}} \tag{A.11}$$

where G, also called *G-factor*, depends on the emission wavelength and is given by:

$$G = \frac{S_V}{S_H} \tag{A.12}$$

G can be experimentally determined from measurements with horizontally polarized excitation light (I_{HH} and I_{HV}). Under this condition both emission polarization directions become perpendicular to the polarization of excitation, and proportional to $I_{\perp}$. Differences between I_{HH} and I_{HV} are due to the detection system only:

$$\frac{I_{HV}}{I_{HH}} = \frac{S_V I_{\perp}}{S_H I_{\perp}} = \frac{S_V}{S_H} = G \tag{A.13}$$

Once the G-factor is known, anisotropy can be calculated as:

$$r = \frac{I_{VV} - GI_{VH}}{I_{VV} - 2GI_{VH}} \tag{A.14}$$

In this Thesis, anisotropy was exploited to explore the polarization of the excited-states in a variety of fluorophores. Thus, we chose experimental conditions minimizing rotational diffusion during the excited-state lifetime, ensuring $r = r_0$.

Anisotropy measurements were performed on dilute solutions to minimize scattering and re-absorption processes and, depending on the system under investigation, we employed either a viscous or glassy solvent. Polytetrahydrofuran is a mildly polar and viscous solvent at room temperature, and was used as received. Measurements in glassy solution required instead more careful sample preparation. The solvents chosen were methylcyclohexane and 2-methyltetrahydrofuran, and both of them undergo the formation of a transparent glass when rapidly cooled below their glass transition temperature. To remove traces of moisture, that could lead to solvent crystallization, solvents were stored overnight under molecular sieves (0.3 nm) and were filtered on Teflon® disposable filter before use to eliminate residual dust.

2-methyltetrahydrofuran solutions were vitrified in a OptistatDN (Oxford Instruments) cryostat, using liquid nitrogen as the cooling agent. The cryostat is equipped with an external chamber for thermal insulation kept under high vacuum. Samples, contained in special cuvettes for cryogenics, were inserted in the central chamber of the cryostat, located in the lower part, and possessing transparent windows to allow optical contact with the exterior. The sample chamber was evacuated with a rotatory pump and filled with dry Helium at ambient pressure which, having a good thermal conductivity, ensures good thermal exchange. The liquid nitrogen stored in a reservoir flows by gravity on a capillary tube at a flow rate controlled by a valve, cooling the sample by convection. The maximum speed of cooling of this system is ~ 20°C/min. Once the minimum temperature (77 K) was reached, the sample was left equilibrating for a few minutes before measurement.

The maximum cooling speed of this setup was too slow to induce vitrification of methylcyclohexane, for which a different technique was adopted.

In this case the solution, contained in a special quartz tube, was directly immersed into a transparent quartz dewar filled with liquid nitrogen and fitted into the fluorometer, promoting instantaneous formation of a good quality glass.

Appendix B

An introduction to (Time-dependent) Density Functional Theory

B.1 The electronic problem

A molecule is a collection of nuclei and electrons interacting *via* electrostatic forces. The molecular Hamiltonian can be written as:

$$\hat{H}(\boldsymbol{r},\boldsymbol{R}) = \hat{T}_N(\boldsymbol{R}) + \hat{T}_e(\boldsymbol{r}) + \hat{V}(\boldsymbol{r},\boldsymbol{R}) + \hat{U}(\boldsymbol{r}) + \hat{W}(\boldsymbol{R}) \tag{B.1}$$

where we indicated with $\boldsymbol{r}$ and $\boldsymbol{R}$ the families of electronic and nuclear coordinates respectively.

The first two terms, $\hat{T}_N$ and $\hat{T}_e$, are the kinetic energy operators for nuclei and electrons:

$$\hat{T}_e = -\sum_{i=1}^{N} \frac{\hbar^2}{2m_e}\nabla_i^2 \tag{B.2}$$

$$\hat{T}_N = -\sum_{\alpha=1}^{N_n} \frac{\hbar^2}{2M_\alpha}\nabla_\alpha^2 \tag{B.3}$$

where m_e is the mass of the electron, M_α the mass of the α-th nucleus and summations run over the N electrons and the N_n nuclei of the molecule.

The operator $\hat{V}$ describes the total potential acting on the electrons:

$$\hat{V} = \sum_{i=1}^{N} v(\boldsymbol{r_i}) \tag{B.4}$$

which is given by the Coulomb interaction of the electrons with the distribution of nuclei:

$$v(\boldsymbol{r}) = -\sum_{\alpha=1}^{N_n} \frac{Z_\alpha e^2}{|\boldsymbol{r} - \boldsymbol{R}_\alpha|} \tag{B.5}$$

where we indicated with Z_α the charge of nucleus α.

$\hat{U}$ represents the electron-electron interaction

$$\hat{U} = \frac{1}{2}\sum_{i=1}^{N}\sum_{j=1}^{N} \frac{e^2}{|\boldsymbol{r}_i - \boldsymbol{r}_j|} \tag{B.6}$$

while the last term $\hat{W}$ accounts for the repulsive interactions between nuclei:

$$\hat{W} = \frac{1}{2}\sum_{\alpha=1}^{N_n}\sum_{\beta=1}^{N_n} \frac{Z_\alpha Z_\beta e^2}{|\boldsymbol{R}_\alpha - \boldsymbol{R}_\beta|} \tag{B.7}$$

The j-th wavefunction Ψ_j of the system can be obtained from the resolution of the Schrödinger equation

$$\hat{H}\Psi_j(\boldsymbol{r}_1, ..., \boldsymbol{r}_N) = E_j\Psi_j(\boldsymbol{r}_1, ..., \boldsymbol{r}_N), \quad j = 0, 1, 2, ... \tag{B.8}$$

As far as we are concerned with a molecule in the ground-state, we are interested in the ground-state wavefunction Ψ_0. The wavefunction contains all the information needed on the system. For example, if we are interested in the property expressed by the quantum mechanical observable $\hat{O}$, we can simply calculate its expectation value in the ground-state by

$$O_{gs} = \langle\Psi_0|\,\hat{O}\,|\Psi_0\rangle \tag{B.9}$$

Solution of Eq. B.8 is a nontrivial task. A simplification of the problem can be achieved resorting to the Born-Oppenheimer (BO) approximation, which allows for the separation of nuclear and electronic degrees of freedom. The nuclear mass is several orders of magnitude larger than the mass of the electron, so that nuclear and electronic motions occur on a different timescale. The nuclei move slowly compared to electrons, and thus we can assume they are fixed. This corresponds to neglecting the nuclear kinetic energy in Eq. B.1 by setting $\hat{T}_N = 0$. Under this assumption, $\hat{W}(\boldsymbol{R})$ becomes a constant depending on the configuration of the nuclei and the remaining Hamiltonian depends parametrically on $\boldsymbol{R}$.

In the BO approximation, the many-body Hamiltonian describing the motion of the electrons in the field of fixed nuclei reads

$$\hat{H}(\boldsymbol{r}, \boldsymbol{R}) = \hat{T}(\boldsymbol{r}) + \hat{V}(\boldsymbol{r}, \boldsymbol{R}) + \hat{U}(\boldsymbol{r}) \tag{B.10}$$

where we set $\hat{T}_e = \hat{T}$ to simplify the notation.

Once the system is defined, i.e. a specific $\hat{V}$ is chosen, the solution of Schrödinger equation B.8 returns Ψ_0, that allows to calculate any property of interest.

The Schrödinger equation can be solved exactly only for non-interacting systems. So far, many approaches have been developed to solve the many-body problem in an approximate way. For example, Hartree-Fock (HF) and Configuration Interaction (CI) methods, known as 'wavefunction-based techniques', expand the wavefunction in terms of Slater determinants and look for a variational solution of the Schrödinger equation. Although the wavefunction-based approach proved successful, it suffers from high computational cost and its application is limited to systems of small size. More efficient techniques are required to deal with complex and large systems [487].

B.2 Density Functional Theory

Density Functional Theory (DFT) constitutes an alternative and complementary approach to traditional wavefunction-based quantum chemical methods. In principle, DFT is equivalent to solving the Schrödinger equation, but focuses, rather than on the wavefunction, on the electron density [157, 487–489].

DFT is an electronic structure method for the ground state of quantum chemical systems. It is based on the idea that all the information on a many-electron system can be obtained from the electron density of the ground-state, without the need of calculating the wavefunction. Today it is the method mostly employed for electronic structure calculations in physics and chemistry, thanks to its versatility and satisfactory accuracy for fairly complex and sizable systems.

The electron density $n_0(\boldsymbol{r})$ describes the spatial distribution of the N electrons:

$$n_0(\boldsymbol{r}) = N \int d^3 r_2 \ldots \int d^3 r_N |\Psi_0(\boldsymbol{r}, \boldsymbol{r}_2, \ldots, \boldsymbol{r}_N)|^2 \tag{B.11}$$

The main assumption of DFT is that knowledge of $n_0(\boldsymbol{r})$ implies the knowledge of the wavefunction and all other observables.

Foundations of DFT rely on the Hohenberg-Kohn (HK) theorems [155]. The first HK theorem states that given a ground-state density $n_0(\boldsymbol{r})$, it is possible to calculate the corresponding ground-state wavefunction $\Psi_0(\boldsymbol{r}_1, ...\boldsymbol{r}_N)$. In other words, the ground-state wavefunction is a unique functional of the ground-state density: $\Psi_0[n_0]$. It follows that any other observable $\hat{O}$ is a functional of the density as well.

According to the second HK theorem, the variational principle for the wavefunctions holds true also for the density. The energy E_{v0} of a system described by a potential $v_0(\boldsymbol{r})$ can be calculated as

$$E_{v0}[n] = \langle \Psi[n] | \, \hat{T} + \hat{V}_0 + \hat{U} \, | \Psi[n] \rangle \tag{B.12}$$

where $\Psi[n]$ is a generic ground-state wavefunction reproducing the density n. Following a variational treatment, the density which minimizes the energy B.12 is the ground-state density n_0 corresponding to $v_0(\boldsymbol{r})$ or, in more general terms

$$\begin{aligned} E_v[n_0] &< E_v[n'] \quad \text{for} \quad n_0 \neq n' \\ E_v[n_0] &= E_v[n'] \quad \text{for} \quad n_0 = n' \end{aligned} \tag{B.13}$$

The energy of the system can also be written as

$$E_v[n] = T[n] + U[n] + V[n] \tag{B.14}$$

In the equation above, $T[n]$ and $U[n]$, defined by the expectation values of the operators $\hat{T}$ and $\hat{U}$ (Eq. B.2 and B.6) are universal functionals, i.e. they are independent of the choice of $v_0(\boldsymbol{r})$. On the opposite $V[n]$, defined as the expectation value of the operator $\hat{V}$ (Eq. B.4), depends on the specific system at hand and, once the potential is fixed, assumes the explicit form

$$V[n] = \int d^3 r n(\boldsymbol{r}) v(\boldsymbol{r}) \tag{B.15}$$

However, minimization of the energy functional B.12 is not the most efficient technique for the calculation of n_0, and a more convenient strategy will be described below.

So far, DFT introduces an enormous simplification of the problem. Indeed, the use of the density is a very convenient choice: it is an intuitive

physical observable and, most of all, it is a function of only three spatial coordinates, irrespective of the size of the system. Conversely, the wavefunction is much difficult to handle, since it contains $4N$ variables, three spatial coordinates and one spin coordinate for each electron, and its dimensionality increases exponentially with the number of electrons.

The following step is to obtain the electron density bypassing the solution of the Schrödinger equation. This problem is solved in the Kohn-Sham (KS) formalism [156]. Specifically, we define a non-interacting system, the KS system, possessing the same ground-state electron density of the interacting system. For the non-interacting system, the electron density can be easily retrieved as the sum of the squares of the single-particle orbitals $\psi_j(\boldsymbol{r})$

$$n_0(\boldsymbol{r}) = \sum_{j=1}^{N} |\psi_j(\boldsymbol{r})|^2 \tag{B.16}$$

where the orbitals satisfy the Kohn-Sham equation

$$\Big[-\frac{\hbar^2\nabla^2}{2m_e} + v_s[n](\boldsymbol{r})\Big]\psi_j(\boldsymbol{r}) = \varepsilon_j\psi_j(\boldsymbol{r}) \tag{B.17}$$

The KS equation is a single-particle Schrödinger equation whose solution is a single Slater determinant. The potential v_s is chosen as the single-particle potential that yields orbitals which, inserted in Eq. B.16, give the exact electron density of the interacting system. This effective potential is, of course, functional of the density: $v_s[n](\boldsymbol{r})$. v_s is unknown, and can be conveniently decomposed into different contributions:

$$v_s[n](\boldsymbol{r}) = v_0(\boldsymbol{r}) + v_H(\boldsymbol{r}) + v_{xc}[n](\boldsymbol{r}) \tag{B.18}$$

The first term, v_0, is the external potential arising from the interaction between electrons and nuclei, while $v_H(\boldsymbol{r})$ is the classical Coulomb electron-electron interaction, also known as Hartree potential. The last term, v_{xc}, is called exchange-correlation (xc) potential and contains all the many-body effects:

$$v_{xc}[n] = \frac{\delta E_{xc}[n]}{\delta n(\boldsymbol{r})} \tag{B.19}$$

v_{xc} is the only unknown contribution to v_s and it can be calculated explicitly only when an approximation for $E_{xc}[n]$ is chosen.

It can be demonstrated [487] that the density B.16 obtained from the exact solution of B.17 is precisely the energy that minimizes B.12. In this

way, the problem of minimizing $E[n]$ reduces to the solution of a Schrödinger equation for a noninteracting system, i.e. a many-body problem is converted into a single-body problem. Since v_H and v_{xc} depend on n, which in turn depends on v_s *via* the orbitals ψ_j, this problem is solved adopting an iterative procedure. Starting from a guess of $n(\boldsymbol{r})$, an estimate of $v_s(\boldsymbol{r})$ is obtained which, inserted in Eq. B.17, allows to get ψ_j. With ψ_j, a new estimate of $n(\boldsymbol{r})$ is calculated and the cycle repeated until convergence is attained. Once n_0 has converged, the total energy of the system can be obtained by Eq. B.14.

DFT theory is formally exact. However, its practical application requires at least two levels of approximation [487]. The first and most important one arises from the choice of the xc energy functional. The second concerns the computational scheme adopted for the solution of the differential equation B.17, which is a source of numerical inaccuracies.

Many approximate models have been developed for the xc energy functional. $E_{xc}[n]$ is usually divided into an exchange part and a correlation part. Both of them can be local, i.e. functionals of the electron density only, or gradient-corrected, i.e. functionals of both n and its gradient ∇n.

The simplest model is known as Local Density Approximation (LDA), and adopts the xc energy of an homogeneous electron gas. It is a good option for solid state physics but a poor approximation for atoms and molecules. Gradient-corrected functionals offer an improvement over the LDA approach, and are of different classes: in Generalized Gradient Approximation (GGA) methods, the variables are the density and its first derivative, while meta-GGA methods also include higher-order derivatives of n.

Very popular and accurate methods are the so-called hybrid methods, which include a mixture of Hartree-Fock (HF) exact exchange energy and DFT exchange and correlation. They differ for the type of functionals that are mixed and for the different weight assigned to the HF and the DFT parts. One of the most popular hybrid functionals is B3LYP, a combination of a GGA functional (LYP) [490] for correlation with the hybrid functional B3 for exchange [158].

B.3 Time-dependent DFT

DFT offers a solution to the stationary many-body problem, describing atoms and molecules in their ground-states. Interaction of electromagnetic field with matter, as relevant to spectroscopy, requires an extension of the DFT theory, called Time-Dependent DFT (TDDFT). TDDFT is a theoretical approach to non-stationary systems providing a formally exact method to calculate excitation energies [487, 491–496].

Over the past 20 years TDDFT became increasing popular for the modelling of the optical properties of molecules. Properties and phenomena investigated so far include linear and nonlinear optical spectra, circular dichroism, X-ray absorption and photoisomerization, to cite a few [165, 494, 497]. Applications range from chemistry to biology, including organic dyes, transition metal complexes, polymers, clusters of different nature and size, solids, metals and semiconductors [165, 497–499]. In the future TDDFT aims at the description of more complex systems, for example macromolecules, biomolecules like DNA fragments and light harvesting complexes [487].

TDDFT borrows many concepts from DFT, such as the idea of replacing the role of the wavefunction with the electron density and the definition of an auxiliary system allowing to map the problem of an interacting system onto a non-interacting system.

The evolution of a N-electron system is described by the time-dependent Schrödinger equation

$$i\frac{\delta}{\delta t}\Psi_j(\boldsymbol{r}_1,\ldots,\boldsymbol{r}_N,t) = \hat{H}(\boldsymbol{r}_1,\ldots,\boldsymbol{r}_N,t)\Psi_j(\boldsymbol{r}_1,\ldots,\boldsymbol{r}_N,t) \tag{B.20}$$

where the time-dependent Hamiltonian $\hat{H}(t)$ reads

$$\hat{H}(t) = \hat{T} + \hat{V}(t) + \hat{U} \tag{B.21}$$

In the equation above, $\hat{T}$ and $\hat{U}$ are the operators associated to kinetic energy and electron-electron interaction, as in the stationary Hamiltonian B.10, while $\hat{V}$ is a time-dependent external potential, that can be written as a sum of one-body potentials:

$$\hat{V}(t) = \sum_{j=1}^{N} v(\boldsymbol{r}_j, t) \tag{B.22}$$

TDDFT deals with systems in which the external potential can be treated as a weak perturbation, as it is the case for optical spectroscopy.

In this context, the electron density $n(\boldsymbol{r},t)$ is a time-dependent function giving the probability of finding the electron at position $\boldsymbol{r}$ at time t:

$$n(\boldsymbol{r},t) = N \int d^3\boldsymbol{r}_2 \dots d^3\boldsymbol{r}_N |\Psi(\boldsymbol{r},\boldsymbol{r}_2 \dots \boldsymbol{r}_N,t)|^2 \tag{B.23}$$

The central theorem of TDDFT is the so-called Runge-Gross theorem [162], stating that, for a system evolving from a fixed initial state, there is a one-to-one correspondence between the external time-dependent potential $v(\boldsymbol{r},t)$ and the electronic density $n(\boldsymbol{r},t)$. Namely, the potential, as well as the time-dependent wavefunction and all the other observables, is a functional of the density.

As for ground-state DFT, one can resort to Kohn-Sham formalism, defining a system of N noninteracting particles subject to an external local potential v_{KS}, chosen as the potential that gives for the KS system the same electron density of the interacting system. Electrons of the KS system obey the time-dependent Schrödinger equation B.20, where the KS Hamiltonian reads

$$\hat{H}_{KS}(r,t) = \Big[-\frac{\hbar^2\nabla^2}{2m_e} + v_{KS}[n](\boldsymbol{r},t) \Big] \tag{B.24}$$

The potential $v_{KS}[n](\boldsymbol{r},t)$ is usually written as the sum of three contributions:

$$v_{KS}[n](\boldsymbol{r},t) = v(\boldsymbol{r},t) + v_H(\boldsymbol{r},t) + v_{xc}[n](\boldsymbol{r},t) \tag{B.25}$$

The first term, v, is the external potential, v_H accounts for the time-dependent electrostatic electron-electron interactions and v_{xc}, the xc potential, includes all the many-body effects and is the only unknown part. v_{xc} is a functional of the electron density, the initial state of the system Ψ_0 and the initial state of the KS system Φ_0: $v_{xc}[n,\Psi_0,\Phi_0](\boldsymbol{r},t)$. However, since we are usually interested in systems evolving from their ground-state which, according to the first HK theorem, is a functional of the ground-state density, the xc potential can be regarded as a functional of the density only: $v_{xc}[n](\boldsymbol{r},t)$. The explicit form chosen for v_{xc} is the only approximation at the heart of TDDFT, as in ground-state DFT. Usually, in the choice of the xc functional, the dependence of the xc potential at time t on the history of the density is neglected, in the so-called adiabatic approximation [487,494]. Many functionals developed for DFT are also available in TDDFT.

The choice of the xc functional is a delicate issue and must be done according to the specific system at hand and the target properties. For example, it is well-known that standard hybrid functionals such as B3LYP are affected by over-polarization problems, giving spurious CT states and/or sizable errors in the excitation energies of CT transitions [167–169]. A better choice for CT systems are range-separated hybrid functionals [500,501], such as CAM-B3LYP [170] and ωWB97X-D [266], which provide a more accurate description of the electron-hole interaction [165].

Excitation energies, one of the key informations contained in photoabsorption spectra, can be obtained from a TDDFT calculation adopting the linear response theory (LR-TDDFT) [502].

The key quantity is the response function $\chi(\omega)$, quantifying the change in density corresponding to a minimal variation of the applied potential:

$$\delta n_\sigma(\boldsymbol{r},\omega) = \sum_{\sigma'} \int d^3r' \chi_{\sigma\sigma'}(\boldsymbol{r},\boldsymbol{r'},\omega)\delta v_{\sigma'}(\boldsymbol{r'},\omega) \tag{B.26}$$

The poles of $\chi(\omega)$ are the true excitation frequencies of the system. The numerical calculation of $\chi(\omega)$ is a tough task, and a preferred procedure is to replace the explicit calculation of $\chi(\omega)$ with the solution of a pseudo eigenvalue equation yielding directly the excitation energies [492]. It was demonstrated [503] that the solutions of $\chi^{-1}(\omega) = 0$ are also solutions of the following eigenvalue problem, also known as Casida equation, nowadays implemented in most TDDFT codes [504]:

$$\begin{pmatrix} \boldsymbol{A} & \boldsymbol{B} \\ \boldsymbol{B} & \boldsymbol{A} \end{pmatrix} \begin{pmatrix} \boldsymbol{X} \\ \boldsymbol{Y} \end{pmatrix} = \omega \begin{pmatrix} \mathbf{1} & \mathbf{0} \\ \mathbf{0} & \mathbf{-1} \end{pmatrix} \begin{pmatrix} \boldsymbol{X} \\ \boldsymbol{Y} \end{pmatrix} \tag{B.27}$$

where $\boldsymbol{A}$ and $\boldsymbol{B}$ are Hessian matrices defined in the product space $\mathcal{S}_i \times \mathcal{S}_a$ being $\mathcal{S}_i$ and $\mathcal{S}_a$ the space of the occupied and virtual states, and $\boldsymbol{X}$ and $\boldsymbol{Y}$ define the character of the transition in terms of excitations and de-excitations respectively.

Briefly, the procedure for extracting transition frequencies involves the solution of the ground-state KS equation in order to find the KS orbitals and their eigenvalues. This information is used to build the $\boldsymbol{A}$ and $\boldsymbol{B}$ matrices and then Eq. B.27 is solved numerically to find at least the lowest eigenvalues ω, corresponding to the vertical excitation energies of the system. Vectors $\boldsymbol{X}$

and $\boldsymbol{Y}$ provide information on the character of the transitions and, together with the dipole matrix, can be used to retrieve oscillator strengths.

An approximation to TDDFT is the so-called Tamm-Dancoff Approximation (TDA) [271]. TDA consists in decoupling excitations and de-excitations, setting $\boldsymbol{B} = 0$ in Eq. B.27. It corresponds to allow only excitations from occupied to virtual orbitals (and not also *vice-versa*), and practically consists in the solution of $\boldsymbol{AX} = \omega \boldsymbol{X}$. Not only TDA is beneficial in reducing the computational cost of full TDDFT calculations, but it also overcomes the triplet instability problem [505, 506] and gives a better estimate of triplet energies, usually underestimated by full TDDFT. However, care should be taken in the interpretation of the oscillator strengths obtained from TDA calculations, since they do not satisfy the Thomas-Reiche-Kuhn sum rule [507–509]. It has also to be noted that the TDA accuracy on triplet states comes at the price of less accurate energy of the singlets, compared to their TDDFT counterpart [165].

Solvation effects are included in both DFT and TDDFT calculations according to two different schemes: explicit and implicit models. In the former, the solute is surrounded by a finite number of solvent molecules treated explicitly, usually within molecular mechanics. This method has the advantage of a detailed description of specific solvent-solute interactions, however it is computationally demanding. Conversely, implicit models treat the solvent as a continuum equilibrated with the charge distribution of the solute [510].

The most common implicit model is the Polarizable Continuum Model (PCM), in which the solute is embedded in a cavity inside the solvent, treated as a polarizable dielectric characterized by its dielectric constant [511]. Within PCM, different schemes have been proposed for the calculation of excitation energies, among them the linear response (LR) method [160] and state-specific (SS) method [166, 512]. In the SS approach, for each transition the Schrödinger equations are solved for both the ground and the excited-state, and the transition energy is calculated as difference between the corresponding energies. Conversely, in the LR approach the excitation energies are obtained directly as the poles of the linear response function, without explicitly calculating the wavefunctions. This method is largely adopted for solvated molecules in general: it is efficient in terms of compu-

tational resources, and allows to access the properties of several states at once. A drawback of the LR approach is that the excited-state dipole moments are approximated by the transition dipole moments, that could lead to large errors on CT states. SS offers a more complete physical description, but is computationally expensive and allows the calculation of the energy only and for one state at a time. For this reason SS is usually exploited for the refinement of the energy output of a LR calculation, only for a few states of interest [513], and is specifically recommended for CT systems.

TDDFT usually provides accurate results on excited-states. The average error on transition energies amounts to ~ 0.4 eV compared to experiment. The accuracy on structural properties of excited-states is comparable to that of DFT for the ground-state: the estimated error amounts to 1% for bond lengths and 5% for dipole moments and vibrational frequencies [494]. Depending on the implementation, the computational cost of TDDFT scales as N^2 or N^3, one or two orders of magnitude better than wavefunction-based methods. For this reason, while the latter are limited to systems with 50 atoms at most, TDDFT allows to study systems of hundreds of atoms with current average available computer resources [487].

Bibliography

[1] B. H. Cumpston, S. P. Ananthavel, S. Barlow, D. L. Dyer, J. E. Ehrlich, L. L. Erskine, A. A. Heikal, S. M. Kuebler, I. Y. S. Lee, D. McCord-Maughon, et al., Nature 1999, 398, 51–54.

[2] R. Kirchain, L. Kimerling, Nat. Photonics 2007, 1, 303–305.

[3] B. E. A. Saleh, M. C. Teich, Fundamentals of Photonics, Wiley, 2007.

[4] A. F. Koenderink, A. Alù, A. Polman, Science 2015, 348, 516–521.

[5] I. A. Walmsley, Science 2015, 348, 525–530.

[6] F. Cacialli, Adv. Funct. Mater. 2019, 29, 1–3.

[7] J. Clark, G. Lanzani, Nat. Photonics 2010, 4, 438–446.

[8] A. Buckley, Ed. , Organic Light-Emitting Diodes (OLEDs), Woodhead Publishing, 2013.

[9] P. E. Burrows, S. R. Forrest, M. E. Thompson, Curr. Opin. Solid State Mater. Sci. 1997, 2, 236–243.

[10] P. T. Chou, Y. Chi, Chem. - A Eur. J. 2007, 13, 380–395.

[11] M. O'Neill, S. M. Kelly, Adv. Mater. 2011, 23, 566–584.

[12] A. Zampetti, A. Minotto, F. Cacialli, Adv. Funct. Mater. 2019, 29, 1807623.

[13] A. McEvoy, T. Markvart, T. Castaner, Eds. , Practical Handbook of Photovoltaics, Elsevier Academic Press, 2011.

[14] M. J. Currie, J. K. Mapel, T. D. Heidel, S. Goffri, M. A. Baldo, Science 2008, 321, 226–228.

[15] J. L. Bredas, J. R. Durrant, Acc. Chem. Res. 2009, 42, 1689–1690.

[16] J. Haus, Optical Sensors. Basics and Applications, Wiley-VCH, 2010.

[17] R. Narayanaswamy, O. S. Wolfbeis, Eds. , Optical Sensors. Industrial Environmental and Diagnostic Applications, Springer-Verlag, Berlin Heidelberg, 2004.

[18] S. M. Ng, M. Koneswaran, R. Narayanaswamy, RSC Adv. 2016, 6, 21624-21661.

[19] J. Yao, M. Yang, Y. Duan, Chem. Rev. 2014, 114, 6130–6178.

[20] G. Zerbi, Ed. , Organic Materials for Photonics, North Holland, 1993.

[21] D. W. Bruce, D. O'Hare, R. I. Walton, Eds. , Molecular Materials, Wiley-VCH, 2010.

[22] O. Ostroverkhova, Ed. , Handbook of Organic Materials for Electronic and Photonic Devices, Woodhead Publishing, 2018.

[23] Y. Lin, Y. Li, X. Zhan, Chem. Soc. Rev. 2012, 41, 4245–4272.

[24] Y. Yan, Y. S. Zhao, Chem. Soc. Rev 2014, 43, 4325–4340.

[25] W. Yao, Y. S. Zhao, Nanoscale 2014, 6, 3467–3473.

[26] C. Zhang, Y. Yan, Y. S. Zhao, J. Yao, Acc. Chem. Res. 2014, 47, 3448–3458.

[27] M. Pawlicki, H. A. Collins, R. G. Denning, H. L. Anderson, Angew. Chemie - Int. Ed. 2009, 48, 3244–3266.

[28] S. J. Chung, K. S. Kim, T. C. Lin, G. S. He, J. Swiatkiewicz, P. N. Prasad, J. Phys. Chem. B 1999, 103, 10741–10745.

[29] S. R. Marder, Chem. Commun. 2006, 131–134.

[30] S. Barlow, S. R. Marder, in Functional Organic Materials: Syntheses, Strategies and Applications (Eds.: J. J. Muller, U. H. F. Bunz), Wiley-VCH Verlag GmbH, Weinheim, Germany, 2007, pp. 393–437.

[31] F. Terenziani, C. Katan, E. Badaeva, S. Tretiak, M. Blanchard-Desce, Adv. Mater. 2008, 20, 4641–4678.

[32] A. Slama-Schwok, M. Blanchard-Desce, J.-M. Lehn, J. Phys. Chem. 1990, 94, 3894–3902.

[33] H. Zhu, X. Wang, R. Ma, Z. Kuang, Q. Guo, A. Xia, ChemPhysChem 2016, 17, 3245–3251.

[34] F. Bureš, RSC Adv. 2014, 4, 58826–58851.

[35] R. R. Tykwinski, U. Gubler, R. E. Martin, F. Diederich, C. Bosshard, P. Günter, J. Phys. Chem. B 1998, 102, 4451–4465.

[36] E. Zojer, D. Beljonne, P. Pacher, J. L. Brédas, Chem. - A Eur. J. 2004, 10, 2668–2680.

[37] F. Bureš, W. B. Schweizer, J. C. May, C. Boudon, J. P. Gisselbrecht, M. Gross, I. Biaggio, F. Diederich, Chem. Eur. J. 2007, 13, 5378–5387.

[38] M. Kivala, F. Diederich, Acc. Chem. Res. 2009, 42, 235–248.

[39] G. Qian, Z. Y. Wang, Chem. - An Asian J. 2010, 5, 1006–1029.

[40] A. Cesaretti, P. Foggi, C. G. Fortuna, F. Elisei, A. Spalletti, B. Carlotti, J. Phys. Chem. C 2020, 124, 15739–15748.

[41] A. Painelli, F. Terenziani, Chem. Phys. Lett. 1999, 312, 211–220.

[42] A. Painelli, Chem. Phys. 1999, 245, 185–197.

[43] A. Painelli, F. Terenziani, Synth. Met. 2001, 116, 135–138.

[44] F. Terenziani, A. Painelli, Phys. Rev. B 2003, 68, 165405–165413.

[45] F. Terenziani, A. Painelli, J. Lumin. 2005, 112, 474–478.

[46] G. D'Avino, F. Terenziani, A. Painelli, J. Phys. Chem. B 2006, 110, 25590–25592.

[47] E. Buncel, S. Rajagopal, Acc. Chem. Res. 1990, 23, 226–231.

[48] P. Suppan, J. Photochem. Photobiol. A Chem. 1990, 50, 293–330.

[49] E. Vauthey, ChemPhysChem 2012, 13, 2001–2011.

[50] B. Dereka, E. Vauthey, J. Phys. Chem. Lett. 2017, 8, 3927–3932.

[51] M. Söderberg, B. Dereka, A. Marrocchi, B. Carlotti, E. Vauthey, J. Phys. Chem. Lett. 2019, 10, 2944–2948.

[52] B. Dereka, D. Svechkarev, A. Rosspeintner, A. Aster, M. Lunzer, R. Liska, A. M. Mohs, E. Vauthey, Nat. Commun. 2020, 11, 1–11.

[53] G. Scheibe, Angew. Chem. 1936, 49, 563.

[54] G. Scheibe, Angew. Chem. 1937, 50, 212–219.

[55] E. E. Jelley, Nature 1936, 138, 1009–1010.

[56] J. Knoester, in Organic Nanostructures: Science and Applications, IOS Press, Amsterdam, 2002.

[57] Y. Hong, J. W. Y. Lam, B. Z. Tang, Chem. Commun. 2009, 4332–4353.

[58] S. K. Saikin, A. Eisfeld, S. Valleau, A. Aspuru-Guzik, Nanophotonics 2013, 2, 21–38.

[59] F. Terenziani, S. Ghosh, A. C. Robin, P. K. Das, M. Blanchard-Desce, J. Phys. Chem. B 2008, 112, 11498–11505.

[60] E. Campioli, D. M. Nikolaidou, V. Hugues, M. Campanini, L. Nasi, M. Blanchard-Desce, F. Terenziani, J. Mater. Chem. C 2015, 3, 7483–7491.

[61] S. Sanyal, C. Sissa, F. Terenziani, S. K. Pati, A. Painelli, Phys. Chem. Chem. Phys. 2017, 19, 24979–24984.

[62] M. S. Wong, C. Bosshard, P. Günter, Adv. Mater. 1997, 9, 837–842.

[63] J. M. Hales, S. Barlow, H. Kim, S. Mukhopadhyay, J. L. Brédas, J. W. Perry, S. R. Marder, Chem. Mater. 2014, 26, 549–560.

[64] S. B. Anantharaman, T. Stöferle, F. A. Nüesch, R. F. Mahrt, J. Heier, Adv. Funct. Mater. 2019, 29, 1806997.

[65] A. Liess, A. Arjona-Esteban, A. Kudzus, J. Albert, A. M. Krause, A. Lv, M. Stolte, K. Meerholz, F. Würthner, Adv. Funct. Mater. 2019, 29, 1805058.

[66] S. Yagai, S. Okamura, Y. Nakano, M. Yamauchi, K. Kishikawa, T. Karatsu, A. Kitamura, A. Ueno, D. Kuzuhara, H. Yamada, et al., Nat. Commun. 2014, 5, 4013.

[67] J. Deisenhofer, J. R. Norris, Eds. , The Photosynthetic Reaction Center, Academic Press, New York, 1993.

[68] A. Roda, M. Guardigli, E. Michelini, M. Mirasoli, Anal. Bioanal. Chem. 2009, 393, 109–123.

[69] D. Geißler, S. Linden, K. Liermann, K. D. Wegner, L. J. Charbonnière, N. Hildebrandt, Inorg. Chem. 2014, 53, 1824–1838.

[70] D. Geißler, N. Hildebrandt, Anal. Bioanal. Chem. 2016, 408, 4475–4483.

[71] H. Sahoo, J. Photochem. Photobiol. C 2011, 12, 20–30.

[72] L. K. Chao, R. M. Clegg, Wiley Encyclopedia of Chemical Biology 2008, Wiley-VCH.

[73] Q. Zou, K. Liu, M. Abbas, X. Yan, Adv. Mater. 2016, 28, 1031–1043.

[74] S. Fukuzumi, in Functional Organic Materials: Syntheses, Strategies and Applications (Eds.: T. J. J. Muller, U. H. F. Bunz), Wiley-VCH Verlag GmbH, Weinheim, Germany, 2007, pp. 465–510.

[75] M. D. Ward, P. R. Raithby, Chem. Soc. Rev. 2013, 42, 1619–1636.

[76] P. Ensslen, H. A. Wagenknecht, Acc. Chem. Res. 2015, 48, 2724–2733.

[77] J. Cornil, D. Beljonne, J. P. Calbert, J. L. Brédas, Adv. Mater. 2001, 13, 1053–1067.

[78] C. Katan, S. Tretiak, M. H. V. Werts, A. J. Bain, R. J. Marsh, N. Leonczek, N. Nicolaou, E. Badaeva, O. Mongin, M. Blanchard-Desce, J. Phys. Chem. B 2007, 111, 9468–9483.

[79] K. Brymora, L. Ducasse, A. Delaure, L. Hirsch, T. Jarrosson, C. Niebel, F. Serein-Spirau, R. Peresutti, O. Dautel, F. Castet, Dye. Pigment. 2018, 149, 882–892.

[80] D. Jacquemin, B. Mennucci, C. Adamo, Phys. Chem. Chem. Phys. 2011, 13, 16987–16998.

[81] A. S. Davidov, Theory of Molecular Excitons, Plenum Press, New York, 1971.

[82] R. S. Mulliken, J. Am. Chem. Soc. 1952, 74, 811–824.

[83] A. Painelli, Chem. Phys. Lett. 1998, 285, 352–358.

[84] A. Painelli, F. Terenziani, J. Phys. Chem. A 2000, 104, 11041–11048.

[85] F. Terenziani, A. Painelli, C. Katan, M. Charlot, M. Blanchard-Desce, J. Am. Chem. Soc. 2006, 128, 15742–15755.

[86] F. Terenziani, C. Sissa, A. Painelli, J. Phys. Chem. B 2008, 112, 5079–5087.

[87] S. R. Marder, L. T. Cheng, B. G. Tiemann, A. C. Friedli, M. Blanchard-Desce, J. W. Perry, J. Skindhøj, Science 1994, 263, 511–514.

[88] A. Painelli, F. Terenziani, ChemPhysChem 2009, 10, 527–531.

[89] H. Myung Kim, B. Rae Cho, Chem. Commun. 2009, 153–164.

[90] K. Ogawa, Appl. Sci. 2014, 4, 1–18.

[91] T. Kim, K. Lee, Macromol. Rapid Commun. 2015, 36, 943–958.

[92] S. R. Marder, B. Kippelen, A. K. Jen, N. Peyghambarian, Nature 1997, 388, 845–851.

[93] M. Albota, D. Beljonne, J.-L. Brédas, J. E. Ehrlich, J.-Y. Fu, A. A. Heikal, S. E. Hess, T. Kogej, M. D. Levin, S. R. Marder, et al., Science 1998, 281, 1653–1656.

[94] W. Liptay, Angew. Chemie - Int. Ed. 1969, 8, 177–188.

[95] B. Strehmel, A. M. Sarker, H. Detert, ChemPhysChem 2003, 4, 249–259.

[96] L. Ji, R. M. Edkins, L. J. Sewell, A. Beeby, A. S. Batsanov, K. Fucke, M. Drafz, J. A. K. Howard, O. Moutounet, F. Ibersiene, et al., Chem. Eur. J. 2014, 13618–13635.

[97] M. Monçalves, D. da Silveira Rampon, P. E. Schneider, F. S. Rodembusch, C. da Cruz Silveira, Dye. Pigment. 2014, 102, 71–78.

[98] F. Ricci, F. Elisei, P. Foggi, A. Marrocchi, A. Spalletti, B. Carlotti, J. Phys. Chem. C 2016, 120, 23726–23739.

[99] S. A. Kurhuzenkau, M. Yezabel, C. Gomez, K. D. Belfield, Y. O. Shaydyuk, D. J. Hagan, E. W. Van Stryland, C. Sissa, M. V Bondar, A. Painelli, J Phys Chem C 2018, 122, 5664–5672.

[100] M. M. Raikwar, D. S. Patil, E. Mathew, M. Varghese, I. H. Joe, N. Sekar, J. Photochem. Photobiol. A 2019, 373, 45–58.

[101] B. Carlotti, A. Cesaretti, G. Cacioppa, F. Elisei, I. Odak, I. Škoric, A. Spalletti, J. Photochem. Photobiol. A 2019, 368, 190–199.

[102] N. Dozova, L. Ventelon, G. Clermont, M. Blanchard-Desce, P. Plaza, Chem. Phys. Lett. 2016, 664, 56–62.

[103] J. S. Beckwith, A. Rosspeintner, G. Licari, M. Lunzer, B. Holzer, J. Fro, E. Vauthey, J. Phys. Chem. Lett. 2017, 8, 5878–5883.

[104] B. Dereka, A. Rosspeinter, R. Stezycki, C. Ruckebusch, D. T. Gryko, E. Vauthey, J. Phys. Chem. Lett. 2017, 6029–6034, 6–11.

[105] B. Dereka, A. Rosspeintner, M. Krzeszewski, D. T. Gryko, E. Vauthey, Angew. Chemie - Int. Ed. 2016, 55, 15624–15628.

[106] W. Kim, J. Sung, M. Grzybowski, D. T. Gryko, D. Kim, J. Phys. Chem. Lett. 2016, 7, 3060–3066.

[107] T. Kim, J. Kim, H. Mori, S. Park, M. Lim, A. Osuka, D. Kim, Phys. Chem. Chem. Phys. 2017, 19, 13970–13977.

[108] T. Kim, W. Kim, H. Mori, A. Osuka, D. Kim, J. Phys. Chem. C 2018, 122, 19409–19415.

[109] B. Boldrini, E. Cavalli, A. Painelli, F. Terenziani, J. Phys. Chem. A 2002, 106, 6286–6294.

[110] B. Bardi, M. Krzeszewski, D. T. Gryko, A. Painelli, F. Terenziani, Chem. Eur. J. 2019, 25, 13930–13938.

[111] J. L. Oudar, D. S. Chemla, J. Chem. Phys. 1977, 66, 2664–2668.

[112] F. Terenziani, O. V. Przhonska, S. Webster, L. A. Padilha, Y. L. Slominsky, I. G. Davydenko, A. O. Gerasov, Y. P. Kovtun, M. P. Shandura, A. D. Kachkovski, et al., J. Phys. Chem. Lett. 2010, 1, 1800–1804.

[113] C. Sissa, V. Parthasarathy, D. Drouin-Kucma, M. H. V. Werts, M. Blanchard-Desce, F. Terenziani, Phys. Chem. Chem. Phys. 2010, 12, 11715–11727.

[114] J. Campo, A. Painelli, F. Terenziani, T. Van Regemorter, D. Beljonne, E. Goovaerts, W. Wenseleers, J. Am. Chem. Soc. 2010, 132, 16467–16478.

[115] L. Grisanti, C. Sissa, F. Terenziani, A. Painelli, D. Roberto, F. Tessore, R. Ugo, S. Quici, I. Fortunati, E. Garbin, et al., Phys. Chem. Chem. Phys. 2009, 11, 9450–9457.

[116] C. Sissa, V. Calabrese, M. Cavazzini, L. Grisanti, F. Terenziani, S. Quici, A. Painelli, Chem. Eur. J. 2013, 19, 924–935.

[117] C. Katan, M. Charlot, O. Mongin, C. Le Droumaguet, V. Jouikov, F. Terenziani, E. Badaeva, S. Tretiak, M. Blanchard-Desce, J. Phys. Chem. B 2010, 114, 3152–3169.

[118] F. Terenziani, A. Painelli, Chem. Phys. 2003, 295, 35–46.

[119] E. Campioli, S. Sanyal, A. Marcelli, M. Di Donato, M. Blanchard-Desce, O. Mongin, A. Painelli, F. Terenziani, ChemPhysChem 2019, 20, 2860–2873.

[120] C. Sissa, A. Painelli, M. Blanchard-Desce, F. Terenziani, J. Phys. Chem. B 2011, 115, 7009–7020.

[121] C. Sissa, F. Terenziani, A. Painelli, J. Phys. Chem. A 2008, 112, 8697–8705.

[122] F. Terenziani, A. Painelli, D. Comoretto, J. Phys. Chem. A 2000, 104, 11049–11054.

[123] F. Terenziani, A. Painelli, Phys. Chem. Chem. Phys. 2015, 17, 13074–13081.

[124] A. Painelli, L. Del Freo, F. Terenziani, Chem. Phys. Lett. 2001, 346, 470–478.

[125] L. Del Freo, A. Painelli, Chem. Phys. Lett. 2001, 338, 208–216.

[126] C. Sissa, P. M. Jahani, Z. G. Soos, A. Painelli, ChemPhysChem 2012, 13, 2795–2800.

[127] C. Sissa, F. Terenziani, A. Painelli, R. B. K. Siram, S. Patil, J. Phys. Chem. B 2012, 116, 4959–4966.

[128] C. Sissa, F. Terenziani, A. Painelli, A. Abbotto, L. Bellotto, C. Marinzi, E. Garbin, C. Ferrante, R. Bozio, J. Phys. Chem. B 2010, 114, 882–893.

[129] S. Sanyal, A. Painelli, S. K. Pati, F. Terenziani, C. Sissa, Phys. Chem. Chem. Phys. 2016, 18, 28198–28208.

[130] B. Bardi, C. Dall'Agnese, K. I. Moineau-Chane Ching, A. Painelli, F. Terenziani, J. Phys. Chem. C 2017, 121, 17466–17478.

[131] B. Bardi, C. Dall'Agnese, M. Tassé, S. Ladeira, A. Painelli, K. I. Moineau-Chane Ching, F. Terenziani, ChemPhotoChem 2018, 2, 1027–1037.

[132] C. Sissa, A. K. Manna, F. Terenziani, A. Painelli, S. K. Pati, Phys. Chem. Chem. Phys. 2011, 13, 12734–12744.

[133] F. Di Maiolo, A. Painelli, J. Chem. Theory Comput. 2018, 14, 5339–5349.

[134] F. Di Maiolo, A. Painelli, Phys. Chem. Chem. Phys. 2020, 22, 1061–1068.

[135] H. J. Kim, J. T. Hynes, Int. J. Quantum Chem. 1990, 38, 821–833.

[136] L. Onsager, J. Am. Chem. Soc. 1936, 58, 1486–1493.

[137] G. Ponterini, D. Vanossi, Z. A. Krasnaya, A. S. Tatikolov, F. Momicchioli, Phys. Chem. Chem. Phys. 2011, 13, 9507–9517.

[138] Ł. G. Łukasiewicz, M. Rammo, C. Stark, M. Krzeszewski, D. Jacquemin, A. Rebane, D. T. Gryko, ChemPhotoChem 2020, 4, 508-519.

[139] T. Liu, X. Liu, W. Wang, Z. Luo, M. Liu, S. Zou, C. Sissa, A. Painelli, Y. Zhang, M. Vengris, et al., J Phys Chem C 2018, 122, 3994–4008.

[140] H. Hu, O. V. Przhonska, F. Terenziani, A. Painelli, D. Fishman, T. R. Ensley, M. Reichert, S. Webster, J. L. Bricks, A. D. Kachkovski, et al., Phys. Chem. Chem. Phys. 2013, 15, 7666–7678.

[141] M. Krzeszewski, T. Kodama, E. M. Espinoza, V. I. Vullev, T. Kubo, D. T. Gryko, Chem. Eur. J. 2016, 22, 16478–16488.

[142] M. Krzeszewski, D. Gryko, D. T. Gryko, Acc. Chem. Res. 2017, 50, 2334–2345.

[143] A. Janiga, E. Glodkowska-Mrowka, T. Stoklosa, D. T. Gryko, Asian J. Org. Chem. 2013, 2, 411–415.

[144] M. Krzeszewski, B. Thorsted, J. Brewer, D. T. Gryko, J. Org. Chem. 2014, 79, 3119–3128.

[145] K. Oki, M. Takase, S. Mori, A. Shiotari, Y. Sugimoto, K. Ohara, T. Okujima, H. Uno, J. Am. Chem. Soc. 2018, 140, 10430–10434.

[146] H. Yokoi, Y. Hiraoka, S. Hiroto, D. Sakamaki, S. Seki, H. Shinokubo, Nat. Commun. 2015, 6, 8215–8223.

[147] D. Myśliwiec, M. Stępień, Angew. Chemie - Int. Ed. 2013, 1713–1717.

[148] Ł. G. Łukasiewicz, H. G. Ryu, A. Mikhaylov, C. Azarias, M. Banasiewicz, B. Kozankiewicz, K. H. Ahn, D. Jacquemin, A. Rebane, D. T. Gryko, Chem. - An Asian J. 2017, 12, 1736–1748.

[149] D. H. Friese, A. Mikhaylov, M. Krzeszewski, Y. M. Poronik, A. Rebane, K. Ruud, D. T. Gryko, Chem. Eur. J. 2015, 21, 18364–18374.

[150] M. Tasior, K. Hassanein, M. M. Leszek, I. Sakellari, D. Gray, M. Farsari, M. Samoc, F. Santoro, B. Ventura, D. T. Gryko, Phys. Chem. Chem. Phys. 2018, 22260–22271.

[151] J. R. Lakowicz, Principles of Fluorescence Spectroscopy, Springer, New York, USA, 2006.

[152] B. Valeur, Molecular Fluorescence. Principles and Applications, Wiley-VCH Verlag GmbH, 2001.

[153] V. Weisskopf, E. Wigner, Zeitschrift für Phys. 1930, 54–73.

[154] P. Meystre, M. Sargent, in Elements of Quantum Optics, Springer, Heidelberg, 2007, pp. 51–91.

[155] P. Hohenberg, W. Kohn, Phys. Rev. 1964, 136, B864–B871.

[156] W. Kohn, L. J. Sham, Phys. Rev. 1965, 140, A1133–A1138.

[157] R. G. Parr, W. Yang, Density Functional Theory for Atoms and Molecules, Oxford University Press, New York, 1989.

[158] A. D. Becke, J. Chem. Phys. 1993, 98, 1372.

[159] M. J. Frisch, G. W. Trucks, H. B. Schlegel, G. E. Scuseria, M. A. Robb, J. R. Cheeseman, G. Scalmani, V. Barone, G. A. Petersson, H. Nakatsuji, et al., Gaussian16, revision B.01, Gaussian, Inc., Wallingford CT.

[160] J. Tomasi, B. Mennucci, R. Cammi, Chem. Rev. 2005, 8, 2999–3094.

[161] G. Scalmani, M. J. Frisch, B. Mennucci, J. Tomasi, R. Cammi, V. Barone, J. Chem. Phys. 2006, 124, 094107.

[162] E. Runge, E. K. U. Gross, Phys. Rev. Lett. 1984, 52, 997–1000.

[163] R. Bauernschmitt, R. Ahlrichs, Chem. Phys. Lett. 1996, 256, 454–464.

[164] M. E. Casida, C. Jamorski, K. C. Casida, D. R. Salahub, J. Chem. Phys. 1998, 108, 4439–4449.

[165] C. Adamo, D. Jacquemin, Chem. Soc. Rev. 2013, 42, 845–856.

[166] R. Improta, G. Scalmani, M. J. Frisch, V. Barone, J. Chem. Phys. 2007, 127, 074504.

[167] Z. L. Cai, K. Sendt, J. R. Reimers, J. Chem. Phys. 2002, 117, 5543–5549.

[168] S. Grimme, M. Parac, ChemPhysChem 2003, 4, 292–295.

[169] A. Dreuw, M. Head-Gordon, J. Am. Chem. Soc. 2004, 126, 4007–4016.

[170] T. Yanai, D. P. Tew, N. C. Handy, Chem. Phys. Lett. 2004, 393, 51–57.

[171] F. L. Hirshfeld, Theor. Chem. Acc. 1977, 44, 129–138.

[172] A. Treibs, K. Jacob, Angew. Chemie - Int. Ed. 1965, 4, 694–694.

[173] W. Ziegenbein, H. -E Sprenger, Angew. Chemie - Int. Ed. 1966, 5, 893–894.

[174] S. Yagi, H. Nakazumi, in Top. Heterocycl. Chem. Vol. 14 (Ed.: Strekowski), Springer, Berlin, Heidelberg, 2008, pp. 133–181.

[175] O. V. Przhonska, S. Webster, L. A. Padilha, H. Hu, A. D. Kachkovski, D. J. Hagan, E. W. Van Stryland, in Advanced Fluorescence Reporters in Chemistry and Biology I: Fundamentals and Molecular Design (Ed.: A.P. Demchenko), Springer-Verlag, Berlin, Heidelberg, 2010, pp. 105–148.

[176] A. Ajayaghosh, Acc. Chem. Res. 2005, 38, 449–459.

[177] S. Sreejith, P. Carol, P. Chithra, A. Ajayaghosh, J. Mater. Chem. 2008, 18, 264–274.

[178] L. Beverina, P. Salice, European J. Org. Chem. 2010, 1207–1225.

[179] L. D. Patsenker, A. L. Tatarets, E. A. Terpetschnig, in Advanced Fluorescence Reporters in Chemistry and Biology I: Fundamentals and Molecular Design (Ed.: A.P. Demchenko), Springer-Verlag, Berlin, Heidelberg, 2010, pp. 65–104.

[180] A. S. Tatikolov, J. Photochem. Photobiol. C 2012, 13, 55-90.

[181] G. Chen, H. Sasabe, T. Igarashi, Z. Hong, J. Kido, J. Mater. Chem. A 2015, 3, 14517–14534.

[182] D. Saccone, S. Galliano, N. Barbero, P. Quagliotto, G. Viscardi, C. Barolo, European J. Org. Chem. 2016, 2016, 2244–2259.

[183] G. Xia, H. Wang, J. Photochem. Photobiol. C Photochem. Rev. 2017, 31, 84–113.

[184] K. Ilina, W. M. MacCuaig, M. Laramie, J. N. Jeouty, L. R. McNally, M. Henary, Bioconjug. Chem. 2020, 31, 194–213.

[185] K. Srinivas, C. Prabhakar, C. L. Devi, K. Yesudas, K. Bhanuprakash, V. J. Rao, J. Phys. Chem. A 2007, 111, 3378–3386.

[186] A. L. Puyad, G. K. Chaitanya, J. Mol. Model 2013, 19, 275–287.

[187] F. J. Avila Ferrer, C. Angeli, J. Cerezo, S. Coriani, A. Ferretti, F. Santoro, ChemPhotoChem 2019, 3, 778–793.

[188] K. M. Shafeekh, S. Das, C. Sissa, A. Painelli, J. Phys. Chem. B 2013, 117, 8536–8546.

[189] D. Scherer, R. Dörfler, A. Feldner, T. Vogtmann, M. Schwoerer, U. Lawrentz, W. Grahn, C. Lambert, Chem. Phys. 2002, 279, 179–207.

[190] J. Fu, L. A. Padilha, D. J. Hagan, E. W. Van Stryland, O. V. Przhonska, M. V. Bondar, Y. L. Slominsky, A. D. Kachkovski, J. Opt. Soc. Am. B 2007, 24, 67–76.

[191] S. Webster, L. A. Padilha, O. V. Przhonska, D. Peceli, H. Hu, G. Nootz, D. J. Hagan, E. W. Van Stryland, S. A. Odom, J. Matichak, et al., J. Phys. Chem. B 2009, 113, 14854–14867.

[192] C. Toro, L. De Boni, S. Yao, J. P. Ritchie, A. E. Masunov, K. D. Belfield, F. E. Hernandez, J. Chem. Phys. 2009, 130, 214504.

[193] S. Webster, D. Peceli, H. Hu, L. A. Padilha, O. V. Przhonska, A. E. Masunov, A. O. Gerasov, A. D. Kachkovski, Y. L. Slominsky, A. I. Tolmachev, et al., J. Phys. Chem. Lett. 2010, 1, 2354–2360.

[194] R. A. Negres, O. V. Przhonska, D. J. Hagan, E. W. Van Stryland, M. V. Bondar, Y. L. Slominsky, A. D. Kachkovski, IEEE J. Sel. Top. Quantum Electron. 2001, 7, 849–863.

[195] S. Webster, J. Fu, L. A. Padilha, O. V. Przhonska, D. J. Hagan, E. W. Van Stryland, M. V. Bondar, Y. L. Slominsky, A. D. Kachkovski, Chem. Phys. 2008, 348, 143–151.

[196] M. A. Qaddoura, K. D. Belfield, P. Tongwa, J. E. Desanto, T. V. Timofeeva, P. A. Heiney, Supramol. Chem. 2011, 23, 731–742.

[197] K. D. Belfield, M. V. Bondar, H. S. Haniff, I. A. Mikhailov, G. Luchita, O. V. Przhonska, ChemPhysChem 2013, 14, 3532–3542.

[198] W. V. Moreshead, O. V. Przhonska, M. V. Bondar, A. D. Kachkovski, I. H. Nayyar, A. E. Masunov, A. W. Woodward, K. D. Belfield, J. Phys. Chem. C 2013, 117, 23133–23147.

[199] R. S. Lepkowicz, C. M. Cirloganu, O. V. Przhonska, D. J. Hagan, E. W. Van Stryland, M. V. Bondar, Y. L. Slominsky, A. D. Kachkovski, E. I. Mayboroda, Chem. Phys. 2004, 306, 171–183.

[200] S. Khopkar, G. Shankarling, Dye. Pigment. 2019, 170, 107645.

[201] A. L. Tatarets, I. A. Fedyunyaeva, E. Terpetschnig, L. D. Patsenker, Dye. Pigment. 2005, 64, 125–134.

[202] A. L. Tatarets, I. A. Fedyunyayeva, T. S. Dyubko, Y. A. Povrozin, A. O. Doroshenko, E. A. Terpetschnig, L. D. Patsenker, Anal. Chim. Acta 2006, 570, 214–223.

[203] L. Beverina, R. Ruffo, C. M. Mari, G. A. Pagani, M. Sassi, F. De Angelis, S. Fantacci, J. H. Yum, M. Grätzel, M. K. Nazeeruddin, ChemSusChem 2009, 2, 621–624.

[204] T. Maeda, S. Mineta, H. Fujiwara, H. Nakao, S. Yagi, H. Nakazumi, J. Mater. Chem. A 2013, 1, 1303–1309.

[205] C. Qin, Y. Numata, S. Zhang, A. Islam, X. Yang, K. Sodeyama, Y. Tateyama, L. Han, Adv. Funct. Mater. 2013, 23, 3782–3789.

[206] C. Qin, Y. Numata, S. Zhang, X. Yang, A. Islam, K. Zhang, H. Chen, L. Han, Adv. Funct. Mater. 2014, 24, 3059–3066.

[207] S. Galliano, V. Novelli, N. Barbero, A. Smarra, G. Viscardi, R. Borrelli, F. Sauvage, C. Barolo, Energies 2016, 9, 486.

[208] G. H. Rao, A. Venkateswararao, L. Giribabu, S. P. Singh, Photochem. Photobiol. Sci. 2016, 15, 287–296.

[209] G. M. Paterno', N. Barbero, S. Galliano, C. Barolo, G. Lanzani, F. Scotognella, R. Borrelli, J. Mater. Chem. C 2018, 6, 2778–2785.

[210] U. Mayerhöffer, B. Fimmel, F. Würthner, Angew. Chemie - Int. Ed. 2012, 51, 164–167.

[211] U. Mayerhöffer, M. Gsänger, M. Stolte, B. Fimmel, F. Würthner, Chem. Eur. J. 2013, 19, 218–232.

[212] A. S. Tatikolov, S. M. B. Costa, J. Photochem. Photobiol. A 2001, 140, 147–156.

[213] G. De Miguel, M. Marchena, M. Zitnan, S. S. Pandey, S. Hayase, A. Douhal, Phys. Chem. Chem. Phys. 2012, 14, 1796–1805.

[214] A. L. Puyad, G. K. Chaitanya, A. Thomas, M. Paramasivam, K. Bhanuprakash, J. Phys. Org. Chem. 2013, 37–46.

[215] H. Ceymann, A. Rosspeintner, M. H. Schreck, C. Mützel, A. Stoy, E. Vauthey, C. Lambert, Phys. Chem. Chem. Phys. 2016, 18, 16404–16413.

[216] S. Ohira, I. Rudra, K. Schmidt, S. Barlow, S. J. Chung, Q. Zhang, J. Matichak, S. R. Marder, J. L. Brédas, Chem. Eur. J. 2008, 14, 11082–11091.

[217] J. Park, C. Barolo, F. Sauvage, N. Barbero, C. Benzi, P. Quagliotto, S. Coluccia, D. Di Censo, M. Grätzel, M. K. Nazeeruddin, et al., Chem. Commun. 2012, 48, 2782.

[218] M. Pope, C. E. Swenberg, Eds. , Electronic Processes in Organic Crystals and Polymers, Oxford Science Publications, New York, 1999.

[219] M. R. Wasielewski, Acc. Chem. Res. 2009, 42, 1910–1921.

[220] F. Terenziani, V. Parthasarathy, A. Pla-Quintana, T. Maishal, A. M. Caminade, J. P. Majoral, M. Blanchard-Desce, Angew. Chemie - Int. Ed. 2009, 48, 8691–8694.

[221] Y. S. Zhao, H. Fu, A. Peng, Y. Ma, Q. Liao, J. Yao, Acc. Chem. Res. 2010, 43, 409–418.

[222] Y. Li, T. Liu, H. Liu, M. Z. Tian, Y. Li, Acc. Chem. Res. 2014, 47, 1186–1198.

[223] S. Di Bella, M. A. Ratner, T. J. Marks, J. Am. Chem. Soc. 1992, 114, 5842–5849.

[224] L. R. Dalton, A. W. Harper, B. H. Robinson, Proc. Natl. Acad. Sci. 1997, 94, 4842–4847.

[225] K.-H. Kim, H. Yu, H. Kang, D. J. Kang, C.-H. Cho, H.-H. Cho, J. H. Oh, B. J. Kim, J. Mater. Chem. A 2013, 1, 14538–14547.

[226] D. Yan, D. G. Evans, Mater. Horizons 2014, 1, 46–57.

[227] A. S. Andersson, K. Qvortrup, E. R. Torbensen, J. P. Mayer, J. P. Gisselbrecht, C. Boudon, M. Gross, A. Kadziola, K. Kilså, M. B. Nielsen, European J. Org. Chem. 2005, 3660–3671.

[228] M. M. Oliva, J. Casado, M. M. M. Raposo, A. M. C. Fonseca, H. Hartmann, V. Hernández, J. T. López Navarrete, J. Org. Chem. 2006, 71, 7509–7520.

[229] P. Sonar, S. P. Singh, S. Sudhakar, A. Dodabalapur, A. Sellinger, Chem. Mater. 2008, 20, 3184–3190.

[230] D. M. Guldi, Angew. Chemie - Int. Ed. 2010, 49, 7844–7846.

[231] A. Datta, F. Terenziani, A. Painelli, ChemPhysChem 2006, 7, 2168–2174.

[232] S. O. Kim, T. K. An, J. Chen, I. Kang, S. H. Kang, D. S. Chung, C. E. Park, Y. H. Kim, S. K. Kwon, Adv. Funct. Mater. 2011, 21, 1616–1623.

[233] C. J. Takacs, Y. Sun, G. C. Welch, L. A. Perez, X. Liu, W. Wen, G. C. Bazan, A. J. Heeger, J. Am. Chem. Soc. 2012, 134, 16597–16606.

[234] F. Fennel, S. Wolter, Z. Xie, P. A. Plötz, O. Kühn, F. Würthner, S. Lochbrunner, J. Am. Chem. Soc. 2013, 135, 18722–18725.

[235] Q. Zhao, J. Liu, H. Wang, M. Li, K. Zhou, H. Yang, Y. Han, J. Mater. Chem. C 2015, 3, 8183–8192.

[236] J. Wu, Y. Cheng, J. Lan, D. Wu, S. Qian, L. Yan, Z. He, X. Li, K. Wang, B. Zou, et al., J. Am. Chem. Soc. 2016, 138, 12803–12812.

[237] Y. Zhang, M. Li, H. Feng, W. Ni, H. Zhang, F. Liu, X. Wan, Y. Chen, Dye. Pigment. 2017, 141, 262–268.

[238] K. Cai, J. Xie, D. Zhang, W. Shi, Q. Yan, D. Zhao, J. Am. Chem. Soc. 2018, 140, 5764–5773.

[239] N. J. Hestand, F. C. Spano, Chem. Rev. 2018, 118, 7069-7163.

[240] V. M. Agranovich, M. V. Galanin, Electronic Excitation Energy Transfer in Condensed Matter, North-Holland, Amsterdam, 1982.

[241] A. Painelli, F. Terenziani, J. Am. Chem. Soc. 2003, 125, 5624–5625.

[242] F. Terenziani, G. D'Avino, A. Painelli, ChemPhysChem 2007, 8, 2433–2444.

[243] G. D'Avino, L. Grisanti, J. Guasch, I. Ratera, J. Veciana, A. Painelli, J. Am. Chem. Soc. 2008, 130, 12064–12072.

[244] F. C. Spano, Annu. Rev. Phys. Chem. 2006, 57, 217–243.

[245] F. C. Spano, Acc. Chem. Res. 2010, 43, 429–439.

[246] T. Kobayashi, Ed. , J-Aggregates, World Scientific, Singapore, 1996.

[247] F. Würthner, T. E. Kaiser, C. R. Saha-Möller, Angew. Chemie - Int. Ed. 2011, 50, 3376–3410.

[248] S. Banerjee, E. B. Veale, C. M. Phelan, S. A. Murphy, G. M. Tocci, L. J. Gillespie, D. O. Frimannsson, J. M. Kelly, T. Gunnlaugsson, Chem. Soc. Rev. 2013, 42, 1601–1618.

[249] D. Gudeika, Synth. Met. 2020, 262, 116328.

[250] M. Poddar, G. Sivakumar, R. Misra, J. Mater. Chem. C 2019, 7, 14798–14815.

[251] P. Gopikrishna, N. Meher, P. K. Iyer, ACS Appl. Mater. Interfaces 2018, 10, 12081–12111.

[252] A. R. Mallia, P. S. Salini, M. Hariharan, J. Am. Chem. Soc. 2015, 137, 15604–15607.

[253] A. R. Mallia, A. M. Philip, V. Bhat, M. Hariharan, J. Phys. Chem. C 2017, 121, 4765–4777.

[254] D. Kolosov, V. Adamovich, P. Djurovich, M. E. Thompson, C. Adachi, J. Am. Chem. Soc. 2002, 124, 9945–9954.

[255] B. Ventura, A. Bertocco, D. Braga, L. Catalano, S. D'Agostino, F. Grepioni, P. Taddei, J. Phys. Chem. C 2014, 118, 18646–18658.

[256] X. Chen, C. Xu, T. Wang, C. Zhou, J. Du, Z. Wang, H. Xu, T. Xie, G. Bi, J. Jiang, et al., Angew. Chemie - Int. Ed. 2016, 55, 9872–9876.

[257] M. S. Alexiou, V. Tychopoulos, S. Ghorbanian, J. H. P. Tyman, R. G. Brown, P. I. Brittain, J. Chem. Soc. Perkin Trans. 2 1990, 837–842.

[258] V. Wintgens, P. Valat, J. Kossanyi, L. Biczók, A. Demeter, T. Bérces, J. Chem. Soc. Faraday Trans. 1994, 90, 411–421.

[259] A. Demeter, T. Berces, L. Biczok, V. Wintgens, P. Valat, J. Kossanyi, J. Phys. Chem. 1996, 100, 2001–2011.

[260] O. V Prezhdo, B. V Uspenskii, V. V Prezhdo, W. Boszczyk, V. B. Distanov, Dye. Pigment. 2007, 72, 42–46.

[261] P. Kucheryavy, G. Li, S. Vyas, C. Hadad, K. D. Glusac, J. Phys. Chem. A 2009, 113, 6453–6461.

[262] D. Jacquemin, G. Scalmani, M. J. Frisch, E. A. Perpe, I. Ciofini, C. Adamo, Chem. Phys. Lett. 2007, 448, 3–6.

[263] P. K. Samanta, S. K. Pati, J. Mol. Model. 2018, 246.

[264] T. Xia, L. Wang, Y. Qu, Y. Rui, J. Cao, Y. Hu, J. Yang, J. Wu, J. Xu, J. Mater. Chem. C 2016, 4, 5696–5701.

[265] M. T. Chen, Y. Zhang, M. O. Vysotsky, J. O. Lindner, M. H. Li, M. J. Lin, F. Würthner, Org. Chem. Front. 2019, 6, 3731–3740.

[266] J. Da Chai, M. Head-Gordon, Phys. Chem. Chem. Phys. 2008, 10, 6615–6620.

[267] E. Cancès, B. Mennucci, J. Tomasi, J. Chem. Phys. 1997, 107, 3032–3041.

[268] D. W. Cho, M. Fujitsuka, A. Sugimoto, U. C. Yoon, P. S. Mariano, T. Majima, J. Phys. Chem. B 2006, 110, 11062–11068.

[269] C. V. Kumar, L. Qin, P. K. Das, J. Chem. Soc., Faraday Trans. 1984, 80, 783-793.

[270] W. E. Ford, P. V. Kamat, J. Phys. Chem. 1987, 91, 6373-6380.

[271] S. Hirata, M. Head-Gordon, Chem. Phys. Lett. 1999, 314, 291–299.

[272] C. M. Marian, Wiley Interdiscip. Rev. Comput. Mol. Sci. 2012, 2, 187–203.

[273] J. Zhao, W. Wu, J. Sun, S. Guo, Chem. Soc. Rev. 2013, 42, 5323–5351.

[274] J. Zhao, K. Chen, Y. Hou, Y. Che, L. Liu, D. Jia, Org. Biomol. Chem. 2018, 3692–3701.

[275] Z. Havlas, M. Kyvala, J. Michl, in Computational Methods in Photochemistry (Ed.: A.G. Kutateladze), Taylor & Francis, Boca Raton, USA, 2005, pp. 111–166.

[276] T. Itoh, Chem. Rev. 2012, 112, 4541–4568.

[277] P. K. Samanta, D. Kim, V. Coropceanu, J. L. Brédas, J. Am. Chem. Soc. 2017, 139, 4042–4051.

[278] M. Bixon, J. Jortner, J. Cortes, H. Heitele, M. E. Michel-Beyerle, J. Phys. Chem. 1994, 98, 7289–7299.

[279] M. A. El-Sayed, J. Chem. Phys. 1963, 38, 2834.

[280] S. Mukherjee, P. Thilagar, Chem. Commun. 2015, 51, 10988–11003.

[281] B. M. Aveline, S. Matsugo, R. W. Redmond, J. Am. Chem. Soc. 1997, 119, 11785–11795.

[282] R. L. Martin, J Chem Phys 2003, 118, 4775–4777.

[283] M. Moral, L. Muccioli, W. J. Son, Y. Olivier, J. C. Sancho-Garcia, J. Chem. Theory Comput. 2015, 11, 168–177.

[284] F. Neese, Wiley Interdiscip. Rev. Comput. Mol. Sci. 2012, 2, 73–78.

[285] E. Van Lenthe, J. G. Snijders, E. J. Baerends, J. Chem. Phys. 1996, 105, 6505–6516.

[286] Y. S. Lin, G. De Li, S. P. Mao, J. Da Chai, J. Chem. Theory Comput. 2013, 9, 263–272.

[287] F. Weigend, R. Ahlrichs, Phys. Chem. Chem. Phys. 2005, 7, 3297–3305.

[288] F. Weigend, Phys. Chem. Chem. Phys. 2006, 8, 1057–1065.

[289] V. Barone, M. Cossi, J. Phys. Chem. A 1998, 102, 1995–2001.

[290] T. Gerbich, H. C. Schmitt, I. Fischer, R. Mitrić, J. Petersen, J. Phys. Chem. A 2016, 120, 2089–2095.

[291] T. N. Singh-Rachford, F. N. Castellano, Coord. Chem. Rev. 2010, 254, 2560–2573.

[292] J. Zhao, S. Ji, H. Guo, RSC Adv. 2011, 1, 937–950.

[293] C. Kerzig, O. S. Wenger, Chem. Sci. 2018, 9, 6670–6678.

[294] L. Bruzzone, R. Badía, M. E. Díaz García, Crit. Rev. Anal. Chem. 2000, 30, 163–178.

[295] I. Sánchez-Barragán, J. M. Costa-Fernández, M. Valledor, J. C. Campo, A. Sanz-Medel, Trends Anal. Chem. 2006, 25, 958–967.

[296] M. E. Díaz-García, A. Fernández-González, R. Badía-Laíño, Appl. Spectrosc. Rev. 2007, 42, 605–624.

[297] G. Zhou, W. Y. Wong, S. Suo, J. Photochem. Photobiol. C 2010, 11, 133–156.

[298] B. Minaev, G. Baryshnikov, H. Agren, Phys. Chem. Chem. Phys. 2014, 16, 1719–1758.

[299] Y. Li, M. Gecevicius, J. Qiu, Chem. Soc. Rev. 2016, 45, 2090–2136.

[300] W. Zhao, Z. He, B. Z. Tang, Nat. Rev. Mater. 2020, 5, 869-885.

[301] X. Zhang, Y. Hou, X. Xiao, X. Chen, M. Hu, X. Geng, Z. Wang, J. Zhao, Coord. Chem. Rev. 2020, 417, 213371.

[302] M. Baroncini, G. Bergamini, P. Ceroni, Chem. Commun. 2017, 53, 2081–2093.

[303] Kenry, C. Chen, B. Liu, Nat. Commun. 2019, 10, 2111.

[304] W. Jia, Q. Wang, H. Shi, Z. An, W. Huang, Chem. Eur. J. 2020, 26, 4437–4448.

[305] Y. Gong, G. Chen, Q. Peng, W. Z. Yuan, Y. Xie, S. Li, Y. Zhang, B. Z. Tang, Adv. Mater. 2015, 27, 6195–6201.

[306] S. Ohtani, M. Gon, K. Tanaka, Y. Chujo, Chem. - A Eur. J. 2017, 23, 11827–11833.

[307] J. Yang, Z. Ren, B. Chen, M. Fang, Z. Zhao, B. Z. Tang, Q. Peng, Z. Li, J. Mater. Chem. C 2017, 5, 9242–9246.

[308] E. G. Mc Rae, M. Kasha, J. Chem. Phys. 1958, 28, 721–722.

[309] A. Forni, E. Lucenti, C. Botta, E. Cariati, J. Mater. Chem. C 2018, 6, 4603–4626.

[310] L. Xiao, H. Fu, Chem. Eur. J. 2019, 25, 714–723.

[311] K. Zheng, F. Ni, Z. Chen, C. Zhong, C. Yang, Angew. Chemie - Int. Ed. 2020, 59, 9972–9976.

[312] O. Toma, N. Mercier, M. Allain, A. Forni, F. Meinardi, C. Botta, Dalt. Trans. 2015, 44, 14589–14593.

[313] J. Wang, Z. Chai, J. Wang, C. Wang, M. Han, Q. Liao, A. Huang, P. Lin, C. Li, Q. Li, et al., Angew. Chemie - Int. Ed. 2019, 58, 17297–17302.

[314] K. Wang, H. Zhang, S. Chen, G. Yang, J. Zhang, W. Tian, Z. Su, Y. Wang, Adv. Mater. 2014, 26, 6168–6173.

[315] P. Xue, J. Ding, P. Wang, R. Lu, J. Mater. Chem. C 2016, 4, 6688–6706.

[316] F. Todescato, I. Fortunati, S. Carlotto, C. Ferrante, L. Grisanti, C. Sissa, A. Painelli, A. Colombo, C. Dragonetti, D. Roberto, Phys. Chem. Chem. Phys. 2011, 13, 11099–11109.

[317] E. Quartapelle Procopio, M. Mauro, M. Panigati, D. Donghi, P. Mercandelli, A. Sironi, G. D'Alfonso, L. De Cola, J. Am. Chem. Soc. 2010, 132, 14397–14399.

[318] E. V. Tsiper, Z. G. Soos, Phys. Rev. B 2001, 64, 1–12.

[319] W. C. H. Choy, W. K. Chan, Y. Yuan, Adv. Mater. 2014, 26, 5368–5399.

[320] S. Tavazzi, L. Silvestri, P. Spearman, A. Borghesi, P. Mercandelli, M. Panigati, G. D'Alfonso, A. Sironi, L. De Cola, Cryst. Growth Des. 2012, 12, 742–749.

[321] D. Donghi, G. D'Alfonso, M. Mauro, M. Panigati, P. Mercandelli, A. Sironi, P. Mussini, L. D'Alfonso, Inorg. Chem. 2008, 47, 4243–4255.

[322] M. Mauro, E. Q. Procopio, Y. Sun, C. H. Chien, D. Donghi, M. Panigati, P. Mercandelli, P. Mussini, G. D'Alfonso, L. De Cola, Adv. Funct. Mater. 2009, 19, 2607–2614.

[323] Y. You, H. S. Huh, K. S. Kim, S. W. Lee, D. Kim, S. Y. Park, Chem. Commun. 2008, 3998–4000.

[324] D. Andrae, U. Häußermann, M. Dolg, H. Stoll, H. Preuß, Theor. Chim. Acta 1990, 77, 123–141

[325] S. Xue, X. Qiu, Q. Sun, W. Yang, J. Mater. Chem. C 2016, 4, 1568–1578.

[326] K. C. Naeem, K. Neenu, V. C. Nair, ACS Omega 2017, 2, 9118–9126.

[327] P. Sonar, S. P. Singh, P. Leclère, M. Surin, R. Lazzaroni, T. T. Lin, A. Dodabalapur, A. Sellinger, J. Mater. Chem. 2009, 19, 3228–3237.

[328] A. Kaeser, I. Fischer, R. Abbel, P. Besenius, D. Dasgupta, M. A. J. Gillisen, G. Portale, A. L. Stevens, L. M. Herz, A. P. H. J. Schenning, ACS Nano 2013, 7, 1, 408-416.

[329] Z. Chi, X. Zhang, B. Xu, X. Zhou, C. Ma, Y. Zhang, S. Liua, J. Xu, Chem. Soc. Rev. 2012, 41, 3878–3896.

[330] Z. Ma, M. Teng, Z. Wang, S. Yang, X. Jia, Angew. Chemie - Int. Ed. 2013, 52, 12268–12272.

[331] R. Li, S. Xiao, Y. Li, Q. Lin, R. Zhang, J. Zhao, C. Yang, K. Zou, D. Li, T. Yi, Chem. Sci. 2014, 5, 3922–3928.

[332] Z. Ma, Z. Wang, M. Teng, Z. Xu, X. Jia, ChemPhysChem 2015, 16, 1811–1828.

[333] J. Wei, B. Liang, X. Cheng, Z. Zhang, H. Zhang, Y. Wang, RSC Adv. 2015, 5, 71903–71910.

[334] X. Du, F. Xu, M. Sen Yuan, P. Xue, L. Zhao, D. E. Wang, W. Wang, Q. Tu, S. W. Chen, J. Wang, J. Mater. Chem. C 2016, 4, 8724–8730.

[335] Y. Sagara, S. Yamane, M. Mitani, C. Weder, T. Kato, Adv. Mater. 2016, 28, 1073–1095.

[336] C. Wang, Y. Yu, Z. Chai, F. He, C. Wu, Y. Gong, M. Han, Q. Li, Z. Li, Mater. Chem. Front. 2019, 3, 32–38.

[337] C. Dou, D. Chen, J. Iqbal, Y. Yuan, H. Zhang, Y. Wang, Langmuir 2011, 27, 6323–6329.

[338] T. Ishi-i, I. Kitahara, S. Yamada, Y. Sanada, K. Sakurai, A. Tanaka, N. Hasebe, T. Yoshihara, S. Tobita, Org. Biomol. Chem. 2015, 13, 1818–28.

[339] C. Zhang, X. Zhu, Acc. Chem. Res. 2017, 50, 1342–1350.

[340] B. A. D. Neto, A. A. M. Lapis, E. N. Da Silva Jùnior, J. Dupont, European J. Org. Chem. 2013, 228–255.

[341] J. E. Coughlin, A. Zhugayevych, R. C. Bakus, T. S. Van Der Poll, G. C. Welch, S. J. Teat, G. C. Bazan, S. Tretiak, J. Phys. Chem. C 2014, 118, 15610–15623.

[342] C. Chen, D. H. Maldonado, D. Le Borgne, F. Alary, B. Lonetti, B. Heinrich, B. Donnio, K. I. Moineau-Chane Ching, New J. Chem. 2016, 40, 7326-7337.

[343] F. E. Critchfield, J. A. Gibson jr., J. L. Hall, J. Am. Chem. Soc. 1953, 75, 6044–6045.

[344] C. Zheng, C. Zhong, C. J. Collison, F. C. Spano, J. Phys. Chem. C 2019, 123, 3203–3215.

[345] Y. Zhang, B. Kim, S. Yao, M. V Bondar, Langmuir 2013, 29, 11005–11012.

[346] H. Sakae, H. Nagatani, K. Morita, H. Imura, Langmuir 2014, 30, 937–945.

[347] V. Balzani, Ed. , Electron Transfer in Chemistry, Wiley-VCH Verlag GmbH, Weinheim, Germany, 2001.

[348] V. May, O. Kühn, Charge and Energy Transfer Dynamics in Molecular Systems, Wiley-VCH, 2011.

[349] I. L. Medintz, N. Hildebrandt, Eds. , FRET - Forster Resonance Energy Transfer, Wiley-VCH Verlag GmbH, Weinheim, Germany, 2014.

[350] K. E. Sapsford, L. Berti, I. L. Medintz, Angew. Chemie - Int. Ed. 2006, 45, 4562–4589.

[351] R. E. Blankenship, Molecular Mechanisms of Photosynthesis, Blackwell Science, Oxford, 2002.

[352] R. Emerson, W. Arnold, J. Gen. Physiol. 1932, 16, 191–205.

[353] X. Hu, A. Damjanović, T. Ritz, K. Schulten, Proc. Natl. Acad. Sci. U. S. A. 1998, 95, 5935–5941.

[354] V. Balzani, A. Credi, M. Venturi, ChemSusChem, 2008, 1, 26-58.

[355] V. Balzani, P. Ceroni, M. Maestri, V. Vicinelli, Curr. Opin. Chem. Biol. 2003, 7, 657–665.

[356] F. D'Souza, P. M. Smith, M. E. Zandler, A. L. McCarty, M. Itou, Y. Araki, O. Ito, J. Am. Chem. Soc. 2004, 126, 7898–7907.

[357] W. J. Shi, M. E. El-Khouly, K. Ohkubo, S. Fukuzumi, D. K. P. Ng, Chem. Eur. J. 2013, 19, 11332–11341.

[358] V. Balzani, A. Credi, M. Venturi, Chem. Eur. J. 2008, 14, 26–39.

[359] J. I. Basham, G. K. Mor, C. A. Grimes, ACS Nano 2010, 4, 1253–1258.

[360] J. Barber, Chem. Soc. Rev. 2009, 38, 185–196.

[361] K. Feron, W. J. Belcher, C. J. Fell, P. C. Dastoor, Int. J. Mol. Sci. 2012, 13, 17019–17047.

[362] T. J. Meyer, Acc. Chem. Res. 1989, 22, 163–170.

[363] G. D. Scholes, C. Curutchet, B. Mennucci, R. Cammi, J. Tomasi, J. Phys. Chem. B 2007, 111, 6978–6982.

[364] D. Gust, T. A. Moore, A. L. Moore, Acc. Chem. Res. 1993, 26, 198–205.

[365] H. Kurreck, M. Huber, Angew. Chemie - Int. Ed. 1995, 34, 849–866.

[366] D. Gust, T. A. Moore, A. L. Moore, Acc. Chem. Res. 2001, 34, 40–48.

[367] D. M. Guldi, Chem. Soc. Rev. 2002, 31, 22–36.

[368] M. J. Brites, C. Santos, S. Nascimento, B. Gigante, H. Luftmann, A. Fedorov, M. N. Berberan-Santos, New J. Chem. 2006, 30, 1036–1045.

[369] J. Baffreau, S. Leroy-Lhez, N. V. Anh, R. M. Williams, P. Hudhomme, Chem. Eur. J. 2008, 14, 4974–4992.

[370] J. Jose, Y. Ueno, J. C. Castro, L. Li, K. Burgess, Tetrahedron Lett. 2009, 50, 6442–6445.

[371] R. K. Dubey, T. Kumpulainen, A. Efimov, N. V. Tkachenko, H. Lemmetyinen, European J. Org. Chem. 2010, 3428–3436.

[372] M. Di Donato, A. Iagatti, A. Lapini, P. Foggi, S. Cicchi, L. Lascialfari, S. Fedeli, S. Caprasecca, B. Mennucci, J. Phys. Chem. C 2014, 118, 23476–23486.

[373] M. E. El-Khouly, S. Fukuzumi, F. D'Souza, ChemPhysChem 2014, 15, 30–47.

[374] D. M. Guldi, M. Maggini, G. Scorrano, M. Prato, J. Am. Chem. Soc. 1997, 119, 974–980.

[375] S. E. Miller, A. S. Lukas, E. Marsh, P. Bushard, M. R. Wasielewski, J. Am. Chem. Soc. 2000, 122, 7802–7810.

[376] B. Pelado, F. Abou-Chahine, J. Calbo, R. Caballero, P. De La Cruz, J. M. Junquera-Hernández, E. Ortí, N. V. Tkachenko, F. Langa, Chem. Eur. J. 2015, 21, 5814–5825.

[377] M.-Z. Asfari, V. Böhmer, J. Harrowfield, J. Vicens, Eds. , Calixarenes 2001, Kluwer Academic Publisher, Dordrecht, 2001.

[378] D. C. Gutsche, Calixarenes, The Royal Society Of Chemistry, London, 2008.

[379] A. Arduini, M. Fabbi, M. Mantovani, L. Mirone, A. Pochini, A. Secchi, R. Ungaro, J. Org. Chem. 1995, 60, 1454–1457.

[380] M. Lazzarotto, F. Sansone, L. Baldini, A. Casnati, P. Cozzini, R. Ungaro, Eur. J. Org. Chem. 2001, 595-602.

[381] I. Tosi, M. Segado Centellas, E. Campioli, A. Iagatti, A. Lapini, C. Sissa, L. Baldini, C. Cappelli, M. Di Donato, F. Sansone, et al., ChemPhysChem 2016, 17, 1686–1706.

[382] J. S. Kim, D. T. Quang, Chem. Rev. 2007, 107, 3780–3799.

[383] C. Hippius, F. Schlosser, M. O. Vysotsky, V. Böhmer, F. Würthner, J. Am. Chem. Soc. 2006, 128, 3870–3871.

[384] C. Hippius, I. H. M. Van Stokkum, M. Gsänger, M. M. Groeneveld, R. M. Williams, F. Würthner, J. Phys. Chem. C 2008, 112, 2476–2486.

[385] N. V. Anh, F. Schlosser, M. M. Groeneveld, I. H. M. Van Stokkum, F. Würthner, R. M. Williams, J. Phys. Chem. C 2009, 113, 18358–18368.

[386] G. Pognon, J. A. Wytko, P. D. Harvey, J. Weiss, Chem. Eur. J. 2009, 15, 524–535.

[387] I. Tosi, B. Bardi, M. Ambrosetti, E. Domenichini, A. Iagatti, L. Baldini, C. Cappelli, M. Di Donato, F. Sansone, C. Sissa, et al., Dye. Pigment. 2019, 171, 107652.

[388] B. Bardi, I. Tosi, F. Faroldi, L. Baldini, F. Sansone, C. Sissa, F. Terenziani, Chem. Commun. 2019, 55, 8098–8101.

[389] G. S. Engel, T. R. Calhoun, E. L. Read, T. K. Ahn, T. Mančal, Y. C. Cheng, R. E. Blankenship, G. R. Fleming, Nature 2007, 446, 782–786.

[390] G. D. Scholes, J. Phys. Chem. Lett. 2010, 1, 2–8.

[391] G. D. Scholes, G. R. Fleming, L. X. Chen, A. Aspuru-Guzik, A. Buchleitner, D. F. Coker, G. S. Engel, R. Van Grondelle, A. Ishizaki, D. M. Jonas, et al., Nature 2017, 543, 647–656.

[392] T. Mančal, Chem. Phys. 2020, 532, 110663.

[393] T. Förster, Radiat. Res. Suppl. 1960, 2, 326.

[394] H. Bucher, K. H. Drelhage, M. Fleck, H. Kuhn, D. Mobius, F. P. Schafer, J. Sondermann, W. Sperling, P. Tillmann, J. Wiegand, Mol Cryst 1967, 2, 199–230.

[395] R. P. Haugland, J. Yguerabide, L. Stryer, Proc. Natl. Acad. Sci. 1969, 63, 23–30.

[396] L. Stryer, R. P. Haugland, Prot. Natl. Acad. Sci. 1967, 58, 719–726.

[397] L. Stryer, Ann. Rev. Biochem. 1978, 47, 819–846.

[398] P. F. Barbara, T. J. Meyer, M. A. Ratner, J. Phys. Chem. 1996, 100, 13148–13168.

[399] R. A. Marcus, N. Sutin, Biochim. Biophys. Acta 1985, 811, 265–322.

[400] R. A. Marcus, Rev. Mod. Phys. 1993, 65, 599–610.

[401] J. S. Lee, N. Y. Kang, K. K. Yun, A. Samanta, S. Feng, K. K. Hyeong, M. Vendrell, H. P. Jung, Y. T. Chang, J. Am. Chem. Soc. 2009, 131, 10077–10082.

[402] A. Loudet, K. Burgess, Chem. Rev. 2007, 107, 4891–4932.

[403] M. Baruah, W. Qin, C. Flors, J. Hofkens, R. A. L. Vallée, D. Beljonne, M. Van Der Auweraer, W. M. De Borggraeve, N. Boens, J. Phys. Chem. A 2006, 110, 5998–6009.

[404] J. Karolin, L. B. A. Johansson, L. Strandberg, T. Ny, J. Am. Chem. Soc. 1994, 116, 7801–7806.

[405] I. H. M. Van Stokkum, D. S. Larsen, R. Van Grondelle, Biochim. Biophys. Acta 2004, 1657, 82–104.

[406] J. J. Snellenburg, S. Laptenok, R. Seger, K. M. Mullen, I. H. M. Van Stokkum, J. Stat. Softw. 2012, 49, 1–22.

[407] A. Iagatti, L. Cupellini, G. Biagiotti, S. Caprasecca, S. Fedeli, A. Lapini, E. Ussano, S. Cicchi, P. Foggi, M. Marcaccio, et al., J. Phys. Chem. C 2016, 120, 16526–16536.

[408] M. A. Filatov, S. Karuthedath, P. M. Polestshuk, H. Savoie, K. J. Flanagan, C. Sy, E. Sitte, M. Telitchko, M. O. Senge, J. Am. Chem. Soc. 2017, 6282–6285.

[409] J. Bloino, M. Biczysko, F. Santoro, V. Barone, J. Chem. Theory Comput. 2010, 6, 1256–1274.

[410] M. Biczysko, J. Bloino, G. Brancato, I. Cacelli, C. Cappelli, A. Ferretti, A. Lami, S. Monti, A. Pedone, G. Prampolini, et al., Theor. Chem. Acc. 2012, 131, 1–19.

[411] J. Bloino, A. Baiardi, M. Biczysko, Int. J. Quantum Chem. 2016, 116, 1543–1574.

[412] M. F. Iozzi, B. Mennucci, J. Tomasi, R. Cammi, J. Chem. Phys. 2004, 120, 7029–7040.

[413] C. Curutchet, B. Mennucci, J. Am. Chem. Soc. 2005, 127, 16733–16744.

[414] K. Rurack, M. Kollmannsberger, J. Daub, Angew. Chemie - Int. Ed. 2001, 40, 385–387.

[415] M. Kollmannsberger, T. Gareis, S. Heinl, J. Breu, J. Daub, Angew. Chemie - Int. Ed. 1997, 36, 1333–1335.

[416] L. Baklouti, J. Harrowfield, B. Pulpoka, J. Vicens, Mini. Rev. Org. Chem. 2006, 3, 355–384.

[417] J. Strahan, B. C. Popere, P. Khomein, C. A. Pointer, S. M. Martin, A. N. Oldacre, S. Thayumanavan, E. R. Young, Dalt. Trans. 2019, 48, 8488–8501.

[418] C. Sissa, F. Terenziani, A. Painelli, A. K. Manna, S. K. Pati, Chem. Phys. 2012, 404, 9–15.

[419] F. Zhou, C. Jehoulet, A. J. Bard, J. Am. Chem. Soc. 1992, 114, 11004–11006.

[420] B. M. Illescas, N. Martín, Comptes Rendus Chim. 2006, 9, 1038–1050.

[421] A. Hirsch, Ed. , Fullerene and Related Structures, Springer, Berlin, 1999.

[422] H. Imahori, K. Hagiwara, T. Akiyama, M. Aoki, S. Taniguchi, T. Okada, M. Shirakawa, Y. Sakata, Chem. Phys. Lett. 1996, 263, 545–550.

[423] D. M. Guldi, K. D. Asmus, J. Am. Chem. Soc. 1997, 119, 5744–5745.

[424] D. M. Guldi, C. Luo, M. Prato, E. Dietel, A. Hirsch, Chem. Commun. 2000, 373–374.

[425] D. González-Rodríguez, T. Torres, D. M. Guldi, J. Rivera, M. Ángeles, J. Am. Chem. Soc. 2004, 126, 6301–6313.

[426] D. Kuciauskas, S. Lin, G. R. Seely, A. L. Moore, T. a Moore, D. Gust, T. Drovetskaya, C. a Reed, P. D. W. Boyd, J. Phys. Chem. 1996, 100, 15926–15932.

[427] I. B. Martini, B. Ma, T. Da Ros, R. Helgeson, F. Wudl, B. J. Schwartz, Chem. Phys. Lett. 2000, 327, 253–262.

[428] J. L. Segura, R. Gómez, N. Martín, C. Luo, D. M. Guldi, Chem. Commun. 2000, 701–702.

[429] Y. Araki, Y. Yasumura, O. Ito, J. Phys. Chem. B 2005, 109, 9843–9848.

[430] S. a Vail, D. I. Schuster, D. M. Guldi, M. Isosomppi, N. Tkachenko, H. Lemmetyinen, A. Palkar, L. Echegoyen, X. Chen, J. Z. H. Zhang, J. Phys. Chem. B 2006, 110, 14155–14166.

[431] Y. Luo, K. Barthelmes, M. Wächtler, A. Winter, U. S. Schubert, B. Dietzek, Chem. Eur. J. 2017, 4917–4922.

[432] S. Anandan, M. Yoon, Spectrochim. Acta - Part A 2004, 60, 885–888.

[433] J. F. Deye, T. A. Berger, A. G. Anderson, Anal. Chem. 1990, 62, 615–622.

[434] J. P. Hare, H. W. Kroto, R. Taylor, Chem. Phys. Lett. 2013, 589, 57–60.

[435] R. M. Williams, J. M. Zwier, J. W. Verhoeven, J. Am. Chem. Soc. 1995, 117, 4093–4099.

[436] R. M. Williams, M. Koeberg, J. M. Lawson, Y.-Z. An, Y. Rubin, M. N. Paddon-Row, J. W. Verhoeven, J. Org. Chem. 1996, 61, 5055–5062.

[437] D. M. Guldi, M. Prato, Acc. Chem. Res. 2000, 33, 695–703.

[438] Y. P. Sun, P. Wang, N. B. Hamilton, J. Am. Chem. Soc. 1993, 115, 6378–6381.

[439] Y. X. Liu, M. A. Summers, S. R. Scully, M. D. McGehee, J. Appl. Phys. 2006, 99, 093521.

[440] T. Kato, T. Kodama, T. Shida, Chem. Phys. Lett. 1993, 205, 405–409.

[441] B. B. Lowell, B. M. Spiegelman, Nature 2000, 404, 652–660.

[442] K. M. McCabe, M. Hernandez, Pediatr. Res. 2010, 67, 469–475.

[443] K. Okabe, N. Inada, C. Gota, Y. Harada, T. Funatsu, S. Uchiyama, Nat. Commun. 2012, 3, 705.

[444] C. Gosse, C. Bergaud, P. Löw, in Thermal Nanosystems and Nanomaterials, Topics in Applied Physics (Ed.: S. Volz), Springer-Verlag, Berlin Heidelberg, 2009, pp. 301–341.

[445] C. D. S. Brites, P. P. Lima, N. J. O. Silva, A. Millán, V. S. Amaral, F. Palacio, L. D. Carlos, Nanoscale 2012, 4, 4799–4829.

[446] M. Quintanilla, L. M. Liz-Marzán, Nano Today 2018, 19, 126–145.

[447] X. Wang, O. S. Wolfbeis, R. J. Meier, Chem. Soc. Rev. 2013, 42, 7834.

[448] C. F. Chapman, Y. Liu, G. J. Sonek, B. J. Tromberg, Photochem. Photobiol. 1995, 62, 416–425.

[449] S. Hirata, T. Watanabe, Adv. Mater. 2006, 18, 2725–2729.

[450] D. Gong, T. Cao, S. C. Han, X. Zhu, A. Iqbal, W. Liu, W. Qin, H. Guo, Sensors Actuators B 2017, 252, 577–583.

[451] J. Feng, K. Tian, D. Hu, S. Wang, S. Li, Y. Zeng, Y. Li, G. Yang, Angew. Chemie - Int. Ed. 2011, 50, 8072–8076.

[452] J. Feng, L. Xiong, S. Wang, S. Li, Y. Li, G. Yang, Adv. Funct. Mater. 2013, 23, 340–345.

[453] X. Liu, S. Li, Y. Li, G. Yang, Chem. Commun. 2014, 50, 2778–2780.

[454] D. Ross, M. Gaitan, L. E. Locascio, Anal. Chem. 2001, 73, 4117–4123.

[455] Y. Li, Z. Li, Y. Hou, Y. N. Fan, C. Y. Su, Inorg. Chem. 2018, 57, 13235–13245.

[456] S. A. Thompson, I. A. Martínez, P. Haro-González, A. P. Adam, D. Jaque, J. B. Nieder, R. De La Rica, ACS Photonics 2018, 5, 2676–2681.

[457] S. Otto, N. Scholz, T. Behnke, U. Resch-Genger, K. Heinze, Chem. Eur. J. 2017, 23, 12131–12135.

[458] J. Rocha, C. D. S. Brites, L. D. Carlos, Chem. Eur. J. 2016, 22, 14782–14795.

[459] J. C. Fister, D. Rank, J. M. Harris, Anal. Chem. 1995, 67, 4269–4275.

[460] J. Lou, T. A. Hatton, P. E. Laibinis, Anal. Chem. 1997, 69, 1262–1264.

[461] G. A. Baker, S. N. Baker, T. M. McCleskey, Chem. Commun. 2003, 3, 2932–2933.

[462] C. Baleizão, M. N. Berberan-Santos, J. Fluoresc. 2006, 16, 215–219.

[463] C. Y. Chen, C. T. Chen, Chem. Commun. 2011, 47, 994–996.

[464] M. Han, Y. Tian, Z. Yuan, L. Zhu, B. Ma, Angew. Chemie - Int. Ed. 2014, 53, 10908–10912.

[465] A. Steinegger, I. Klimant, S. M. Borisov, Adv. Opt. Mater. 2017, 5, 1700372.

[466] L. Shi, W. Song, C. Lian, W. Chen, J. Mei, J. Su, H. Liu, H. Tian, Adv. Opt. Mater. 2018, 6, 1800190.

[467] J. R. Macairan, D. B. Jaunky, A. Piekny, R. Naccache, Nanoscale Adv. 2019, 1, 105–113.

[468] G. Ke, C. Wang, Y. Ge, N. Zheng, Z. Zhu, C. J. Yang, J. Am. Chem. Soc. 2012, 134, 18908–18911.

[469] C. Li, J. Hu, S. Liu, Soft Matter 2012, 8, 7096–7102.

[470] X. Hu, Y. Li, T. Liu, G. Zhang, S. Liu, ACS Appl. Mater. Interfaces 2015, 7, 15551–15560.

[471] Y. Wu, J. Liu, Y. Wang, K. Li, L. Li, J. Xu, D. Wu, ACS Appl. Mater. Interfaces 2017, 9, 11073–11081.

[472] D. Zhao, D. Yue, K. Jiang, Y. Cui, Q. Zhang, Y. Yang, G. Qian, J. Mater. Chem. C 2017, 5, 1607–1613.

[473] Z. Ding, C. Wang, G. Feng, X. Zhang, Polymers 2018, 10, 283.

[474] S. Uchiyama, C. Gota, Rev. Anal. Chem. 2016, 36, 20160021.

[475] J. Qiao, Y. H. Hwang, C. F. Chen, L. Qi, P. Dong, X. Y. Mu, D. P. Kim, Anal. Chem. 2015, 87, 10535–10541.

[476] N. Xie, J. Huang, X. Yang, X. He, J. Liu, J. Huang, H. Fang, K. Wang, Anal. Chem. 2017, 89, 12115–12122.

[477] J. Scheerder, R. H. Vreekamp, J. F. J. Engbersen, W. Verboom, J. P. M. Van Duynhoven, D. N. Reinhoudt, J. Org. Chem. 1996, 61, 3476–3481.

[478] F. C. Krebs, M. Larsen, M. Jørgensen, P. R. Jensen, M. Bielecki, K. Schaumburg, J. Org. Chem. 1998, 63, 9872–9879.

[479] M. Jørgensen, M. Larsen, P. Sommer-Larsen, W. Batsberg Petersen, H. Eggert, J. Chem. Soc., Perkin Trans. 1 1997, 6, 2851–2855.

[480] L. Baldini, F. Sansone, G. Faimani, C. Massera, A. Casnati, R. Ungaro, European J. Org. Chem. 2008, 869–886.

[481] X. Huang, J. Song, B. C. Yung, X. Huang, Y. Xiong, X. Chen, Chem. Soc. Rev. 2018, 47, 2873–2920.

[482] J. D. Cauwood, W. Ernest, S. Turner, J. Chem. Soc., Trans. 1915, 276–282.

[483] S. Valkai, J. Liszi, I. Szalai, J. Chem. Thermodyn. 1998, 30, 825–832.

[484] H. El-Kashef, Rev. Sci. Instrum. 1998, 69, 1243–1245.

[485] K. Rurack, M. Spieles, Anal. Chem. 2011, 83, 1232–1242.

[486] G. A. Crosby, J. N. Demas, J. Phys. Chem. 1971, 75, 991–1024.

[487] C. A. Ullrich, Z. hui Yang, Brazilian J. Phys. 2014, 44, 154–188.

[488] F. Jensen, Introduction to Computational Chemistry, Wiley, England, 2007, pp. 232–267.

[489] K. Capelle, Brazilian J. Phys. 2006, 36, 1318–1343.

[490] C. Lee, W. Yang, R. G. Parr, Phys. Rev. B 1988, 37, 785.

[491] M. A. L. Marques, N. T. Maitra, F. M. S. Nogueira, E. K. U. Gross, A. Rubio, Eds. , Fundamentals of Time-Dependent Density Functional Theory, Springer-Verlag, Berlin, 2012.

[492] C. A. Ullrich, Time-Dependent Density Functional Theory. Concepts and Applications, Oxford University Press, New York, 2012.

[493] M. A. L. Marques, E. K. U. Gross, Annu. Rev. Phys. Chem. 2004, 55, 427–455.

[494] K. Burke, J. Werschnik, E. K. U. Gross, J. Chem. Phys. 2005, 123, 062206.

[495] A. Dreuw, M. Head-Gordon, Chem. Rev. 2005, 105, 4009–4037.

[496] M. E. Casida, M. Huix-Rotllant, Annu. Rev. Phys. Chem. 2012, 63, 287–323.

[497] F. Furche, D. Rappoport, in Computational Photochemistry (Ed.: M. Olivucci), Elsevier, Amsterdam, 2005, pp. 93–128.

[498] A. D. Laurent, C. Adamo, D. Jacquemin, Phys. Chem. Chem. Phys. 2014, 16, 14334–14356.

[499] C. Adamo, T. Le Bahers, M. Savarese, L. Wilbraham, G. García, R. Fukuda, M. Ehara, N. Rega, I. Ciofini, Coord. Chem. Rev. 2015, 304–305, 166–178.

[500] R. Baer, E. Livshits, U. Salzner, Annu. Rev. Phys. Chem. 2010, 61, 85–109.

[501] A. D. Laurent, D. Jacquemin, Int. J. Quantum Chem. 2013, 113, 2019–2039

[502] M. Petersilka, U. J. Gossman, E. K. U. Gross, Phys. Rev. Lett. 1996, 76, 1212.

[503] M. E. Casida, in Recent Advances in Density Functional Methods. Recent Advances in Computational Chemistry (Ed.: D.. Chong), World Scientific, Singapore, 1995, pp. 155–192.

[504] F. Furche, R. Ahlrichs, J. Chem. Phys. 2002, 117, 7433–7447.

[505] M. J. G. Peach, M. J. Williamson, D. J. Tozer, J. Chem. Theory Comp. 2011, 7, 3578–3585.

[506] M. J. G. Peach, D. J. Tozer, J Phys. Chem. A 2012, 116, 9783–9789.

[507] W. Thomas, Naturwissenchaften 1925, 13, 627–628.

[508] F. Reiche, W. Z. Thomas, Phys. 1925, 34, 510–525.

[509] W. Z. Kuhn, Phys. 1925, 33, 408–412.

[510] J. Tomasi, Theor. Chem. Acc. 2004, 112, 184–203.

[511] B. Mennucci, Wiley Interdiscip. Rev. Comput. Mol. Sci. 2012, 2, 386–404.

[512] R. Cammi, S. Corni, B. Mennucci, J. Tomasi, J. Chem. Phys. 2005, 122, 104513.

[513] M. Caricato, J. Chem. Phys. 2013, 139, 044116.

Acknowledgements

I wish to express my deepest gratitude to my supervisor, Prof. Francesca Terenziani, for her constant guidance throughout the PhD training, and for her encouraging and priceless suggestions. I am also indebted to Prof. Anna Painelli, for her valuable advice and for introducing me to the fascinating world of quantum chemistry. I also thank Dr. Cristina Sissa for fruitful discussions, and all past and present members of the host laboratory for the valuable time spent together.

I thank all the collaborators who put many efforts in the synthesis of the molecular systems investigated in this Thesis: Prof. Daniel T. Gryko and Dr. Maciej Krzeszewski (Institute of Organic Chemistry, Polish Academy of Sciences, Warsaw, Poland) for the synthesis of the aza-nanographene dye presented in Chapter 1, Dr. Nadia Barbero and Prof. Claudia Barolo (Department of Chemistry, University of Torino, Italy) for the synthesis of indolenine-based squaraines, Prof. Mahesh Hariharan and Dr. Remya Ramakrishnan (Indian Institute for Scientific Education and Research, Trivandrum, India) for the synthesis and characterization of NI-based systems, Dr. Kathleen I. Moineau-Chane Ching and Dr. Chunxiang Dall'Agnese (Laboratory of Coordination Chemistry, CNRS, Toulouse, France) for providing the BDT derivatives studied in Chapter 2, Prof. Laura Baldini, Prof. Francesco Sansone, Dr. Irene Tosi and Dr. Federica Faroldi (Departiment of Chemisrty, Life Sciences and Environmental Sustainability, University of Parma, Italy) for the design and synthesis of calixarene-based dyads.

I acknowledge Dr. Mariangela di Donato and coworkers (European Laboratory for Non-Linear Spectroscopy, Florence, Italy) for time-resolved measurements and Prof. Chiara Cappelli and coworkers (Scuola Normale Superiore, Pisa, Italy) for the computational work on BODIPY-based dyads.

I thank Prof. Monica Panigati (Department of Chemistry, University of Milano, Italy) for suggesting the computational study on the dinuclear Rhenium(I) complex.

Financial support from the Italian Ministero dell'Istruzione, dell'Università e della Ricerca (MIUR) through the program FIRB 'Futuro in Ricerca 2010' grant RBFR10Y5VW and grant 'Dipartimenti di Eccellenza' (DM 11/05/2017 n. 262) is gratefully acknowledged. This project has received funding from the European Union's Horizon 2020 Research and Innovation programme under grant agreement No. 812872 (TADFlife).

This research benefits from the HPC (High Performance Computing) facility of the University of Parma, Italy.

List of Publications

B. Bardi, M. Krzeszewski, D. T. Gryko, A. Painelli, F. Terenziani, *Excited-state symmetry breaking in an aza-nanographene dye*, Chem. Eur. J. 2019, 25, 13930-13938

I. Tosi, B. Bardi, M. Ambrosetti, E. Domenichini, A. Iagatti, L. Baldini, C. Cappelli, M. Di Donato, F. Sansone, C. Sissa, F. Terenziani, *Investigation of electronic energy transfer in a BODIPY-decorated calix[4]arene*, Dyes Pigm. 2019, 171, 107652

B. Bardi, I. Tosi, F. Faroldi, L. Baldini, F. Sansone, C. Sissa, F. Terenziani, *A calixarene-based fluorescent ratiometric temperature probe*, Chem. Commun. 2019, 55, 8098-81101

B. Bardi, C. Dall'Agnese, M. Tassé, S. Ladeira, A. Painelli, K. I. Moineau-Chane Ching, F. Terenziani, *Multistimuli-responsive materials from benzothiadiazole-based charge-transfer chromophores: interdependence of optical properties and aggregation*, ChemPhotoChem 2018, 2, 1027-1037

B. Bardi, C. Dall'Agnese, K. I. Moineau-Chane Ching, A. Painelli, F. Terenziani, *Spectroscopic investigation and theoretical modeling of benzothiadiazole-based charge-transfer chromophores: from solution to nanoaggregates*, J. Phys. Chem. C 2017, 121, 17466-17478

Attachments

Permission for the reproduction of Figure 1.12, p. 41.

ACS Publications
Most Trusted. Most Cited. Most Read.

Near-Unity Quantum Yields for Intersystem Crossing and Singlet Oxygen Generation in Polymethine-like Molecules: Design and Experimental Realization

Author: Scott Webster, Davorin Peceli, Honghua Hu, et al
Publication: Journal of Physical Chemistry Letters
Publisher: American Chemical Society
Date: Aug 1, 2010

PERMISSION/LICENSE IS GRANTED FOR YOUR ORDER AT NO CHARGE

This type of permission/license, instead of the standard Terms & Conditions, is sent to you because no fee is being charged for your order. Please note the following:

- Permission is granted for your request in both print and electronic formats, and translations.
- If figures and/or tables were requested, they may be adapted or used in part.
- Please print this page for your records and send a copy of it to your publisher/graduate school.
- Appropriate credit for the requested material should be given as follows: "Reprinted (adapted) with permission from (COMPLETE REFERENCE CITATION). Copyright (YEAR) American Chemical Society." Insert appropriate information in place of the capitalized words.
- One-time permission is granted only for the use specified in your request. No additional uses are granted (such as derivative works or other editions). For any other uses, please submit a new request.

If credit is given to another source for the material you requested, permission must be obtained from that source.

BACK CLOSE WINDOW